Description of hyperonic matter and hypernuclei within the Brueckner–Hartree–Fock theory

Isaac Vidaña Haro

Departament d'Estructura i
Constituents de la Matèria
Universitat de Barcelona

Description of hyperonic matter and hypernuclei within the Brueckner–Hartree–Fock theory

Memòria presentada per
Isaac Vidaña Haro
per optar al grau de
Doctor en Ciències Físiques.

Barcelona, 2001.

Programa de doctorat
"Partícules, Camps i
Fenòmens Quàntics Col.lectius"
del Departament d'Estructura
i Constituents de la Matèria.
Bienni 1996-98
Universitat de Barcelona.

Directors de Tesi

Artur Polls Martí.

Àngels Ramos Gómez.

Description of hyperonic matter and hypernuclei within the Brueckner–Hartree–Fock theory

I. Vidaña
Departament d'Estructura i Constituents de la Matèria
Universitat de Barcelona, Juny 2001

A mis padres y muy especialmente a mi hermano

"¡Pero sin tesis!"–exclamó D'Artagnan–. "¡Las tesis son insoportables, y solicito su supresión!".

Alejandro Dumas, **Los Tres Mosqueteros**

Contents

Agradecimientos

Escribir los agradecimientos de una tesis no es tarea sencilla pues implica un gran esfuerzo de memoria a fin de no omitir a todas aquellas personas a las que en su momento se prometió casi de manera solemne no olvidar incluirlas en los mismos. Es por ello que creo que, a pesar de haberme devanado durante días los pocos sesos que a estas alturas aún me quedan, será inevitable que esto suceda. Quisiera pues empezar disculpándome ante todas ellas por mi falta de memoria, pedirles que no me lo tengan en cuenta y que no me retiren el saludo cuando me vean por la calle.

Dicho esto, me gustaría agradecer en primer lugar a mis padres el papel vital que han tenido, por razones obvias, en la realización de esta tesis. Muchas gracias por vuestro apoyo y por aguantar a este hijo vuestro, en ocasiones, un tanto gruñón.

Pero aparte de mis padres, hay dos personas a quienes les debo la totalidad de lo que puede encontrarse entre estas páginas. Dos personas, sin cuya ayuda y apoyo no hubiese llegado jamás al final de este largo, permítaseme una pequeña referencia jacobea, camino: Artur y Àngels, o Àngels y Artur, que para mí los dos son iguales. A los dos muchas gracias por ser como sois y por haberme enseñado que la física también tiene su lado humano.

Parte fundamental de esta tesis ha sido sin duda Morten Hjorth-Jensen, o Martino para los amigos, un atípico ejemplo de noruego mediterráneo, con quién he tenido la suerte de trabajar. Gracias a él, creo poder afirmar, sin ánimo de resultar pedante, que me encuentro entre las pocas personas capaces de comprender y saber usar a un noruego. Martino, muchas gracias por tu hospitalidad y por haberme dado la oportunidad de comprender el verdadero sentido de la palabra invierno.

Mención especial para los *sospechosos habituales* con los que he compartido las elevadas temperaturas de ese despacho sin ventanas que ha llegado a convertirse en mi segunda, qué digo segunda, mi primera casa. Manu, quién con su sapiencia cinéfila ha logrado que yo vaya al cine prácticamente dos veces por semana y una de ellas hasta en versión original. Agustí, co-devorador todas las mañanas junto al que suscribe de esos deliciosos y chorreantes croissanes de chocolate del bar de biología. Napo, que al igual que su histórico tocayo nos invade periódicamente desde el departamento de Física Fundamental. Y finalmente, Laura, quién entre viaje y viaje supone el contrapunto imprescindible a tanta monodia masculina. A vosotros muchas gracias por todas las risas que nos hemos echado y por soportar mis reiteradas historias peregrinas.

De todos es conocido que yo soy persona de buen comer, y esto mejor que nadie lo sabe Assum, que ha sufrido con resignación mis constantes incursiones en su despacho en busca de alguna cosa rica con la que engañar a mis escandalosas tripas en las horas que median entre el desayuno y la comida, y entre la comida y la cena. Assum, muchas gracias por ser para mí como una hermana mayor y en especial por los palitroques de pan.

De entre las demás gentes de este departamento no quisiera olvidarme de Marta, la siguiente en estas lides doctorales que, como yo, pronto podrá recetar aspirinas; de Jordi, a quién le debo alguna de las citas que pueden leerse al principio de cada capítulo y cuyo humor ha añadido un punto de causticidad al grupo de nuclear; de Hans, teutón donde los haya, constantemente sorprendido por la cantidad de fiestas que salpican de rojo el calendario laboral de este país; de Suresh, que con su *"I have a question"* y su gran sentido del humor nos ha acercado un poquito al país del Ganges y el Taj Mahal; de José María, quién recuerdo, me vigiló el primer examen que hice en esta santa casa hará ya por lo menos un porrón de años o más; y de Muntsa, que me dió en su momento los problemas de atómica y a quién hasta hace unos meses no había tenido la suerte de conocer mejor.

Gracias también a Francesc, del que echamos de menos sus constantes arengas y soflamas, además del sonoro golpe de tacón con que habitualmente nos saludaba; a Jose Mari, vasco de nacimiento que emulando a sus ilustres predecesores anda haciendo las Américas o, según me han dicho hace poco, el lusitano; a César, compañero, más aplicado que yo, en esto de la física y desde hace unos años en la árdua empresa de aprender la lengua de Chéspir; a Joan, que fiel a sus cuerdas y branas se ha ido a una de las zonas más enredadas de esta bola en la que vivimos; a Ester, una de las pocas personas que conozco capaces de soltar una carcajada cada tres palabras y que ha ayudado a hacer esta tesis más digerible al prestarme su libro de citas; a mi mesetario amiguete David, compañero de juegos en la infancia y de alzacuellos y sotana en la madurez, como no nos echemos novia antes de los treinta; a Jorge, Pedro y Emilio, nefastos musolaris aunque excelentes jugadores de brisca a los que conozco desde hace ya veinte años, sin ellos todos y cada uno de los fines de semana de estos años hubiesen sido ... diferentes; a Elisabeth y Emi, que con su amabilidad y simpatía han hecho que mis comidas en farmacia sean prácticamente caseras; a Javier, gracias a quién mi PSS está resultando un verdadero paseo militar; y finalmente, a mis abuelas, a Isidre, Marcos, Miquel, Jordi, Jose, Pep, Toni, Zacarías, Jesús, Oliver, Miguel Ángel, Miguel, Pepi, María, Yiyo, Ángeles y Augusto, Ariadna, Marina, Pico, Marisa y Adrián, Miguel y Encarni, y otras gentes.

Si llegados a este punto alguien no se ha encontrado todavía le remito al primer párrafo y me reitero en mis disculpas por tal omisión.

Una tesis es prácticamente como un libro, basta que comprobéis el grosor de ésta, lo cual significa que sólo me queda plantar un árbol y tener un hijo para poder morirme tranquilo.

Introduction

“Lasciate ogne speranza, voi ch’intrate”.

Dante Alighieri, **Divina Commedia**, Inferno, canto 3.

The presence of strange baryons, i.e., hyperons (Λ, Σ, Ξ), in finite and infinite nuclear systems has received a lot of attention in the last decades, both from the theoretical and experimental points of view [Ga77, Po78, Ba85, Do89, Os90, Co90, Ba90, Gi95, Ak97, Os98]. Strangeness adds a new dimension to the evolving picture of nuclear physics, and gives us an opportunity to study the fundamental baryon-baryon interactions from an enlarged perspective.

Hypernuclei are bound systems composed of neutrons, protons and one or more hyperons. They were first observed in 1952 with the discovery of a hyperfragment by Danysz and Pniewsli in a balloon–flown emulsion stack [Da53]. The initial cosmic-ray observations of hypernuclei were followed by pion and proton beam production in emulsions and then ^{4}He bubble chambers. The weak decay of the Λ particle into a π^- plus a proton was used to identify the Λ-hypernuclei and to determine binding energies, spins, and lifetimes for masses up to $A = 15$ [Ju73, Da91]. Average properties of heavier systems were estimated from spallation experiments, and two double-Λ hypernuclei were reported from Ξ^- capture [Da63, Pr66]. More systematic investigations of hypernuclei began with the advent of separated K^- beams, which permitted the realization of counter experiments [Pa73].

Although major achievements in hypernuclear physics have been taken at very slow pace due to the limited statistics, the in-flight (K^-, π^-) counter experiments carried out at CERN [Br75, Be79] and Brookhaven (BNL) [Ch79] have revealed a considerable amount of hypernuclear features such as that the Λ particle essentially retains its identity in a nucleus, the small spin-orbit strength, or the, nowadays discarded, narrow widths of Σ-hypernuclei, injecting a renewed interest in the field. Since then, the experimental facilities have been upgraded and experiments using the (π^+, K^+) and $(K^-_{\text{stopped}}, \pi^0)$ reactions are being conducted at the Brookhaven AGS and KEK accelerators with higher intensities and improved energy resolution of the beams.

The electromagnetic production of hypernuclei at the Thomas Jefferson National Laboratory (TJNL), through the reaction $(e, e'K^+)$, promises to provide a new high-precision tool to study Λ-hypernuclear spectroscopy, with resolutions of several hundred keV [Hu94]. In addition, the study of electromagnetic decays of hypernuclear levels using large solid-angle Ge-detectors, should help to define the spectra of lighter hypernuclei. It is also possible that more intense beams of kaons and heavy-ions, coupled with new detection technologies, may provide the means to detect multi-hyperon hypernuclei [Gr88].

In connection with this latter aspect, much less is known about Ξ-hypernuclei or multi-hyperon hypernuclei [Do83]. A few emulsion events [Wi59, Ba63, Bh63, Be68, Ca69, Mo79] have been interpreted as multi-strange hypernuclei, but accelerator-based counter experiments have not been successful in observing the creation of such systems. From the point of view of the conventional many-body problem, a study of the hyperon-hyperon (YY) interaction is very important, and it can be done within a multi-strange hypernucleus. One is reminded here of the recent attempts to find the H-dibaryon [Ba92], whose absence in the experimental data must be telling us something about the hyperon-hyperon interaction. Of course, a direct study of hyperon-hyperon scattering would be extremely valuable, but because these particles have very short lifetimes, this is not possible. Still, there are emulsion events which have been interpreted as either Ξ- or double-Λ hypernuclei. These events, if interpreted correctly, would give the well depth for the $\Lambda\Lambda$ potential [Do91], but the interpretations are open to debate. Clearly, much more experimental information must be obtained on this subject.

From the theoretical side, one of the goals of hypernuclear research is to relate the hypernuclear observables to the bare hyperon-nucleon (YN) and hyperon-hyperon interactions. The experimental difficulties associated with the short lifetime of hyperons and low intensity beam fluxes have limited the number of ΛN and ΣN scattering events to less than one thousand [En66, Al68, Se68, Ka71, Ei71], not being enough to fully constrain the YN interaction. At present, there are two meson-exchange YN potentials: that of the Nijmegen group [Na77, Ma89], where the corresponding baryon-baryon-meson vertices are subject to strict SU(3) symmetry, and that of the Jülich group [Ho89], which assumes a stronger SU(6) symmetry and, therefore, all the coupling constants at strange vertices can be related to those of the nucleon-nucleon (NN) interaction. Recently, the group of Nijmegen has built an extension of its NN and YN interactions to account for the complete octet of baryons, including the YY interaction [Ri99, St99]. Although the Nijmegen and Jülich models are able to describe the scattering data, their spin-isospin structure is very different. Therefore, more data on scattering, especially the measurement of spin observables, are highly desirable.

In the lack of such data, alternative information can be obtained from the study of hypernuclei. One possibility is to focus on light hypernuclei, such as $^{3}_{\Lambda}$H, $^{3}_{\Lambda}$He and $^{4}_{\Lambda}$He, which can be treated "exactly" by solving the 3-body Faddeev [Mi93, Mi95] and 4-body Yakubovsky [Gi88] equations. However, the power of these techniques is limited by the scarce amount of spectroscopic data. Only the ground state energies and a particle stable excited state for each $A = 4$ species can be used to put further constraints on the interaction. Another possibility is the study of hypernuclei with larger masses.

Attempts to derive the hyperon properties in a finite nucleus have followed several approaches. Traditionally, they have been reasonably well described by a shell-model picture using Λ-nucleus potentials of the Woods-Saxon type that reproduce quite well the measured hypernuclear states of medium to heavy hypernuclei [Bo76, Do80, Mo88]. Non-localities and density dependent effects, included in non-relativistic Hartree-Fock calculations using Skyrme hyperon-nucleon interactions [Mi88, Ya88, Fe89, La97, Vi01], improve the overall fit to the single-particle binding energies. The properties of hypernuclei have also been studied in a relativistic framework, such as Dirac phenomenology, where the hyperon-nucleus potential has been derived from the nucleon-nucleus one [Br81, Ch91], or relativistic mean field theory [Ma89b, Ma94, Lo95, Gl93, In96, Su94, Ma96, Ts97].

Microscopic hypernuclear structure calculations, which provide the desired link of the hypernuclear observables to the bare hyperon-nucleon interaction, are also available. They are based on the construction of an effective hyperon-nucleon interaction (G-matrix), which is obtained from the bare hyperon-nucleon potential through a Bethe-Goldstone equation. In earlier microscopic calculations, Gaussian parametrizations of the G-matrix calculated in nuclear matter at an average density [Ya85, Ya90, Ya92, Ya94] were employed. A G-matrix obtained directly in finite nuclei was used to study the single-particle energy levels of various hypernuclei [Ha93]. Nuclear matter G-matrix elements were also used as an effective interaction in a calculation of the $^{17}_{\Lambda}$O spectrum [Ha93b]. In this thesis we will derive microscopically, along the similar lines of Ref. [Hj96], the s- and p-wave Λ single-particle properties for a variety of Λ-hypernuclei, from $^{5}_{\Lambda}$He to $^{208}_{\Lambda}$Pb, constructing a finite nucleus YN G-matrix obtained from a nuclear matter G-matrix. This method was first employed to study the nucleon and Δ properties in nuclei [Bo92, Hj94].

In addition to hypernuclei, nuclear physicists have also been interested in hyperonic matter (nuclear matter with nucleonic and hyperonic degrees of freedom), especially in connection with the physics of neutron star interiors. These objects are an excellent observatory to test our understanding of the theory of strong interacting matter at extreme densities. The interior of neutron stars is dense enough to allow for the appearance of new particles with strangeness content besides the conventional nucleons and leptons by virtue of weak equilibrium. There is a growing evidence that hyperons appear as the first strange hadrons in neutron star matter at around twice normal nuclear density [Gl85], as has been recently confirmed within effective non-relativistic potential models [Ba97], the Quark-Meson Coupling Model [Pa99], extended relativistic mean field approaches [Kn95, Sc96], relativistic Hartree–Fock [Hu98] and Brueckner–Hartree–Fock theory [Ba00, Vi00b].

Properties of neutron stars are closely related to the underlying Equation of State

(EoS) of matter at high densities. These properties are affected by the presence of strangeness [Gl97, Pr97]. A strong deleptonization of the neutron star matter occurs when hyperons appear, since it is energetically more convenient to maintain charge neutrality through hyperon formation than from β-decay. In addition, it is clear that the main effect of the presence of hyperons in dense matter is to soften the EoS, which translates into a lower maximum mass of the neutron star [Gl97]. Other properties, such as thermal and structural evolution of neutron stars, are also very sensitive to the composition and, therefore, to the strangeness content of neutron star interiors. From the observational point of view, measurements of the surface temperature of neutron stars, possible with satellite-based X-ray observatories, could tell us whether these exotic components of nuclear matter are playing a role in the cooling processes. Furthermore, one of the major goals of the Laser Interferometer Gravitational-wave Observatory (LIGO) is to measure gravity waves emitted in the coalescence of two neutron stars. The pattern of the emitted waves just prior to the merging is sensitive to the structure of the stars and to the Equation of State.

Despite hyperonic matter is obviously an idealized physical system, the theoretical determination of the corresponding EoS is an essential step towards the understanding of the physical properties of neutron stars. In addition, the comparison of the theoretical predictions for the properties of these objects with the observations can provide strong constraints on the interactions among their constituents. Therefore, a detailed knowledge of the EoS over a wide range of densities is required [Sh83]. This is a very hard task from the theoretical point of view. Traditionally, two approaches have been followed to describe the baryon-baryon interaction in the nuclear medium and, to construct from it the EoS: the so-called phenomenological approach and the microscopic approach.

In the phenomenological approach the input is a density-dependent effective interaction which contains a certain number of parameters adjusted to reproduce experimental data, such as the properties of nuclei or the empirical saturation properties of nuclear matter. There exists an enormous number of different phenomenological interactions, such as the Migdal [Mi67] and Gogny [Go75] forces. But the most popular of them is the Skyrme interaction [Sk56, Va72]. This force has gained so much importance because it reproduces the nuclear binding energies and the nuclear radii over the whole periodic table with a reasonable set of parameters [Va72]; there is a connection [Ne72] between this force and the more fundamental G-matrix commented below, and its mathematical form is extremely simple. Balberg and Gal [Ba97, Ba99] have recently derived an analytic effective EoS using density-dependent baryon-baryon potentials based on Skyrme-type forces including hyperonic degrees of freedom. The features of this Equation of State rely on the properties of nuclei for the nucleon-nucleon interaction, and mainly on experimental data from hypernuclei for the hyperon-nucleon and hyperon-hyperon interactions. It reproduces typical properties of high density matter found in theoretical microscopic models.

An alternative phenomenological approach involves the formulation of an effective relativistic mean field (RMF) theory of interacting hadrons [Se86, Se97]. This approach treats the baryonic and mesonic degrees of freedom explicitly, is fully relativistic, and is, in general, easier to handle because it only involves local densities and fields. The EoS of dense matter with hyperons was first described within the RMF model by Glendenning [Gl82, Gl85, Gl87]. Among other shortcomings the standard RMF approach is not suited to reproduce the strong attractive hyperon-hyperon interaction seen in double-Λ hypernuclei. Nevertheless, Schaffner *et al.* [Sc93, Sc94] have solved the problem by incorporating additional strange meson fields into the standard lagrangian of the model. The set of parameters of this model is fixed by the properties of nuclei and nuclear bulk matter for the nucleonic sector, whereas the coupling constants of the hyperons are fixed by SU(6)-symmetry relations and hypernuclear observables.

In a microscopic approach, on the other hand, the input is a two-body baryon-baryon interaction that describes the scattering observables in free space, such as the Bonn-Jülich [Ma87, Ho89] or Nijmegen [Na73, Na77, Na78, Ma89, St94, Ri99, St99] potentials. These realistic interactions are constructed within the framework of a meson exchange theory. In order to obtain the EoS one has to solve the complicated many-body problem. The main great difficulty of this problem lies in the treatment of the strong repulsive core, which dominates the short-range behaviour of the interaction. Various methods have been considered to solve the many-body problem, the most employed ones being the variational approach and the Brueckner–Bethe–Goldstone theory.

The variational approach suggested by Jastrow [Ja55] makes use of trial wave functions to treat the two-nucleon correlations. The EoS of asymmetric nuclear matter has been considered by several authors [Wi88, Ak97b, Bo98] within this approach and, in fact, the calculation of Akmal *et al.* [Ak98], using the Argonne V_{18} NN interaction [Wi95] with relativistic boost corrections and a fitted three-body interaction model, may be viewed as the currently most realistic approach to the nucleonic sector. Nevertheless, hyperons have not been considered within this approach yet.

An alternative way to the variational approach for treating the many-body problem is provided by the Brueckner–Bethe–Goldstone (BBG) theory. Brueckner and co-workers [Br54] developed a method to sum to infinite order the so-called particle-particle ladder diagrams, which take into account the short-range two-particle correlations. A step forward towards the application to nuclear systems was established by Bethe [Be56] through the development of the hole-line expansion. A formal basis for this approach was provided by Goldstone [Go57] who, using perturbation methods, established the so-called linked-cluster expansion. The BBG theory has been extensively applied to the study of normal nuclear matter, and recently to hyperonic matter. Schulze *et al.* [Sc98] performed a many-body calculation of the Brueckner-type in order to study the onset of hyperon formation in neutron star matter. Recently, these authors have extended their study to neutron stars with hyperons [Ba00], paying special attention to the role played by three-body nucleon forces. Nevertheless, these studies do not include the hyperon-hyperon interaction, which is, however, essential as soon as the first hyperon, the Σ^-, appears in matter. In this sense, one of the goals of this thesis is to include the hyperon-hyperon interaction in a microscopic many-body calculation of the Brueckner-type and to study the properties of β-stable neutron star matter with hyperonic degrees of freedom.

In order to make things easier to the reader we give here an outlook of the way this thesis is organized:

A brief summary of the meson exchange theory and the Brueckner–Bethe–Goldstone theory is given in Chapter 1.

Following the theoretical framework presented in Chapter 1, in Chapter 2 we show results from microscopic Brueckner-type calculations of dense matter that include all types of baryon-baryon interactions and allow one to treat any asymmetry in the fractions of the different species ($n, p, \Lambda, \Sigma^-, \Sigma^0, \Sigma^+, \Xi^-$ and Ξ^0). We also present results for the single-particle potentials and the binding energy per baryon, focusing on baryonic densities and hyperonic fractions that can be relevant in neutron star matter with strangeness in β-equilibrium, a problem that will be discussed in Chapter 4.

With regard to the hyperon properties in finite nuclei, in Chapter 3 we determine the single-particle energy and wave function of the Λ hyperon in several nuclei obtained from the relevant self-energy. The latter is constructed within the framework of a perturbative many-body approach employing present realistic hyperon-nucleon interactions such as the models of the Jülich and Nijmegen groups. The effects of non-locality and energy dependence of the self-energy on the bound states are investigated. It is shown that, although the single-particle hyperon energies are well reproduced by local Woods-Saxon potentials, the wave functions from the non-local self-energy are more extended.

As mentioned before, in Chapter 4 we present results from Brueckner–Hartree–Fock calculations for β-stable neutron star matter with nucleonic and hyperonic degrees of freedom, employing the most recent parametrization of the baryon-baryon interaction of the Nijmegen group. It is found that the only strange baryons emerging in β-stable matter up to total baryonic densities of 1.2 fm^{-3} are the Σ^- and Λ. We compute the corresponding EoS and determine properties of neutron stars such as the mass, radius and moment of inertia.

The main conclusions of this work are summarized and exposed at the end of the manuscript.

Chapter 1

The baryon-baryon interaction and the nuclear many-body problem

> "How empty is theory in the presence of fact".
>
> *Mark Twain*, **A Connecticut Yankee in King Arthur's Court**.

We devote this chapter to present the theoretical background in which this thesis is seated. Due to the fact that the starting point of our theoretical scheme is the baryon-baryon interaction, section 1.1 reviews briefly the basic ideas of the meson exchange theory, the Bethe–Salpeter equation and its non-relativistic reductions, and some of the main features of the Jülich [Ho89] hyperon-nucleon and Nijmegen Soft-Core [Ma89, Ri99, St99] baryon-baryon interactions. A little tour through the Goldstone expansion, the Brueckner reaction matrix, the Bethe–Golstone equation and the hole-line expansion is performed in section 1.2. Finally, all the technicalities required in solving the Bethe-Goldstone equation are given in section 1.3.

1.1 The baryon-baryon interaction

Quantum chromodynamics (QCD) is commonly recognized as the fundamental theory of the strong interaction, and therefore, in principle, the baryon-baryon interaction V can be completely determined by the underlying quark-gluon dynamics in QCD. Nevertheless, due to the mathematical problems raised by the non-perturbative character of QCD at low and intermediate energies (at this range of energies the coupling constants become too large for perturbative approaches), one is still far from a quantitative understanding of the baryon-baryon interaction from the QCD point of view. This problem is, however, usually circumvented by introducing a simplified model in which only hadronic degrees of freedom are assumed to be relevant. Quarks are confined inside the hadrons by the strong interaction and the baryon-baryon force arises from meson exchange [Na73, Ma87]. Such an effective description is presently the most quantitative representation of the fundamental theory in the energy regime of nuclear physics, although a big effort is being invested recently in understanding the baryon-baryon interaction from an Effective Field Theory perspective [Ko99]. Quark degrees of freedom are expected to become important only at very short distances and high energies. Short-range parts of the interaction are treated, in all meson exchange models, by including form factors which take into account, in an effective way, the extended structure of the hadrons.

In the next section we briefly present the phenomenological lagrangians which define the interactions among the various baryons and mesons, and review the general properties of the meson-exchange theory. To avoid unnecessary overlaps with already existing review articles and books on the subject, only a brief account of the underlying theory is given. In section 1.1.2 we discuss the three-dimensional reduction of the Bethe–Salpeter equation, which defines the scattering matrix. Finally, we devote section 1.1.3 to show some of the characteristics of the Jülich [Ho89] hyperon-nucleon and Nijmegen Soft-Core [Ma89, Ri99, St99] baryon-baryon interaction models, which are the ones employed in all the calculations of the present thesis.

1.1.1 The one-boson-exchange interaction

The three relevant meson field types that mediate the interaction among the different baryons are:

- the scalar (s) field: σ, δ
- the pseudoscalar (ps) field: $\boldsymbol{\pi}$, η, η', $\boldsymbol{K}$
- the vector (v) field: $\boldsymbol{\rho}$, ω, $\boldsymbol{K}^*$

Guided by symmetry principles, simplicity and physical intuition the most commonly employed interaction lagrangians that couple these meson fields to the baryon ones are

$$\mathcal{L}_s = g_s \bar{\Psi}\Psi\phi^{(s)} \ , \tag{1.1}$$

$$\mathcal{L}_{ps} = g_{ps} \bar{\Psi} i\gamma^5 \Psi\phi^{(ps)} \ , \tag{1.2}$$

$$\mathcal{L}_v = g_v \bar{\Psi}\gamma^\mu\Psi\phi^{(v)}_\mu + g_t \bar{\Psi}\sigma^{\mu\nu}\Psi \left(\partial_\mu\phi^{(v)}_\nu - \partial_\nu\phi^{(v)}_\mu\right) \ , \tag{1.3}$$

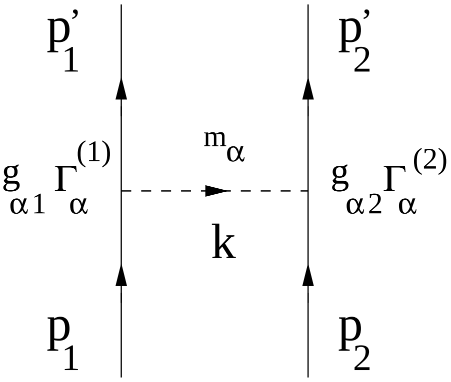

Figure 1.1: Diagrammatic representation of the one-boson-exchange contribution to baryon-baryon scattering. The solid lines denote the baryons, the dashed line the meson with mass m_α and four-momentum $k = p_1 - p_1'$. At the vertices, the coupling constants are denoted by $g_{\alpha 1}$ and $g_{\alpha 2}$, while $\Gamma_\alpha^{(1)}$ and $\Gamma_\alpha^{(2)}$ denote the corresponding Dirac structures.

for scalar, pseudoscalar and vector coupling, respectively. Alternatively, for the pseudoscalar field there is also the so-called pseudovector (pv) or gradient coupling, which is suggested as an effective coupling by chiral symmetry [We67, Br79]

$$\mathcal{L}_{pv} = g_{pv} \bar{\Psi} \gamma^5 \gamma^\mu \Psi \partial_\mu \phi^{(ps)} \ . \tag{1.4}$$

In the above expressions Ψ denotes the baryon field for spin 1/2 baryons, while $\phi^{(s)}, \phi^{(ps)}$ and $\phi^{(v)}$ are the corresponding scalar, pseudoscalar and vector meson fields. The factor g_s is the phenomenological coupling constant coefficient for scalar mesons, while g_{ps} and g_{pv} are the corresponding pseudoscalar and pseudovector coupling constants for pseudoscalar meson exchange. Similarly, g_v and g_t are the vector and tensor coupling constants, respectively. These coupling constants may be constrained by e.g. scattering data. Note that the above lagrangians are for isoscalar mesons, however, for isovector mesons, the fields ϕ trivially modify to $\boldsymbol{\tau} \cdot \boldsymbol{\phi}$ with $\boldsymbol{\tau}$ being the familiar isospin Pauli matrices.

Employing the above lagrangians, it is possible to construct a one-boson-exchange (OBE) potential model. A typical contribution to the baryon-baryon scattering amplitude arising from the exchange of a certain meson α is depicted in Fig. 1.1. Applying the corresponding Feynman diagram rules this contribution is given by

$$\langle p_1' p_2' | V_\alpha^{OBE} | p_1 p_2 \rangle = \frac{\bar{u}(p_1') g_{\alpha 1} \Gamma_\alpha^{(1)} u(p_1) P_\alpha \bar{u}(p_2') g_{\alpha 2} \Gamma_\alpha^{(2)} u(p_2)}{(p_1 - p_1')^2 - m_\alpha^2} \ , \tag{1.5}$$

where m_α is the mass of the exchanged meson, $P_\alpha / ((p_1 - p_1')^2 - m_\alpha^2)$ represents the meson propagator, u is the familiar Dirac spinor

$$u(k, \boldsymbol{\sigma}) = \sqrt{\frac{E(k) + M}{2M}} \begin{pmatrix} \chi \\ \frac{\boldsymbol{\sigma} \cdot \mathbf{k}}{E(k)+M} \chi \end{pmatrix} \ , \tag{1.6}$$

and $\bar{u}$ its adjoint ($\bar{u}u = 1$, $\bar{u} = u^\dagger \gamma^0$). The symbols $g_{\alpha 1}$ and $g_{\alpha 2}$ are the coupling constants at the vertices, and $\Gamma_\alpha^{(1)}$ and $\Gamma_\alpha^{(2)}$ denote the corresponding Dirac structures, i.e.,

$$\Gamma_s^{(i)} = \mathbf{1}, \quad \Gamma_{ps}^{(i)} = i\gamma^5 \ , \tag{1.7}$$

$$\Gamma_v^{(i)} = \gamma^\mu, \quad \Gamma_t^{(i)} = \sigma^{\mu\nu} \ , \quad \Gamma_{pv}^{(i)} = \gamma^5 (\gamma^\mu \cdot \partial_\mu) \ , \tag{1.8}$$

the label i referring to the interacting baryon 1 or 2.

In general, when all types of mesons are included, the one-boson-exchange interaction is given by the sum of all the partial contributions

$$\langle p_1' p_2' | V^{OBE} | p_1 p_2 \rangle = \sum_\alpha \langle p_1' p_2' | V_\alpha^{OBE} | p_1 p_2 \rangle \ . \tag{1.9}$$

Expanding the free Dirac spinor in terms of $1/M$ (M is here the mass of the relevant baryon) to lowest order leads to the familiar non-relativistic expressions for the baryon-baryon potentials, which through Fourier transformation give the configuration space version of the interaction. The general expression for the local approximation of the baryon-baryon interaction in configuration space is

$$\begin{aligned} V(\mathbf{r}) = \sum_\alpha \Bigg\{ & C_{C_\alpha} + C_{\sigma_\alpha} \boldsymbol{\sigma}_1 \cdot \boldsymbol{\sigma}_2 + C_{T_\alpha} \left(1 + \frac{3}{m_\alpha r} + \frac{3}{(m_\alpha r)^2} \right) S_{12}(\hat{r}) \\ & + C_{LS_\alpha} \left(\frac{1}{m_\alpha r} + \frac{1}{(m_\alpha r)^2} \right) \mathbf{L} \cdot \mathbf{S} \Bigg\} \frac{e^{-m_\alpha r}}{m_\alpha r} \ , \end{aligned} \tag{1.10}$$

where $C_{C_\alpha}, C_{\sigma_\alpha}, C_{T_\alpha}$ and C_{LS_α} are numerical factors, and S_{12} is the familiar tensor term in configuration space

$$S_{12}(\hat{r}) = 3 \frac{(\boldsymbol{\sigma_1} \cdot \mathbf{r})(\boldsymbol{\sigma_2} \cdot \mathbf{r})}{r^2} - (\boldsymbol{\sigma_1} \cdot \boldsymbol{\sigma_2}) \ . \tag{1.11}$$

Finally, we have to remember that in the meson exchange theory all meson-baryon vertices must be necessarily modified by the introduction of the so-called form factors. Each vertex is multiplied by a form factor of the type

$$F_\alpha(\vec{k}^2) = \left(\frac{\Lambda_\alpha^2 - m_\alpha^2}{\Lambda_\alpha^2 + \vec{k}^2} \right)^{n_\alpha} \ , \tag{1.12}$$

as is done in the Jülich models [Ho89], or by

$$F_\alpha(\vec{k}^2) = e^{-\frac{\vec{k}^2}{2\Lambda_\alpha^2}} \ , \tag{1.13}$$

as is preferred in the Nijmegen models [Ma89, Ri99, St99].

In the above expressions the quantity n_α is usually taken equal to 1 (monopole form factor) or 2 (dipole form factor). The vector $\vec{k}$ denotes the three-momentum transfer, whereas m_α is the mass of the corresponding exchanged meson, and Λ_α are the so-called cut-off masses, typically of the order $1.2 - 2$ GeV.

Originally the form factors were introduced for purely mathematical reasons, namely, to avoid divergences in the scattering equation. Nevertheless, our present knowledge of the (quark) substructure of baryons and mesons provides a physical reason for their presence. Obviously, it does not make sense to take meson exchange seriously in a region in which modifications due to the extended structure of hadrons come into play.

1.1.2 The Bethe–Salpeter equation

In order to fix the parameters which define the baryon-baryon potential derived from OBE models, the Bethe–Salpeter equation is used as the starting point for most calculations. In an arbitrary frame, the full covariant Bethe–Salpeter equation reads (suppressing spin and isospin labels for simplicity)

$$\begin{aligned}\langle p_1'p_2'|\mathcal{T}|p_1p_2\rangle = \langle p_1'p_2'|\mathcal{V}|p_1p_2\rangle + \frac{i}{(2\pi)^4}\int d^4k \langle p_1'p_2'|\mathcal{V}|P+k, P-k\rangle \\ \times S_{(1)}(P+k)S_{(2)}(P-k)\langle P+k, P-k|\mathcal{T}|p_1p_2\rangle \ , \qquad (1.14)\end{aligned}$$

where we have defined P to be half the total four-momentum, i.e., $P = \frac{1}{2}(p_1 + p_2)$, and k to be the relative four-momentum. The term $S_{(i)}$ is the relativistic fermion propagator, which for spin 1/2 baryons reads

$$S_{(i)} = \frac{1}{\not{p}_i - M_i + i\epsilon} \ , \qquad (1.15)$$

$\mathcal{T}$ represents the invariant amplitude for the two-particle scattering process, commonly called T-matrix, and $\mathcal{V}$ is the sum of all linked two-particle irreducible diagrams.

As this four-dimensional integral equation is rather tedious to solve, it is commonly replaced by three-dimensional reductions, which are more practical for numerical solution. Nevertheless, the three-dimensional reduction is not unique, and in principle infinitely many choices exist. It is common to the derivation of all three-dimensional reductions to fix the time component of the relative four-momentum in some way, so that it no longer appears as a separate variable in the propagator.

Based on a suggestion by Blankenbecler and Sugar [Bl66], one possible three-dimensional approach to the Bethe–Salpeter equation in the centre-of-mass frame (omitting angular momentum, spin and isospin assignments, and assuming $M_1 = M_2 = M$ for simplicity) reads

$$T(\mathbf{k},\mathbf{k}') = V(\mathbf{k},\mathbf{k}') + \int_0^\infty \frac{d^3q}{(2\pi)^3} V(\mathbf{k},\mathbf{q}) \frac{M^2}{E_q} \frac{1}{\hbar^2\mathbf{k}^2 - \hbar^2\mathbf{q}^2 + i\epsilon} T(\mathbf{q},\mathbf{k}') \ . \tag{1.16}$$

Within the OBE model, the quasi-potential V is a sum of OBE amplitudes (see Eq. (1.9)). The Bethe–Salpeter equation is also denoted as the ladder approximation when the quasi-potential V is iterated in it. If we define

$$\hat{T}(\mathbf{k},\mathbf{k}') = \sqrt{\frac{M}{E_k}} T(\mathbf{k},\mathbf{k}') \sqrt{\frac{M}{E_{k'}}} \ , \tag{1.17}$$

and

$$\hat{V}(\mathbf{k},\mathbf{k}') = \sqrt{\frac{M}{E_k}} V(\mathbf{k},\mathbf{k}') \sqrt{\frac{M}{E_{k'}}} \ , \tag{1.18}$$

which has become known as "minimal relativity", we can rewrite Eq. (1.16) as

$$\hat{T}(\mathbf{k},\mathbf{k}') = \hat{V}(\mathbf{k},\mathbf{k}') + \int_0^\infty \frac{d^3q}{(2\pi)^3}\hat{V}(\mathbf{k},\mathbf{q})\frac{M}{\hbar^2\mathbf{k}^2 - \hbar^2\mathbf{q}^2 + i\epsilon}\hat{T}(\mathbf{q},\mathbf{k}') \ , \tag{1.19}$$

which has the same form as the non-relativistic Lippmann-Schwinger equation, and can therefore be applied to conventional non-relativistic nuclear structure calculations in the usual way.

Another choice that has frequently been applied is the version suggested by Thompson [Th70] which reads

$$T(\mathbf{k},\mathbf{k}') = V(\mathbf{k},\mathbf{k}') + \int_0^\infty \frac{d^3q}{(2\pi)^3}V(\mathbf{k},\mathbf{q})\frac{M^2}{E_q^2}\frac{1}{2E_k - 2E_q + i\epsilon}T(\mathbf{q},\mathbf{k}') \ , \tag{1.20}$$

and defining

$$\hat{T}(\mathbf{k},\mathbf{k}') = \frac{M}{E_k}T(\mathbf{k},\mathbf{k}')\frac{M}{E_{k'}} \ , \tag{1.21}$$

$$\hat{V}(\mathbf{k},\mathbf{k}') = \frac{M}{E_k}V(\mathbf{k},\mathbf{k}')\frac{M}{E_{k'}} \ , \tag{1.22}$$

we can rewrite Eq. (1.18) as

$$\hat{T}(\mathbf{k},\mathbf{k}') = \hat{V}(\mathbf{k},\mathbf{k}') + \int_0^\infty \frac{d^3q}{(2\pi)^3}\hat{V}(\mathbf{k},\mathbf{q})\frac{1}{2E_k - 2E_q + i\epsilon}\hat{T}(\mathbf{q},\mathbf{k}') \ , \tag{1.23}$$

which has also the form of the Lippmann-Schwinger equation, but with relativistic energies. The Thompson choice is therefore useful for relativistic nuclear structure calculations.

Many more choices have been suggested in the literature. A thorough discussion of the Bethe–Salpeter equation and/or a systematic study of a large family of possible three-dimensional reductions can be found in [Na69, Wo73, Ho75, Br76].

1.1.3 The Jülich and Nijmegen Soft-Core models

Until now all we have said is general and nothing has been commented about the specific baryon-baryon interactions employed in our calculations. These interactions are in particular the Jülich B [Ho89], the Nijmegen Soft-Core 89 [Ma89] hyperon-nucleon interactions, and the recent Nijmegen Soft-Core 97 [Ri99, St99] baryon-baryon interaction for the complete octet of baryons. We present briefly in the following some of the main features of these models and refer the interested reader to the original works for detailed information.

To begin with, we must say that these three models are meson-exchange potentials, and therefore they are constructed following the basic ideas exposed in section 1.1.1.

The Jülich B hyperon-nucleon interaction is constructed in complete analogy to the Bonn nucleon-nucleon interaction [Ma87]. It is defined in momentum space and contains the full energy-dependence and non-locality structure. Besides single-meson exchange processes, it includes higher-order processes involving π- and ρ-exchange processes (correlated 2π-exchange are conveniently parametrized in terms of an effective σ-exchange) and, in addition, KK, KK^*, K^*K^* processes with N, Δ, Λ, Σ and $\Sigma^*(1385)$ intermediate states. Therefore, the model not only includes the couplings between the ΛN and ΣN channels, but also couplings to the $\Delta\Lambda, \Delta\Sigma$ and NΣ^* ones. The exchange of pseudoscalar mesons η and η' is not considered. Parameters (coupling constants and cut-off masses) at NN and NΔ vertices are taken from the Bonn model. Coupling constants at the vertices involving strange particles are fixed by relating them, under the assumption of SU(6) symmetry, to the NN and NΔ values. Thus, the only free parameters are the cut-off masses at the strange vertices which are adjusted to the existing hyperon-nucleon data. The form factors at the vertices are parametrized in the conventional monopole form or dipole form when the vertex involves both a spin-$\frac{3}{2}$ and a vector meson.

The Nijmegen Soft-Core 89 hyperon-nucleon interaction (hereafter and in the next Chapters referred to as NSC89) is obtained by a straightforward extension of the Nijmegen nucleon-nucleon model [Na78] through the application of SU(3) symmetry. It is defined both in momentum space and in configuration space. The model is generated by the exchange of nonets of pseudoscalar and vector mesons, and scalar mesons. Assuming SU(3) symmetry all the coupling constants at the vertices with strange particles are related to the NN ones. Gaussian form factors are taken at the vertices to guarantee a soft behaviour of the potentials in configuration space at small distances.

Finally, the recent Nijmegen Soft-Core 97 (NSC97a-f) baryon-baryon interaction for the complete octet of baryons is based on SU(3) extensions of the Nijmegen potential models for the nucleon-nucleon [Na78] and the hyperon-nucleon [Ma89] interactions. It describes not only the sectors of strangeness 0 (NN) and -1 (ΛN, ΣN), but also the ones of strangeness -2 ($\Lambda\Lambda, \Lambda\Sigma, \Sigma\Sigma, \Xi$N), -3 ($\Lambda\Xi, \Sigma\Xi$) and -4 ($\Xi\Xi$). It is parametrized in terms of one-boson exchanges, and all coupling constants are determined by a fit to the NN and YN scattering data and using SU(3) relations. However, the fit to the NN and YN data still allows for some freedom in the parameters and so there are six different models (from NSC97a to NSC97f). These models are characterized by different choices for the magnetic vector $F/(F+D)$ ratio, α_v^m, which serves to produce different scattering lengths in the ΛN and ΣN channels, but at the same time allows to describe the available YN and NN scattering data equally well. Within each model, there are no free parameters left, and so each parameter set defines a baryon-baryon potential that models all possible two-baryon interactions. Gaussian form factors are taken as in the case of the NSC89 model.

1.2 The nuclear many-body problem

One of the main difficulties with nuclear many-body systems such as finite nuclei or nuclear matter arises from the fact that, generally, the baryon-baryon interaction V is repulsive at short distances and thus any perturbation expansion in terms of V becomes meaningless: all the terms of the perturbation series are very large for a "soft core" potential, or infinite in the case of a "hard core" potential (i.e., infinitely repulsive core). The first step towards the solution of this problem was proposed by Brueckner [Br54], who remarked that the situation was similar to that encountered in the single-particle scattering by a hard sphere: although all the terms of the Born series for the T-matrix diverge, the T-matrix itself is a well-defined finite object which can be obtained by solving the Lippmann-Schwinger integral equation. Hence for hard sphere scattering the solution of the problem is obtained by working with T instead of V. For the nuclear many-body problem, the idea was thus to replace the bare interaction by a generalized T-matrix in order to take into account the presence of the other particles. Using diagram techniques Goldstone [Go57] showed how this generalization of the T-matrix, usually referred to as Brueckner's reaction matrix, could be obtained from perturbation theory.

The Goldstone expansion is presented, although not derived, in section 1.2.1. The

Brueckner reaction matrix is introduced in section 1.2.2. Section 1.2.3 is devoted to the convergence of the Brueckner-Goldstone expansion and 1.2.4 to the choice of the auxiliary potential U, introduced in section 1.2.1.

1.2.1 The Goldstone expansion

The Goldstone expansion [Go57] is a linked-cluster perturbation series for the ground-state energy of a fermionic many-body system. We will not derive the Goldstone expansion, but we will try to present it in a simple way.

The Goldstone expansion works for any number of particles as long as the unperturbed ground state is non-degenerate. Let us consider a system of a certain number A of identical fermions in a volume Ω whose dynamics is described by the hamiltonian

$$H = \sum_{i=1}^{A} T_i + \sum_{i<j}^{A} V_{ij} \ , \tag{1.24}$$

where T_i is the kinetic energy of particle i, and V_{ij} denotes the two-body interaction between particles i and j.

If an appropriate single-particle potential U_i is added and subtracted, then, the hamiltonian can be rewritten as an unperturbed part

$$H_0 = \sum_{i=1}^{A} (T_i + U_i) \ , \tag{1.25}$$

and a perturbation

$$H_1 = \sum_{i<j}^{A} V_{ij} - \sum_{i=1}^{A} U_i \ . \tag{1.26}$$

This single-particle potential U_i is introduced in order to make numerical calculations easier. Obviously, the final result should in principle be independent of U_i, since the total hamiltonian does not involve it. However, as we will see below, the energy is calculated as an expansion in powers of H_1, and the expansion will converge more rapidly for some choices of U_i than for others. Thus, we must choose U_i in such a way that the energy expansion converges rapidly enough to be useful for practical calculations.

The unperturbed ground state satisfies the Schrödinger equation

$$H_0|\Phi_0\rangle = E_0|\Phi_0\rangle \ . \tag{1.27}$$

Since H_0 contains only one-body operators, to solve the unperturbed part we only need to find the one-particle eigenstates $|\alpha_i\rangle$ of the operator $T_i + U_i$ which satisfy the one-particle Schrödinger equation

$$(T_i + U_i)|\alpha_i\rangle = \epsilon_i|\alpha_i\rangle \ . \tag{1.28}$$

The one-particle states $|\alpha_i\rangle$ are assumed to form a complete orthonormal set, which in the particular case of an infinite many-body system (i.e., $A \to \infty$, $\Omega \to \infty$ but keeping $\rho = A/\Omega =$ constant), such as nuclear matter, are plane waves. The unperturbed and uncorrelated ground state $|\Phi_0\rangle$ is then represented by a Slater determinant constructed by putting the particles into the A one-particle states of lowest energy, making up in this way the so-called Fermi sea, which corresponds to the particle-hole vacuum field defined in Goldstone theory. All states of higher energy are above the Fermi sea.

It is this state which is assumed to be non-degenerate. The eigenvalue E_0 is the sum of the one-particle energies of the occupied states,

$$E_0 = \sum_{i \leq A} \epsilon_i = \sum_{i \leq A} \langle \alpha_i | T + U | \alpha_i \rangle \quad . \tag{1.29}$$

The exact correlated ground state $|\Psi\rangle$ satisfies

$$H|\Psi\rangle = E|\Psi\rangle \ , \tag{1.30}$$

being E the true energy of the system. It can be written as the sum of the unperturbed energy E_0 plus the so-called ground state energy shift ΔE,

$$E = E_0 + \Delta E \ . \tag{1.31}$$

Perturbation theory gives the formal expression for the energy shift, which up to third order in H_1 is

$$\begin{aligned}\Delta E = \langle \Phi_0 | H_1 | \Phi_0 \rangle + \langle \Phi_0 | H_1 \frac{P}{E_0 - H_0} H_1 | \Phi_0 \rangle + \\ + \langle \Phi_0 | H_1 \frac{P}{E_0 - H_0} H_1 \frac{P}{E_0 - H_0} H_1 | \Phi_0 \rangle - \\ - \langle \Phi_0 | H_1 | \Phi_0 \rangle \langle \Phi_0 | H_1 \frac{P}{(E_0 - H_0)^2} H_1 | \Phi_0 \rangle \ ,\end{aligned} \tag{1.32}$$

where

$$P = \mathbf{1} - |\Phi_0\rangle\langle\Phi_0| \tag{1.33}$$

projects off $|\Phi_0\rangle$ ensuring that $|\Phi_0\rangle$ does not occur as an intermediate state in any of the matrix elements, i.e., in the intermediate states at least one particle has to be excited.

Taking into account that the correlated wave function $|\Psi\rangle$ and the uncorrelated one $|\Phi_0\rangle$ satisfy the integral equation [Ma80]

$$|\Psi\rangle = |\Phi_0\rangle + \frac{P}{E_0 - H_0} H_1 |\Psi\rangle \ , \tag{1.34}$$

it is possible to write the perturbation expansion in the form

$$E = E_0 + \frac{\langle\Phi_0|H_1|\Psi\rangle}{\langle\Phi_0|\Psi\rangle} \ . \tag{1.35}$$

Using diagram techniques Goldstone showed [Go57] that the quantity $\langle\Phi_0|H_1|\Psi\rangle$ can be factorized into the product of a quantity which is equal to $\langle\Phi_0|\Psi\rangle$ (and which thus cancels the denominator in Eq. (1.35)) multiplied by a quantity which *only contains linked diagrams* (i.e. those diagrams which cannot be separated into two pieces by a vertical cut which would not cross any line). The perturbation expansion then reads

$$E = E_0 + \langle\Phi_0|H_1 \sum_{n=0}^{\infty} \left[\frac{1 - |\Phi_0\rangle\langle\Phi_0|}{E_0 - H_0} H_1 \right]^n |\Phi_0\rangle_l \ , \tag{1.36}$$

which is the so-called Goldstone expansion. The lower index l refers to the fact that one should only retain those contributions which are represented by *linked* diagrams.

The first-order diagrams which contribute to ΔE are shown in Fig. 1.2 (a), (b) and (c). Diagram (a) is the direct term, (b) the exchange term and (c) involves the

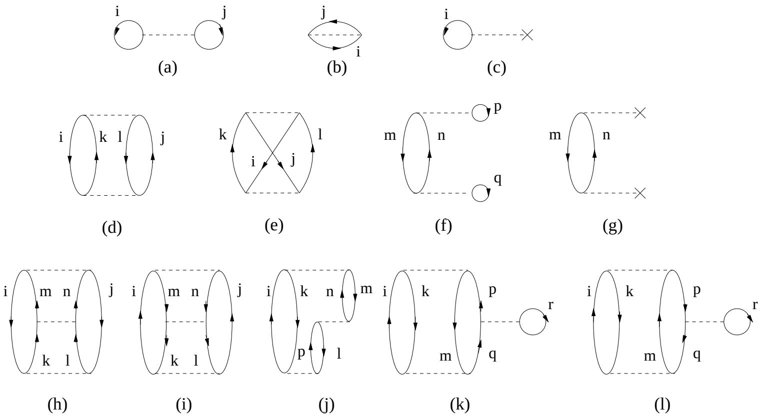

Figure 1.2: First-order ((a), (b), (c)), second-order ((d), (e), (f), (g)) and third-order ((h), (i), (j), (k), (l)) diagrams appearing in the linked-cluster Goldstone expansion.

single-particle potential U. Their contributions are, respectively

$$\frac{1}{2}\sum_{i,j\leq A}\langle\alpha_i\alpha_j|V|\alpha_i\alpha_j\rangle, \quad -\frac{1}{2}\sum_{i,j\leq A}\langle\alpha_i\alpha_j|V|\alpha_j\alpha_i\rangle, \\ -\sum_{i\leq A}\langle\alpha_i|U|\alpha_i\rangle \ . \tag{1.37}$$

Therefore we can write

$$\Delta E^{1^{st}} = \langle\Phi_0|H_1|\Phi_0\rangle = \frac{1}{2}\sum_{i,j\leq A}\langle\alpha_i\alpha_j|V|\alpha_i\alpha_j\rangle_{\mathcal{A}} - \sum_{i\leq A}\langle\alpha_i|U|\alpha_i\rangle \ , \tag{1.38}$$

where we have defined

$$\langle\alpha_i\alpha_j|V|\alpha_i\alpha_j\rangle_{\mathcal{A}} \equiv \langle\alpha_i\alpha_j|V|\alpha_i\alpha_j\rangle - \langle\alpha_i\alpha_j|V|\alpha_j\alpha_i\rangle \ . \tag{1.39}$$

Note that the last term in (1.38) cancels the potential energy contribution from Eq. (1.29). This cancellation is automatic and does not depend on a particular choice for U.

Diagrams (d), (e), (f) and (g) of Fig. 1.2 contribute to the second-order of the Goldstone expansion. Nevertheless, in the case of nuclear matter diagrams (f) and (g) do not contribute. This is because the intermediate states of these two diagrams do not conserve the total momentum. Therefore, in nuclear matter, only diagrams (d) and the corresponding exchange diagram (e) of Fig. 1.2 would contribute to the second-order, being this contribution

$$\Delta E^{2^{nd}} = \langle\Phi_0|H_1\frac{P}{E_0 - H_0}H_1|\Phi_0\rangle = \frac{1}{2}\sum_{i,j\leq A}\sum_{k,l>A}\frac{\langle\alpha_i\alpha_j|V|\alpha_k\alpha_l\rangle\langle\alpha_k\alpha_l|V|\alpha_i\alpha_j\rangle_{\mathcal{A}}}{\epsilon_i + \epsilon_j - \epsilon_k - \epsilon_l} \ . \quad (1.40)$$

The Goldstone expansion (1.36) gets more complicated in third-order. Among the diagrams that contribute to this order are the ones shown in Fig. 1.2 (h), (i), (j), (k) and (l).

The Goldstone expansion provides a simple and explicit prescription for calculating every order of perturbation theory. Nevertheless, it cannot be used in its present form for nuclear matter calculations because the short-range repulsion in the baryon-baryon potentials makes all the matrix elements very large, and the perturbation series cannot converge. The solution to this problem is provided by the well-known Brueckner theory, in which the perturbation expansion in terms of the bare potential is replaced by another one in terms of the so-called Brueckner reaction matrix. All terms in this new perturbation series, the so-called Brueckner–Goldstone expansion, are finite and of reasonable size.

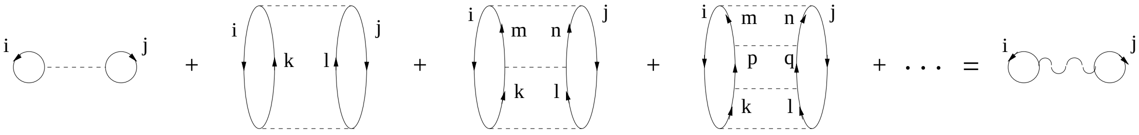

Figure 1.3: Illustration of the summation of ladder diagrams to obtain the G-matrix. The sum of the infinite sequence of ladder diagrams is depicted by the diagram on the right-hand side, in which the wiggly line represents the G-matrix.

1.2.2 The Brueckner–Goldstone expansion and the Brueckner reaction matrix

In order to introduce the Brueckner reaction matrix, commonly called G-matrix, let us consider the series of Goldstone diagrams shown in Fig. 1.3. These diagrams provide the simplest of ladder series. They are obtained from the first one by allowing the interaction V to act any number of times between the particles ejected from the Fermi sea. The sum of this series is given by

$$
\begin{aligned}
S = \frac{1}{2} \sum_{i,j<A} \langle \alpha_i \alpha_j | \Bigg\{ V + V \sum_{k,l>A} \frac{|\alpha_k \alpha_l\rangle\langle\alpha_k\alpha_l|}{\epsilon_i + \epsilon_j - \epsilon_k - \epsilon_l} V + \\
+ V \sum_{k,l>A} \frac{|\alpha_k \alpha_l\rangle\langle\alpha_k\alpha_l|}{\epsilon_i + \epsilon_j - \epsilon_k - \epsilon_l} V \sum_{m,n>A} \frac{|\alpha_m \alpha_n\rangle\langle\alpha_m\alpha_n|}{\epsilon_i + \epsilon_j - \epsilon_m - \epsilon_n} V + \cdots \Bigg\} |\alpha_i \alpha_j\rangle_A \ .
\end{aligned} \tag{1.41}
$$

Note that the value of the sum depends on the quantity $\omega = \epsilon_i + \epsilon_j$ usually referred to as “starting energy”. Let us define the summation of the ladder series by the quantity

$$
G(\omega) = V + V \frac{Q}{\omega - H_0} V + V \frac{Q}{\omega - H_0} V \frac{Q}{\omega - H_0} V + \cdots \ , \tag{1.42}
$$

where

$$\frac{Q}{\omega - H_0} = \sum_{p,q>A} \frac{|\alpha_p\alpha_q\rangle\langle\alpha_p\alpha_q|}{\omega - \epsilon_p - \epsilon_q} \tag{1.43}$$

is the propagator of the intermediate state $|\alpha_p\alpha_q\rangle$, being Q the so-called Pauli operator which restricts the summation to the states above the Fermi level, and $\omega - H_0$ the energy difference between the initial state and the intermediate state. The right-hand side of Eq. (1.42) can be resumed to yield the integral equation

$$G(\omega) = V + V\frac{Q}{\omega - H_0}G(\omega) \ , \tag{1.44}$$

which is the familiar Bethe–Goldstone equation. The quantity $G(\omega)$ is the Brueckner reaction matrix. For values of ω larger than the sum of the Fermi energies of the intermediate states $|\alpha_p\rangle$ and $|\alpha_q\rangle$, the kernel of the Bethe–Goldstone equation may become singular, and then it is necessary to add a quantity $i\eta$ in the energy denominator to properly treat the intermediate propagator. The G-matrix becomes then a complex quantity.

We have seen that the summation of the sequence of ladder diagrams has led to a single diagram (last diagram in Fig. 1.3) in which one V interaction line has been replaced by the reaction matrix $G(\omega)$. This is very desirable because the matrix elements of $G(\omega)$ turn out to be well-behaved even when the short-range repulsion causes the matrix elements of V to become very large or infinite. This suggests that the next step is therefore to try to convert each V interaction line into a G-matrix line by summing the proper sequences of ladder diagrams avoiding double counting. In doing this, one obtains a new expansion, the so-called Brueckner–Goldstone expansion, in which every term is finite and well behaved. Some of the diagrams appearing in this new expansion

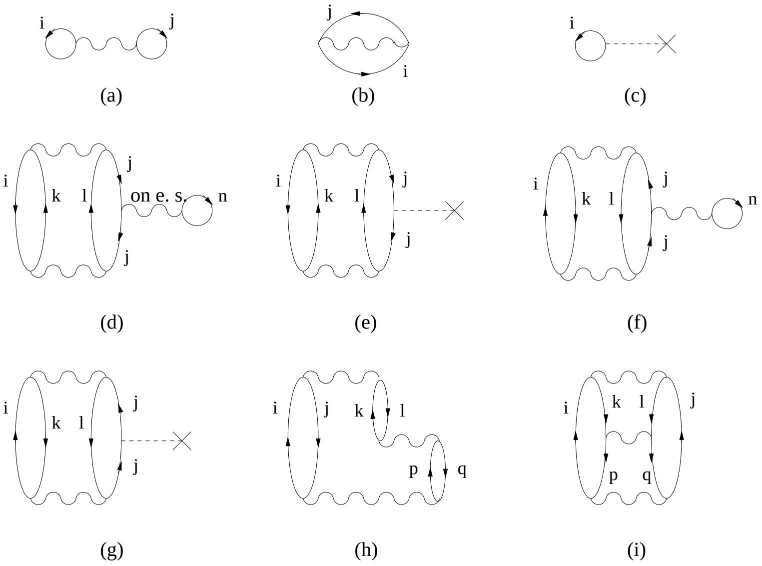

Figure 1.4: First-order ((a), (b), (c)) and some third-order ((d), (e), (f), (g), (h), (i)) diagrams appearing in the Brueckner–Goldstone expansion.

are shown in Fig. 1.4.

This attempt of converting the V interaction lines into G-matrix lines was, nevertheless, not the original motivation of Brueckner when he introduced the reaction matrix $G(\omega)$. He was interested in the problem of finding a way of describing the scattering between two particles which are immersed in a Fermi sea of other particles and which can interact strongly. Brueckner found that the G-matrix could be interpreted as describing the collision of two particles in the presence of a medium, as can be seen by direct comparison of Eq. (1.44) with the Lippmann-Schwinger satisfied by the T-matrix

$$T(\omega) = V + V \frac{1}{\omega - K + i\eta} T(\omega) \ , \tag{1.45}$$

where K is the kinetic energy operator.

The medium effects in the case of the G-matrix appear through the Pauli operator

Q, the actual value taken by the starting energy, and the auxiliary potential U as far as it is chosen on physical grounds.

1.2.3 Convergence of the Brueckner–Goldstone expansion

We have just seen that the Goldstone expansion may be rewritten in terms of the reaction matrix, leading in this way to the Brueckner–Goldstone expansion. However, we have said nothing about its convergence yet.

At first, it was believed that a converging expansion could be obtained by regrouping the diagrams according to their number of G-matrices: the largest contribution would be given by those diagrams with a single G-matrix, while those diagrams with $2, 3, \cdots$ G-matrices would give smaller and smaller contributions. Nevertheless, this is not the case. Rajaraman and Bethe [Ra63] showed that one can find diagrams which have the same order of magnitude although they contain different number of G-matrices. They showed that, in fact, the diagrams should be grouped according to their number of hole lines: the diagrams with h hole lines being more important than those with $(h+1)$ hole lines for any h. The end product of all this is now called the Brueckner–Bethe—Goldstone expansion, or simply the hole-line expansion.

The grouping of diagrams according to the number of hole lines corresponds to the following very simple physical idea. Two particles are strongly correlated, in the sense that $|\Psi\rangle$ differs appreciably from $|\Phi_0\rangle$, only when the distance between them is less than some "correlation length" which is of the order of the core radius, c, of the interaction. Within a sphere of radius r_0 (where r_0 is related with the density ρ through the relation $4\pi r_0^3/3 = 1/\rho$) centered on any particular particle, there will be on average one other particle. The probability that this other particle is close enough to the first one to be strongly correlated with it, is of the order $(c/r_0)^3$. Thus, the probability of strong two-body correlations is proportional to $(c/r_0)^3$. Similarly, the probability of three-body correlations is of the order $(c/r_0)^6$, and so on. Therefore, an expansion in which the first term is the energy due to two-body correlations, the next is from three-body correlations, etc., is characterized by an expansion parameter $(c/r_0)^3$ and should converge well. This is just the type of expansion obtained by grouping the diagrams according to the number of hole lines. The diagrams with h independent hole lines represent the energy arising from h-body correlations.

The leading term of the hole-line expansion, i.e., the one containing two independent hole lines, is given by the sum of diagrams (a), (b) and (c) of Fig. 1.4, and its calculation only requires the knowledge of the G-matrix. The total energy in the two-hole line approximation reads then

$$E^{BHF} = \sum_{i \leq A} \langle \alpha_i | T | \alpha_i \rangle + \frac{1}{2} \mathrm{Re} \sum_{i,j \leq A} \langle \alpha_i \alpha_j | G(\omega = \epsilon_i + \epsilon_j) | \alpha_i \alpha_j \rangle_{\mathcal{A}} \ , \tag{1.46}$$

where the contribution from diagram (c) of 1.4 cancels with the one from Eq. (1.29).

This approximation is also usually called the Brueckner–Hartree–Fock (BHF) approximation due to its analogy with the Hartree-Fock approximation. The only difference is that the interaction V has been replaced by the Brueckner reaction matrix $G(\omega)$, which thus plays the role of an *effective interaction* between two particles in states $|\alpha_i\rangle$ and $|\alpha_j\rangle$.

The next term appearing in the hole-line expansion will be given by the sum of all those diagrams with three hole-lines. Its numerical evaluation implies the knowledge of a three-body effective interaction $T^{(3)}$ which is formally given by the solution of the so-called Bethe–Faddeev equation

$$T^{(3)} = G + GX\frac{Q_3}{E}T^{(3)} , \tag{1.47}$$

where G is the reaction matrix, Q_3/E is the appropriate three-body propagator and X is an operator which avoids that two successive G-matrices can be present in the same pair of particle lines, since the G-matrix already sums up all the two-body ladder processes. Bethe gave an approximate solution to this equation and concluded that the contribution to the energy from three-body correlations is smaller than the one from two-body correlations by a factor of the order $(c/r_0)^3$, where c is the hard core radius of the interaction and r_0 the interparticle distance.

There are many classes of four, five, ... hole-line diagrams which represent the contributions from higher order correlations to the hole-line expansion, but they are presumably negligible, and are out of the scope of the present work.

1.2.4 Choice of the auxiliary potential U

The basic idea behind the choice of the auxiliary potential U is to minimize the contributions from higher order correlations, i.e., the contributions of diagrams with three or more hole-lines, reducing the number of diagrams to be explicitly calculated. As the leading contribution to the hole-line expansion is given by the Brueckner–Hartree–Fock approximation, it seems quite natural to make the following choice for the occupied states (i.e., those with $k \leq k_F$)

$$U_i^{BHF} = \mathrm{Re} \sum_{j<A} \langle \alpha_i \alpha_j | G(\omega = \epsilon_i + \epsilon_j) | \alpha_i \alpha_j \rangle_{\mathcal{A}} \ , \tag{1.48}$$

which is usually referred to as the Brueckner–Hartree–Fock single-particle potential, in analogy with the Hartree-Fock potential. This choice is particularly interesting because it leads to a cancellation of diagrams carrying U^{BHF} insertions in the hole lines with the corresponding ones having a bubble insertion, where the G-matrix is calculated on the energy shell, as for instance diagrams (e) and (d) of Fig. 1.4. Note that by virtue of the Bethe–Brandow–Petschek theorem [Be63] the bubble insertion of diagram 1.4(d) with the G-matrix taken on shell corresponds to the sum of all possible diagrams having crossed insertions in the hole line labelled j.

The definition of a single-particle potential for the excited states is a little bit more complicated since a cancellation similar to the one for hole states is not achieved. In the original Brueckner theory the potential U was assumed to be zero above k_F. This is called the “standard choice”, “gap choice” or “discontinuous choice”, since it necessarily implies that the single-particle potential U_i^{BHF} is discontinuous at the Fermi surface. This is illustrated in Fig. 1.5 in the case of the NSC97f nucleon-nucleon interaction, where there is a gap in the potential of around 60 MeV.

The *standard* Brueckner–Hartree–Fock approximation usually underestimates the binding energy of nuclear matter and in consequence it does not reproduce the saturation point as can be seen in Fig. 1.6. Therefore, it is necessary to either modify the corresponding choice of the auxiliary potential and/or to include “higher order”

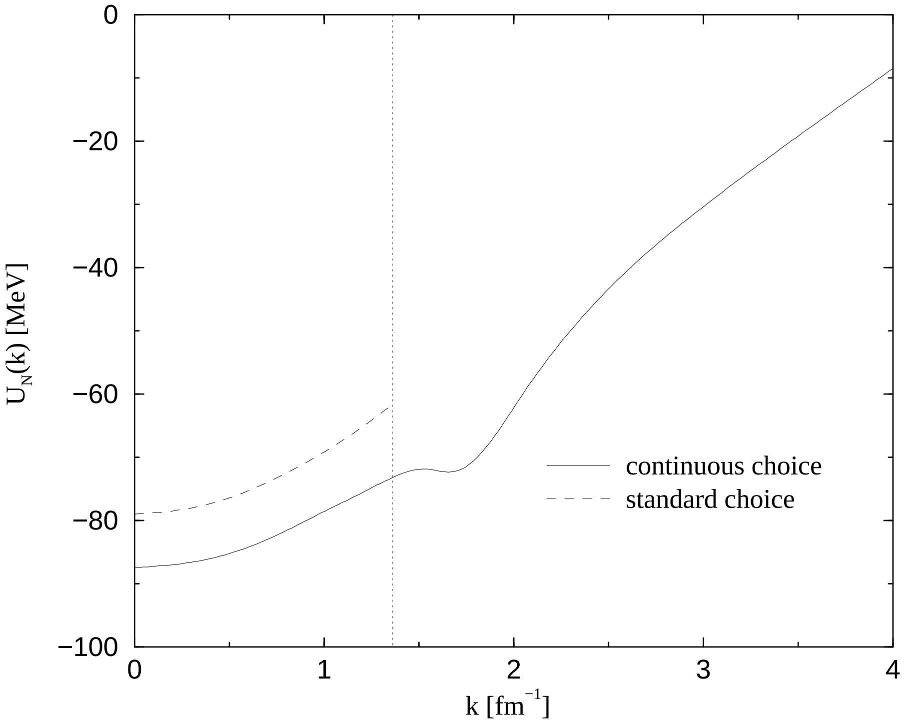

Figure 1.5: Nucleon single-particle potential at $k_F = 1.36$ fm^{-1}. The solid line corresponds to the case obtained with the continuous choice, while the dashed one shows the result for the standard choice. The dotted vertical line denotes the position of the Fermi momentum.

corrections. Mahaux and his collaborators [Je76] considered the following choice

$$U_i = U_i^{BHF} \ , \tag{1.49}$$

for all the states $|\alpha_i\rangle$ under or above the Fermi surface. This prescription is usually referred to as the "continuous choice", and implies the partial cancellation of other higher order diagrams.

As can be seen in Fig. 1.5, there is a structure in the single-particle potential near the Fermi surface whose origin is due to the opening of two-nucleon excitations since

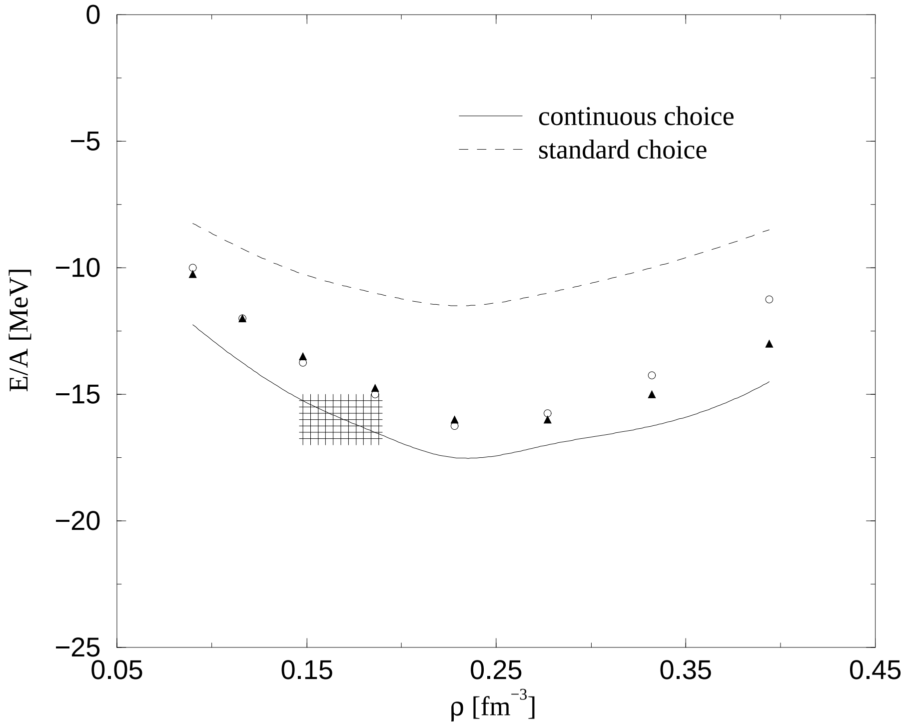

Figure 1.6: Binding energy per particle for symmetric nuclear matter with the Argonne V_{14} force. The dashed line represents the two-hole line contribution obtained with the standard prescription for the single-particle potential. The solid line shows the corresponding result with the continuous option. Triangles and squares include the three-hole line contribution. The shaded region corresponds to the empirical value. These results have been taken from Ref. [En99].

the starting energy of the G-matrix can achieve values larger than twice the Fermi energy of each nucleon. This prescription is not able either to reproduce the saturation point, although more binding is obtained. This additional binding is an indication that the hole-line expansion is very sensitive to the choice of the single-particle potential at this level of approximation.

With regard to the inclusion of higher-order correlations, Day [Da78] performed a calculation with the standard choice employing the Reid soft core nucleon-nucleon interaction finding that the three-hole line correction was of the order $\sim$ 5 MeV at $k_F = 1.36$ fm^{-1}. Recently, Song *et al.* [So98] have done the same calculation for the standard and the continuous choices using the Argonne V_{14} force, and have shown that when the three-hole line contribution is included both approaches essentially give the same result, which may be an indication of the convergence of the hole-line expansion. This interesting result can be seen in Fig. 1.6.

1.3 Solution of the Bethe–Goldstone equation

The Bethe–Goldstone equation is usually solved in the partial wave basis. In this basis, the two-baryon states $|(B_1B_2)\vec{K}kLSJMTM_T\rangle$ are characterized by the total centre-of-mass momentum $\vec{K}$, the modulus k of the relative momentum, the total orbital angular momentum L, the total spin S, the total angular momentum J, the third component M of the angular momentum, the total isospin T, and the third component of isospin M_T. Alternatively, one can choose the total charge q of the baryon pair (B_1B_2) instead of T and M_T to describe the state. In this case the basis is characterized by $|(B_1B_2)\vec{K}kLSJMq\rangle$.

The matrix elements of the baryon-baryon interaction V are commonly given in the partial wave basis, and this is in fact one of the reasons for its use in solving the Bethe–Goldstone equation. Invariance properties of the baryon-baryon interaction allow us to write directly

$$\begin{aligned} \langle(B_3B_4)\vec{K}'k'L'S'J'M'T'M_T'|V|(B_1B_2)\vec{K}kLSJMTM_T\rangle = \delta_{\vec{K}\vec{K}'}\delta_{JJ'}\delta_{MM'} \\ \times\delta_{TT'}\delta_{M_TM_T'}\langle(B_3B_4)\vec{K}k'L'S'JMTM_T|V|(B_1B_2)\vec{K}kLSJMTM_T\rangle \ . \end{aligned} \tag{1.50}$$

Let us now consider how the propagator $Q/E(\omega)$ (where $E(\omega) = \omega - H_0 + i\eta$) is expressed in the partial wave basis. In the decoupled basis $|(B_1B_2)\vec{k}_1 s_1\sigma_1 t_1\tau_1, \vec{k}_2 s_2\sigma_2 t_2\tau_2\rangle$, where $\vec{k}_i, s_i, \sigma_i, t_i$ and τ_i $(i = 1, 2)$ denote respectively, the linear momentum, the spin, the third component of the spin, the isospin and the third component of isospin of the baryon labelled i, this operator is diagonal and reads

$$\langle(B_1B_2)\vec{k}_1 s_1\sigma_1 t_1\tau_1, \vec{k}_2 s_2\sigma_2 t_2\tau_2|\frac{Q}{E(\omega)}|(B_1B_2)\vec{k}_1 s_1\sigma_1 t_1\tau_1, \vec{k}_2 s_2\sigma_2 t_2\tau_2\rangle = A_{B_1B_2}(\vec{k}_1, \vec{k}_2) \ , \tag{1.51}$$

being the expected value $A_{B_1B_2}(\vec{k}_1, \vec{k}_2)$

$$A_{B_1B_2}(\vec{k}_1, \vec{k}_2) = \frac{\theta(|\vec{k}_1| - k_{F_{B_1}})\theta(|\vec{k}_2| - k_{F_{B_2}})}{\omega - \frac{\hbar^2 k_1^2}{2M_1} - \frac{\hbar^2 k_2^2}{2M_2} - U_{B_1}(|\vec{k}_1|) - U_{B_2}(|\vec{k}_2|) + i\eta} \ . \tag{1.52}$$

To express the propagator in the partial wave basis we need to write this basis in terms of the decoupled one. To this end, we first decouple the total angular momentum J so that we can write

$$|(B_1B_2)\vec{K}kLSJMTM_T\rangle = \sum_{M_L M_S} (LSM_LM_S|JM)|(B_1B_2)\vec{K}kLM_LSM_STM_T\rangle \ . \tag{1.53}$$

Now, taking into account that

$$|kLM_L\rangle = \int d\hat{k} Y_{LM_L}(\hat{k})|\vec{k}\rangle \ , \tag{1.54}$$

we have

$$|(B_1B_2)\vec{K}kLSJMTM_T\rangle = \sum_{M_LM_S}(LSM_LM_S|JM)\int d\hat{k}Y_{LM_L}(\hat{k})|(B_1B_2)\vec{K}\vec{k}SM_STM_T\rangle \ . \tag{1.55}$$

Finally, decoupling the the total spin S and isospin T, and writing centre-of-mass $\vec{K}$ and the relative $\vec{k}$ momenta in terms of the single-particle momenta $\vec{k_1}$ and $\vec{k_2}$ according to the transformation

$$\left.\begin{array}{l} \vec{K}=\vec{k_1}+\vec{k_2} \\ \vec{k}=\frac{M_2\vec{k_1}-M_1\vec{k_2}}{M_1+M_2} \end{array}\right\} \longleftrightarrow \left\{\begin{array}{l} \vec{k_1}=\frac{M_1}{M_1+M_2}\vec{K}+\vec{k}\equiv\alpha\vec{K}+\vec{k} \\ \vec{k_2}=\frac{M_2}{M_1+M_2}\vec{K}-\vec{k}\equiv\beta\vec{K}-\vec{k} \end{array}\right. , \tag{1.56}$$

we obtain

$$\begin{aligned} |(B_1B_2)\vec{K}\vec{k}LSJMTM_T\rangle &= \sum_{\substack{\sigma_1\sigma_2\tau_1\tau_2 \\ M_LM_S}}(s_1s_2\sigma_1\sigma_2|SM_S)(t_1t_2\tau_1\tau_2|TM_T) \\ \times(LSM_LM_S|JM)&\int d\hat{k}Y_{LM_L}(\hat{k})|(B_1B_2)\vec{k_1}s_1\sigma_1t_1\tau_1,\vec{k_2}s_2\sigma_2t_2\tau_2\rangle \ . \end{aligned} \tag{1.57}$$

In a similar way, the inverse change (see appendix D) reads

$$\begin{aligned} |(B_1B_2)\vec{k_1}s_1\sigma_1t_1\tau_1,\vec{k_2}s_2\sigma_2t_2\tau_2\rangle &= \sum_{\substack{SM_STM_T \\ LM_LJM}}(s_1s_2\sigma_1\sigma_2|SM_S)(t_1t_2\tau_1\tau_2|TM_T) \\ \times(LSM_LM_S|JM)&Y^*_{LM_L}(\hat{k})|(B_1B_2)\vec{K}kLSJMTM_T\rangle \ , \end{aligned} \tag{1.58}$$

where we have employed the partial wave decomposition of a plane wave

$$|\vec{k}\rangle = \sum_{LM_L}Y^*_{LM_L}(\hat{k})|kLM_L\rangle \ . \tag{1.59}$$

We can now use Eqs. (1.51) and (1.57) to write

$$\begin{aligned}
&\langle (B_1B_2)\vec{K}kL'S'J'M'T'M'_T|\frac{Q}{E(\omega)}|(B_1B_2)\vec{K}kLSJMTM_T\rangle = \\
&\sum_{\substack{\sigma_1\sigma_2\tau_1\tau_2 \\ M_LM_SM'_LM'_S}} (s_1s_2\sigma_1\sigma_2|SM_S)(s_1s_2\sigma_1\sigma_2|S'M'_S)(t_1t_2\tau_1\tau_2|TM_T)(t_1t_2\tau_1\tau_2|T'M'_T) \\
&\times(LSM_LM_S|JM)(L'S'M'_LM'_S|J'M')\int d\hat{k}Y^*_{L'M'_L}(\hat{k})P_{B_1B_2}(\vec{K},\vec{k})Y_{LM_L}(\hat{k}) \ ,
\end{aligned} \tag{1.60}$$

where we have taken into account that the propagator is diagonal in the decoupled basis, and we have defined $P_{B_1B_2}(\vec{K},\vec{k}) \equiv A_{B_1B_2}(\vec{k_1},\vec{k_2})$ with $\vec{k_1}$ and $\vec{k_2}$ written in terms of $\vec{K}$ and $\vec{k}$ according to Eq. (1.56).

Employing the orthogonality property

$$\sum_{m_1m_2}(j_1j_2m_1m_2|jm)(j_1j_2m_1m_2|j'm') = \delta_{jj'}\delta_{mm'} \ , \tag{1.61}$$

we can perform the sum over $\sigma_1\sigma_2$ obtaining

$$\begin{aligned}
&\langle (B_1B_2)\vec{K}'kL'SJ'M'T'M_T|\frac{Q}{E(\omega)}|(B_1B_2)\vec{K}kLSJMTM_T\rangle = \\
&\sum_{\tau_1\tau_2}(t_1t_2\tau_1\tau_2|TM_T)(t_1t_2\tau_1\tau_2|T'M_T) \\
&\times\sum_{M_LM_SM'_L}(LSM_LM_S|JM)(L'SM'_LM_S|J'M')\int d\hat{k}Y^*_{L'M'_L}(\hat{k})P_{B_1B_2}(\vec{K},\vec{k})Y_{LM_L}(\hat{k}) \ ,
\end{aligned} \tag{1.62}$$

where, in addition, we have $M_T = M'_T = \tau_1 + \tau_2$. Finally, taking $\vec{K}$ along the z-axis, it can be shown that $P_{B_1B_2}(\vec{K},\vec{k})$ is independent of the angle ϕ_k and the integral will yield a factor $\delta_{M_LM'_L}$. At this point we can already consider this factor and perform the summation over M'_L. In addition one has $M = M' = M_L + M_S$ because of the Clebsch–Gordan coefficients in Eq. (1.62).

To summarize, the general matrix element of $Q/E(\omega)$ is given by

$$\begin{aligned} &\langle (B_1B_2)\vec{K}kL'SJ'MT'M_T|\frac{Q}{E(\omega)}|(B_1B_2)\vec{K}kLSJMTM_T\rangle = \\ &\sum_{\tau_1\tau_2}(t_1t_2\tau_1\tau_2|TM_T)(t_1t_2\tau_1\tau_2|T'M_T) \\ &\times \sum_{M_LM_S}(LSM_LM_S|JM)(L'SM_LM_S|J'M)\int d\hat{k}Y^*_{L'M_L}(\hat{k})P_{B_1B_2}(\vec{K},\vec{k})Y_{LM_L}(\hat{k}) \ . \end{aligned} \tag{1.63}$$

Therefore, using Eqs. (1.50) and (1.63) the general expression for the Bethe–Goldstone equation in the partial wave basis is given by

$$\begin{aligned} &\langle (B_3B_4)\vec{K}k'L'S'J'MT'M_T|G(\omega)|(B_1B_2)\vec{K}kLSJMTM_T\rangle = \\ &\langle (B_3B_4)\vec{K}k'L'S'J'MT'M_T|V|(B_1B_2)\vec{K}kLSJMTM_T\rangle \\ &+\sum_{B_5B_6}\sum_{\substack{L''S''J'' \\ L'''J'''}}\int\frac{dk''k''^2}{(2\pi)^3}\langle (B_3B_4)\vec{K}k'L'S'J'MT'M_T|V|(B_5B_6)\vec{K}k''L''S''J''MT''M_T\rangle \\ &\times\langle (B_5B_6)\vec{K}k''L''S''J''MT''M_T|\frac{Q}{E(\omega)}|(B_5B_6)\vec{K}k''L'''S''J'''MT'''M_T\rangle \\ &\times\langle (B_5B_6)\vec{K}k''L'''S''J'''MT'''M_T|G(\omega)|\vec{K}kLSJMTM_T\rangle \ . \end{aligned} \tag{1.64}$$

1.3.1 Angle–averaged Bethe–Goldstone equation

In order to simplify the numerical calculation of the G-matrix, it has become a standard practice since the early work of Brueckner and Gammel [Br58] to replace the propagator $Q/E(\omega)$ by some angle-averaged one. This means to replace the function $P_{B_1B_2}(\vec{K},\vec{k})$ by some function $\overline{P}_{B_1B_2}(K,k) = \overline{Q}_{B_1B_2}/\overline{E}(\omega)$ independent of the solid angle $\hat{k}$. Before discussing the exact form of $\overline{P}_{B_1B_2}(K,k)$, let us examine the simplifications which derive from this replacement.

As we have seen in the previous section, the propagator, which is by definition diagonal in the particle basis, becomes non-diagonal when transformed to the isospin basis. Nevertheless, the non-diagonal pieces are built from differences which tend to cancel each other. In particular, in the strangeness $S = 0$ sector the cancellation is exact when the angle average is performed. For these reasons, in our calculations done in the isospin basis we retain only the diagonal pieces of the propagator. In addition, when $P_{B_1B_2}(\vec{K},\vec{k})$ is replaced by $\overline{P}_{B_1B_2}(K,k)$ in Eq. (1.63), the integral over the solid angle $\hat{k}$ can be performed explicitly, yielding a factor $\delta_{LL'}$. Then the sum over M_L and M_S can be done using Eq. (1.61) giving $\delta_{JJ'}$. Hence Eq. (1.63) reduces to

$$\langle (B_1B_2)\vec{K}kLSJMTM_T|\frac{Q}{E(\omega)}|(B_1B_2)\vec{K}kLSJMTM_T\rangle = \overline{P}_{B_1B_2}(K,k) \ , \tag{1.65}$$

and the G-matrix can therefore be replaced by an angle-averaged $\overline{G}$-matrix which satisfies the equation

$$\begin{gathered}\langle (B_3B_4)\vec{K}k'L'S'JMTM_T|\overline{G}(\omega)|(B_1B_2)\vec{K}kLSJMTM_T\rangle = \\ \langle (B_3B_4)\vec{K}k'L'S'JMTM_T|V|(B_1B_2)\vec{K}kLSJMTM_T\rangle \\ +\sum_{B_5B_6}\sum_{L''S''}\int\frac{dk''k''^2}{(2\pi)^3}\langle (B_3B_4)\vec{K}k'L'S'JMTM_T|V|(B_5B_6)\ \vec{K}k''L''S''JMTM_T\rangle \\ \times\overline{P}_{B_5B_6}(K,k'')\langle (B_5B_6)\vec{K}k''L''S''JMTM_T|\overline{G}(\omega)|(B_1B_2)\ \vec{K}kLSJMTM_T\rangle \ .\end{gathered} \tag{1.66}$$

Let us now describe in certain detail the angle average of the propagator. It has become customary to perform the angle average of the Pauli operator, and the one of the energy denominator separately [Br58, Je74].

The expected value of the Pauli operator is given in the laboratory system by

$$Q_{B_1B_2}(\vec{k}_1,\vec{k}_2)=\theta(|\vec{k}_1|-k_{F_{B_1}})\theta(|\vec{k}_2|-k_{F_{B_2}}) \ , \tag{1.67}$$

which in terms of the centre-of-mass momentum $\vec{K}$ and the relative momentum $\vec{k}$ reads

$$Q_{B_1B_2}(\vec{K},\vec{k})=\theta(|\alpha\vec{K}+\vec{k}|-k_{F_{B_1}})\theta(|\beta\vec{K}-\vec{k}|-k_{F_{B_2}}) \ , \tag{1.68}$$

where α and β are given in Eq. (1.56) and

$$\begin{aligned} |\alpha\vec{K}+\vec{k}| &= (\alpha^2K^2+k^2+2\alpha Kk\cos\theta)^{1/2} \\ |\beta\vec{K}-\vec{k}| &= (\beta^2K^2+k^2-2\beta Kk\cos\theta)^{1/2} \end{aligned} \ , \tag{1.69}$$

being θ the angle between the vectors $\vec{K}$ and $\vec{k}$.

Following the suggestion of Ref. [Br58] the angle-averaged expected value of the Pauli operator is defined by

$$\overline{Q}_{B_1B_2}(K,k)\equiv\frac{1}{2}\int_{-1}^{1}Q_{B_1B_2}(\vec{K},\vec{k})d(\cos\theta) \ . \tag{1.70}$$

The Pauli operator is 1 only if the modulus of the two single-particle momenta $\alpha\vec{K}+\vec{k}$ and $\beta\vec{K}-\vec{k}$ lie outside their corresponding Fermi spheres, which imposes the following restriction over $\cos\theta$

$$\frac{k^2_{F_{B_1}}-\alpha^2K^2-k^2}{2\alpha Kk}\leq\cos\theta\leq\frac{\beta^2K^2+k^2-k^2_{F_{B_2}}}{2\beta Kk} \ . \tag{1.71}$$

$k \geq \max(\alpha K + k_{F_{B_1}}, \beta K + k_{F_{B_2}})$	for any value of $\alpha K,\ \beta K,\ k_{F_{B_1}},\ k_{F_{B_2}}$
$k \leq \beta K - k_{F_{B_2}}$	for $\alpha K < k_{F_{B_1}}$ and $\beta K > k_{F_{B_2}}$
$k \leq \alpha K - k_{F_{B_1}}$	for $\alpha K > k_{F_{B_1}}$ and $\beta K < k_{F_{B_2}}$
$k \leq \min(\alpha K + k_{F_{B_1}}, \beta K + k_{F_{B_2}})$	for $\alpha K > k_{F_{B_1}}$ and $\beta K > k_{F_{B_2}}$

Table 1.1: Relative momenta k for which $\overline{Q}_{B_1B_2}(K,k) = 1$.

Therefore, we have

$$\begin{gathered}\overline{Q}_{B_1B_2}(K,k) \equiv \frac{1}{2}\int_{\cos\theta_1}^{\cos\theta_2} d(\cos\theta) = \frac{1}{2}(\cos\theta_2 - \cos\theta_1) = \\ \frac{\alpha\beta K^2 + k^2 - \alpha k^2_{F_{B_2}} - \beta k^2_{F_{B_1}}}{4\alpha\beta K k}\,,\end{gathered} \tag{1.72}$$

together with the constraint $0 \leq \overline{Q}_{B_1B_2}(K,k) \leq 1$, where we have defined

$$\cos\theta_1 \equiv \frac{k^2_{F_{B_1}} - \alpha^2 K^2 - k^2}{2\alpha K k}, \qquad \cos\theta_2 \equiv \frac{\beta^2 K^2 + k^2 - k^2_{F_{B_2}}}{2\beta K k}\ . \tag{1.73}$$

The condition $\overline{Q}_{B_1B_2}(K,k) \geq 0$ implies that for values of the relative momentum

$$k \leq \sqrt{\alpha k^2_{F_{B_2}} + \beta k^2_{F_{B_1}} - \alpha\beta K^2} \tag{1.74}$$

the angle-averaged expected value of the Pauli operator is taken strictly zero.

In addition, for those values of the relative momentum which give $\cos\theta_1 \leq -1$

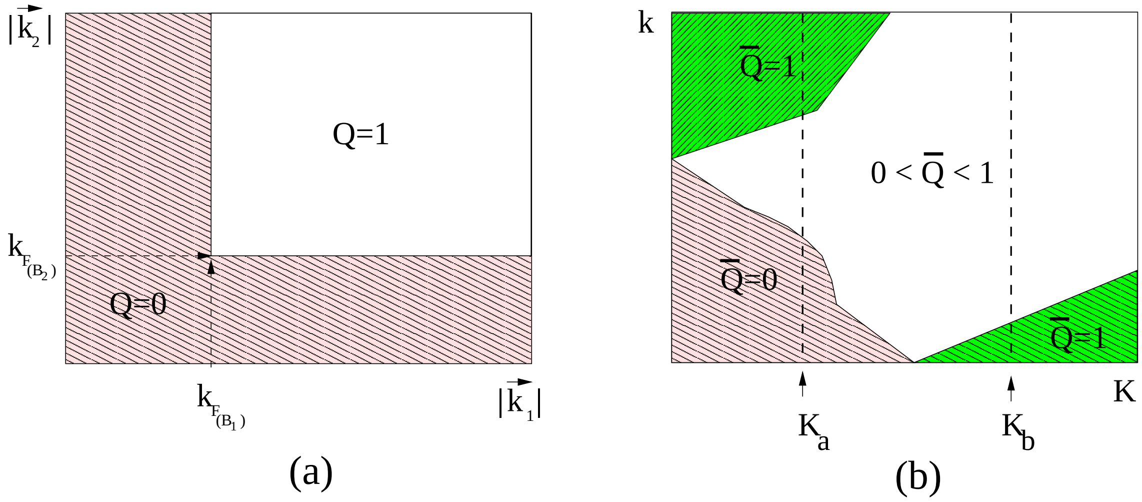

Figure 1.7: Expected value of the Pauli operator in the laboratory system (figure (a)), and its angle average in terms of the centre-of-mass and relative momenta (figure (b)). Regions in figure (a) are defined by Eq. (1.67), whereas in figure (b) are given by Eqs. (1.72), (1.74) and Table 1.1. The vertical dashed lines in figure (b) denote two fixed centre-of-mass momenta, K_a and K_b, for which the angle average is depicted in Fig. 1.8 as function of the relative momentum.

or $\cos\theta_2 \geq 1$ there is no restriction on the phase-space of $\cos\theta$, being therefore the angle-averaged expected value of the Pauli operator equal to 1. These momenta, which depend on the values of $\alpha K, \beta K, k_{F_{B_1}}$ and $k_{F_{B_2}}$, are given in Table 1.1.

In Fig. 1.7 we show for comparison the expected value of the Pauli operator in the laboratory system (a) and its angle average in terms of the centre-of-mass and relative momenta (b). For completeness we show in Fig. 1.8 the angle-averaged expected value of the Pauli operator as function of the relative momentum for two different values of the centre-of-mass momentum.

The energy denominator $E(\omega)$ is given by

$$E(\omega) = \omega - \frac{\hbar^2 k_1^2}{2M_{B_1}} - \frac{\hbar^2 k_2^2}{2M_{B_2}} - U_{B_1}(|\vec{k}_1|) - U_{B_2}(|\vec{k}_2|) + i\eta \ , \tag{1.75}$$

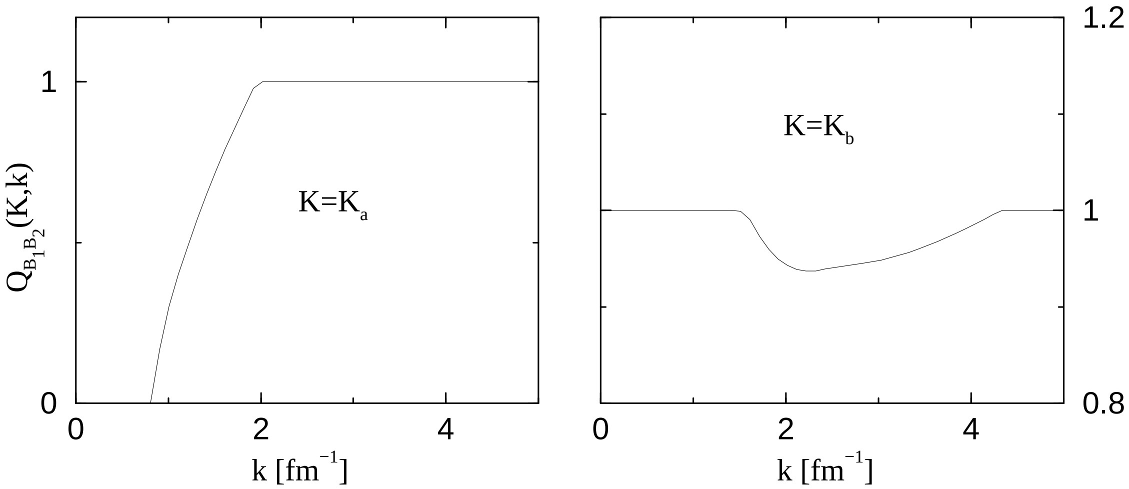

Figure 1.8: Angle-averaged expected value of the Pauli operator as function of the relative momentum for the two values K_a and K_b of the centre-of-mass momentum denoted by dashed lines in Fig. 1.7 (b).

or introducing the centre-of-mass and the relative momenta by

$$E(\omega) = \omega - \frac{\hbar^2 K^2}{2M} - \frac{\hbar^2 k^2}{2\mu} - U_{B_1}(|\alpha\vec{K} + \vec{k}|) - U_{B_2}(|\beta\vec{K} - \vec{k}|) + i\eta \ , \tag{1.76}$$

being $M = M_{B_1} + M_{B_2}$ and $\mu = M_{B_1}M_{B_2}/(M_{B_1} + M_{B_2})$ the total and the reduced masses of the baryon pair (B_1B_2), respectively.

The angle-independent energy denominator $\overline{E}(\omega)$ is constructed from Eq. (1.76) by replacing $|\alpha\vec{K}+\vec{k}|$ and $|\beta\vec{K}-\vec{k}|$ by their angle-averages $\overline{|\alpha\vec{K} + \vec{k}|}$ and $\overline{|\beta\vec{K} - \vec{k}|}$ defined as

$$\begin{array}{l} \overline{|\alpha\vec{K} + \vec{k}|} \equiv (\alpha^2K^2 + k^2 + 2\alpha Kk\overline{\cos\theta})^{1/2} \\ \overline{|\beta\vec{K} - \vec{k}|} \equiv (\beta^2K^2 + k^2 - 2\beta Kk\overline{\cos\theta})^{1/2} \end{array} \ , \tag{1.77}$$

where

$$\overline{\cos\theta} \equiv \sqrt{\langle\cos^2\theta\rangle} \ , \tag{1.78}$$

being

$$\langle\cos^2\theta\rangle \equiv \frac{1}{2}\int_{-1}^{1}\cos^2\theta Q(\vec{K},\vec{k})d(\cos\theta)\ . \tag{1.79}$$

As we have seen above, the Pauli operator restricts the integration over a certain range of angles. Therefore, we have

$$\langle\cos^2\theta\rangle \equiv \frac{1}{2}\int_{\cos\theta_1}^{\cos\theta_2}\cos^2\theta d(\cos\theta) = \frac{1}{6}(\cos^3\theta_2 - \cos^3\theta_1)\ . \tag{1.80}$$

This average is exactly equal to zero for the values of the relative momenta defined in Eq. (1.74), and is equal to 1 for those given in Table 1.1, as in the case of the Pauli operator.

1.3.2 Treatment of the singular kernel

In this section we discuss how to treat properly the poles which may appear in the kernel of the Bethe–Goldstone equation when the starting energy ω is larger than the minimum energy of the intermediate states.

The angle-averaged Bethe–Goldstone equation involves the calculation of an integral of the type

$$I = \int_0^\infty dk'' \frac{N(k'')}{D(k'') + i\eta}\ , \tag{1.81}$$

where in order to simplify notations we have defined:

$$\begin{aligned} N(k'') &= k''^2\langle(B_nB'_n)\vec{K}k'L'S'JMTM_T|V|(B_rB'_r)\vec{K}k''L''S''JMTM_T\rangle \\ &\times\overline{Q}_{B_rB'_r}(K,k'')\langle(B_rB'_r)\vec{K}k''L''S''JMTM_T|\overline{G}(\omega)|(B_mB'_m)\vec{K}kLSJMTM_T\rangle \end{aligned} \tag{1.82}$$

and

$$D(k'') = \omega - \frac{\hbar^2 K^2}{2M} - \frac{\hbar^2 k''^2}{2\mu} - U_{B_r}(\overline{|\alpha\vec{K} - \vec{k''}|}) - U_{B'_r}(\overline{|\beta\vec{K} - \vec{k''}|}) \ . \tag{1.83}$$

The position of a pole k_0 (let us assume it to be simple) is given by the root of the equation

$$D(k_0) = 0 \ . \tag{1.84}$$

We can use the Plemelj formula

$$\frac{1}{x + i\eta} = \mathcal{P}\frac{1}{x} - i\pi\delta(x) \ , \tag{1.85}$$

and the identity

$$\delta(D(k'')) \equiv \frac{1}{|\frac{dD(k'')}{dk''}|_{k_0}}\delta(k'' - k_0) \ , \tag{1.86}$$

to write

$$I = \mathcal{P}\int_0^\infty dk'' \frac{N(k'')}{D(k'')} - i\pi\frac{N(k_0)}{|\frac{dD(k'')}{dk''}|_{k_0}} \ . \tag{1.87}$$

The calculation of the principal part can be performed following a suggestion by Haftel and Tabakin [Ha70], consisting in the subtraction of the following zero quantity

$$N(k_0) \lim_{k'' \to k_0} \left\{ \frac{k''^2 - k_0^2}{D(k'')} \right\} \mathcal{P}\int_0^\infty \frac{dk''}{k''^2 - k_0^2} = 0 \ , \tag{1.88}$$

where by the L'Hôpital rule the limit gives

$$\lim_{k'' \to k_0} \left\{ \frac{k''^2 - k_0^2}{D(k'')} \right\} = \frac{2k_0}{(\frac{dD(k'')}{dk''})_{k_0}} \ . \tag{1.89}$$

Therefore, we can write

$$I = \mathcal{P}\int_0^\infty dk''\frac{N(k'')}{D(k'')} - 2k_0\frac{N(k_0)}{(\frac{dD(k'')}{dk''})_{k_0}}\mathcal{P}\int_0^\infty \frac{dk''}{k''^2 - k_0^2} - i\pi\frac{N(k_0)}{|\frac{dD(k'')}{dk''}|_{k_0}} \ . \tag{1.90}$$

Let us now try to write the same denominator in both integrals. We define the quantity

$$H(k'') = (k''^2 - k_0^2)\frac{N(k'')}{D(k'')} \ , \tag{1.91}$$

whose value at k_0, applying again the L'Hôpital rule, is given by

$$H(k_0) = 2k_0\frac{N(k_0)}{(\frac{dD(k'')}{dk''})_{k_0}} \ . \tag{1.92}$$

Thus, using Eqs. (1.91) and (1.92), Eq. (1.90) can be rewritten as

$$I = \mathcal{P}\int_0^\infty dk''\frac{H(k'') - H(k_0)}{k''^2 - k_0^2} - i\pi\frac{N(k_0)}{|\frac{dD(k'')}{dk''}|_{k_0}} \ . \tag{1.93}$$

Note that the integral is now not singular at k_0, therefore the principal part symbol can be dropped. Finally, we have

$$I = \int_0^\infty dk''\frac{H(k'') - H(k_0)}{k''^2 - k_0^2} - i\pi\frac{N(k_0)}{|\frac{dD(k'')}{dk''}|_{k_0}} \ . \tag{1.94}$$

1.3.3 Numerical solution of the Bethe–Goldstone equation

In this section we outline how the Bethe–Goldstone equation can be numerically solved. In order to present the general ideas of the method let us consider that the conservation of isospin and strangeness, or charge and strangeness depending if one has chosen T and M_T or q to describe the two-baryon states, allows the bare interaction V to describe the transitions between three channels, $(B_1B'_1)$, $(B_2B'_2)$ and $(B_3B'_3)$, denoted by

$$\begin{array}{lll}
V_{B_1B'_1\to B_1B'_1} & V_{B_1B'_1\to B_2B'_2} & V_{B_1B'_1\to B_3B'_3} \\
V_{B_2B'_2\to B_1B'_1} & V_{B_2B'_2\to B_2B'_2} & V_{B_2B'_2\to B_3B'_3} \\
V_{B_3B'_3\to B_1B'_1} & V_{B_3B'_3\to B_2B'_2} & V_{B_3B'_3\to B_3B'_3}
\end{array}$$

For a given starting energy ω and centre-of-mass momentum K, the matrix element $\langle (B_nB'_n)Kk'L'S'JMTM_T|\overline{G}(\omega)|(B_mB'_m)KkLSJMTM_T\rangle$ (with $m, n = 1, 2, 3$) of the reaction matrix describing the transition $B_mB'_m(LS) \to B_nB'_n(L'S')$ is given by the solution of the Bethe–Goldstone equation which, introducing the compact notation

$$G^{nL'S'}_{mLS}(k',k) \equiv \langle (B_nB'_n)\vec{K}k'L'S'JMTM_T|\overline{G}(\omega)|(B_mB'_m)\vec{K}kLSJMTM_T\rangle \ , \tag{1.95}$$

can be written as

$$G^{nL'S'}_{mLS}(k',k) = V^{nL'S'}_{mLS}(k',k) + \sum_{L''S''}\sum_{r}\int_0^\infty \frac{dk''k''^2}{(2\pi)^3} F^{nL'S'}_{rL''S''}(k',k'')G^{rL''S''}_{mLS}(k'',k) \ , \tag{1.96}$$

where

$$F^{nL'S'}_{rL''S''}(k',k'') = \frac{V^{nL'S'}_{rL''S''}(k',k'')\overline{Q}_{B_rB'_r}(K,k'')}{\omega - \frac{\hbar^2K^2}{2M} - \frac{\hbar^2k''^2}{2\mu} - U_{B_r}(\overline{|\alpha\vec{K}+\vec{k''}|}) - U_{B'_r}(\overline{|\beta\vec{K}-\vec{k''}|})} \ . \tag{1.97}$$

Making a discretization of the relative momenta, Eq. (1.96) can be written as

$$G^{nL'S'}_{mLS}(k_j,k_i) = V^{nL'S'}_{mLS}(k_j,k_i) + \sum_{L''S''}\sum_{r}\sum_{p=1}^{N} F^{nL'S'}_{rL''S''}(k_j,k_p)G^{rL''S''}_{mLS}(k_p,k_i)w_p \ . \qquad (1.98)$$

The points of the mesh and their corresponding weights are usually defined by a tangent

$$k_p = C\tan\left(\frac{\pi x_p}{2}\right) , \quad w_p = C\frac{\pi}{2}\cos^{-2}\left(\frac{\pi x_p}{2}\right) v_p, \qquad (1.99)$$

or by a logarithmic mapping

$$k_p = D\ln\left(\frac{1+x_p}{1-x_p}\right) , \quad w_p = D\frac{2}{1-x_p^2}v_p \ , \qquad (1.100)$$

where x_p are Gaussian points chosen from 0 to 1 and v_p are their corresponding weights. Note that formally the range of the mesh points goes from 0 to infinity. The value of the arbitrary constants C and D is chosen to optimize the numerical integration. In practice, we fit a maximum momentum value q_{max} dictated by the range in momentum space of the baryon-baryon interaction and define $C = q_{max}/\tan(\frac{\pi x_N}{2})$ and $D = q_{max}/\ln\left(\frac{1+x_N}{1-x_N}\right)$, being x_N the last point of the Gaussian mesh.

We will see now that Eq. (1.98) can be easily interpreted as a $6N \times 6N$ matrix equation in k-space (being N the number of mesh points). To make things simple, let us first imagine that there exists only one possible transition, $B_mB'_m(LS) \rightarrow B_mB'_m(LS)$, between baryons and that there are no couplings with other partial waves. In this case Eq. (1.98) takes the simpler form

$$G^{mLS}_{mLS}(k_j,k_i) = V^{mLS}_{mLS}(k_j,k_i) + \sum_{p=1}^{N} F^{mLS}_{mLS}(k_j,k_p)G^{mLS}_{mLS}(k_p,k_i)w_p \ , \qquad (1.101)$$

which can be viewed as a matrix equation, if we consider $G^{mLS}_{mLS}(k_j, k_i)$, $V^{mLS}_{mLS}(k_j, k_i)$ and $F^{mLS}_{mLS}(k_j, k_i)$ as $N \times N$ matrices in k-space.

Now, if we want to take into account at the same time all the possible couplings between partial waves with the same total angular momentum J, we can define a 2×2 matrix equation of the type

$$\begin{pmatrix} G^{nLS}_{mLS} & G^{nL'S'}_{mLS} \\ G^{nLS}_{mL'S'} & G^{nL'S'}_{mL'S'} \end{pmatrix} = \begin{pmatrix} V^{nLS}_{mLS} & V^{nL'S'}_{mLS} \\ V^{nLS}_{mL'S'} & V^{nL'S'}_{mL'S'} \end{pmatrix} + \begin{pmatrix} F^{nLS}_{mLS} & F^{nL'S'}_{mLS} \\ F^{nLS}_{mL'S'} & F^{nL'S'}_{mL'S'} \end{pmatrix} \times \begin{pmatrix} G^{nLS}_{mLS} & G^{nL'S'}_{mLS} \\ G^{nLS}_{mL'S'} & G^{nL'S'}_{mL'S'} \end{pmatrix} ,$$

where each matrix element of this 2×2 matrix structure in (L, S)-space is in fact a $N \times N$ matrix of the type (1.101) in k-space, being, therefore, the total dimension of this bigger structure $2N \times 2N$.

Finally, we can treat simultaneously all the possible transitions between the baryons by defining a 3×3 matrix equation

$$\begin{pmatrix} G_{B_1B'_1\to B_1B'_1} & G_{B_1B'_1\to B_2B'_2} & G_{B_1B'_1\to B_3B'_3} \\ G_{B_2B'_2\to B_1B'_1} & G_{B_2B'_2\to B_2B'_2} & G_{B_2B'_2\to B_3B'_3} \\ G_{B_3B'_3\to B_1B'_1} & G_{B_3B'_3\to B_2B'_2} & G_{B_3B'_3\to B_3B'_3} \end{pmatrix} = \begin{pmatrix} V_{B_1B'_1\to B_1B'_1} & V_{B_1B'_1\to B_2B'_2} & V_{B_1B'_1\to B_3B'_3} \\ V_{B_2B'_2\to B_1B'_1} & V_{B_2B'_2\to B_2B'_2} & V_{B_2B'_2\to B_3B'_3} \\ V_{B_3B'_3\to B_1B'_1} & V_{B_3B'_3\to B_2B'_2} & V_{B_3B'_3\to B_3B'_3} \end{pmatrix}$$

$$+ \begin{pmatrix} F_{B_1B'_1\to B_1B'_1} & F_{B_1B'_1\to B_2B'_2} & F_{B_1B'_1\to B_3B'_3} \\ F_{B_2B'_2\to B_1B'_1} & F_{B_2B'_2\to B_2B'_2} & F_{B_2B'_2\to B_3B'_3} \\ F_{B_3B'_3\to B_1B'_1} & F_{B_3B'_3\to B_2B'_2} & F_{B_3B'_3\to B_3B'_3} \end{pmatrix} \times \begin{pmatrix} G_{B_1B'_1\to B_1B'_1} & G_{B_1B'_1\to B_2B'_2} & G_{B_1B'_1\to B_3B'_3} \\ G_{B_2B'_2\to B_1B'_1} & G_{B_2B'_2\to B_2B'_2} & G_{B_2B'_2\to B_3B'_3} \\ G_{B_3B'_3\to B_1B'_1} & G_{B_3B'_3\to B_2B'_2} & G_{B_3B'_3\to B_3B'_3} \end{pmatrix} ,$$

in which each matrix element of this matrix structure is actually a $2N \times 2N$ matrix in the combined (L, S) and k-space of the type described above. The total dimension of this matrix equation is therefore $6N \times 6N$.

Then all the numerical problems of solving the Bethe–Goldstone equation have been reduced to one of solving a $6N \times 6N$ matrix equation. This can be done by the inversion method described as follows

$$\begin{aligned} \mathbf{G} &= \mathbf{V} + \mathbf{F}\mathbf{G} \ , \\ (\mathbf{1} - \mathbf{F})\mathbf{G} &= \mathbf{V} \ , \\ \mathbf{G} &= (\mathbf{1} - \mathbf{F})^{-\mathbf{1}}\mathbf{V} \ , \end{aligned} \tag{1.102}$$

where we have adopted a more compact notation to describe the matrix equation.

So, the G-matrix can be obtained by inverting the matrix $(\mathbf{1} - \mathbf{F})$, and then by multiplying the result of the inversion by the matrix $\mathbf{V}$ which contains the potential.

The extension of the method to the case in which the system is composed of any number of baryon-baryon $(B_l B_l')$ channels is straightforward. There will be a different matrix equation for each total isospin (or charge) and strangeness, and the dimension of the matrices will be in general $2N_c N \times 2N_c N$, being N_c the number of different $(B_l B_l')$ channels for a fixed isospin (or charge) and strangeness.

Let us finally note that, in fact, the numerical implementation of the treatment of the pole in the kernel is achieved by working with a large matrix that contains additional columns and rows associated with the position of the poles. This can easily be understood by looking at the following equation in which the kernel of the equation has been treated as described in section 1.3.2

$$G^{nL'S'}_{mLS}(k_j,k_i) = V^{nL'S'}_{mLS}(k_j,k_i) + \sum_{p=1}^{N} F^{nL'S'}_{mLS}(k_j,k_p) G^{nL'S'}_{mLS}(k_p,k_i) w_p$$
$$- \frac{2k_0^3 F^{nL'S'}_{mLS}(k_j,k_0) G^{nL'S'}_{mLS}(k_0,k_i)}{(\frac{dD(k)}{dk})_{k_0}} \sum_{p=1}^{N} \frac{w_p}{k_p^2 - k_0^2} - i\pi k_0^2 \frac{F^{nL'S'}_{mLS}(k_j,k_0) G^{nL'S'}_{mLS}(k_0 k_i)}{|\frac{dD(k)}{dk}|_{k_0}} \; . \tag{1.103}$$

The last two terms can be interpreted as the additional columns and rows which must be added taking k_0 as the $(N+1)^{th}$ momentum of the mesh. Columns and rows containing zeros may be also added in order to keep a square structure of the matrix equation which, although it is not necessary, makes things simpler. Therefore, in general the total dimension of the matrix equation will be $2N_c(N+1) \times 2N_c(N+1)$. The method just described is rather simple and efficient to implement numerically.

Let us finish this section and the chapter by saying a few words about the self-consistency required in the calculation of the G-matrix and of the single-particle potential U.

In the standard choice $(U(k > k_F) = 0)$ the single-particle potential does not appear in the Bethe–Goldstone equation because the Pauli operator makes the integral start from k_F. This means that the single-particle potential does not play a role in the solution of the Bethe–Goldstone equation, which then can be solved for a suitably chosen series of given values of the starting energy. The $\overline{G}$ matrix elements for the precise starting energy values required by the self-consistent scheme are then obtained by interpolation. Nevertheless, this is not the case when the continuous choice is adopted since $U \neq 0$ for values of $k > k_F$. In this case the solution of the equation requires a self-consistency process which makes the calculation much more time consuming.

Chapter 2

Hyperonic matter

> “Le monde, chère Agnès, est une étrange chose”.
>
> *Molière*, **L’ École des Femmes**, Act II. Sc. 5.

In this chapter we study the single-particle properties of neutrons, protons, Λ, Σ^-, Σ^0, Σ^+, Ξ^- and Ξ^0, embedded in an infinite many body system composed of different concentrations of such baryons. Following the theoretical scheme described in Chapter 1, we present results from microscopic Brueckner-type calculations of dense matter that include all types of baryon-baryon interactions and allow one to treat any asymmetry on the fractions of the different species. The chapter is organized according to the following scheme: first, some generalities are reviewed in section 2.1. Then, the baryon-baryon G-matrices for all the different strangeness channels and single-particle potentials obtained in the Brueckner–Hartree–Fock approximation are given in section

2.2. Finally, the single-particle properties of the different baryons at several densities and fractions of the baryons, are discussed in section 2.3, with special attention focused on those situations that will be relevant in our microscopic study of β-stable neutron star matter with strangeness presented in Chapter 4.

2.1 Generalities

The properties and composition of dense matter at supranuclear densities determine the static and dynamical behaviour of stellar matter [Gl92, La91, Co94, Kn95, Pr97]. The study of dense matter at extreme densities and temperatures has received a renewed interest due to the possibility of attaining such conditions in relativistic heavy-ion collisions at GSI, Brookhaven (BNL) and CERN.

It is believed that at extremely high densities deconfinement will take place resulting in a transition from hadronic to quark matter. The transition point and its characteristics will depend crucially on the Equation of State of matter in both the hadronic and the quark phase. It is well known that the presence of strangeness, in the form of hyperons (Λ, Σ, Ξ) or mesons (K^-) will soften the Equation of State and will delay the transition. Most investigations up to date are made in the framework of the mean field approach, either relativistic [El95, Sc96] or non-relativistic with effective Skyrme interactions [Ba97]. Microscopic theories, on the other hand, aim at obtaining the properties of hadrons in dense matter from the bare free space interaction. In this sense, Brueckner theory, reviewed in the previous chapter, was developed long time ago and successfully allowed one to understand the properties of (non-strange) nuclear matter starting from realistic interactions that reproduce a huge amount of NN scattering observables.

A first attempt to incorporate strangeness in the form of hyperons within Brueckner theory was made in Refs. [Sc95, Sc98], and latter extended to investigations of β-stable nuclear matter [Ba98]. A missing ingredient in these works was the hyperon-hyperon (YY) interaction and the results of single-particle potentials or binding energy per baryon with a finite amount of hyperons were simply orientative.

The recent availability of a baryon-baryon potential [St99] covering the complete SU(3) × SU(3) sector has allowed the incorporation of the YY potential in a microscopic calculation of dense matter with non-zero hyperon fraction [St99b]. Accounting for all possible baryon-baryon interactions required the solution of the G-matrix equation in coupled channels for different strangeness sectors: nucleon-nucleon NN ($S = 0$), hyperon-nucleon YN ($S = -1, -2$), and hyperon-hyperon YY ($S = -2, -3$ and -4). The work of Ref. [St99b] concentrated mainly on isospin saturated systems, i.e., systems with the same fraction of particles within the same isospin and strangeness multiplet: $T = 1/2, S = 0$ (neutrons and protons), $T = 0, S = -1$ (Λ), $T = 1, S = -1$ ($\Sigma^-, \Sigma^0, \Sigma^+$) and $T = 1/2, S = -2$ (Ξ^-, Ξ^0). In this way, the complications associated to different Fermi seas for each species of the same isospin-strangeness multiplet were avoided and the G matrix in each sector was independent of the third component of isospin.

It is well known, however, that the presence of electrons makes neutron star matter, to be equilibrated against the weak β-decay reactions, containing neutron fractions much larger (a factor of 10 or more) than that of protons [Bo91, En94, En96]. Also, the increase of negatively charged leptons with the baryonic density will turn into a decrease when the appearance of negatively charged baryons becomes energetically more favourable. This is the case of the Σ^- hyperon, since neutralizing the proton charge with Σ^- instead of e^- will remove two energetic neutrons ($p\Sigma^- \leftrightarrow nn$) instead of one ($pe^- \leftrightarrow n$). It is therefore clear, that a microscopic study of β-stable neutron star matter with hyperons requires the treatment of highly asymmetric matter, both in the non-strange sector (proton vs. neutrons) and the hyperonic one (Σ^- vs. Σ^0 and Σ^+, and Ξ^- vs. Ξ^0).

In the present chapter we extend the study of Ref. [St99b] to allow for different fractions of each species [Vi00]. We will also explore the effect of the recently available YY interaction on the single-particle potential of the hyperons, a crucial ingredient to determine the baryonic density at which the different hyperons appear. Our aim is to present a thorough analysis of the properties of the different baryons in dense matter, taking into account their mutual interactions. We will explore different baryonic densities and compositions that are relevant in the study of neutron stars. The influence of the hyperons on the properties and structure of neutron stars will be studied in Chapter 4.

2.2 G-matrix and BHF approximation

Although the Brueckner reaction matrix, or G-matrix, was already introduced and described in Chapter 1, in section 2.2.1 we construct the baryon-baryon G-matrices for all the different strangeness channels starting from the new realistic bare baryon-baryon interactions of the Nijmegen group (NSC97a-f) [St99]. A general expression for the Brueckner–Hartree–Fock approximation to the single-particle potential felt by a baryon B_1 embedded in the Fermi sea of baryons B_2 in terms of the partial wave basis is given in section 2.2.2, together with expressions for the non-relativistic energy density and total energy per baryon.

2.2.1 The baryon-baryon G-matrix

The G-matrix which describes the transition $B_1B_2 \rightarrow B_3B_4$ is obtained, for a total isospin T and third component M_T (or, alternatively, charge q) and strangeness S, from the bare baryon-baryon interaction V by solving the corresponding Bethe–Goldstone equation.

In section 1.3.1 we showed that after performing an angle-average over the Pauli operator and the energy denominator this equation reads

$$\begin{aligned}
&\langle (B_3B_4)\overline{K}k'L'S'JMTM_T|\overline{G}(\omega)|(B_1B_2)\overline{K}kLSJMTM_T\rangle = \\
&\langle (B_3B_4)\overline{K}k'L'S'JMTM_T|V|(B_1B_2)\overline{K}kLSJMTM_T\rangle \\
&+\sum_{B_5B_6}\sum_{L''S''}\int dk''k''^2\langle (B_3B_4)\overline{K}k'L'S'JMTM_T|V|(B_5B_6)\ \overline{K}k''L''S''JMTM_T\rangle \\
&\times\frac{\overline{Q}_{B_5B_6}(K,k'';T,M_T)}{\omega-\frac{\hbar^2K^2}{2M}-\frac{\hbar^2k''^2}{2\mu}-U_{B_5}(\overline{|\alpha\vec{K}-\vec{k''}|})-U_{B_6}(\overline{|\beta\vec{K}-\vec{k''}|})-M_{B_5}-M_{B_6}+i\eta} \\
&\times\langle (B_5B_6)\overline{K}k''L''S''JMTM_T|\overline{G}(\omega)|(B_1B_2)\ \overline{K}kLSJMTM_T\rangle\ .
\end{aligned} \tag{2.1}$$

The starting energy ω corresponds to the sum of non-relativistic single-particle energies of the interacting baryons, including in this case their rest masses. The variables k, k', k'' and L, L', L'' denote relative linear momenta and orbital momenta, respectively, and $\overline{K}$ is an angular-averaged centre-of-mass momentum (see appendix B for details on this average). The total angular momentum, spin, isospin and isospin projections are denoted by J, S, T and M_T, respectively.

Note that we show explicitly the dependence of the angle-averaged Pauli operator $\overline{Q}_{B_5B_6}(K, k''; T, M_T)$ on the total isospin T and third component M_T of the intermediate two-baryon state (B_5B_6). In appendix A we show the expressions that define the Pauli operator in a particular (T, M_T) channel in terms of the basis of physical states. Note also that although we keep the index M_T in the bare potential matrix elements, they do not really have a dependence on the third component of isospin since we consider charge-symmetric and charge-independent interactions. The dependence of the G-matrix on the third component of isospin comes exclusively from the Pauli operator, since, as can be clearly seen in Appendix A, it acquires a dependence on M_T when different concentrations of particles belonging to the same isomultiplet (i.e., different values for the corresponding k_F's) are considered.

In comparison with the pure nucleonic calculation, this problem is a little bit more complicated, because of its coupled-channel structure. Whereas for the strangeness sectors 0 and -4 there is only one particle channel (NN→NN and $\Xi\Xi \to \Xi\Xi$, respectively) and two possible isospin states ($T = 0, 1$), in the strangeness $-1(-3)$ sector we are dealing with the ΛN($\Lambda\Xi$) and ΣN($\Sigma\Xi$) channels, coupled to $T = 1/2$,

$$\begin{pmatrix} \overline{G}_{\Lambda N\to\Lambda N} & \overline{G}_{\Lambda N\to\Sigma N} \\ \overline{G}_{\Sigma N\to\Lambda N} & \overline{G}_{\Sigma N\to\Sigma N} \end{pmatrix} \quad \begin{pmatrix} \overline{G}_{\Lambda\Xi\to\Lambda\Xi} & \overline{G}_{\Lambda\Xi\to\Sigma\Xi} \\ \overline{G}_{\Sigma\Xi\to\Lambda\Xi} & \overline{G}_{\Sigma\Xi\to\Sigma\Xi} \end{pmatrix} ,$$

and the ΣN($\Sigma\Xi$) channel in isospin $T = 3/2$

$$\begin{pmatrix} \overline{G}_{\Sigma N\to\Sigma N} \end{pmatrix} \quad \begin{pmatrix} \overline{G}_{\Sigma\Xi\to\Sigma\Xi} \end{pmatrix} .$$

In the strangeness -2 sector we must consider the channels ΛΛ, ΛΣ, ΞN and ΣΣ in isospin states $T = 0$

$$\begin{pmatrix} \overline{G}_{\Lambda\Lambda\to\Lambda\Lambda} & \overline{G}_{\Lambda\Lambda\to\Xi N} & \overline{G}_{\Lambda\Lambda\to\Sigma\Sigma} \\ \overline{G}_{\Xi N\to\Lambda\Lambda} & \overline{G}_{\Xi N\to\Xi N} & \overline{G}_{\Xi N\to\Sigma\Sigma} \\ \overline{G}_{\Sigma\Sigma\to\Lambda\Lambda} & \overline{G}_{\Sigma\Sigma\to\Xi N} & \overline{G}_{\Sigma\Sigma\to\Sigma\Sigma} \end{pmatrix},$$

$T = 1$

$$\begin{pmatrix} \overline{G}_{\Xi N\to\Xi N} & \overline{G}_{\Xi N\to\Lambda\Sigma} & \overline{G}_{\Xi N\to\Sigma\Sigma} \\ \overline{G}_{\Lambda\Sigma\to\Xi N} & \overline{G}_{\Lambda\Sigma\to\Lambda\Sigma} & \overline{G}_{\Lambda\Sigma\to\Sigma\Sigma} \\ \overline{G}_{\Sigma\Sigma\to\Xi N} & \overline{G}_{\Sigma\Sigma\to\Lambda\Sigma} & \overline{G}_{\Sigma\Sigma\to\Sigma\Sigma} \end{pmatrix},$$

and $T = 2$

$$\begin{pmatrix} \overline{G}_{\Sigma\Sigma\to\Sigma\Sigma} \end{pmatrix}.$$

In addition, each box $\overline{G}_{B_1B_2\to B_3B_4}$ has a 2×2 matrix sub-structure to incorporate the couplings between (L, S) states having the same total angular momentum J, as we showed in section 1.3.3. This sub-matrix reads

$$\begin{pmatrix} \langle L=J, S=0|\,\overline{G}\,|L=J, S=0\rangle & \langle L=J, S=0|\,\overline{G}\,|L=J, S=1\rangle \\ \langle L=J, S=1|\,\overline{G}\,|L=J, S=0\rangle & \langle L=J, S=1|\,\overline{G}\,|L=J, S=1\rangle \end{pmatrix},$$

for spin singlet–spin triplet coupling ($L = J, S = 0 \leftrightarrow L = J, S = 1$) and

$$\begin{pmatrix} \langle L=J-1,S=1|\,\overline{G}\,|L=J-1,S=1\rangle & \langle L=J-1,S=1|\,\overline{G}\,|L=J+1,S=1\rangle \\ \langle L=J+1,S=1|\,\overline{G}\,|L=J-1,S=1\rangle & \langle L=J+1,S=1|\,\overline{G}\,|L=J+1,S=1\rangle \end{pmatrix}$$

for tensor coupling ($L = J-1, S = 1 \leftrightarrow L = J+1, S = 1$).

The reader can find in appendix C the corresponding particle channels in the physical basis $|(B_1B_2)\vec{K}kLSJMq\rangle$ (i.e., in which the total charge q of the baryon pair (B_iB_j) is used to describe the states instead of the total isospin T and third component M_T).

2.2.2 Single–particle potential in the BHF approximation

In the Brueckner–Hartree–Fock approximation the single–particle potential of a baryon B_1 which is embedded in the Fermi sea of baryons B_2 is given by Eq. (1.48), which using the partial wave decomposition of the G-matrix can be written as

$$\begin{aligned} U_{B_1}^{(B_2)}(k_{B_1}) &= \frac{(1+\xi_{B_1})^3}{2s_{B_1}+1} \sum_{J,L,S,T,M_T} a(2J+1) \\ &\times (t_{B_1}t_{B_2}\tau_{B_1}\tau_{B_2}|TM_T)^2 \int_0^{k_{max}} k^2 dk f(k,k_{B_1}) \\ &\times \mathrm{Re}\langle (B_1B_2)\overline{K}kLSJMTM_T|\overline{G}(E_{B_1}(k_{B_1})+E_{B_2}(\overline{k_{B_2}}))|(B_1B_2)\overline{K}kLSJMTM_T\rangle \ , \end{aligned} \tag{2.2}$$

where $a = [1-(-1)^{L+S+T-s_{B_1}-s_{B_2}-t_{B_1}-t_{B_2}}]$ if both baryons belong to the same isomultiplet, or $a = 1$ if they belong to different isomultiplets. The imaginary part of the single-particle potential can be easily obtained by taking the imaginary part of the $\overline{G}$-matrix elements instead of the real one in the above expression. For the derivation of this expression see appendix D.

In the actual calculations, we consider all partial waves up to $J = 4$. The labels s_{B_1}, s_{B_2} (t_{B_1}, t_{B_2}) denote the spin (isospin) of baryons B_1 and B_2, respectively, and $(t_{B_1} t_{B_2} \tau_{B_1} \tau_{B_2} | T M_T)$ is the Clebsch–Gordan coefficient coupling to total isospin T. The variable k denotes the relative momentum of the $B_1 B_2$ pair, which is constrained by

$$k_{max} = \frac{k_{F_{B_2}} + \xi_{B_1} k_{B_1}}{1 + \xi_{B_1}} \ , \tag{2.3}$$

with $\xi_{B_1} = M_{B_2}/M_{B_1}$. Finally, the weight function $f(k, k_{B_1})$, given by

$$f(k, k_{B_1}) = \begin{cases} 1 & \text{for } k \leq \frac{k_{F_{B_2}} - \xi_{B_1} k_{B_1}}{1+\xi_{B_1}}, \\ 0 & \text{for } |\xi_{B_1} k_{B_1} - (1 + \xi_{B_1}) k| > k_{F_{B_2}}, \\ \dfrac{k^2_{F_{B_2}} - [\xi_{B_1} k_{B_1} - (1 + \xi_{B_1}) k]^2}{4 \xi_{B_1} (1 + \xi_{B_1}) k_{B_1} k} & \text{otherwise,} \end{cases} \tag{2.4}$$

results from the analytical angular integration once the angular dependence of the G-matrix elements is eliminated (see appendix E for the derivation of this weight function). This is done by choosing appropriate angular averages for the centre-of-mass, $\overline{K}$, of the $B_1 B_2$ pair and for the value of the hole momentum, $\overline{k_{B_2}}$, which enters in the determination of the starting energy. Details on these angular averages are given in appendix B.

If the baryon B_i is embedded in the Fermi seas of several baryons B_1, B_2, …, B_N, including its own Fermi sea, then its single–particle potential is given by the sum of all partial contributions

$$U_{B_i}(k) = \sum_{B_j} U_{B_i}^{(B_j)}(k) \ , \tag{2.5}$$

where $U_{B_i}^{(B_j)}(k)$ is the potential of the baryon B_i due to the Fermi sea of baryons B_j. In this expression k denotes the single–particle momentum of particle B_i. The non–relativistic single–particle energy of baryon B is then given by

$$E_B(k) = \frac{\hbar^2 k^2}{2M_B} + U_B(k) + M_B \ . \tag{2.6}$$

This is precisely the single–particle energy that determines the value of the starting energy ω at which the $G_{B_1B_2\leftrightarrow B_1B_2}$-matrix in Eq. (2.2) should be evaluated. This implies a self-consistent solution of Eqs. (2.1), (2.2) and (2.6). The Fermi energy of each species is determined by setting k to the corresponding Fermi momentum in the above expression.

The total non–relativistic energy density, ε, and the total binding energy per baryon, E/A, can be evaluated from the baryon single–particle potentials in the following way:

$$\varepsilon = 2\sum_B \int_0^{k_F^{(B)}} \frac{d^3k}{(2\pi)^3} \left(\frac{\hbar^2 k^2}{2M_B} + \frac{1}{2} U_B(k) \right) \ , \tag{2.7}$$

$$\frac{E}{A} = \frac{\varepsilon}{\rho} \ , \tag{2.8}$$

where ρ is the total baryonic density. The density of a given baryon species is given by

$$\rho_B = \frac{k_{F_B}^3}{3\pi^2} = x_B \rho \ , \tag{2.9}$$

where $x_B = \rho_B/\rho$ is the fraction of baryons B, which is of course constrained by the condition

$$\sum_B x_B = 1 \ . \tag{2.10}$$

2.3 Nuclear matter results

In this section we present the results for the single-particle properties of each baryon species ($n, p, \Lambda, \Sigma^-, \Sigma^0, \Sigma^+, \Xi^-$, and Ξ^0) obtained within the many-body scheme presented in the previous section and Chapter 1. We start showing in section 2.3.1 results for pure nucleonic matter, i.e, nuclear matter with only nucleonic degrees of freedom. Nuclear matter with strangeness content is analyzed in section 2.3.2, focusing our attention on the role of the hyperon-hyperon interaction in the single-particle potential of the hyperons, a crucial ingredient for the β-stable matter calculations presented in Chapter 4. We show results mainly for the NSC97e baryon-baryon model interaction of the recent Nijmegen parametrization [St99], although for comparison some results for models NSC97a and NSC97f are also given.

2.3.1 Pure nucleonic matter

Before considering the role of hyperons in nuclear matter, we devote this section to review some of the properties of pure nucleonic matter in connection with section 4.5.1 of Chapter 4, in which we will analyze the properties of β-stable neutron star matter with only nucleonic and leptonic degrees of freedom.

In Fig. 2.1 we show the single-particle potential of neutrons and protons as function of the linear momentum k at a nucleonic density $\rho_N = \rho_n + \rho_p = 0.17$ fm^{-3} for three values of the proton fraction, $x_p = \rho_p/\rho_N$, going from symmetric nuclear matter ($x_p = 0.5$) to pure neutron matter ($x_p = 0$). The real part is shown on the left panels, while the imaginary part is given on the right ones. The results have been obtained for the NSC97e nucleon-nucleon interaction model of Ref. [St99], using the continuous

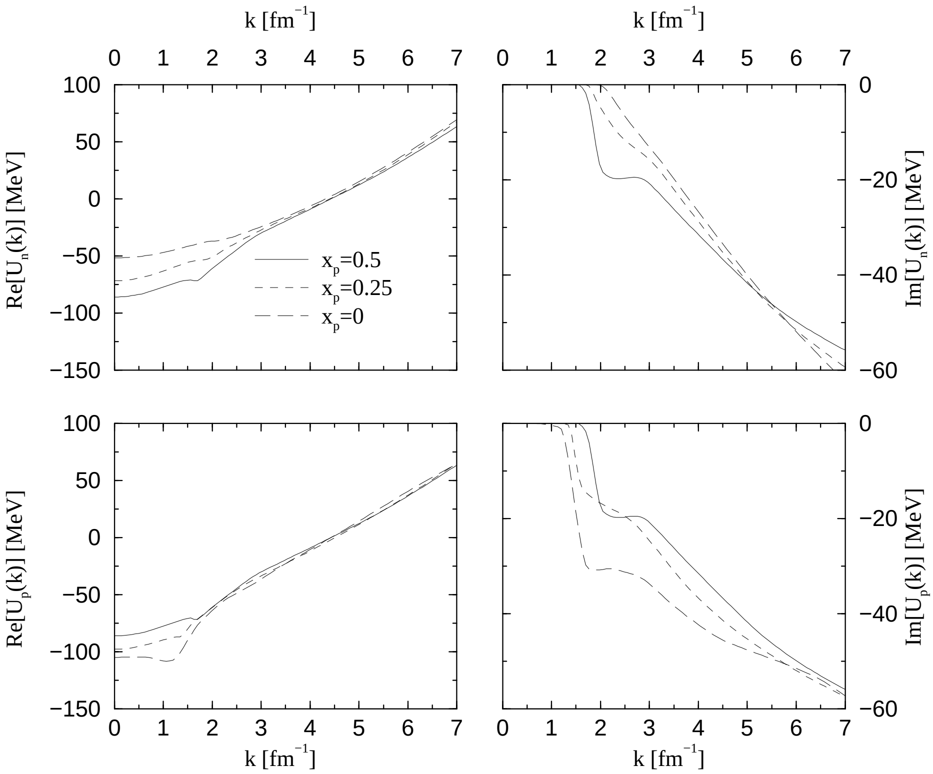

Figure 2.1: Single-particle potential of neutrons (upper panels) and protons (lower panels) at $\rho_N = \rho_0 = 0.17$ fm^{-3} for three values of the proton fraction $x_p = 0, 0.25$ and 0.5. The real part is shown on the left panels, whereas the imaginary part is given on the right ones. The results have been obtained for the NSC97e NN interaction using the continuous prescription in the solution of the Bethe–Goldstone equation.

prescription when solving the Bethe–Goldstone equation. A comparison between the results obtained using the continuous or the discontinuous option was reported in Fig. 1.5 of Chapter 1. We see that neutrons and protons have the same single-particle potential in symmetric nuclear matter, of the order of −86 MeV (−79 MeV for the discontinuous choice) at zero momentum. As the fraction of protons decreases, the protons gain binding while the neutrons lose attraction. This is a consequence of the different behaviour of the nucleon-nucleon interaction in the $T = 0$ and $T = 1$ channels, the $T = 0$ channels being substantially more attractive. Being the minority species in

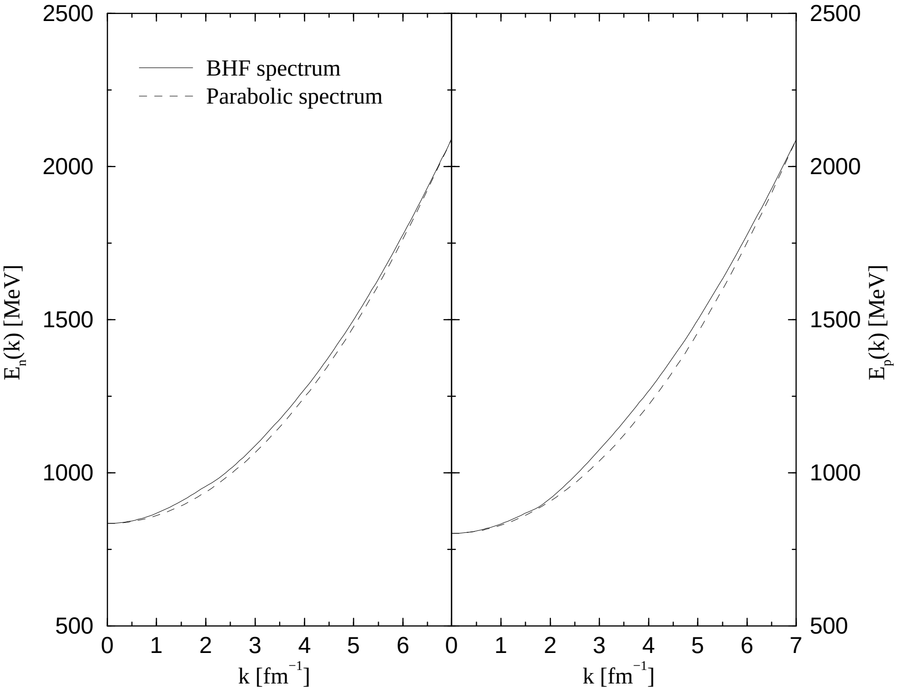

Figure 2.2: Single-particle spectrum of neutrons (left panel) and protons (right panel) as defined by Eq. (2.6) obtained from a BHF calculation (solid lines) in comparison with the parabolic approximation defined by Eq. (2.11) (dashed lines) for $\rho_N = 0.3$ fm^{-3} and $x_p = 0.25$. The NSC97e NN interaction model and continuous prescription have been considered in the calculation.

the asymmetric situation considered in Fig. 2.1, the proton builds up its potential from more $T = 0$ than $T = 1$ pairs and hence becomes more attractive.

The single-particle spectrum of neutrons and protons can be well parametrized by a parabolic spectrum of the type

$$E_{n,p}(k) \approx \frac{\hbar^2 k^2}{2M^*_{n,p}} + U_{n,p}(0) + M_{n,p} \ , \tag{2.11}$$

as can be seen in Fig. 2.2 where we show the spectra of neutrons and protons at $\rho_N = 0.3$ fm^{-3} and $x_p = 0.25$, obtained from the Brueckner–Hartree–Fock calculation

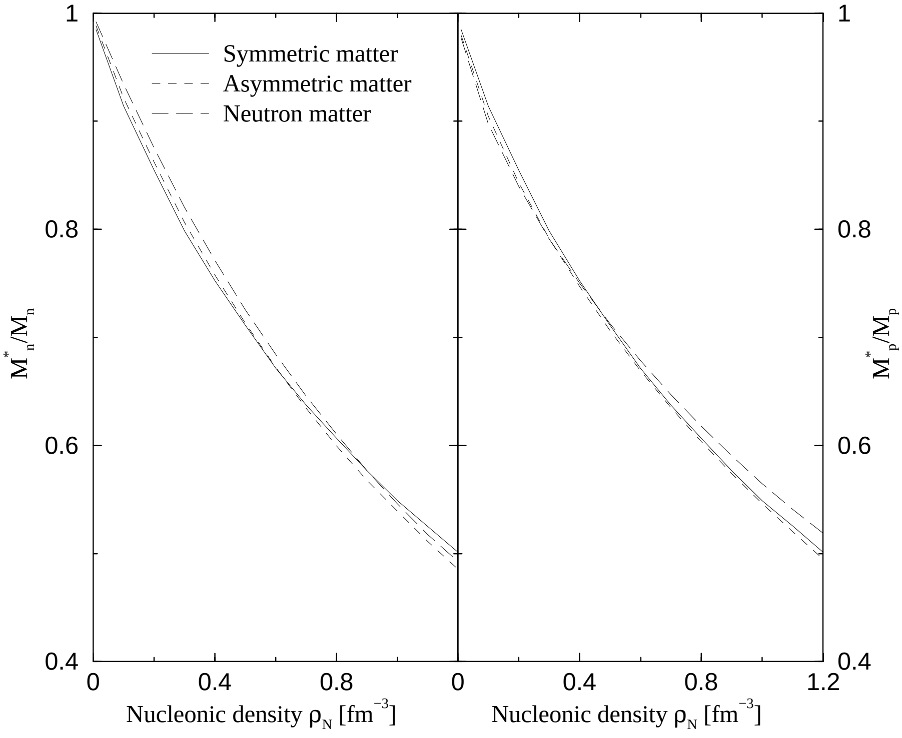

Figure 2.3: Neutron (left panel) and proton (right panel) effective masses as functions of the nucleonic density for symmetric, asymmetric ($x_p = 0.25$) and pure neutron matter calculated from Eq. (2.12).

(solid lines) and with the parabolic parametrization of Eq. (2.11) (dashed lines). In the above equation $M^*_{n,p}$ stands for the neutron, proton effective mass constructed from the value of the single-particle potential taken at $k = 0$ and at a second momentum k_2 (in our case $k_2 = 7$ fm^{-1} as can be seen in Fig. 2.2), according to

$$\frac{M^*_{n,p}}{M_{n,p}} = \left[1 + \frac{U_{n,p}(k_2) - U_{n,p}(0)}{\hbar^2 k_2^2/2M_{n,p}}\right]^{-1} . \tag{2.12}$$

In Fig. 2.3 we show the neutron and proton effective masses as function of nucleonic density for symmetric, asymmetric ($x_p = 0.25$) and pure neutron matter calculated

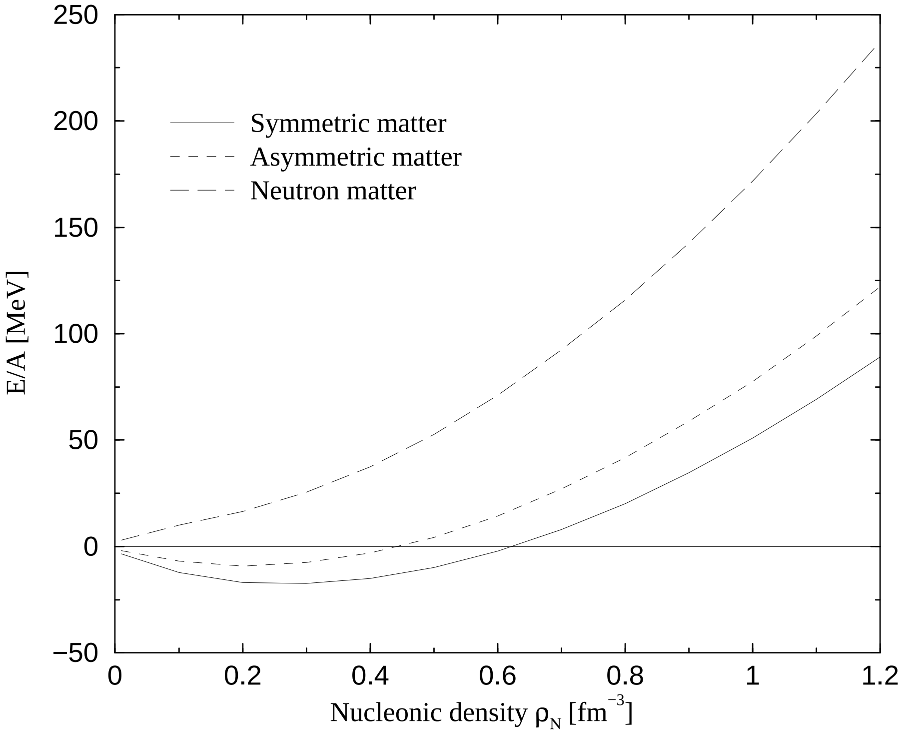

Figure 2.4: Total energy per nucleon as a function of the nucleonic density for symmetric matter ($x_p = 0.5$), asymmetric matter with $x_p = 0.25$ and pure neutron matter ($x_p = 0$). The results have been obtained for the NSC97e NN interaction using the continuous prescription.

according to Eq. (2.12).

The total energy per nucleon as a function of the nucleonic density for symmetric, asymmetric (with $x_p = 0.25$) and pure neutron matter is reported in Fig. 2.4. As before, the results have been obtained for the NSC97e nucleon-nucleon interaction model using the continuous prescription. The calculated energy per nucleon for symmetric matter has a minimum for $\rho_N \sim 0.3$ fm^{-3} ($k_{F_n} = k_{F_p} = 1.64$ fm^{-1}), being its value $E/A \sim -17.3$ MeV. As expected (see Chapter 1) the Brueckner–Hartree–Fock calculation does not reproduce the empirical saturation point, being necessary to include three-body forces to get the empirical values $\rho_N = \rho_0 = 0.17 \pm 0.01$ fm^{-3}, $E/A = -16 \pm 1$ MeV,

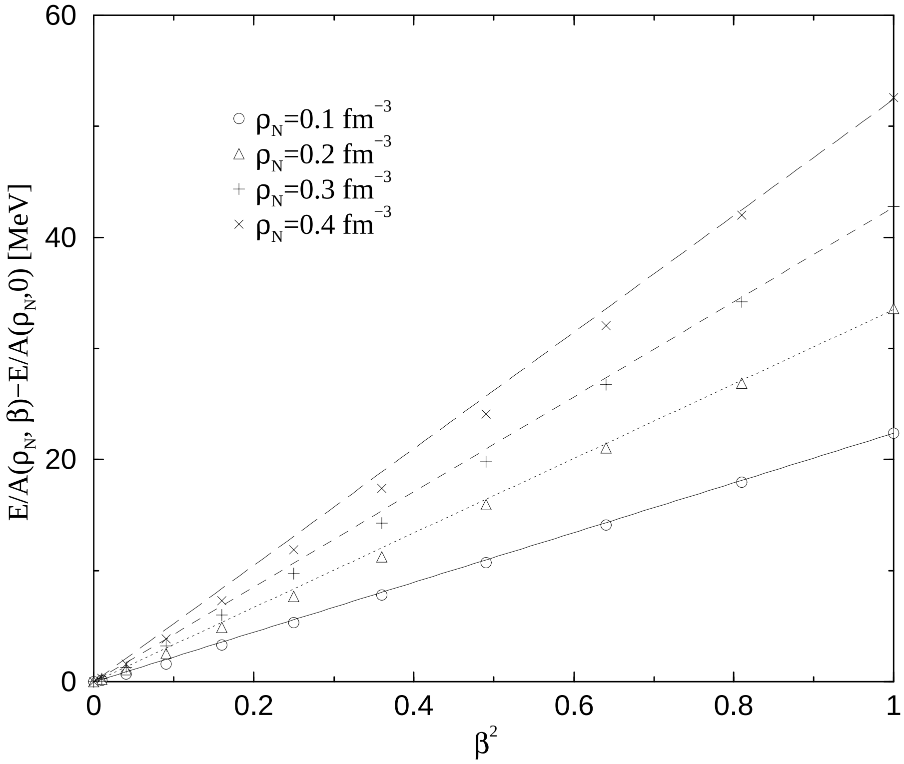

Figure 2.5: Energy difference between asymmetric and symmetric matter as function of the asymmetry parameter squared for four values of the density. Symbols show the results from the BHF calculation, while straight lines correspond to the parabolic fit of Eq. (2.13).

as well as other properties of nuclear matter at saturation. As the proton fraction decreases, the total energy per nucleon shows, as expected, less and less attraction due to the larger number of neutron pairs (coupled to isospin $T = 1$) and to an increase of the kinetic energy.

There is empirical information on asymmetric nuclear matter that indicates that the energy difference between the energy per nucleon in asymmetric matter and the energy per nucleon in symmetric matter, $E/A(\rho_N, \beta) - E/A(\rho_N, 0)$, is proportional to β^2, being $\beta = 1 - 2x_p$ the asymmetry parameter. As can be seen in Fig. 2.5, where

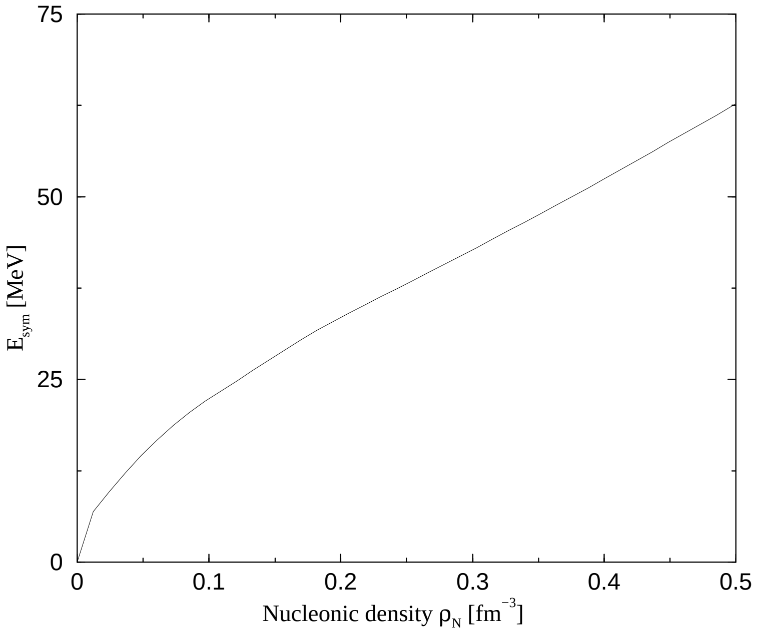

Figure 2.6: Symmetry energy as function of the nucleonic density.

this energy difference going from symmetric to pure neutron nuclear matter is plotted as a function of β^2 for four different values of the nucleonic density, our Brueckner–Hartree–Fock calculation fulfils this law to a very good accuracy.

These results indicate that the energy per nucleon in asymmetric nuclear matter can be well approximated by the parabolic form

$$\frac{E}{A}(\rho_N,\beta) = \frac{E}{A}(\rho_N,0) + E_{sym}(\rho_N)\beta^2 \ , \tag{2.13}$$

where the symmetry energy $E_{sym}(\rho_N)$, defined as

$$E_{sym}(\rho_N) = \frac{1}{2}\frac{\partial^2 E/A(\rho_N,\beta)}{\partial\beta^2}|_{\beta=0} \ , \tag{2.14}$$

can be now expressed in terms of the difference between the energy per nucleon of

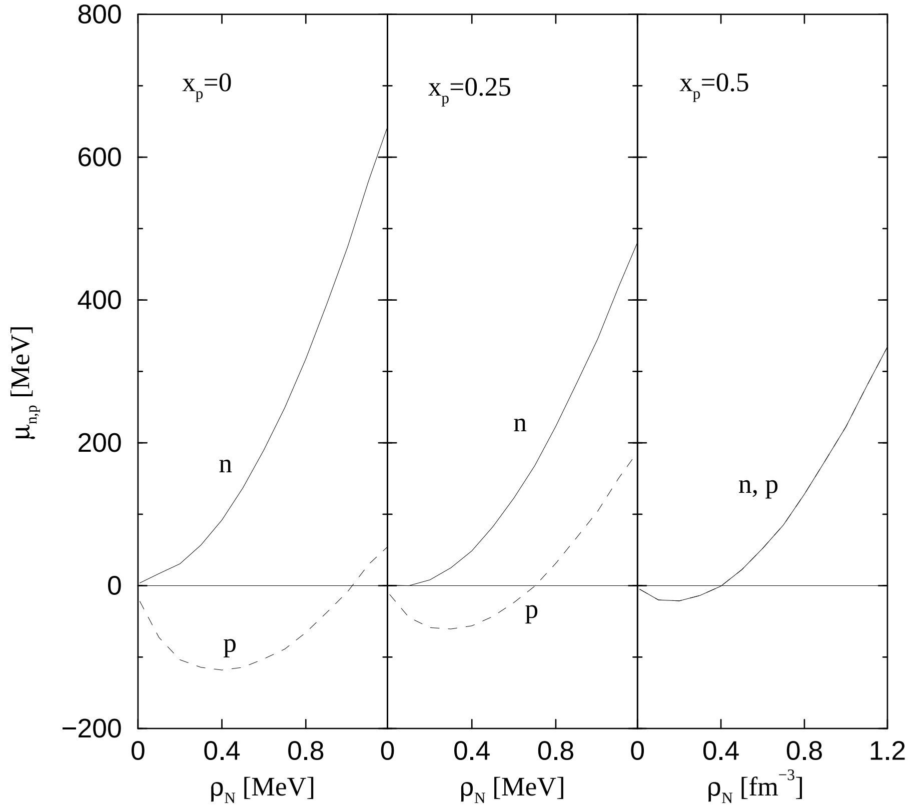

Figure 2.7: Neutron (solid lines) and proton (dashed lines) chemical potentials as functions of the nucleonic density for symmetric, asymmetric ($x_p = 0.25$) and neutron matter obtained using the parabolic approximation of Eq. (2.16).

neutron and symmetric matter

$$E_{sym}(\rho_N) \approx \frac{E}{A}(\rho_N, 1) - \frac{E}{A}(\rho_N, 0) \ . \tag{2.15}$$

We show in Fig. 2.6 the symmetry energy as a function of the nucleonic density obtained from our Brueckner–Hartree–Fock calculations employing the NSC97e nucleon-nucleon interaction model.

Within this parabolic approximation one can obtain the neutron and proton chemical potentials in asymmetric matter in the following way

$$\mu_{n,p}(\rho_N,\beta) = \frac{\partial\varepsilon(\rho_N,\beta)}{\partial\rho_{n,p}} \approx \mu_{n,p}(\rho_N,0) - \left(\beta^2 \mp 2\beta - \beta^2\rho_N\frac{\partial}{\partial\rho_N}\right) E_{sym}(\rho_N) \ , \quad (2.16)$$

where the minus sign is for neutrons and the plus sign for protons. We end this section by showing in Fig. 2.7 the neutron and proton chemical potentials as functions of the nucleonic density for symmetric (right panel), asymmetric (central panel) and pure neutron matter (left panel) obtained from Eq. (2.16) and our BHF calculation with the continuous choice. When the proton fraction decreases, the difference between the neutron and proton chemical potentials becomes more evident because, as we have already said, neutrons become less attractive, whereas protons turn out more attractive.

2.3.2 Nuclear matter with strangeness content

After having reviewed some of the properties of pure nucleonic matter ($\rho_Y = 0$), in this section we consider nuclear matter with strangeness content, focusing our analysis on the role of the hyperon-hyperon interaction.

To begin with, we show in Fig. 2.8 the complete set of nucleon and hyperon single-particle potentials in pure nucleonic symmetric matter at total density $\rho_B = \rho_N = 0.17$ fm^{-3}. Results for the NSC97a, NSC97e and NSC97f baryon-baryon interaction models are shown in the left, central and right panels, respectively. These results have been obtained using the continuous prescription. As can be seen from the figure, there are slight differences between the employed models, giving NSC97e and NSC97f the most similar results. The hyperon single-particle potentials are much less attractive than the nucleonic ones, reflecting the weaker strength of the hyperon-nucleon interaction

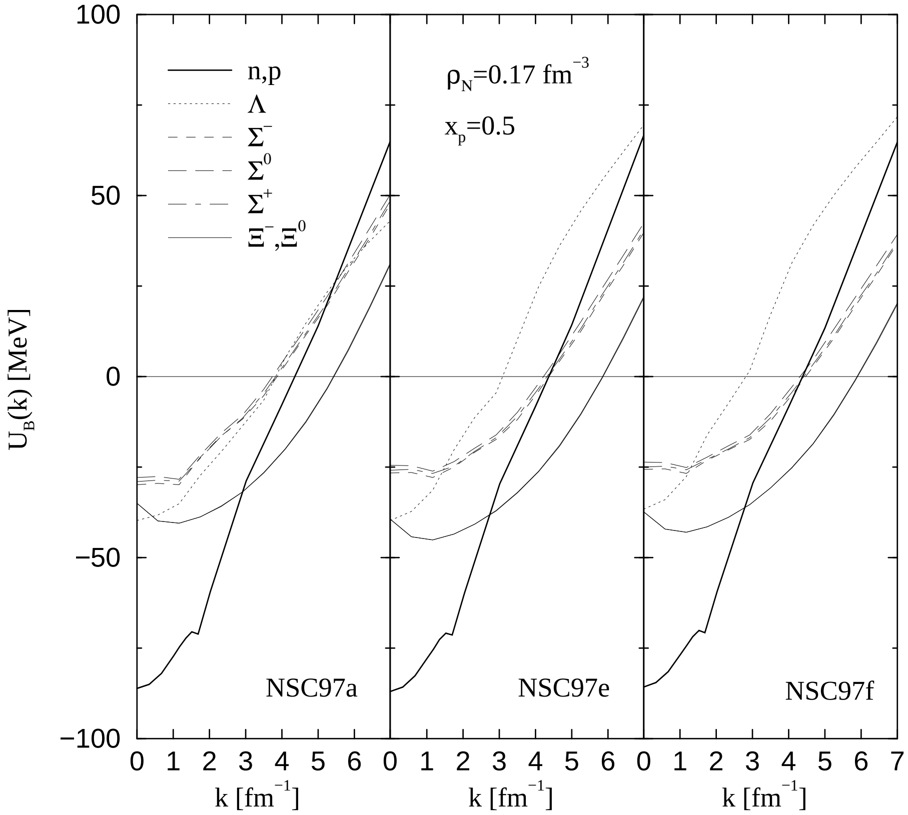

Figure 2.8: Single-particle potentials of the different baryons in pure nucleonic symmetric matter at total baryonic density $\rho_B = \rho_N = 0.17$ fm^{-3} for three different parametrizations, NSC97a, NSC97e and NSC97f, of the Stoks and Rijken baryon-baryon interaction model [St99]. All results have been obtained using the continuous prescription.

compared with the nucleon-nucleon potentials. The most interesting feature that can be extracted from Fig. 2.8 are the hyperon "well depths" $U_Y(k = 0)$. The corresponding results are displayed in Fig. 2.9 as functions of the nucleonic density. One notes that these new Nijmegen models predict relatively strong attraction for all types of hyperons.

The Λ single-particle potential in symmetric nuclear matter at $\rho_N = 0.17\,\mathrm{fm}^{-3}$ turns out to be around -40 MeV at $k = 0$ and has a smooth parabolic behaviour as a function of k. This result is larger than the value of -30 MeV obtained when one extrapolates

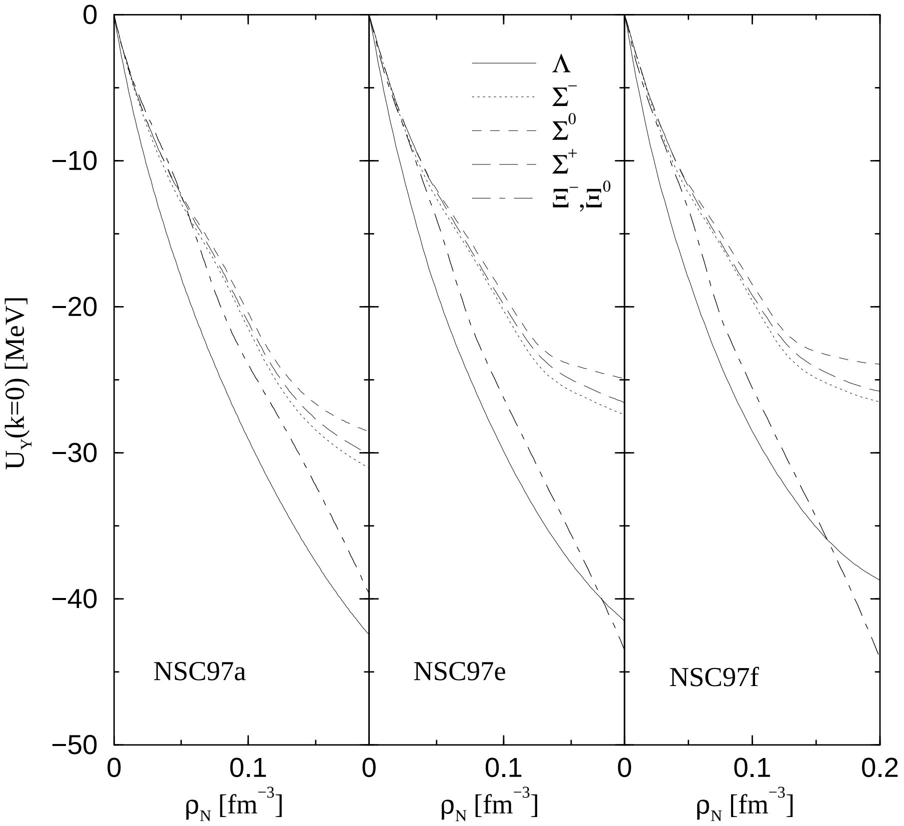

Figure 2.9: Well depths of the different hyperons as functions of the nucleonic density in pure nucleonic symmetric matter ($\rho_Y = 0$). Results obtained with models NSC97a, NSC97e and NSC97f are shown in the left, central and right panel, respectively.

to large A the s-wave Λ single-particle energy of several hypernuclei [Ba90]. It is also much larger in magnitude than the value of around -24 MeV [Ya94, Hj96, Vi98] which is obtained using the NSC89 YN potential [Ma89] with the standard choice for the spectrum of the intermediate YN states in the Bethe-Goldstone equation, or even with the Jülich B model from which a value of ~ -30 MeV is obtained (see Fig. 3.2).

The value of the Σ single-particle potential at $k = 0$ for $\rho_N = 0.17$ fm^{-3} lies between -20 or -25 MeV (depending on the type of Σ and interaction model) which is somewhat more attractive than that obtained with the NSC89 potential of around -17

MeV, and might not be supported by the present experimental information. Although data on Σ^- atoms seemed to be compatible with attractive potentials of around -25 MeV at ρ_0 [Ba78, Os90], more recent fits including data of heavier atoms suggested a repulsive potential in the nuclear interior [Ba94, Ma95, Ba97b]. A recent comparison of $(K^-, \pi^\pm)$ spectra calculated in plane wave impulse approximation [Da99] with data taken at BNL [Sa98] also seems to favour a repulsive Σ-nucleus interaction, although more sophisticated treatments including the distortions of the incoming and outgoing mesons would be convenient before drawing definite conclusions. The differences in binding between the three Σ-hyperons are in the case of the NSC97a-f potentials solely generated by the different masses.

In the case of Ξ-hyperons, early analysis of old emulsion data [Do83] indicated an attractive Ξ-nucleus well potential of around -24 MeV, while recent (K^-, K^+) spectra on ${}^{12}_{\Lambda}\mathrm{C}$, obtained at KEK [Fu98] and BNL [Kh00] and analyzed within the distorted wave Born approximation, favour a shallower potential of around -14 MeV.

Having analyzed the hyperon single-particle potentials in pure nucleonic symmetric matter, we consider now the effect of nucleon asymmetry (i.e., different neutron and proton densities) on these quantities. In Fig. 2.10 we show the baryon single-particle potentials at normal density, $\rho_N = 0.17$ fm^{-3}, for three different proton fractions ($x_p = 0.5x_N, 0.25x_N$ and 0), where $x_N = \rho_N/\rho_B$ is the fraction of non-strange baryons, which in this case is 1. According to our results for β-stable matter shown latter in Chapter 4, we restrict our calculations to the NSC97e baryon-baryon interaction model and use the discontinuous prescription when solving the Bethe–Goldstone equation. In addition, we also show the hyperon single-particle potentials (for Λ and Σ^-), denoted with the label 89, obtained with the Nijmegen Soft-Core 89 version of the YN interaction [Ma89].

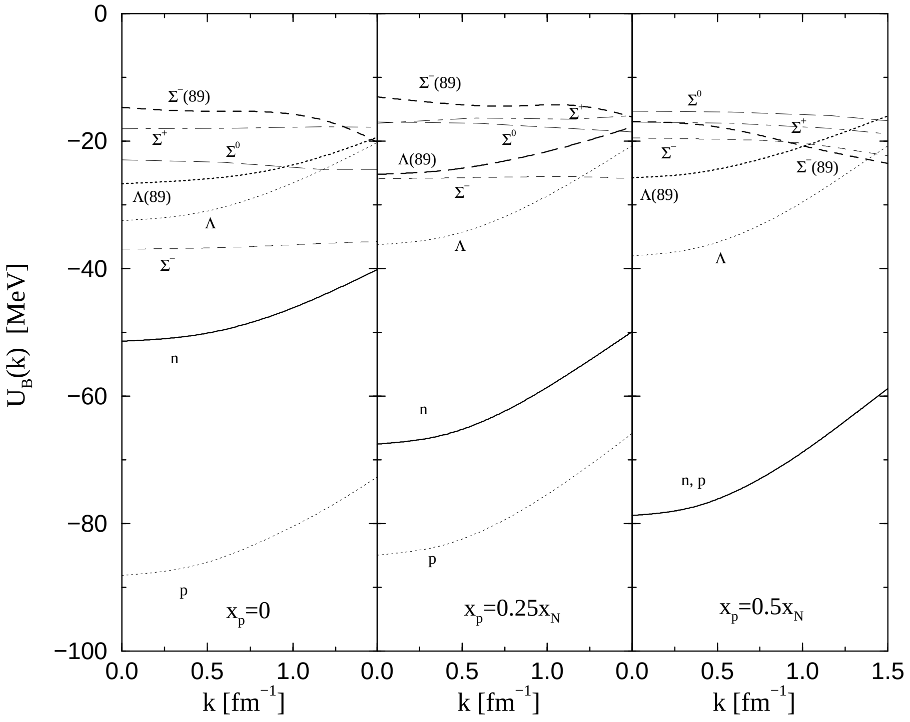

Figure 2.10: Momentum dependence of the single-particle potentials for the different species at $\rho = \rho_0 = 0.17$ fm^{-3}, hyperon fraction $x_y = 0$ and several nucleon asymmetries.

By comparing the right panel (symmetric matter) with Fig. 2.8 (central panel) one sees that less attraction is obtained for all the baryons when the discontinuous choice is adopted in solving the G-matrix equation. This loss of attraction is of the order of 10 MeV in the case of nucleons and around 5 MeV in the case of hyperons.

As the proton fraction decreases, the three Σ's become more bound and the differences between their potentials become more pronounced due to the different behaviour of the ΣN G-matrix in the $T = 1/2$ (repulsive) and $T = 3/2$ (attractive) channels. Whereas $\Sigma^+ n$ and $\Sigma^0 n$ pairs receive contribution from both isospin channels, $\Sigma^- n$ pairs receive only contributions from the attractive isospin 3/2 channel, hence the Σ^-

shows more attraction (see Fig. 2.16 and the corresponding discussion).

Let us consider the differences between the results obtained from the NSC97e model and the NSC89 one. Apart from the different size, the new single-particle hyperon potentials also show a totally different behaviour with increasing asymmetry than that observed for the potentials obtained with the NSC89 YN interaction. While the NSC89 Λ single-particle potential turns out to be slightly more attractive with increasing neutron fraction (i.e., going from the right panel to the left one), the new one becomes slightly more repulsive. The changes for the Σ^- single-particle potential are more drastic. While the NSC89 interaction gives a Σ^- potential which shows little change with increasing neutron fraction, the NSC97e Σ^- potential becomes strongly attractive. The value at $k = 0$ for the Σ^- potential changes from about -20 MeV in symmetric nuclear matter to -37 MeV in neutron matter. This has important consequences in the composition of dense matter: if hyperons feel substantially more attraction, their appearance in dense matter will happen at lower density.

Having established how the nucleons affect the single-particle potential of hyperons it is necessary to investigate the influence of a finite fraction of hyperons on the hyperons themselves and on the nucleons. From now on, we restrict our calculations to matter composed of neutrons, protons, Λ's and Σ^-'s, since these last two hyperon species are the first ones to appear as the density of β-stable neutron star matter increases [Sc98]. This is confirmed in our study of Chapter 4 (see also [Vi00b]) where, up to the density 1.2 fm^{-3} considered there, the hyperons $\Sigma^0, \Sigma^+, \Xi^-$ and Ξ^0 are absent.

In Figs. 2.11 and 2.12 we show the single-particle potentials of the different baryons as functions of the momentum. Figure 2.11 shows results at $\rho = 0.3$ fm^{-3} and a hyperon fraction $x_Y = 0.1$, which is assumed to come only from Σ^- (top panels) or split into

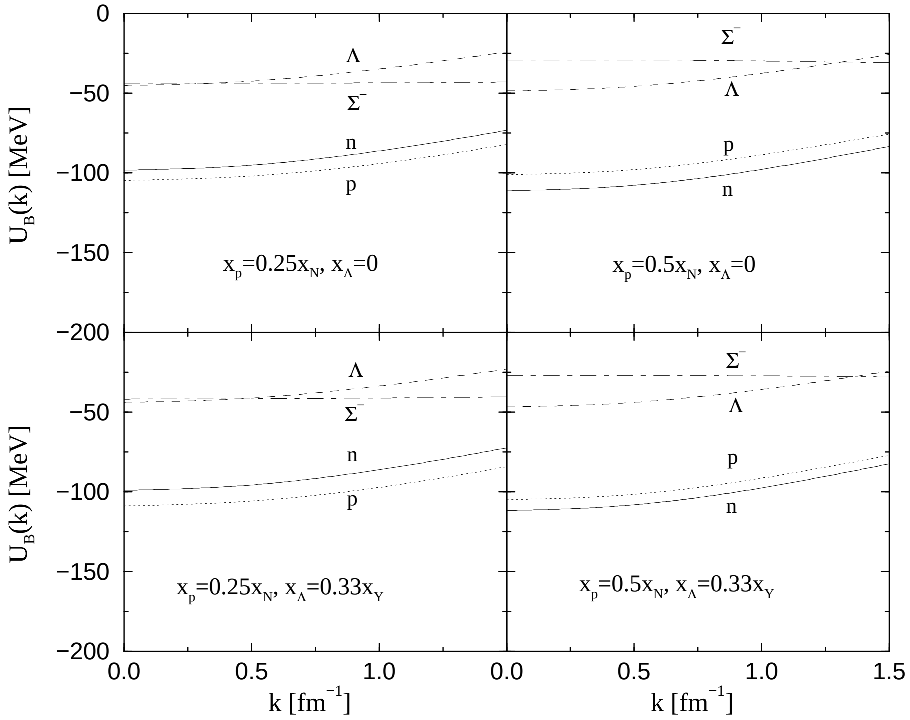

Figure 2.11: Momentum dependence of the single-particle potentials for the different species at $\rho = 0.3$ fm^{-3} and hyperon fraction $x_Y = 0.1$. The right panels correspond to symmetric nuclear matter, $x_n = x_p = 0.5x_N$, while the left ones are for asymmetric nuclear matter with $x_n = 3x_p = 0.75x_N$. In the top panels the hyperon fraction is built exclusively from Σ^- ($x_{\Sigma^-} = x_Y$), while in the bottom ones there is a fraction of Λ's ($x_\Lambda = x_Y/3$) and Σ^-'s ($x_{\Sigma^-} = 2x_Y/3$).

Σ^- and Λ hyperons in a proportion $2:1$, hence $x_{\Sigma^-} = 2x_Y/3$ and $x_\Lambda = x_Y/3$ (bottom panels). The panels on the right correspond to symmetric proton-neutron composition ($x_n = x_p = 0.5x_N$, where $x_N = 0.9$) and the ones on the left correspond to a higher proportion of neutrons ($x_p = 0.25x_N, x_n = 0.75x_N$). Starting at the upper-right panel we observe that the presence of Σ^- hyperons already breaks the symmetry between the proton and the neutron single-particle potentials in a symmetric nucleonic composition, the neutrons feeling around -10 MeV more attraction. This is due to a different behaviour of the $\Sigma^- n$ interaction, which only happens via the attractive $T = 3/2$

isospin channel, with respect to the $\Sigma^- p$ interaction, that also receives contributions from the very repulsive $T = 1/2$ ΣN component. In fact the difference between the neutron and proton potentials is not as pronounced as we move to the lower panel on the right, where some Σ^- hyperons are replaced by Λ hyperons which act identically on protons and neutrons. In the upper left panel, where we have increased the neutron fraction in the non-strange sector, we observe the typical pattern for the nucleon single-particle potentials commented in Fig. 2.1: the particle with the smallest fraction (i.e., the proton) shows more binding. However, this behavior is partially compensated by the presence of a sea of Σ^- which provides attraction (repulsion) to the neutron (proton) single-particle potential. We also observe that the Σ^- feels more attraction, as a consequence of having replaced some repulsive $\Sigma^- p$ pairs by attractive $\Sigma^- n$ ones. The Λ loses binding because the Fermi sea of neutrons is larger and their contribution to the Λ single-particle energy explores higher relative momentum components of the effective Λn interaction, which are less attractive than the small momentum ones. Finally, since the Fermi sea of hyperons is small, the differences observed on the potentials by going from the top panels to the corresponding lower ones (which amounts to replacing Σ^- hyperons by Λ ones) are also small.

Similar effects are found in the results reported in Fig. 2.12, obtained for a baryonic density $\rho = 0.6$ fm^{-3}, at which it is expected that nuclear matter in β equilibrium already contains hyperons [Sc98, Vi00b]. The single-particle potential of the Λ hyperon is less attractive than that for $\rho = 0.3$ fm^{-3}, while that of the Σ^- is very similar. It just gains more attraction when the number of neutrons increases relative to that of protons in going from the right panels to the left ones. As for the nucleon single-particle potentials, we observe, also on the left panels, that the attractive $\Sigma^- n$ interaction is enhanced at these high densities and makes the neutron spectrum more attractive than

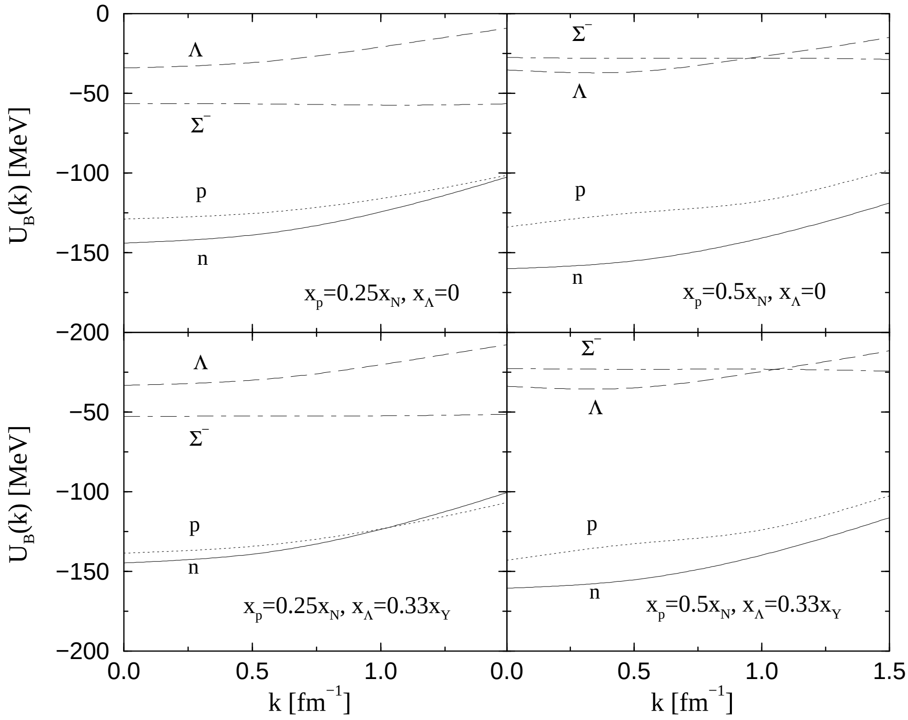

Figure 2.12: The same as Fig. 2.11 for a baryon density $\rho = 0.6$ fm^{-3}.

the proton one, even in the asymmetric situation when one would expect the protons to be more bound.

To assess the influence of the YY interaction, we present the separate contributions building the Λ single-particle potential in Fig. 2.13 and those for the Σ^- one in Fig. 2.14, for a baryonic density of 0.6 fm^{-3}. The hyperon fraction of $x_Y = 0.1$ is split into fractions $x_{\Sigma^-} = 2x_Y/3$ and $x_\Lambda = x_Y/3$ for Σ^- and Λ hyperons, respectively. The results on the right hand side of Figs. 2.13 and 2.14 correspond to the symmetric nuclear case and those on the left to a neutron fraction three times larger than that of protons. We see that the contribution to the Λ potential from Λ hyperons, represented by the dash-dotted line, is attractive and almost negligible, due to a weak attractive $\Lambda\Lambda$ effective interaction [St99b] and to the small amount of Λ particles present. On

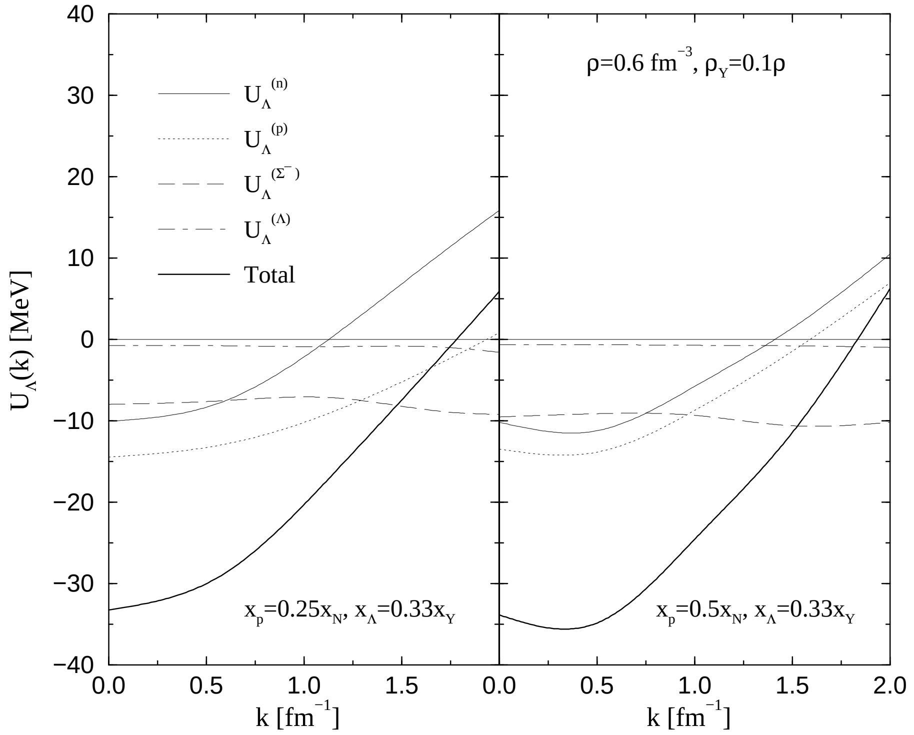

Figure 2.13: Separate contributions of each species to the Λ single-particle potential at $\rho = 0.6$ fm^{-3} and hyperon fraction $x_Y = 0.1$ split into $x_{\Sigma^-} = 2x_Y/3$ and $x_\Lambda = x_Y/3$. The right panel is for symmetric nuclear matter ($x_n = x_p = 0.5x_N$) and the left one for asymmetric nuclear matter ($x_n = 3x_p = 0.75x_N$).

the contrary, the contribution from the Σ^- hyperons is larger, of the order of -10 MeV in nuclear-symmetric matter and slightly less in nuclear-asymmetric matter, which is comparable in size with the contribution from protons and neutrons. This example clearly shows the important role of the YY interaction in modifying the properties of the Λ hyperon. The Λ acquires more attraction and its appearance in dense matter becomes more favourable with respect to the situation in which the YY interaction was neglected. The fact that the neutron (thin solid line) and proton (dotted line) contributions to the Λ single-particle potential are not the same in nuclear-symmetric matter is due to the Σ^- hyperons, which make the neutrons feel more attraction and,

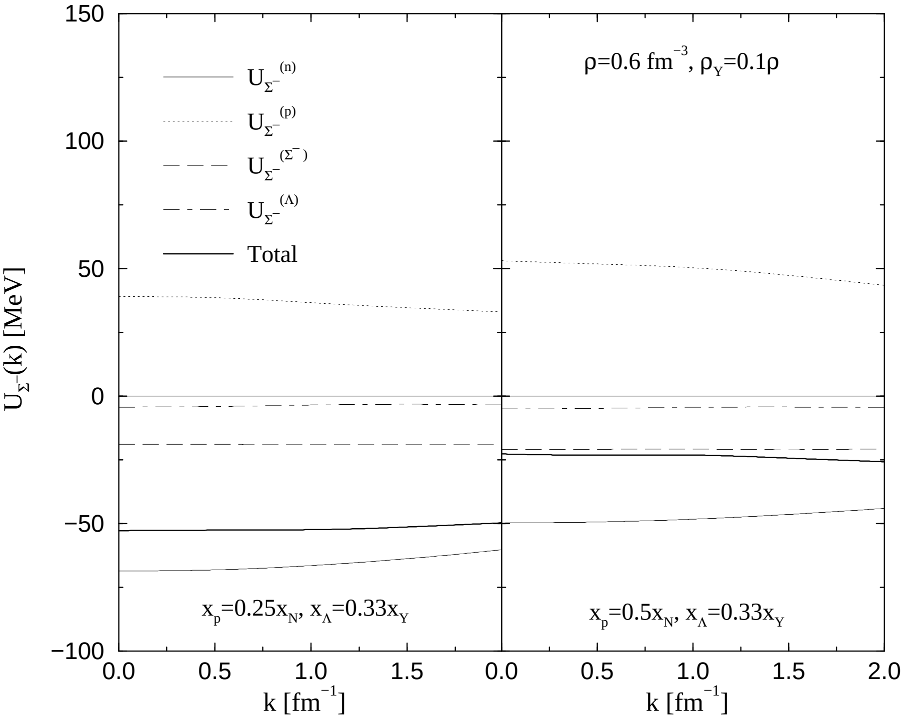

Figure 2.14: The same as Fig. 2.13 for the Σ^- single-particle potential.

consequently, the Λn pairs explore the effective ΛN interaction at smaller energies, where it is less attractive.

The different contributions to the Σ^- are shown in Fig. 2.14. The Λ hyperons (dot-dashed line) contribute very little due to the reduced value of their Fermi momentum. The contribution of the $\Sigma^-\Sigma^-$ pairs (long-dashed line) is very important, of the order of −25 MeV in symmetric nuclear matter, and becomes crucial due to the fact that the neutron (thin solid line) and the proton (dotted line) contributions, which amount each one to about 50 MeV in magnitude, almost cancel each other. In the left panel, the replacement of some protons by neutrons lowers the Σ^- single-particle potential considerably, by about 25 MeV. Again, neglecting the YY interactions here would have made the Σ^- potential around 20 − 25 MeV less attractive.

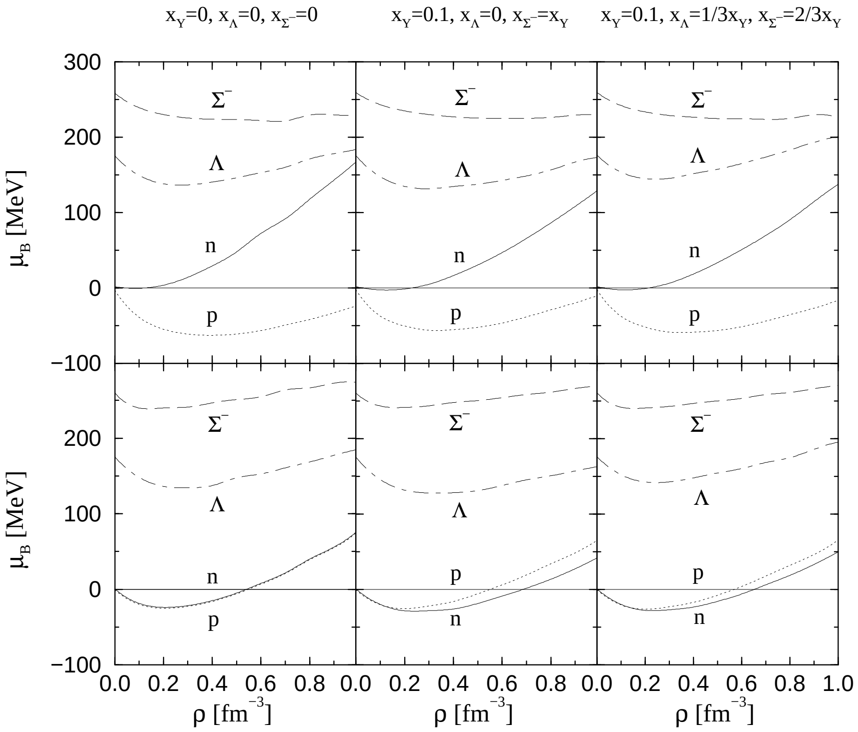

Figure 2.15: Chemical potentials of the different species as functions of total baryonic density, for different nucleonic asymmetries and strangeness fractions. The top panels correspond to the asymmetric nuclear matter case ($x_n = 3x_p = 0.75x_N$), while the bottom ones correspond to symmetric nuclear matter ($x_n = x_p = 0.5x_N$).

The analysis of the structure of β-stable matter requires the knowledge of the chemical potential μ_B of each baryon, defined at zero temperature as the single-particle energy of the Fermi momentum. In Fig. 2.15 we show the chemical potentials as functions of density for different nucleon asymmetries and hyperon fractions. Note that the curves are measured with respect to the nucleon mass and contain, in addition to the non-relativistic Fermi energy, the baryon mass of each species. The top panels show the results for asymmetric nuclear matter ($x_n = 3x_p = 0.75x_N$), whereas the bottom panels stand for the symmetric case. On the left panels we show results for purely nucleonic matter ($x_Y = 0$), on the central panels we have $x_{\Sigma^-} = x_Y = 0.1$, while on the right panels x_Y is distributed into $x_\Lambda = x_Y/3$ and $x_{\Sigma^-} = 2x_Y/3$. The behaviour of the chemical potentials when increasing the nucleonic asymmetry as well as the hyperon fraction follows closely the trends observed in Figs. 2.10, 2.11 and 2.12 for the single-particle potentials at densities $\rho = 0.17, 0.3$ and 0.6 fm^{-3}, respectively. We just have to consider here that the curves in Fig. 2.15 also contain the kinetic energy of the corresponding Fermi momentum. It is interesting to comment on the high density behaviour of the chemical potentials, since this will determine the feasibility of having hyperons in β-stable neutron star matter. In asymmetric nuclear matter, both the Λ and the Σ^- chemical potentials show, from a certain density on, an increase with increasing density which is very mild as compared to that assumed by phenomenological YN interactions [Mi88]. When the number of neutrons over that of protons is increased (top panels), the Λ chemical potential barely changes because of the similarity between the Λn and Λp interaction. However, the Σ^- hyperon acquires more binding due to the dominant $\Sigma^- n$ attractive pairs over the $\Sigma^- p$ repulsive ones. This will favor the appearance of Σ^- in dense neutron matter, through the $nn \to p\Sigma^-$ conversion, when the equilibrium between chemical potentials is achieved at both sides. Once a Fermi sea of Σ^- hyperons starts to build up, however, the neutrons become more attractive, moderating, in turn, the appearance of Σ^- hyperons. As we can see, the composition of dense neutron star matter in β-equilibrium will result from a delicate interplay between the mutual influence among the different species. In fact, one needs to find, at each baryonic density, the particle fractions which balance the chemical potentials in the weak and strong reactions that transform the species among themselves. This study will be presented in Chapter 4.

One of the novelties of this work with respect to that of [St99b] is that we allow for different concentrations of the baryon species. Therefore, we explicitly treat the dependence of the G-matrix on the third component of isospin, which comes from the Pauli operator of species B_5 and B_6 that may have, even when belonging to the same isospin-strangeness multiplet, different Fermi momenta. See Appendix A for more details.

In Fig. 2.16 we report the diagonal $\Sigma\mathrm{N} \to \Sigma\mathrm{N}$ G-matrix elements in the ${}^1S_0$ channel, as a function of the relative momentum for a density $\rho = 0.6$ fm^{-3}, taking $x_\Lambda = 0$ and $x_{\Sigma^-} = x_Y = 0.1$. The top panels correspond to the isospin $T = 1/2$ channel and the lower ones to the $T = 3/2$ one. The panels on the right are for symmetric nuclear matter, $x_n = x_p = 0.5x_N$, while those on the left correspond to $x_p = 0.25x_N$. The starting energy and centre-of-mass momentum is the same for all the curves shown in the same plot; thus the dependence on M_T comes exclusively from the Pauli operator. Note that different pairs of particles contribute to each (T, M_T) combination. The case $(T, M_T) = (1/2, +1/2)$ receives contributions from Σ^+n and Σ^0p pairs, while Σ^-p and Σ^0n contribute to $(T, M_T) = (1/2, -1/2)$. In the case of isospin $T = 3/2$ one has contributions from Σ^-n ($M_T = -3/2$), Σ^0n, Σ^-p ($M_T = -1/2$), Σ^+n, Σ^0p ($M_T = +1/2$), and Σ^+p ($M_T = +3/2$). We observe that the curve corresponding to the third component M_T less affected by Pauli blocking is always more attractive. This is due to the fact that the phase space for intermediate states, which induce attractive corrections to the potential matrix elements, is larger. This is clearly seen in the top panel on the right, since the dotted line contains a channel with the Σ^- hyperon.

When the nucleonic asymmetry is increased by going to the panel on the left, the effects of Pauli blocking on the neutrons are more important than those on the Σ^- hyperons. This is the reason for the solid curve to appear above the dotted one, since the $(T, M_T) = (1/2, +1/2)$ case receives contributions from Σ^0p and Σ^+n in a

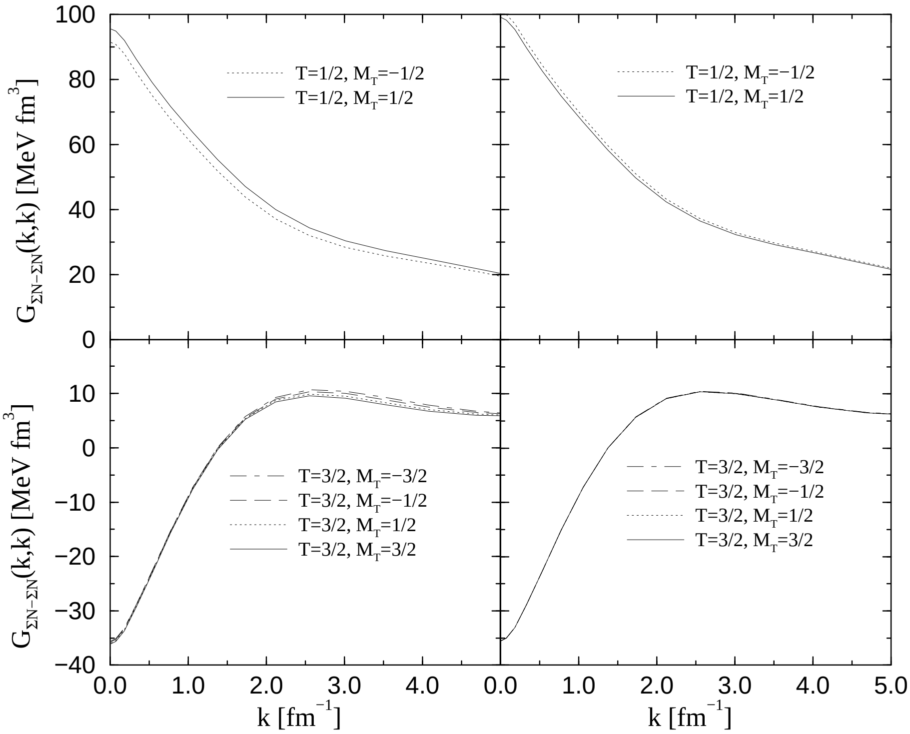

Figure 2.16: Diagonal ΣN G matrix in the $^1S_0$ partial wave as a function of the relative momentum at a density $\rho = 0.6$ fm^{-3}, for the different (T, M_T) isospin channels. The right panels are for symmetric nuclear matter, $x_n = x_p = 0.5x_N$, while the left ones correspond to $x_n = 3x_p = 0.75x_N$. In all cases $x_{\Sigma^-} = 0.1$ and $x_\Lambda = 0$.

proportion 1 : 2 and it contains relatively more neutrons than the case $(T, M_T) = (1/2, -1/2)$ with $\Sigma^- p$ and $\Sigma^0 n$ pairs in a proportion 2 : 1. In the case of $T = 3/2$ we observe that the asymmetry on the Σ multiplet barely induces any dependence on M_T in the G-matrix, as can be seen from the bottom panel on the right. However, one can observe differences when going to asymmetric nuclear matter on the left panel, since the Pauli blocking on $\Sigma^- n$ pairs $(M_T = -3/2)$ is enhanced over that on $\Sigma^+ p$ pairs $(M_T = +3/2)$. As we can see, in all cases considered here the dependence of the G-matrix on the third component of the isospin is very weak and can almost be neglected. We have also encountered this weak dependence in the other $\overline{G}_{B_1 B_2 \to B_3 B_4}$

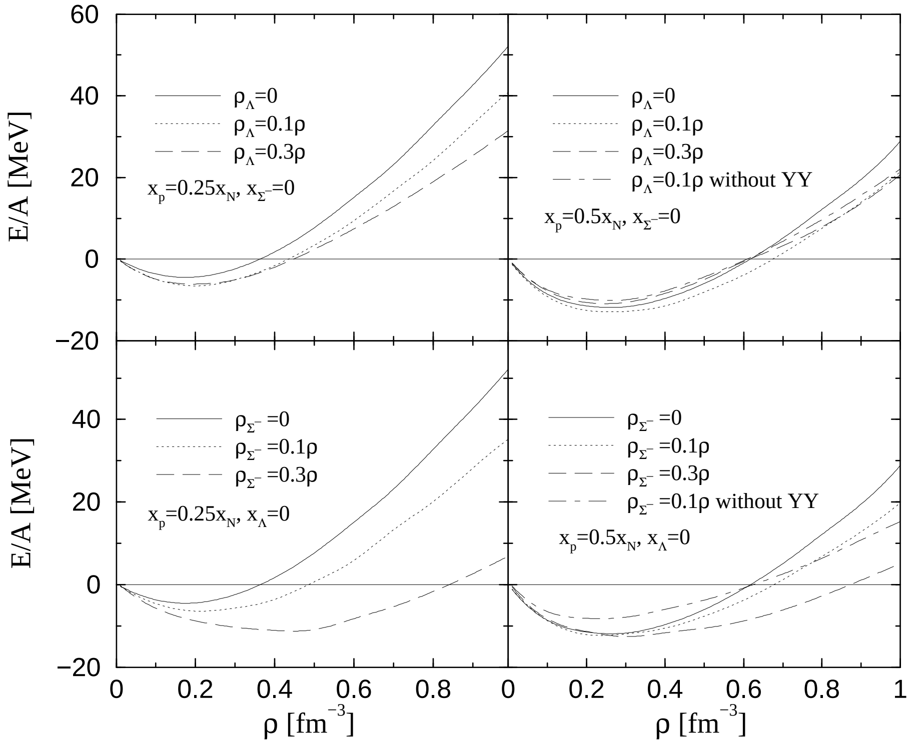

Figure 2.17: Binding energy per baryon as a function of the baryon density. In the top panels we set $x_{\Sigma^-} = 0$ and show results for several values of x_Λ, while the bottom panels correspond to $x_\Lambda = 0$ and different fractions of Σ^-'s. The panels on the right are for symmetric nuclear matter, while the left ones correspond to asymmetric nuclear matter ($x_n = 3x_p = 0.75x_N$). In the case of nuclear symmetric matter with 10 % of hyperons we also show a curve (dash-dotted line) where the YY interaction has been turned off.

matrices. Therefore, a presumably good strategy and less time consuming would be to obtain the G-matrices in isospin-saturated systems and, afterwards, calculate the single-particle potentials by folding the "approximate" effective interactions with the different baryon Fermi seas.

We finish this section and the chapter by reporting in Fig. 2.17 the binding energy per baryon as a function of density. The right and left figures describe symmetric and asymmetric ($x_n = 3x_p = 0.75x_N$) nuclear matter, respectively. In the top panels, we show the binding energy with $x_{\Sigma^-} = 0$ for several values of x_Λ, while in the bottom panels we consider $x_\Lambda = 0$ and vary the concentration of Σ^- hyperons. The binding energy per baryon is the result of a balance between the average kinetic energy of each baryon Fermi sea and the contribution from the mutual interactions, given by the average of the single-particle potential of each species. In order to identify the effects of the YY interaction on the binding energy per baryon we have also included a curve corresponding to a calculation with a 10% of hyperons (either Λ's or Σ^-'s) where the YY interaction is turned off (dash-dotted line). In both cases, turning the YY interaction on, results in a gain of binding energy which is larger in the case of Σ^-. The binding energy per baryon shows a saturation density, i.e., a density for which the thermodynamic pressure is zero, which is too high when we consider the composition with only nucleons. The location of this saturation density is little affected when the percentage of hyperons is increased. When a small amount of nucleons is substituted by hyperons, there is automatically a decrease of the kinetic energy contribution because the hyperons can be accommodated in lower momentum states and in addition have a larger bare mass. The analysis of the influence of the effective interaction on the binding energy must be made separately for Λ's and Σ^-'s. Although the effective ΛN and $\Lambda\Lambda$ interactions are clearly less attractive than the NN one, the reduction of kinetic energy is clearly enough to compensate for the loss of binding energy when a 10% of nucleons is substituted by Λ's. Notice, however, that we have to consider the $\Lambda\Lambda$ interaction in order to obtain this increase of binding with respect to the pure nucleonic case. At $x_\Lambda = 30\%$ the loss of kinetic energy is not enough to compensate for the loss of attraction from the effective interactions and less binding energy than the case with only nucleonic degrees of freedom is obtained. Looking at the lower panels for the Σ^- hyperons we observe that the binding energy per baryon gains more attraction as compared to the case for Λ's. This is, essentially, due to the larger loss of kinetic energy due to the larger mass of the Σ^-. In general, the replacement of nucleons by hyperons produces a gain in binding energy and a softening of the Equation of State. The appearance of hyperons in β-stable matter, the softening of the Equation of State and its implications on the properties of neutron stars are deferred to Chapter 4.

Chapter 3

Hyperon properties in finite nuclei

> "Though this be madness, yet there is method in it".
>
> *William Shakespeare*, **Hamlet**, Act. II, Sc 2.

The aim of this chapter is to present a method to obtain an effective hyperon-nucleon interaction in finite nuclei based on an expansion over a G-matrix calculated in nuclear matter. Our purpose is to set up a reliable frame for hypernuclear structure calculations with the aim of obtaining information about the hyperon-nucleon interaction, complementary to that provided by hyperon-nucleon scattering experiments. The chapter is organized in the following way: section 3.1 is devoted to the derivation of the effective hyperon-nucleon interaction in finite nuclei and of the finite nucleus hyperon self-energy. The convergence of the method is examined in section 3.2. Finally, results for the properties of single-particle states of the Λ hyperon in several nuclei are presented in section 3.3.

3.1 Hyperon single-particle properties in finite nuclei

Several features of the Λ single-particle properties in the nucleus, being essentially different from those of the nucleon, have clearly emerged from the efforts performed on hypernuclear physics during the last decades. It is well accepted nowadays that the depth of the Λ-nucleus potential is around -30 MeV, which is 20 MeV less attractive than the corresponding nucleon-nucleus one. The spin-orbit splittings of single particle levels in Λ hypernuclei were found to be much smaller than their nucleonic counterparts [Br78], typically more than one order of magnitude. Moreover, the Λ, contrary to the nucleon, maintains its single-particle character even for states well below the Fermi surface [Pi91, Ha96] indicating a weaker interaction with other nucleons. On the other hand, studies of the mesonic weak decay of light Λ hypernuclei [Mo91, St93, Ku95] have shown that the data [Sz91] favour Λ-nucleus potentials which show a repulsion at short distances. This seems also to be a characteristic of the Σ-nucleus potential for light Σ-hypernuclei [Ha90], which reproduces the recently measured bound Σ^+ state in ${}^4_\Sigma$He with the in-flight ^{4}He(K^-,π^-) reaction [Na98], confirming with new and better statistics the earlier results from the ^{4}He$(K^-_{\text{stopped}},\pi^-)$ reaction [Ha89].

The purpose of this chapter is to study the self-energy of hyperons in several nuclei using a microscopic many-body approach. Our starting point is a nuclear matter G-matrix at a fixed energy and density, which is used to calculate the G-matrix for a finite nucleus including the two-particle-one hole second-order correction. This correction incorporates the correct energy and density dependence of the G-matrix. The hypernuclear structure calculations of Refs. [Ya92, Ya94] take the nuclear matter G-matrix at the Fermi momentum k_F (density) that reproduces the binding energy of the Λ in the hypernucleus under study. Our finite nucleus calculation eliminates the need of choosing such an effective Fermi momentum for each single-particle state and hypernucleus. In this sense it is comparable with the finite nucleus calculations of Refs. [Ha93, Ha93b].

In this section we show how to obtain the hyperon single-particle properties in finite nuclei using an effective interaction derived microscopically from realistic hyperon-nucleon interactions. We first present in section 3.1.1 how a finite nucleus hyperon-nucleon G-matrix is obtained from an expansion over a G-matrix calculated in nuclear matter at fixed density and starting energy. Then, in section 3.1.2, we construct the hyperon self-energy in the nucleus in the Brueckner–Hartree–Fock approximation. The single-particle binding energies and the corresponding wave functions for the different orbits can then be obtained by using this self-energy as a single-particle potential in the Schrödinger equation, as it is explained in section 3.1.3.

3.1.1 Hyperon-nucleon G-matrix in finite nuclei

One possible way to construct a finite nucleus hyperon-nucleon G_{FN}-matrix is to solve directly its corresponding Bethe–Goldstone equation, which in a compact notation reads

$$G_{FN} = V + V \left(\frac{Q}{E}\right)_{FN} G_{FN}. \tag{3.1}$$

However, we can take profit from the fact that we have already obtained the hyperon-nucleon G-matrix in nuclear matter (see Chapter 2), and try to find the appropriate finite nucleus G_{FN}-matrix by relating it to the nuclear matter one.

Recalling that the corresponding Bethe–Goldstone equation for the nuclear matter G-matrix is just

$$G = V + V \left(\frac{Q}{E}\right)_{NM} G \; , \tag{3.2}$$

we can eliminate the bare interaction V in Eqs. (3.1) and (3.2) to obtain G_{FN} through the following integral equation

$$\begin{aligned} G_{FN} &= G + G \left[\left(\tfrac{Q}{E}\right)_{FN} - \left(\tfrac{Q}{E}\right)_{NM}\right] G_{FN} \\ &= G + G \left[\left(\tfrac{Q}{E}\right)_{FN} - \left(\tfrac{Q}{E}\right)_{NM}\right] G + \\ &+ G \left[\left(\tfrac{Q}{E}\right)_{FN} - \left(\tfrac{Q}{E}\right)_{NM}\right] G \left[\left(\tfrac{Q}{E}\right)_{FN} - \left(\tfrac{Q}{E}\right)_{NM}\right] G + \dots \; , \end{aligned} \tag{3.3}$$

which involves the nuclear matter G-matrix and the difference between the finite nucleus and nuclear matter propagators, which account for the relevant intermediate states. The expansion (3.3) can be truncated up to the second-order because the difference between the finite nucleus and the nuclear matter propagator is in fact quite small. Therefore, we have

$$G_{FN} \simeq G + G \left[\left(\frac{Q}{E}\right)_{FN} - \left(\frac{Q}{E}\right)_{NM}\right] G \; . \tag{3.4}$$

3.1.2 Hyperon self-energy in finite nuclei

The self–energy of a Λ or Σ hyperon in a finite hypernucleus can be obtained using a finite nucleus G_{FN}-matrix, such as the one we have constructed in the previous section,

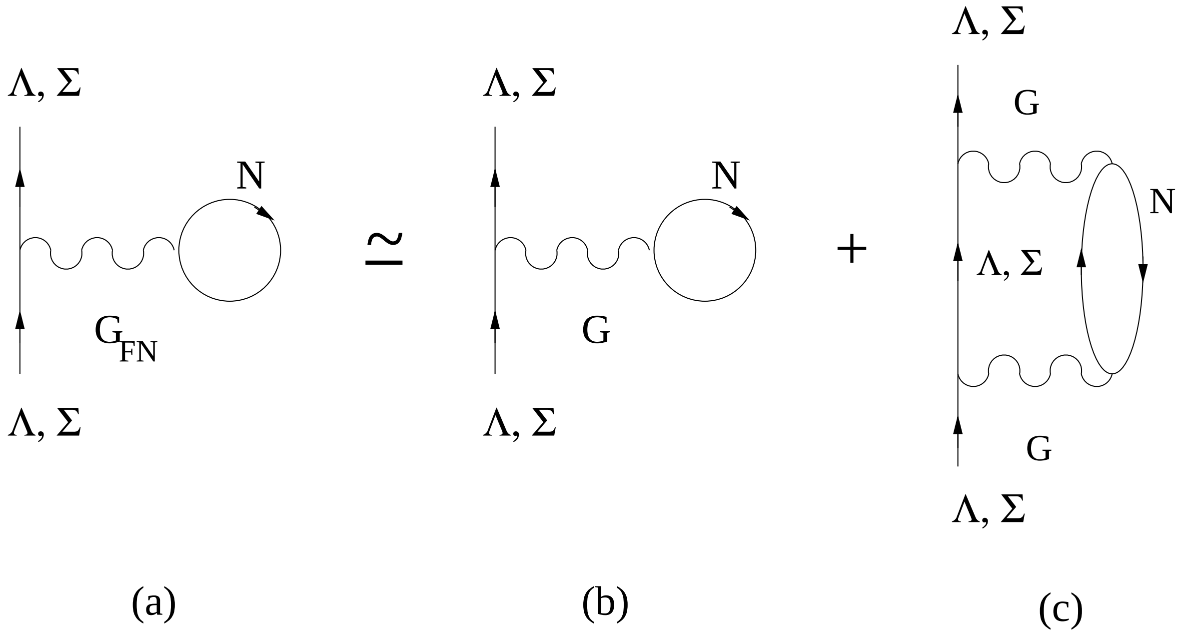

Figure 3.1: Brueckner–Hartree–Fock approximation to the finite nuclei hyperon self-energy (diagram (a)), split into the sum of a first-order contribution (diagram (b)), and a second-order $2p1h$ correction (diagram (c)).

as an effective hyperon-nucleon interaction.

In the Brueckner–Hartree–Fock approximation the finite nucleus hyperon self-energy is given by diagram (a) of Fig. 3.1. According to Eq. (3.4) it can be split into the sum of diagram (b), which represents the first-order term on the right-hand side of Eq. (3.4), and diagram (c), which stands for the so-called second-order two-particle-one-hole ($2p1h$) correction, where the intermediate propagator has to be viewed as the difference of propagators appearing in Eq. (3.4).

We can construct the expressions for the diagrams considered, taking the incoming (outgoing) hyperon as a plane wave and the nucleon hole states as harmonic oscillator ones. The first-order term of Fig. 3.1(b) yields a real and energy-independent contribution to the self–energy given by

$$\mathcal{V}_{1^{st}}(k_Y k'_Y l_Y j_Y t_{z_Y}) = \frac{1}{\hat{j}_Y^{\,2}} \sum_{\mathcal{J}} \sum_{n_h l_h j_h t_{z_h}} \hat{\mathcal{J}}^2$$
$$\times \langle (k'_Y l_Y j_Y t_{z_Y})(n_h l_h j_h t_{z_h})\mathcal{J} | \overline{G} | (k_Y l_Y j_Y t_{z_Y})(n_h l_h j_h t_{z_h})\mathcal{J} \rangle, \tag{3.5}$$

where $k_Y(k'_Y)l_Y j_Y t_{z_Y}$ and $n_h l_h j_h t_{z_h}$ denote, respectively, the quantum numbers of the incoming (outgoing) hyperon and the nucleon hole states, $\vec{\mathcal{J}} = \vec{j_Y} + \vec{j_h}$ is the total angular momentum in the laboratory frame and $\hat{x} \equiv \sqrt{2x+1}$. Although not denoted explicitly, it is understood, in Eqs. 3.5 and the following lines, that the isospin value of the nucleon, the Λ and the Σ is $1/2, 0$ and 1, respectively.

The computation of the contribution coming from the two-particle-one-hole ($2p1h$) diagram of Fig. 3.1(c) requires some more work. First, we evaluate the imaginary part of the term $G(Q/E)_{FN}G$ in Eq. (3.4). This term has an explicit energy dependence and reads

$$\mathcal{W}^{(1)}_{2p1h}(k_Y k'_Y l_Y j_Y t_{z_Y} \omega) = -\frac{1}{\hat{j}_Y^{\,2}} \sum_{n_h l_h j_h t_{z_h}} \sum_{\mathcal{L} L S J \mathcal{J} T M_T} \sum_{Y'=\Lambda\Sigma} \int k^2 dk \int K^2 dK \hat{\mathcal{J}}^2$$
$$\times \langle (k'_Y l_Y j_Y t_{z_Y})(n_h l_h j_h t_{z_h})\mathcal{J} | \overline{G} | (Y'N) K \mathcal{L} k L S J \mathcal{J} T M_T \rangle$$
$$\times \langle (Y'N) K \mathcal{L} k L S J \mathcal{J} T M_T | \overline{G} | (k_Y l_Y j_Y t_{z_Y})(n_h l_h j_h t_{z_h})\mathcal{J} \rangle$$
$$\times \pi \delta \left(\omega + \varepsilon_h - \frac{K^2}{2(M_N + M_{Y'})} - \frac{k^2(M_N + M_{Y'})}{2 M_N M_{Y'}} - M_{Y'} + M_Y \right) , \tag{3.6}$$

where ω is the energy of the hyperon measured with respect to the hyperon rest mass, k, L are the relative and orbital angular momentum, $K, \mathcal{L}$ are the corresponding quantum numbers of the centre-of-mass motion, S is the total spin, $M_T = t_{z_Y} + t_{z_h}$ is the total isospin third component, and $\vec{J} = \vec{L} + \vec{S}$.

The single-hole energies ε_h have been taken equal to the experimental single-particle energies in most of the nuclei studied (e.g., ^{4}He, ^{12}C, ^{16}O, ^{40}Ca) and have been calculated from a Woods-Saxon potential with Spin-Orbit and Coulomb terms appropriately fitted in other cases (e.g., ^{90}Zr and ^{208}Pb). The contribution to the real part of the self-energy from Eq. (3.6) can be obtained through the dispersion relation

$$\mathcal{V}^{(1)}_{2p1h}(k_Y k'_Y l_Y j_Y t_{z_Y} \omega) = \frac{1}{\pi}\mathcal{P}\int_{-\infty}^{\infty} \frac{\mathcal{W}_{2p1h}(k_Y k'_Y l_Y j_Y t_{z_Y} \omega')}{\omega' - \omega} d\omega', \tag{3.7}$$

where $\mathcal{P}$ means a principal value integral.

Finally, we must evaluate the $2p1h$ correction term coming from the nuclear matter intermediate propagator (i.e., the term $G(Q/E)_{NM}G$ in Eq. (3.4)). It reads

$$\begin{aligned}
\mathcal{V}^{(2)}_{2p1h}(k_Y k'_Y l_Y j_Y t_{z_Y}) = {} & \frac{1}{\hat{j}_Y^{\,2}} \sum_{n_h l_h j_h t_{z_h}} \sum_{\mathcal{L} L S J \mathcal{J} T M_T} \sum_{Y'=\Lambda\Sigma} \int k^2 dk \int K^2 dK \hat{\mathcal{J}}^2 \\
& \times \langle (k'_Y l_Y j_Y t_{z_Y})(n_h l_h j_h t_{z_h})\mathcal{J} | \overline{G} | (Y'N) K \mathcal{L} k L S J \mathcal{J} T M_T \rangle \\
& \times \langle (Y'N) K \mathcal{L} k L S J \mathcal{J} T M_T | \overline{G} | (k_Y l_Y j_Y t_{z_Y})(n_h l_h j_h t_{z_h})\mathcal{J} \rangle \\
& \times \overline{Q}_{Y'N}(K,k) \left(\omega_{NM} - \tfrac{K^2}{2(M_N + M_{Y'})} - \tfrac{k^2 (M_N + M_{Y'})}{2 M_N M_{Y'}} - M_{Y'} + M_Y \right)^{-1} ,
\end{aligned} \tag{3.8}$$

where $\overline{Q}_{YN}$ is the nuclear matter angle-averaged Pauli operator and ω_{NM} is the nuclear matter starting energy. This term only contributes to the real part of the hyperon self–energy and avoids the double counting over intermediate Y'N states contained already in the nuclear matter G-matrix of the Brueckner–Hartree-Fock contribution $\mathcal{V}_{1^{st}}$.

From Eqs. (3.5), (3.6) and (3.8) we see that typical matrix elements in the calculation are

$$\langle (k_Y l_Y j_Y t_{z_Y})(n_h l_h j_h t_{z_h})\mathcal{J} | \overline{G} | (k'_Y l_Y j_Y t_{z_Y})(n_h l_h j_h t_{z_h})\mathcal{J} \rangle , \tag{3.9}$$

for the first-order diagram of Fig. 3.1b, or

$$\langle (k_Y l_Y j_Y t_{z_Y})(n_h l_h j_h t_{z_h})\mathcal{J}|\,\overline{G}\,|(YN)K\mathcal{L}kLSJ\mathcal{J}TM_T\rangle \,, \tag{3.10}$$

appearing in the second-order diagram of Fig. 3.1c. The two-body mixed representation states involving a plane wave and an harmonic oscillator can be expressed in terms of momentum and angular variables in the laboratory frame using

$$|(n_h l_h j_h t_{z_h})(k_Y l_Y j_Y t_{z_Y})\mathcal{J}\rangle = \int k_h^2 dk_h R_{n_h l_h}(\alpha k_h)\,|(k_h l_h j_h t_{z_h})(k_Y l_Y j_Y t_{z_Y})\mathcal{J}\rangle \,, \tag{3.11}$$

where, as we said before, $n_h l_h j_h t_{z_h}$ and $k_Y l_Y j_Y t_{z_Y}$ are the quantum numbers of the nucleon hole state and the hyperon state, respectively. Further, α is the oscillator parameter appropriate to describe the single-particle wave functions of the bound nucleons in the nuclear core, defined as

$$\alpha = \frac{\hbar}{\sqrt{M_N \hbar\omega}} \tag{3.12}$$

with $\hbar\omega$ chosen as the following function of the mass number:

$$\hbar\omega = \left(45A^{-\frac{1}{3}} - 25A^{-\frac{2}{3}}\right) \ \text{MeV} \,. \tag{3.13}$$

With appropriate transformation coefficients [Ku79, Wo72], one can express the two-body states with laboratory coordinates in terms of the variables in the centre-of-mass system used in the solution of the G-matrix

$$\begin{aligned}
|(k_a l_a j_a t_{z_a})(k_b l_b j_b t_{z_b})\mathcal{J}\rangle = \sum_{\mathcal{L}\lambda LSJ}\int k^2dk\int K^2dK\left\{\begin{array}{ccc} l_a & l_b & \lambda \\ \frac{1}{2} & \frac{1}{2} & S \\ j_a & j_b & \mathcal{J}\end{array}\right\} \\
\times(-1)^{\lambda+J-\mathcal{L}-S}\hat{J}\hat{\lambda}^2\hat{j}_a\hat{j}_b\hat{S}\left\{\begin{array}{ccc} \mathcal{L} & L & \lambda \\ S & \mathcal{J} & J\end{array}\right\}\langle K\mathcal{L}kL\lambda|k_a l_a k_b l_b\lambda\rangle\,|K\mathcal{L}kLSJ\mathcal{J}TM_T\rangle\,,
\end{aligned} \tag{3.14}$$

where the curly brackets stand for the $9-j$ and $6-j$ symbols, $\vec{\lambda}=\vec{l_a}+\vec{l_b}=\vec{\mathcal{L}}+\vec{L}$, and $\langle K\mathcal{L}kL\lambda|k_a l_a k_b l_b\lambda\rangle$ are the transformation coefficients from the centre-of-mass system to the laboratory system,

$$\langle K\mathcal{L}kL\lambda|k_a l_a k_b l_b\lambda\rangle = \frac{(4\pi)^2\delta(w)\theta(1-x^2)}{k_a k_b k K}A\ , \tag{3.15}$$

where

$$w = k^2+\alpha\beta K^2-\beta k_a^2-\alpha k_b^2\ , \tag{3.16}$$

$$x = \frac{k_a^2-k^2-\alpha^2K^2}{2\alpha Kk}\ , \tag{3.17}$$

with $\alpha = M_a/(M_a+M_b)$, $\beta = M_b/(M_a+M_b)$ and

$$\begin{aligned}
A = \sum_{mM}\begin{pmatrix} \mathcal{L} & L & \lambda \\ m & M & -\mu\end{pmatrix}\begin{pmatrix} l_a & l_b & \lambda \\ 0 & \mu & -\mu\end{pmatrix}\ , \\
\times(-1)^{-L-l_a+l_b+\mathcal{L}+m}Y_{Lm}(\delta,0)Y_{\mathcal{L}M}(\phi,0)Y_{l_a0}(0,0)Y_{l_b\mu}(\gamma,0)
\end{aligned} \tag{3.18}$$

being the parenthesis the so-called $3-j$ symbols and

$$\cos\delta = \frac{k_a^2 + k^2 - \alpha^2 K^2}{2kk_a} \ , \tag{3.19}$$

$$\cos\phi = \frac{k_a^2 + \alpha^2 K^2 - k^2}{2\alpha K k_a} \ , \tag{3.20}$$

$$\cos\gamma = \frac{\beta^2 k_a^2 + \alpha^2 k_b^2 - K^2}{2\alpha\beta k_a k_b} \ . \tag{3.21}$$

Thus, inserting the transformations (3.11) and (3.14) in Eqs. (3.5), (3.6) and (3.8), these equations can be expressed in terms of the nuclear matter G-matrix elements evaluated in the centre-of-mass frame. Let us note that in Eq. (3.6) the delta function is used to perform the K-integration, while the remaining integral over the relative momentum k sums over the intermediate plane wave states. These states must be distorted in order to make them orthogonal to the occupied bound states. We use the orthogonalization method described in Ref. [Bo92]. The empty nucleon bound states are lacking in our sum over intermediate states, but they represent a minor correction due to the much larger phase space of the continuum.

In summary, the self–energy of the hyperon in the Brueckner–Hartree–Fock approximation reads

$$\Sigma^{BHF}(k_Y k_Y' l_Y j_Y \omega) = V(k_Y k_Y' l_Y j_Y \omega) + iW(k_Y k_Y' l_Y j_Y \omega), \tag{3.22}$$

with the real part given by

$$V(k_Y k_Y' l_Y j_Y \omega) = \mathcal{V}_{1^{st}}(k_Y k_Y' l_Y j_Y) + \mathcal{V}_{2p1h}^{(1)}(k_Y k_Y' l_Y j_Y \omega) - \mathcal{V}_{2p1h}^{(2)}(k_Y k_Y' l_Y j_Y) \tag{3.23}$$

and the imaginary part by

$$W(k_Y k'_Y l_Y j_Y \omega) = \mathcal{W}^{(1)}_{2p1h}(k_Y k'_Y l_Y j_Y \omega). \tag{3.24}$$

Note that the self-energy obtained is non-local and energy-dependent.

3.1.3 Non-local single-particle hyperon-nucleus potential

The self-energy of Eq. (3.22) can be used as a single-particle potential in a Schrödinger equation in order to investigate bound and scattering states of a hyperon in a finite nucleus. The different approximations to the self-energy, i.e., whether we include the $2p1h$ contribution or not, result in different single-particle hamiltonians. The Schrödinger equation is solved by diagonalizing the corresponding single-particle hamiltonian in a complete basis within a spherical box of radius R_{box}. The radius of the box should be larger than the radius of the nucleus considered. The calculated observables are independent of the choice of R_{box}, if it is chosen to be around 20 fm or larger. This method is especially suitable for non-local potentials defined either in coordinate or in momentum space [Bo92, Hj94].

A complete and orthonormal set of regular basis functions within this box is given by

$$\Phi_{nljm}(\vec{r}) = \langle \vec{r} | k_n l j m \rangle = N_{nl}\; j_l(k_n r) \psi_{ljm}(\theta, \phi) \ , \tag{3.25}$$

where $\psi_{ljm}(\theta, \phi)$ represent the spherical harmonics including the spin degrees of freedom and $j_l(k_n r)$ denote the spherical Bessel functions for the discrete momenta k_n which fulfil the condition

$$j_l(k_n R_{box}) = 0 \ . \tag{3.26}$$

For the specific case of $l = 0$ the normalization constant is

$$N_{n0} = \frac{n\pi\sqrt{2}}{R_{box}^{3/2}} \ . \tag{3.27}$$

In this way, the basis functions defined in Eq. (3.25) are orthogonal and normalized within the box. The single-particle hamiltonian for the hyperons, consisting of the kinetic energy and the real part of the self-energy, can be evaluated in this basis and the resulting eigenvalue problem

$$\sum_{p=1}^{N_{max}} \langle k_n | \frac{\hbar^2 k_n^2}{2M_Y} \delta_{np} + V(\omega = E_\gamma) | k_p \rangle \langle k_p | \gamma \rangle = E_\gamma \langle k_n | \gamma \rangle \ , \tag{3.28}$$

restricted typically to 20 or 30 states, can easily be solved. Notice that a self-consistent process is performed for each eigenvalue, i.e., the self-energy needs to be evaluated at the energy of the resulting eigenvalue. As a first result, one obtains the negative energies for the bound states and the corresponding wave functions, which are expressed in terms of coefficients of the basis defined in Eq. (3.25). Furthermore, one also obtains discrete positive energies that correspond to scattering states with radial functions which are zero at $r = R_{box}$. Taking into account this fact it is possible to evaluate the phase shifts for those energies.

3.2 Convergence of the method

As described before, our method provides the binding energies of the different hyperon orbits in finite hypernuclei starting from a G-matrix calculated in nuclear matter in the YN centre-of-mass frame at fixed starting energy ω_{NM} and Fermi momentum k_F.

By adding the $2p1h$ correction to the first-order term one incorporates, up to second-order in the nuclear matter G-matrix, the correct energy dependence and Pauli blocking in the finite nucleus. Therefore, the complete calculation $(1^{st} + 2p1h)$ has to be viewed as a Brueckner–Hartree-Fock approach which uses an effective interaction derived microscopically with the appropriate density and energy dependence of the hypernucleus under study. This is in contrast to previous calculations [Ya85, Ya90, Ya92, Ya94], where the determination of the finite hypernucleus effective interaction from the nuclear matter G-matrix implied a sort of average over the nuclear density. In these works several local and energy independent effective YN interactions of Gaussian form (YNG) were derived by parametrizing the corresponding nuclear matter G-matrices obtained from various YN potentials. The parametrization of the G-matrix into a local effective interaction YNG to be used in finite hypernuclei calculations required the use of an appropriate value of the Fermi momentum k_F. This value was determined, for each nucleus, by averaging the corresponding nuclear density weighted by the modulus squared of the Λ single-particle wave function of the single-particle level under study. The parameters of the effective YNG interaction were adjusted to reproduce the Λ potential energy $U_\Lambda(0)$ in nuclear matter at the average value of k_F. With these parametrizations, Λ single-particle energies and excited hypernuclear levels in several Λ hypernuclei were obtained through a shell-model calculation, with the aim of learning about the bare YN interaction.

It seems therefore appropriate to explore, using our method, how much the hyperon single-particle energy depends on the starting energy and density of the nuclear matter G-matrix used in the calculation. This will allow us to assess how reliable energy independent effective interactions obtained from local density averages might be.

Let us first show, in Fig. 3.2, the binding energy $B_Y(k=0)$ of a Λ (curves on the left) or a Σ (curves on the right) in nuclear matter at $k_F = 1.36$ fm^{-1} as a function of the starting energy parameter $\omega = \omega_{NM} + \Delta = \langle B_N \rangle + B_Y(k=0) + \Delta$, where $\langle B_N \rangle = -50$ MeV is an average of the nucleon binding energy over the Fermi sea at $k_{F_N} = 1.36$ fm^{-1} and $\Delta = M_Y - M_\Lambda$. The long-dashed (full) lines are for the Nijmegen Soft Core 89 [Ma89] (Jülich B [Ho89]) interaction. An estimate of the self-consistent solution is obtained where the line $\omega = \omega_{NM} + \Delta = \langle B_N \rangle + B_Y(k=0) + \Delta$ crosses the calculated value of $B_Y(k=0)$. This is indicated by the dotted lines in the figure. In the case of the Nijmegen interaction we obtain $\omega = -74.3$ MeV ($B_\Lambda(0) = -24.3$ MeV) for the Λ and $\omega = 15.8$ MeV ($B_\Sigma(0) = -11.7$ MeV) for the Σ, whereas, in the case of the Jülich interaction, $\omega = -80.2$ MeV for the Λ ($B_\Lambda(0) = -30.2$ MeV) and $\omega = -36.0$ MeV ($B_\Sigma(0) = -63.5$ MeV) for the Σ.

Several features emerge from Fig. 3.2. First, the Σ hyperon is unrealistically overbound in nuclear matter by the Jülich interaction. It is therefore necessary to readjust the parameters of this interaction if one wants to use it in shell model calculations of Σ hypernuclei. Secondly, we observe that the energy dependence of $U_Y(k=0)$ is slightly stronger in the case of the Nijmegen interaction, especially for the Σ hyperon which is more sensitive to the ΣN - ΛN coupling because the starting energy is closer to the energies of the intermediate ΛN states (which propagate with the kinetic energy spectrum). Finally, we observe that the Λ binding energy varies at most by 10 MeV

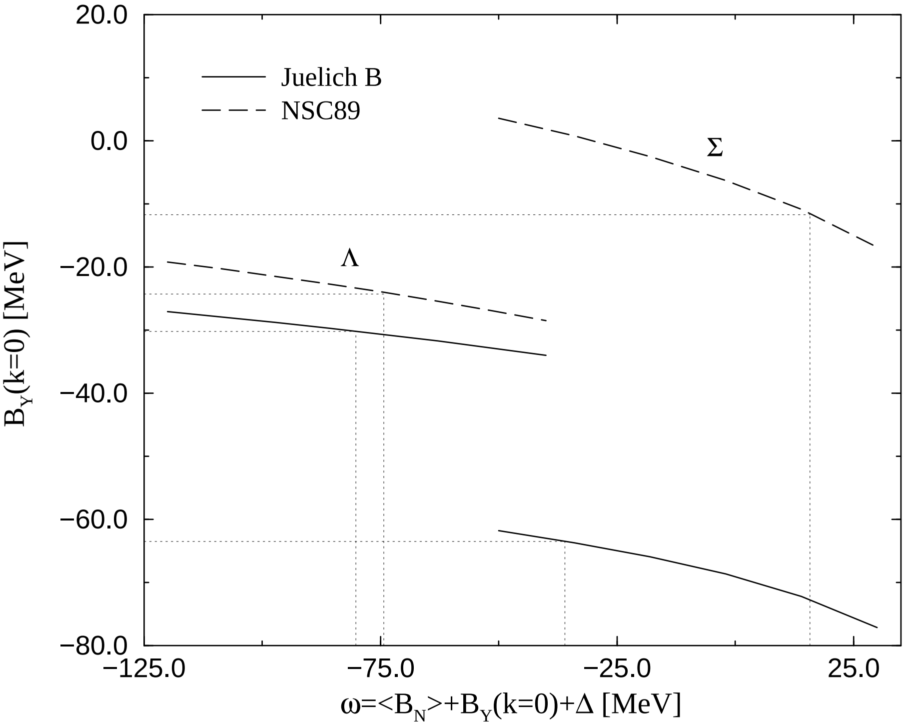

Figure 3.2: Dependence of the hyperon energy $B_Y(k=0)$ in nuclear matter on the starting energy ω. The curves on the left are for the Λ, whereas the ones on the right are for the Σ. Long-dashed (full) lines correspond to Nijmegen Soft-Core 89 (Jülich B) interaction. The dotted lines show the positions of the self-consistent solutions for $B_Y(k=0)$.

in a starting energy range of 80 MeV, while the variation of the Σ binding amounts to twice as much. As we will see below, this has consequences in the results for finite hypernuclei. We note that our results are in agreement with other nuclear matter calculations [Ya85, Ya90, Ya92, Ya94, Sc98].

In Tables 3.1 and 3.2 we show the binding energy of the Λ and Σ^0, respectively, in ${}^{17}_{Y}$O calculated for the Jülich B and NSC89 interactions. The columns denoted by 1^{st} correspond to our lowest-order calculation (see Eq. (3.5)), which uses, as effective interaction, the nuclear matter G-matrix calculated in the YN centre-of-mass frame

$k_F = 1.36$ fm^{-1}	Jülich B		NSC89	
ω (MeV)	1^{st}	$1^{st} + 2p1h$	1^{st}	$1^{st} + 2p1h$
-100	-9.25	-11.85	-3.83	-7.43
-80	-10.15	-11.83	-4.76	-7.39
-50	-11.73	-11.84	-5.59	-7.36

Table 3.1: Dependence of the Λ single-particle energy in ${}^{17}_{\Lambda}$O on the starting energy of the nuclear matter G-matrix. Our notation is $\omega = \langle B_N \rangle + B_\Lambda(k=0)$, with $\langle B_N \rangle = -50$ MeV. Units are given in MeV.

$k_F = 1.36$ fm^{-1}	Jülich B		NSC89	
ω (MeV)	1^{st}	$1^{st} + 2p1h$	1^{st}	$1^{st} + 2p1h$
0	-36.70	-50.70	-0.16	-22.79
20	-40.38	-50.94	-2.01	-23.35
50	-51.34	-50.38	-10.65	-24.62

Table 3.2: Dependence of the Σ^0 single-particle energy in ${}^{17}_{\Sigma^0}$O on the starting energy of the nuclear matter G-matrix. Our notation is $\omega = \langle B_N \rangle + B_\Sigma(k=0) + \Delta$, with $\langle B_N \rangle = -50$ MeV and $\Delta = M_\Sigma - M_\Lambda$. Units are given in MeV.

at fixed Fermi momentum of $k_F = 1.36$ fm^{-1} and at several values of the starting energy (shown in the first column), $\omega = \omega_{NM} + \Delta = \langle B_N \rangle + B_Y(k=0) + \Delta$. Columns labelled $(1^{st} + 2p1h)$ include the $2p1h$ corrections (see Eqs. (3.7) and (3.8)) to bring the nuclear matter G-matrix to the finite nucleus one, with the proper energy and density dependence. We see that the lowest order results depend quite strongly on the starting energy used, especially in the case of the Σ hyperon. However, it is worth noticing how, no matter what starting energy is used in solving the nuclear matter G-matrix, the corrected calculation $(1^{st} + 2p1h)$ ends up giving practically the same result for the hyperon binding energy. Particularly stable are the results for the Λ hyperon. This weaker energy dependence is due to the fact that the energies involved in the calculation lie further away from the threshold of intermediate YN states and

$\omega = -50$ MeV	Jülich B		NSC89	
k_F (fm^{-1})	1^{st}	$1^{st} + 2p1h$	1^{st}	$1^{st} + 2p1h$
1.00	−13.71	−11.74	−9.33	−7.30
1.25	−12.56	−11.83	−7.66	−7.34
1.36	−11.73	−11.84	−5.59	−7.36

Table 3.3: Dependence of the Λ single-particle energy in ${}^{17}_{\Lambda}$O on the Fermi momentum of the nuclear matter G-matrix. Our notation is $\omega = \langle B_N \rangle + B_\Lambda(k=0)$, with $\langle B_N \rangle = -50$ MeV. Units are given in MeV.

$\omega = 0$ MeV	Jülich B		NSC89	
k_F (fm^{-1})	1^{st}	$1^{st} + 2p1h$	1^{st}	$1^{st} + 2p1h$
1.00	−43.94	−51.74	−2.64	−25.03
1.25	−39.41	−51.16	−0.82	−23.37
1.36	−36.70	−50.70	−0.16	−22.79

Table 3.4: Dependence of the Σ^0 single-particle energy in ${}^{17}_{\Sigma^0}$O on the Fermi momentum of the nuclear matter G-matrix. Our notation is $\omega = \langle B_N \rangle + B_\Sigma(k=0) + \Delta$, with $\langle B_N \rangle = -50$ MeV and $\Delta = M_\Sigma - M_\Lambda$. Units are given in MeV.

therefore the strong ΛN-ΣN coupling is less pronounced.

In Tables 3.3 and 3.4 we show the binding energy of the Λ and Σ^0, respectively, again in ${}^{17}_{Y}$O using nuclear matter G-matrices calculated at several values of the Fermi momentum and a fixed value of the starting energy ($\omega = -50$ MeV for the Λ and $\omega = 0$ for the Σ). The lowest-order calculation for the hyperon-single particle energy depends quite strongly on the value of k_F. The results of Tables 3.3 and 3.4 should not be interpreted as showing a dependence of the hyperon binding energy on the nuclear density. The single-nucleon states are the same in all the calculations and correspond to the harmonic oscillator wave functions appropriate for ^{16}O. The Fermi momentum shown in the first column refers to the value used in the solution of the nuclear matter G-matrix. The first-order result just shows the decrease of attraction as

k_F increases due to the increasing number of Pauli blocked intermediate states in the Bethe-Goldstone equation. However, one finds again that, when the $2p1h$ correction is included to incorporate the proper intermediate propagator of the finite nucleus, the results nicely converge to practically the same value, no matter what was the density used in the solution of the nuclear matter G-matrix.

For completeness, we have also examined the dependence of the Λ single-particle energies in finite nuclei on the choice (standard or continuous) adopted for solving the nuclear matter G-matrix. In order to illustrate this analysis, we show in Table 3.5 the results for two nuclei, ${}^{5}_{\Lambda}$He and ${}^{17}_{\Lambda}$O, calculated with the NSC97f baryon-baryon interaction. As can be seen from the table, the first-order depends quite strongly on the prescription chosen to solve the nuclear matter G-matrix. Nevertheless, also in this case, for both nuclei, the inclusion of the $2p1h$ correction brings both calculations, the one performed with the standard prescription and the one with the continuous option, to a similar final result. It is interesting to observe that the first-order, when using the continuous choice, is closer to the final result including the $2p1h$ correction than when using the discontinuous prescription. This indicates that the symmetrical treatment of the single-particle spectrum for particles ($k > k_F$) and holes ($k < k_F$) in the continuous prescription gives rise to an intermediate nuclear matter propagator more similar to the one in the finite nucleus.

All these results are interesting in the sense that they confirm that the finite nucleus G_{FN}-matrix is already well approximated by the second-order term in the expansion in terms of the nuclear matter G-matrix. The inclusion of the $2p1h$ correction, whose size depends on the starting energy, the Fermi momentum or the choice adopted in the solution of the nuclear matter G-matrix, already leads to practically the same value for

Nuclei	Orbit	Standard Choice		Continuous Choice		Exp.
		1^{st}	$1^{st} + 2p1h$	1^{st}	$1^{st} + 2p1h$	
${}^{5}_{\Lambda}$He	$1s_{1/2}$	-1.98	-3.59	-3.60	-3.96	(${}^{5}_{\Lambda}$He) -3.12
${}^{17}_{\Lambda}$O	$1s_{1/2}$	-11.17	-14.02	-15.69	-16.03	(${}^{16}_{\Lambda}$O) -12.5

Table 3.5: Dependence of the Λ single-particle energy in finite nuclei on the choice adopted for solving the nuclear matter G-matrix. The results have been derived from the NSC97f baryon-baryon interaction.

the hyperon single-particle energy. Higher order terms could only help in bringing the results closer than what they already are. Moreover, our results also show that in some cases this correction is quite appreciable, not only for the Σ^0 binding energies shown in Tables 3.2 and 3.4, but also for the Λ energies in the case of the Nijmegen interactions. Therefore, if the effective interaction is taken directly as the nuclear matter G-matrix at an averaged density [Ya85, Ya90, Ya92, Ya94] it may not lead to the proper effective interaction in the finite nucleus one is studying.

We note that the Λ single-particle energy obtained in the case of the NSC89 interaction is in excellent agreement with that obtained by Halderson (see column 3 in Fig. 7 of Ref. [Ha93]), where the G-matrix was calculated directly in the finite nucleus for various Nijmegen interactions. Hence, our method can also be viewed as an alternative and cheaper way of building up a finite nucleus effective interaction. It was also shown by Halderson that the Pauli corrections were very large for the NSC89 potential. This again supports our belief that finite nucleus calculations based on nuclear matter G-matrices at an average density will carry uncertainties tied to the chosen value of the Fermi momentum.

3.3 Finite nuclei results

Once the method has been well established and tested for the specific cases of $^{17}_{\Lambda}$O and $^{17}_{\Sigma^0}$O, it is the right moment to study the systematics of the Λ binding energies through the periodic table. We will present results for calculations performed with the Jülich B, NSC89, NSC97a and NSC97f interactions. Results for interactions NSC97b, NSC97c, NSC97d and NSC97e are not presented because their differences with respect to the results of NSC97a and NSC97f are smaller than 10%. So we will consider these two last interactions as representative of the Nijmegen Soft Core 97 models. In the studies of single-particle states below, we will refrain from studying the Σ single-particle ones, since the results presented in Tables 3.2 and 3.4 for $^{17}_{\Sigma^0}$O show binding energies which are even more attractive than the binding energy of this hyperon in nuclear matter.

3.3.1 Λ single-particle states

The values of the Λ single-particle binding energies obtained in what has been called 1^{st} and $1^{st} + 2p1h$ approximations are reported in Tables 3.6 and 3.7 together with the available experimental data. These binding energies have been calculated using the Jülich B, NSC89, NSC97a and NSC97f interaction models, employing the standard prescription in the calculation of the nuclear matter G-matrix, a Fermi momentum of $k_F = 1.36$ fm^{-1} and a starting energy of $\omega = -80$ MeV.

For convenience in the technicalities of the algorithm we have always considered hypernuclei with a number of nucleons closing a subshell plus a Λ. Unfortunately, experimental data for those nuclei do not always exist and, as indicated in Tables 3.6 and 3.7, we have taken the closest representative nucleus for which the experimental

Nuclei	Orbit	Jülich B		NSC89		Exp.
		1^{st}	$1^{st}+2p1h$	1^{st}	$1^{st}+2p1h$	
$^{5}_{\Lambda}$He						($^{5}_{\Lambda}$He)
	$1s_{1/2}$	-1.43	-2.28	-0.04	-0.58	-3.12
$^{13}_{\Lambda}$C						($^{13}_{\Lambda}$C)
	$1s_{1/2}$	-7.93	-9.48	-3.42	-5.69	-11.69
$^{17}_{\Lambda}$O						($^{16}_{\Lambda}$O)
	$1s_{1/2}$	-10.15	-11.83	-4.76	-7.39	-12.5
	$1p_{3/2}$		-0.87			-2.5 ($1p$)
	$1p_{1/2}$	-0.08	-1.06			
$^{41}_{\Lambda}$Ca						($^{40}_{\Lambda}$Ca)
	$1s_{1/2}$	-16.85	-19.60	-10.24	-15.04	$-20.$
	$1p_{3/2}$	-6.70	-9.64	-3.07	-6.92	$-12.$ ($1p$)
	$1p_{1/2}$	-6.92	-9.92	-2.33	-6.29	
$^{91}_{\Lambda}$Zr						($^{89}_{\Lambda}$Zr)
	$1s_{1/2}$	-22.24	-25.80	-16.35	-22.77	$-23.$
	$1p_{3/2}$	-14.74	-18.19	-10.13	-17.08	$-16.$ ($1p$)
	$1p_{1/2}$	-14.86	-18.30	-9.73	-16.68	
$^{209}_{\Lambda}$Pb						($^{208}_{\Lambda}$Pb)
	$1s_{1/2}$	-26.28	-31.36	-23.58	-29.52	$-27.$
	$1p_{3/2}$	-21.22	-27.13	-21.42	-26.01	$-22.$ ($1p$)
	$1p_{1/2}$	-21.30	-27.18	-21.18	-25.72	

Table 3.6: Λ binding energies (in MeV) in the $1s_{1/2}$, $1p_{3/2}$ and $1p_{1/2}$ single-particle orbits for different nuclei. The available experimental data, indicating the hypernucleus for which they have been measured, are taken from the compilation of [Ba90] supplemented by new measures reported in [Pi91] and [Ha96]. The results have been derived from the Jülich B and the Nijmegen Soft-Core 89 (NSC89) hyperon-nucleon interaction.

information is available. Nevertheless, the differences between the calculated and the experimental values should not be associated to this fact but to the approximations used in the calculation or to the potential itself.

For the density and starting energy ($k_F = 1.36$ fm^{-1}, $\omega = -80$ MeV) used to

Nuclei	Orbit	NSC97a		NSC97f		Exp.
		1^{st}	$1^{st} + 2p1h$	1^{st}	$1^{st} + 2p1h$	
${}^{5}_{\Lambda}$He						(${}^{5}_{\Lambda}$He)
	$1s_{1/2}$	-1.91	-3.16	-1.98	-3.59	-3.12
${}^{13}_{\Lambda}$C						(${}^{13}_{\Lambda}$C)
	$1s_{1/2}$	-9.54	-11.46	-8.77	-11.37	-11.69
	$1p_{3/2}$		-0.24		-0.01	-0.7 ($1p$)
	$1p_{1/2}$		-0.12			
${}^{17}_{\Lambda}$O						(${}^{16}_{\Lambda}$O)
	$1s_{1/2}$	-12.40	-14.31	-11.17	-14.02	-12.5
	$1p_{3/2}$	-1.26	-2.57	-0.56	-2.17	-2.5 ($1p$)
	$1p_{1/2}$	-0.81	-2.16		-1.41	
${}^{41}_{\Lambda}$Ca						(${}^{40}_{\Lambda}$Ca)
	$1s_{1/2}$	-20.86	-23.09	-18.19	-21.96	$-20.$
	$1p_{3/2}$	-10.44	-12.37	-8.37	-11.09	$-12.$ ($1p$)
	$1p_{1/2}$	-10.03	-12.10	-7.50	-10.45	
${}^{91}_{\Lambda}$Zr						(${}^{89}_{\Lambda}$Zr)
	$1s_{1/2}$	-28.51	-31.38	-25.08	-29.56	$-23.$
	$1p_{3/2}$	-20.56	-23.92	-17.41	-22.25	$-16.$ ($1p$)
	$1p_{1/2}$	-20.47	-23.82	-17.03	-21.88	
${}^{209}_{\Lambda}$Pb						(${}^{208}_{\Lambda}$Pb)
	$1s_{1/2}$	-39.60	-38.85	-34.52	-39.30	$-27.$
	$1p_{3/2}$	-36.34	-33.49	-32.59	-31.03	$-22.$ ($1p$)
	$1p_{1/2}$	-36.22	-33.38	-32.33	-30.72	

Table 3.7: As in Table 3.6, but for NSC97a and NSC97f interactions.

calculate the Λ-nucleon G-matrix in nuclear matter, which has been used as effective interaction in our finite nucleus calculation, it turns out that the $2p1h$ correction is almost always attractive (it is only repulsive in the case of ${}^{209}_{\Lambda}$Pb for NSC97a (s- and p-waves) and NSC97f (p-waves)). This attraction can be understood from the following argument: The total $2p1h$ contribution is given by $\mathcal{V}^{(1)}_{2p1h}$, see Eq. (3.7), minus the nuclear matter correction term $\mathcal{V}^{(2)}_{2p1h}$ of Eq. (3.8). Thus, Eq. (3.7) introduces the finite

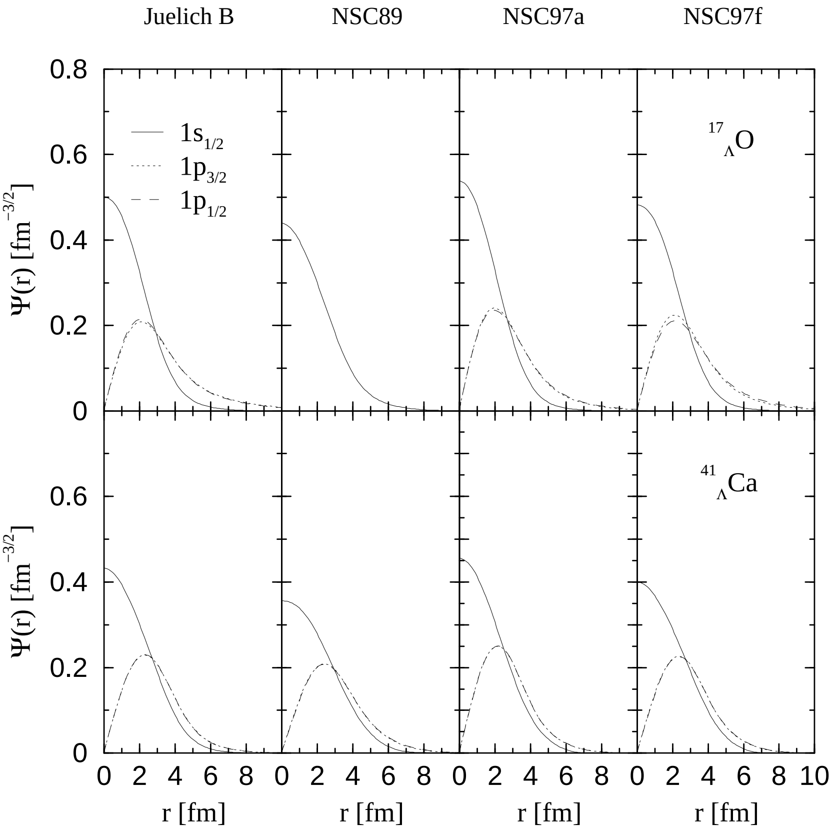

Figure 3.3: Wave function of the $1s_{1/2}, 1p_{3/2}$ and $1p_{1/2}$ states of a Λ hyperon in ${}^{17}_{\Lambda}$O (upper panels) and ${}^{41}_{\Lambda}$Ca (lower panels) for four different interactions: Jülich B, NSC89, NSC97a and NSC97f.

nucleus Pauli operator which is less restrictive than the nuclear matter Pauli operator. Therefore, by allowing for a larger phase space in the sum over the intermediate states, the finite nucleus second-order contribution is more attractive than the corresponding nuclear matter result, producing an overall attractive second-order correction.

In agreement with the experimental information, the difference between the $p_{3/2}$ and $p_{1/2}$ Λ single-particle binding energies is very small. Note that in the case of the Jülich B interaction the $p_{1/2}$ energy is lower than the $p_{3/2}$. This is a characteristic of the Jülich interaction which yields too much attraction in the ${}^3S_1$ partial wave, as

Nuclei	Jülich B	NSC89	NSC97a	NSC97f
${}^{5}_{\Lambda}$He	3.08	4.83	2.79	2.70
${}^{13}_{\Lambda}$C	2.43	2.79	2.34	2.40
${}^{17}_{\Lambda}$O	2.47	2.80	2.39	2.47
${}^{41}_{\Lambda}$Ca	2.71	2.99	2.66	2.83
${}^{91}_{\Lambda}$Zr	3.11	3.31	3.01	3.20
${}^{209}_{\Lambda}$Pb	3.49	3.96	3.65	3.96

Table 3.8: Root-mean-square radius (r.m.s.) of the $1s_{1/2}$ Λ-orbit in different nuclei. Units are given in fm.

noted already in [Ya92, Ya94] where the 0^+ and 1^+ states of ${}^{4}_{\Lambda}$He were calculated and shown to appear in reverse order with respect to the experimental values.

The calculated Λ single-particle energies for ${}^{209}_{\Lambda}$Pb appear clearly overbound with respect to the experimental data, especially for the case of NSC97a-f models. This is due first to the fact that the distortion of the plane wave associated with the nucleon in the intermediate state of the $2p1h$ diagram of Fig. 3.1c, necessary to ensure its orthogonalization to the nucleon hole states, has been considered only approximately. The orthogonalization procedure is described in Ref. [Bo92] and has been optimized for the case of ${}^{17}_{\Lambda}$O. Actually, this feature is already sizable for ${}^{91}_{\Lambda}$Zr and in the case of ${}^{209}_{\Lambda}$Pb leads to the unrealistic result of a Λ that is more bound than in nuclear matter. In addition, for the case of the NSC97a and NSC97f models this large overbinding of the Λ in heavy nuclei is in fact not surprising if we recall (see previous chapter) that the value of the Λ binding energy in nuclear matter obtained with these potentials is already very large (~ -40 MeV).

For completeness we show in Fig. 3.3 the wave function of the $1s_{1/2}, 1p_{3/2}$ and $1p_{1/2}$ states of a Λ in ${}^{17}_{\Lambda}$O (upper panels) and ${}^{41}_{\Lambda}$Ca (lower panels) for the four interactions

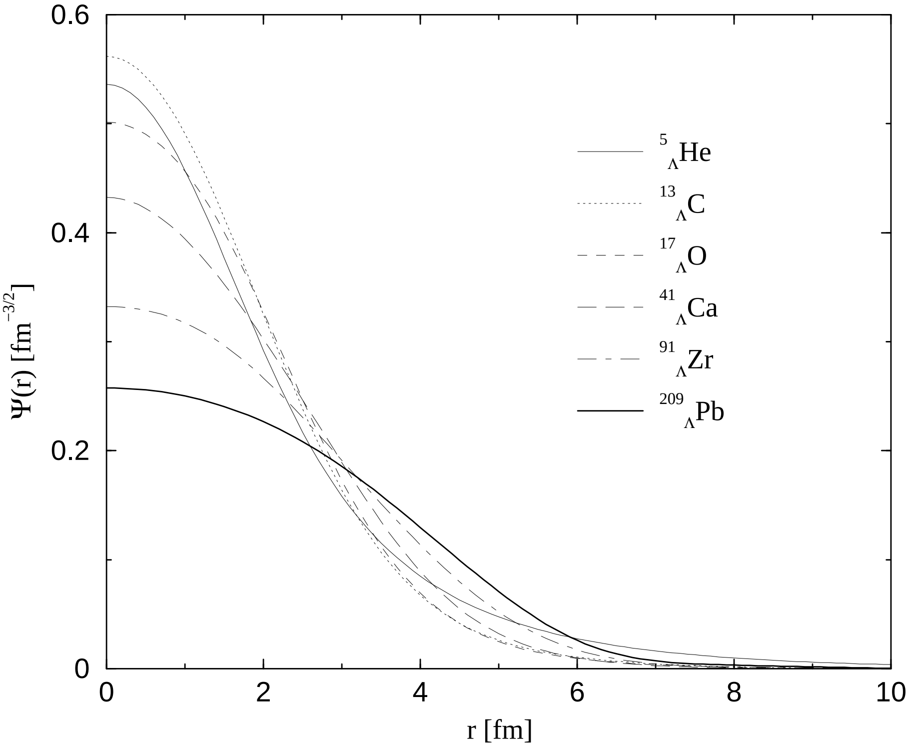

Figure 3.4: Wave function of the $1s_{1/2}$ state of a Λ hyperon in different nuclei from $^{5}_{\Lambda}$He to $^{209}_{\Lambda}$Pb determined from the Jülich B interaction.

considered: Jülich B, NSC89, NSC97a and NSC97f. We have explicitly excluded the $1p_{3/2}$ and $1p_{1/2}$ states in the case of oxygen for the NSC89 interaction because it gives no binding for these states. As can be seen from Tables 3.6 and 3.7, the NSC89 interaction predicts the smallest binding energies, which results in a larger radius for the bound Λ states and therefore in more extended wave functions. In a similar way, the NSC97a model predicts the largest binding energies, which therefore results in more localized wave functions. These features can be seen in Fig. 3.3 and in Table 3.8, where we show the root-mean-square radius (r.m.s.) of the $1s_{1/2}$ Λ-orbit for the different nuclei and the four interactions considered.

Finally, in Fig. 3.4 we show the $1s_{1/2}$ Λ-wave function in different nuclei obtained with the Jülich B interaction. As we move from light to heavy nuclei the probability of finding the Λ at $r = 0$ decreases and the wave function becomes more and more extended due to the larger extension of the nuclear density over which the Λ particle wants to be distributed. Only the lightest hypernucleus, ${}^{5}_{\Lambda}$He, falls out of this pattern due to the fact that the corresponding binding energy is also pretty small, resulting in a very extended wave function.

3.3.2 Local parametrization of the hyperon self-energy

In this section we want to explore if our Λ single-particle energies, obtained from a self-energy which is non-local both in k- and r-space, can be reproduced by local potentials.

Hjorth-Jensen *et al.* [Hj96] have shown that one can generate a local representation of the self–energy by performing an appropriate average of the non-local self–energy $\hat{\Sigma}_\alpha(r,r')$, where α indicates the quantum numbers of the single-particle state, over the coordinate r',

$$\hat{\Sigma}^{loc}_\alpha(r) = \frac{\displaystyle\int dr' r'^2 \hat{\Sigma}_\alpha(r,r')\Psi(r')_\alpha}{\Psi(r)_\alpha} , \tag{3.29}$$

where

$$\hat{\Sigma}_\alpha(r,r') = \frac{2}{\pi}\int k^2 dk \int k'^2 dk' j_l(k'r')\Sigma_\alpha(k,k')j_l(kr) . \tag{3.30}$$

is the Fourier-Bessel transform of the non-local self-energy from momentum space to r-space and $\Psi(r)_\alpha$ is the radial wave function of the α-state. This procedure ensures that the local potential $\hat{\Sigma}^{loc}_\alpha(r)$, when inserted into the Schrödinger equation, will give rise to the same bound state $\Psi(r)_\alpha$.

This local representation might, in first approximation, be characterized by the shape of a Woods-Saxon potential,

$$V_{WS}(r) = \frac{V_0}{1+\exp\left[(r-R)/a\right]} \ , \tag{3.31}$$

with a given diffusivity a and depth V_0, independent of the mass number, and a radius $R = r_0(A)A^{1/3}$ determined by requiring the Woods-Saxon potential to reproduce the same eigenvalue as the microscopic non-local energy-dependent self-energy. A reasonable value for the depth V_0 is the Λ binding energy in nuclear matter, which is taken to be -30.2 MeV, and for the diffusivity one may take $a = 0.6$ fm. The resulting values of R, when we apply this procedure to the deepest s state of ${}^{13}_{\Lambda}$C, ${}^{17}_{\Lambda}$O and ${}^{41}_{\Lambda}$Ca are 2.25 fm, 2.53 fm and 3.82 fm respectively. Fitting these three values with a functional form similar to the one used by Millener *et al.* in [Mi88] for the analysis of the experimental data, one obtains

$$r_0(A) = 1.229 - 1.390A^{-2/3} \ . \tag{3.32}$$

As an example we show in Fig. 3.5 the local single-particle potential for a Λ in the $1s_{1/2}$ state in ${}^{17}_{\Lambda}$O obtained from the localization of the self-energy, calculated with the Jülich B interaction, according to Eq. (3.29) and a Woods-Saxon parametrization (with $V_0 = -30.2$ MeV, $a = 0.6$ fm, $R = 2.53$ fm), which reproduces the binding energy of the Λ. Let us note that in the following we will employ only the Jülich B interaction to illustrate the discussions. Similar results to the ones we will show have been obtained for the other interactions, although they have not been included in order to make the discussions more transparent.

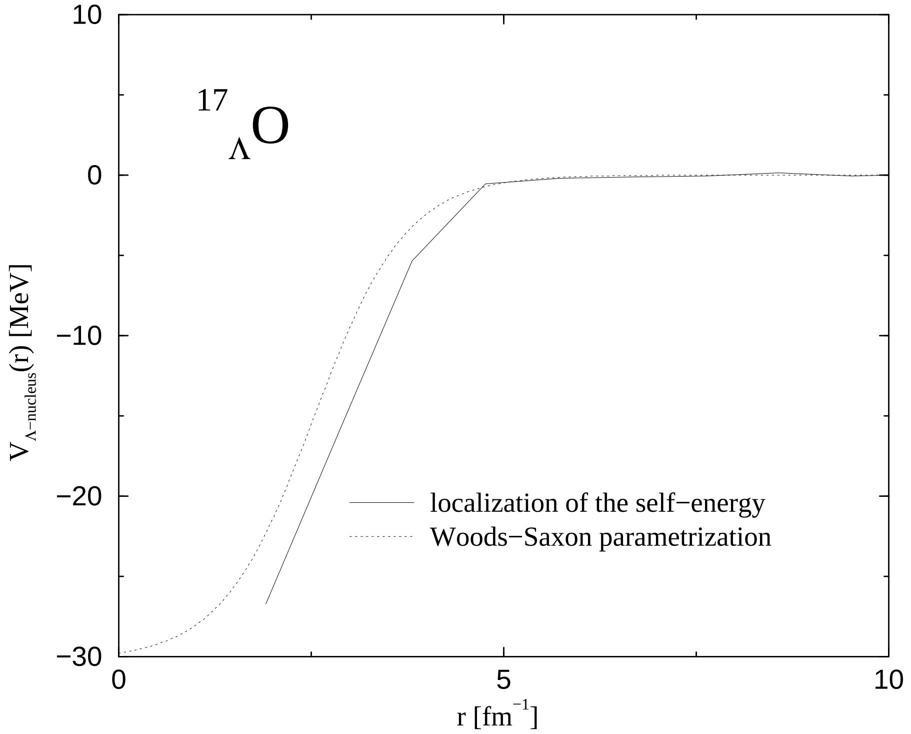

Figure 3.5: Local single-particle potentials for a Λ in the $1s_{1/2}$ state in ${}^{17}_{\Lambda}$O employing the Jülich B interaction. The solid line represents the result obtained from Eq. (3.29), while the dotted line is the result obtained from a Woods-Saxon parametrization with $V_0 = -30.2$ MeV, $a = 0.6$ fm, $R = 2.53$ fm.

In order to visualize the quality of these fits, we show in Fig. 3.6 the binding energies for the s- and p-waves of ${}^{12}_{\Lambda}$C, ${}^{17}_{\Lambda}$O, ${}^{41}_{\Lambda}$Ca and ${}^{91}_{\Lambda}$Zr calculated with our non-local self–energies (triangles) using the Jülich B interaction together with the values obtained with a Woods-Saxon potential with the parameters just defined above (solid lines). As the spin-orbit splitting is so small we have reported the average value of the $p_{3/2}$ and $p_{1/2}$ energies obtained from the non-local self–energies and have not considered any spin-orbit term in the adjusted Woods-Saxon potential. The results of ${}^{209}_{\Lambda}$Pb have not been included in the plot because, as mentioned before, the s-wave binding energy was larger than the binding energy in nuclear matter which we have taken as the

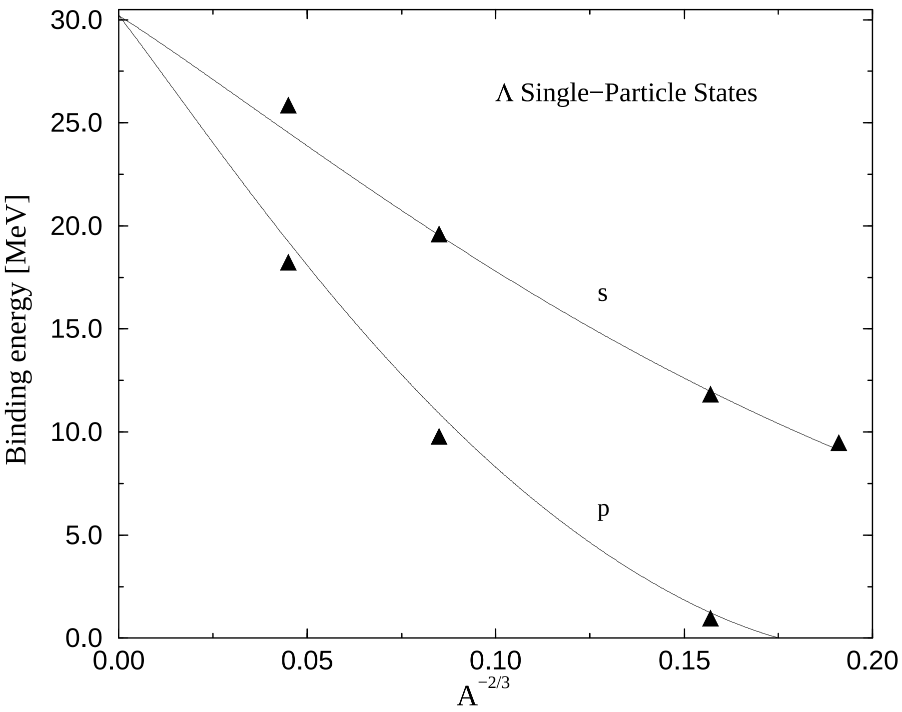

Figure 3.6: Calculated Λ binding energies in $1s$ and $1p$ single-particle orbits for different nuclei employing the Jülich B interaction. The solid lines correspond to the solutions obtained for a Woods-Saxon potential which fits the experimental s-wave results and whose parameters are $V_0 = -30.2$ MeV, $a = 0.6$ fm and $R = r_0(A)A^{1/3}$ with $r_0(A)$ given in Eq. (3.32). Triangles show the results obtained from our non-local self-energy.

depth of the Woods-Saxon potential. The s and p binding energies obtained from the non-local self-energy are well reproduced by the Woods-Saxon shape and, as expected, both partial waves extrapolate to the binding energy for nuclear matter because in this system the single-particle wave functions become plane waves.

Of course the binding energies are not enough to characterize the single-particle states since potentials giving rise to the same binding energies can generate substantial differences in the corresponding wave functions. Therefore, in order to analyze the microscopically calculated self–energy we should also study the single-particle wave

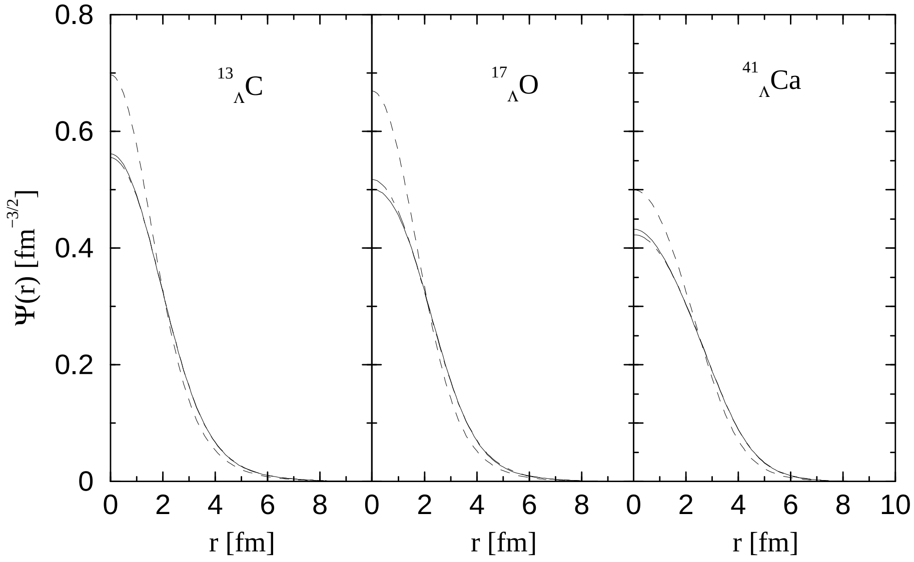

Figure 3.7: The wave function in r-space for the $1s_{1/2}$ Λ in $^{13}_{\Lambda}$C, $^{17}_{\Lambda}$O and $^{41}_{\Lambda}$Ca obtained from the Λ self-energy (solid lines) is compared with the one obtained using a Woods-Saxon potential of fixed (A-independent) depth (dashed lines) or with both radius and depth adjusted (dot-dashed lines) to maximize the overlap with the wave function provided by the self-energy (solid lines). Parameters of the Woods-Saxon potential are given in the text. The Jülich B interaction has been employed in all the calculations.

functions. To be specific we will consider in particular the $1s_{1/2}$ state of a Λ in three representative hypernuclei such as $^{13}_{\Lambda}$C, $^{17}_{\Lambda}$O and $^{41}_{\Lambda}$Ca.

To have a measure of the quality of the wave functions generated by the Woods-Saxon potential, we calculate their overlap with the wave functions obtained by solving the Schrödinger equation using the self–energy. The overlaps for $^{13}_{\Lambda}$C, $^{17}_{\Lambda}$O and $^{41}_{\Lambda}$Ca are 0.9917, 0.9869 and 0.9924 respectively, which are not close enough to 1 to guarantee the equality of the wave functions. This is visualized in Fig. 3.7, where the wave function for the s-wave in these nuclei obtained with the Woods-Saxon potential (dashed lines) is compared with the one obtained directly from the non-local self–energy (solid lines).

In order to maximize the overlap with the eigenfunction provided by the self-energy, we will also allow the depth V_0 to vary. The values of V_0 by applying this procedure to the s-wave of the three nuclei considered above are respectively -23.11, -23.56 and -27.84 MeV whereas the values of the radius R are 2.92, 3.32 and 4.39 fm. With these values of V_0 and R the overlaps are 0.9999 for the three nuclei considered. The eigenfunctions obtained by this procedure for these nuclei are also drawn in Fig. 3.7 (dot-dashed lines) and show a large overlap with the self–energy eigenfunction (solid lines).

In conclusion, the single-particle energies of closed-shell nuclei with one Λ are well reproduced by using both the microscopic self–energy or the simpler parametrization of Woods-Saxon type in the Schrödinger equation. Nevertheless, the wave functions provided by the microscopic self–energy differ from the ones originated by a Woods-Saxon potential with a fixed depth and diffusivity and a A-dependent radius. It is important to note that the mean square radius of the self–energy eigenfunction is larger than that from the corresponding Woods-Saxon wave function. This can have important consequences in the study of the mesonic decay of these Λ hypernuclei. Indeed, it has been observed that the mesonic decay rates of light hypernuclei, such as ${}^4_\Lambda$H, ${}^4_\Lambda$He and ${}^5_\Lambda$He, could be better reproduced if the Λ wave function was pushed out to the surface by the effect of a repulsive hyperon-nucleus potential at short distances. This would favour the mesonic decay of these hypernuclei because the Λ would be exploring smaller nuclear density regions and the Pauli blocking effects, which prevent the mesonic decay from occurring, would be less pronounced. The mesonic decay rates of light hypernuclei have been calculated using repulsive Λ-nucleus potentials at short distances that have been obtained either phenomenologically [Ku95], from a quark based bare YN interaction [St93] or from a microscopic YNG effective interaction folded with an extremely compact ^{4}He density [Mo91]. At present, no calculation exists that combines the use of an YN effective interaction with an appropriate density treatment of the host nucleus. Our method provides such ingredients and has been shown to produce Λ wave functions that are pushed out to the surface. This is a consequence of the non-localities of the self–energy and is not necessarily related to a repulsive character of the Λ-nucleus potential at short distances. The implications of our results on the mesonic decay of Λ hypernuclei are out of the scope of this thesis, but they will be explored in the future.

Chapter 4

Neutron Star Matter

> "I have crossed many mountains and many rivers, and trodden many plains, even into the far countries of Rhûn and Harad where the stars are strange"
> *J.R.R. Tolkien*, **The Lord of the Rings**, Part One: The Fellowship of the Ring.

In this chapter we apply the formalism described in the previous chapters to study β-stable neutron star matter including hyperonic degrees of freedom and the structure of neutron stars. The chapter is organized in the following way: a historical overview on neutron stars, first theoretical calculations and first observations are given in section 4.1. Section 4.2 is devoted to showing the basic properties and the structure of neutron stars. Chemical equilibrium conditions in neutron star matter are discussed in section

4.3. The Equation of State of β-stable neutron star matter is constructed in section 4.4 following the many-body scheme described in Chapters 1 and 2. Finally, in section 4.5 the results for the EoS and composition of β-stable neutron star matter are presented, and their implications on the structure of neutron stars are discussed in section 4.6

4.1 Historical overview

The possible existence of neutron stars was proposed by Baade and Zwicky [Ba34] in 1934 only two years after the discovery of the neutron by Chadwick. They pointed out that a massive object consisting mainly of neutrons at very high density, would be much more gravitationally bound than ordinary stars. Baade and Zwicky also made the suggestion that such object could be formed in supernova explosions. In 1939 Oppenheimer and Volkoff [Op39], and Tolman [To39] did the first theoretical calculation of the equilibrium conditions for neutron star properties assuming an ideal gas of free neutrons at high density.

The idea that neutron cores in massive normal stars might be a source of stellar energy focused the work on neutron stars at that time. However, when the details of thermonuclear fusion became understood this motivation faded. As a consequence, neutron stars were gradually being ignored by the astronomical community for the next 30 years. A reason often given for the neglect of the neutron star idea is that because of their small area, their residual thermal radiation would be too faint to be observed at astronomical distances with optical telescopes in comparison with ordinary stars. Nevertheless, the situation changed in 1967 when the first radio pulsar was discovered by Bell and Hewish [He68]. They identified a 81.5 MHz source with a pulsating period of

1.377 s. The identification of pulsars with neutron stars was not immediately obvious to most astrophysicists. The first argument that the observed pulsars were in fact rotating neutron stars with strong surface magnetic fields of the order 10^{12} Gauss was put forward by Gold [Go68]. He pointed out that such objects could explain many of the observed features of pulsars, such as the remarkable stability of the pulse period. Gold predicted a small increase in the period as rotational energy is lost due to radiation. Shortly after, this was confirmed when a slowdown of the Crab pulsar was discovered. Because of this success and the failure of other models, pulsars are generally believed to be highly magnetized rotating neutron stars.

Since 1968, there has been much theoretical work on properties of neutron stars. This was further stimulated by the discovery of pulsating, compact X-ray sources ("X-ray pulsars") by the UHURU satellite in 1971. These sources are believed to come from a neutron star in a close binary system which is accreting gas from its normal companion star.

The evidence for the formation of neutron stars in supernova explosions was provided by the simultaneous discoveries of the Crab and Vela pulsars in the late fall of 1968, both of which are situated in supernova remnants (the Crab nebula is in fact the remnant of the supernova explosion observed by Chinese astronomers in 1054 A.D.)

The best determined neutron star masses are found in binary pulsars and all lie in the range $(1.35\pm0.04)M_\odot$ [Th99] except for the nonrelativistic pulsar PSR J1012+5307 of mass $M = (2.1 \pm 0.8)M_\odot$ [Pa99b]. Several X-ray binary masses have been measured of which the heaviest are Vela X-1 with $M = (1.9 \pm 0.2)M_\odot$ [Ba99b] and Cygnus X-2 with $M = (1.78\pm0.2)M_\odot$ [Or99]. The recent discovery of high-frequency brightness oscillations in low-mass X-ray binaries provides a promising new method for determining

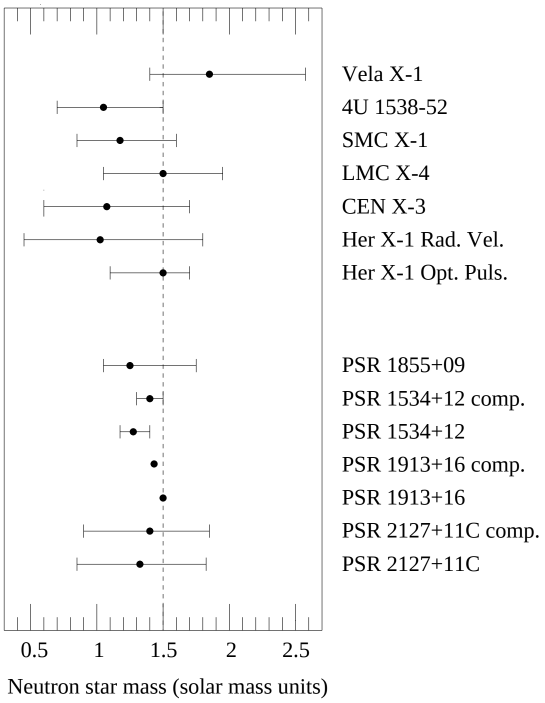

Figure 4.1: Observational determinations of neutron star masses. The first seven masses are derived from observation of X-ray binary systems and the others are derived from observation of radio pulsars and their companions. The results are from Kerkwijk *et al.* [Ke95].

masses and radii of neutron stars, see Ref. [Mi98]. The kilohertz quasi-periodic oscillations (QPO) occur in pairs and are most likely the orbital frequencies of accreting matter in Keplerian orbits around neutron stars of mass M and their beat frequencies with the neutron star spin. According to Zhang *et al.* [Zh98] and Kaaret *et al.* [Ka97] the accretion can for a few QPO's be tracked to its innermost stable orbit. For slowly rotating stars the resulting mass is $M \simeq 2.2 M_{\odot}(\mathrm{kHz}/\nu_{QPO})$. For example, the maximum frequency of 1060 Hz upper QPO observed in 4U 1820-30 gives $M \simeq 2.25 M_{\odot}$ after correcting for the neutron star rotation frequency. If the maximum QPO frequencies of 4U 1608-52 ($\nu_{QPO} = 1125$ Hz) and 4U 1636-536 ($\nu_{QPO} = 1228$ Hz) also correspond to innermost stable orbits the corresponding masses are $2.1 M_{\odot}$ and $1.9 M_{\odot}$.

These observations define a range of variation for the mass between $M \sim 1.35 M_\odot$ and $M \sim 2.2 M_\odot$, which severely restricts the EoS for dense matter. In Fig. 4.1 we show some of the observational determinations of neutron star masses. The results have been taken from Kerkwijk *et al.* [Ke95].

The discoveries made in the past few decades will continue, as enormous earth-based and satellite experiments are running at present and more will be launched. Probably the future will be full of great surprises and discoveries in this field.

4.2 Basic properties and structure of neutron stars

A neutron star is the remnant of an ordinary star with a mass greater than $\sim 5 M_\odot$, where $M_\odot \sim 2 \times 10^{33}$ g is the solar mass, after it has undergone a supernova explosion. A supernova explosion will occur when the star has exhausted its possibilities for energy production by nuclear fusion. The pressure gradient provided by radiation will then not be sufficient to balance the gravitational attraction, and then the star becomes unstable. Eventually, it collapses. The inner dense regions of the star collapse first and gravitational energy is released and transferred to the outer layers of the star, blowing them away. After the supernova explosion only a fraction of the star is left, and this final product might be a white dwarf, a neutron star or a black hole, depending on the initial mass of the star.

Neutron stars are supported against gravitational collapse mainly by the neutron degeneracy pressure and may have typically masses of order $(1-2) M_\odot$ and radii ~ 10 km. Such masses and radii yield an averaged density for neutron stars of order 10^{14} g/cm^3. However, the expected densities in neutron stars span a rather wide range

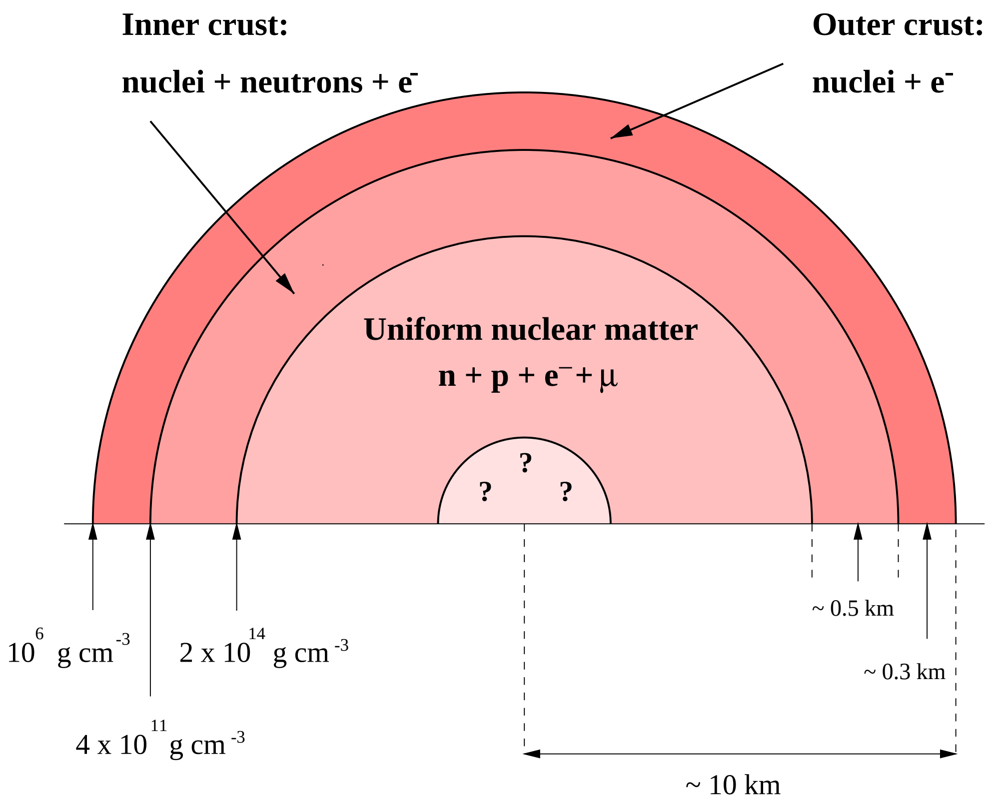

Figure 4.2: A schematic cross section of a neutron star illustrating the various regions discussed in the text.

and in fact the internal structure of a neutron star can be described by an "onion" model. In Fig. 4.2 a schematic cross section of a neutron star is shown. At the surface, densities are typically $\rho < 10^6$ g/cm^3. The outer crust, with densities ranging from 10^6 g/cm^3 to 4×10^{11} g/cm^3, is a solid region where heavy nuclei, mainly around the iron mass number, in a Coulomb lattice coexist in β-equilibrium with an electron gas. When density increases the electron chemical potential goes up and then the electronic capture process

$$p + e^- \rightarrow n + \nu_e \ , \tag{4.1}$$

opens, the nuclei becoming more and more neutron-rich. The only available levels for the neutrons at $\sim 4.3 \times 10^{11}$ g/cm^3 are in the continuum, and thus they start to "drip out" of the nuclei. We have then reached the inner crust, consisting of a Coulomb lattice of very neutron-rich nuclei together with a superfluid neutron gas and an electron gas with densities going from 4×10^{11} g/cm^3 to 2×10^{14} g/cm^3. At density $\sim 10^{14}$ g/cm^3, nuclei start to dissolve and one enters the quantum fluid interior. In this region matter is mainly composed of superfluid neutrons with a smaller concentration of superconducting protons and normal electrons and muons [El96]. In the core of the star, the density is of the order of 10^{15} g/cm^3. The composition of this region is not well known, and thus is subject to much speculation. Suggestions range from a mixed phase of quark and nuclear matter [Gl92, He93, He94], kaon [Ka86] or pion condensates [Ak97, Ak98], and hyperonic matter [Gl92, Sc98, Vi00b], which is one of the main subjects of this thesis.

A neutron star is one of the densest objects in the universe, therefore Einstein's General Relativity Theory is needed in order to determine its structure. Einstein's equations (see e.g. [We72, Mi73]) for a spherical static star take the form of the familiar Tolman–Oppenheimer–Volkoff (hereafter referred to as TOV) equations [To39, Op39]:

$$\frac{dp(r)}{dr} = -\frac{G}{c^2}\frac{(p(r)+\epsilon(r)c^2)(M(r)c^2+4\pi r^3 p(r))}{r(rc^2-2GM(r))} \tag{4.2}$$

$$\frac{dM(r)}{dr} = 4\pi r^2 \epsilon(r). \tag{4.3}$$

By rewriting Eq. (4.2) in the form

$$\frac{dp(r)}{dr} = -\frac{GM(r)\epsilon(r)}{r^2}\frac{(1+\frac{p(r)}{\epsilon(r)c^2})(1+\frac{4\pi r^3 p(r)}{M(r)c^2})}{(1-\frac{2GM(r)}{rc^2})}, \tag{4.4}$$

we can read explicitly the Newtonian part and arrive at an interpretation of the equations that is quite instructive. Think of a shell of matter in the star of radius r and thickness dr. Eq. (4.3) gives the mass-energy in this shell. The pressure of matter exterior to the shell is $p(r)$ and interior to it $p(r) + dp(r)$. The left side of Eq. (4.4) is the net force acting outward on the surface of the shell by the pressure difference $dp(r)$ and the first factor on the right side is the attractive Newtonian force of gravity acting on the shell by the mass interior to it. The remaining factor is the exact correction for General Relativity. So these equations express the balance at each r between the internal pressure as it supports the overlying material against the gravitational attraction of the mass-energy interior to r. They are just the equations of hydrostatic equilibrium in General Relativity.

The Equation of State (EoS) $p = p(\epsilon)$ is the manner in which matter enters the equations of stellar structure. For a given Equation of State, the TOV equations can be integrated from the origin with the initial conditions that $M(0) = 0$ (since near $r = 0$ we may write $M(r) \sim 4\pi r^3\epsilon(0)/3$), and an arbitrary value for the central energy density $\epsilon(0)$, until the pressure becomes zero. Zero pressure can support no overlying material against the gravitational attraction exerted on it from the mass within and so marks the edge of the star. The point R where the pressure vanishes defines the radius of the star and $M(R)$ its gravitational mass,

$$M_G \equiv M(R) = 4\pi \int_0^R r^2 \epsilon(r) dr. \tag{4.5}$$

Neutron stars are, however, rotating objects. We expect the rotation to flatten the star more or less depending on its angular velocity. Spherical symmetry is thereby broken, although the star maintains its axial symmetry. This symmetry breaking makes the equations of structure much more complicated. In addition to Eqs. (4.2) and (4.3) new coupled equations need to be solved. In this thesis we have followed the method developed in [We91], which is a refined version of Hartle's perturbation method [Ha67]. The reader is referred to the original work of Hartle for explicit details of the equations.

4.3 Chemical equilibrium in a neutron star

The equilibrium conditions in a neutron star are governed by the weak processes (normally referred to as processes for β-equilibrium)

$$b_1 \rightarrow b_2 + l + \bar{\nu}_l, \quad b_2 + l \rightarrow b_1 + \nu_l \ , \tag{4.6}$$

where b_1 and b_2 refer to two different types of baryons, l represents a lepton and ν_l and $\bar{\nu}_l$ its respective neutrino and anti-neutrino.

It is generally understood that the knowledge of the particular path that a body or substance may follow in reaching its equilibrium state is not needed to determine that state. One possible way to find it consists in minimizing the total energy density of the system constrained by the subsidiary conditions that express the conservation of some components or attributes (hereafter referred to as "charges") on a timescale longer than a characteristic time of the system. This can be done by the method of Lagrange multipliers [Mo53]. In the case of a cold neutron star, there are only two conserved charges: the total baryonic density and the total electric charge, which is zero (charge neutrality). Strangeness is not conserved on the scale of a star because the timescale of the electro-weak interaction ($\mathcal{T} \sim 10^{-10}$ seconds) is short in comparison to macroscopic scales. In addition, in a cold neutron star, neutrinos have diffuseed out of the star, and therefore, there is no conservation of the leptonic numbers.

One can then construct a function, $F(\rho_{b_1}, \rho_{b_2}, ..., \rho_{b_B}, \rho_{l_1}, \rho_{l_2}, ..., \rho_{l_L})$, from the total energy density $\epsilon(\rho_{b_1}, \rho_{b_2}, ..., \rho_{b_B}, \rho_{l_1}, \rho_{l_2}, ..., \rho_{l_L})$ and the two constraint equations which express conservation of the total baryonic density and charge neutrality:

$$\begin{aligned} F(\rho_{b_1}, \rho_{b_2}, ..., \rho_{b_B}, \rho_{l_1}, \rho_{l_2}, ..., \rho_{l_L}) &= \epsilon(\rho_{b_1}, \rho_{b_2}, ..., \rho_{b_B}, \rho_{l_1}, \rho_{l_2}, ..., \rho_{l_L}) \\ &+\alpha \left(\rho_B - \sum_i B_i \rho_{b_i}\right) + \beta \left(\sum_i q_{b_i}\rho_{b_i} + \sum_j q_{l_j}\rho_{l_j}\right) . \end{aligned} \tag{4.7}$$

Subscripts b_i and l_i stand for baryons and leptons respectively, running b_i over all types of baryons and l_i over all types of leptons. The quantities α and β are the corresponding Lagrange multipliers. The products $q_{b_i}\rho_{b_i}$ and $q_{l_i}\rho_{l_i}$, denote the charge density of those charged particles, with q_{b_i} and q_{l_i} being the corresponding charge numbers, and B_i denotes the baryonic number.

The minimization condition requires

$$\begin{gathered} \frac{\partial F}{\partial \rho_{b_1}} = 0, \quad ... \quad , \quad \frac{\partial F}{\partial \rho_{b_B}} = 0, \frac{\partial F}{\partial \rho_{l_1}} = 0, \quad ... \quad , \quad \frac{\partial F}{\partial \rho_{l_L}} = 0 \ , \\ \frac{\partial F}{\partial \alpha} = 0, \quad \frac{\partial F}{\partial \beta} = 0 \ . \end{gathered} \tag{4.8}$$

Remembering that the chemical potential of a species "i" is just $\mu_i = \partial\epsilon/\partial\rho_i$, the above conditions on F yield a set of equations of the type

$$\mu_{b_i} - B_i\alpha + q_{b_i}\beta = 0, \quad i = 1, ..., B \ , \tag{4.9}$$

for the baryons. And a set of equations of the type

$$\mu_{l_j} + q_{l_j}\beta = 0, \quad j = 1, ..., L \ , \tag{4.10}$$

for the leptons.

Eliminating the Lagrange multipliers α and β, one can obtain a set of relationships among the chemical potentials. In general there are as many *independent* chemical potentials as there are conserved charges, and all the others can be written in terms of them. As it was said, in the case of a neutron star there are only two conserved charges, and their corresponding chemical potentials are μ_n (associated with conservation of the total baryonic density) and μ_e (associated with charge neutrality). Applying then Eqs. (4.9) and (4.10) to the neutron and the electron it is found

$$\alpha = \mu_n, \quad \beta = \mu_e \ , \tag{4.11}$$

and replacing (4.11) on those equations one has that in general the chemical potential of any particle can be obtained as a linear combination of μ_n and μ_e, weighted by the baryonic number and electric charge carried by the particle:

$$\begin{aligned} \mu_{b_i} &= B_i\mu_n - q_{b_i}\mu_e, \quad i = 1, ..., B-1, \\ \mu_{l_j} &= -q_{l_j}\mu_e, \quad j = 1, ..., L-1 \ . \end{aligned} \tag{4.12}$$

There is an alternative way of deriving this set of equations. It consists of writing down all the possible reactions among the components of matter. One then rewrites the reactions in terms of the different chemical potentials μ_i. If several reactions are possible, there is an equation for each one and the resulting relationships between the chemical potentials allow one to express the chemical potentials of all the components of matter in terms of the independent ones.

The solution of this set of equations determines the composition of matter at its ground state for a given density and types of particles. However, it is clear from these equations that not only the weak interaction rules the composition of matter, but also the strong interaction through the explicit value of the chemical potentials.

4.4 Neutron star matter Equation of State

As we already said in Section 4.2 the Equation of State is the manner in which matter enters the equations of stellar structure. Following the many-body method described in Chapters 1 and 2 we construct in this section the Equation of State for β-stable neutron star matter including hyperonic degrees of freedom. In addition a causal parametrization of the pure nucleonic Equation of State is described. The section is finished with a brief comment on the Equation of State of the neutron star crust.

4.4.1 The EoS for the neutron star interior

Our many-body scheme starts with the most recent parametrization of the free baryon-baryon potentials for the complete octet of baryons as defined by Stoks and Rijken in

Ref. [St99]. Effects from the nuclear medium are introduced through the so-called G matrix, which takes into account short-range correlations for all strangeness sectors,

$$\begin{aligned}\langle B_1 B_2|\overline{G}(\omega)|B_3 B_4\rangle &= \langle B_1 B_2|V|B_3 B_4\rangle \\ + \sum_{B_5 B_6} \langle B_1 B_2|V|B_5 B_6\rangle & \frac{\overline{Q}_{B_5 B_6}}{\omega - E_{B_5} - E_{B_6} + i\eta} \langle B_5 B_6|\overline{G}(\omega)|B_3 B_4\rangle \ ,\end{aligned} \tag{4.13}$$

where B_i represents all possible baryons n, p, Λ, Σ^-, Σ^0, Σ^+, Ξ^- and Ξ^0 and their quantum numbers.

The single-particle energies are given by

$$E_{B_i} = T_{B_i} + U_{B_i} + M_{B_i} \ , \tag{4.14}$$

where T_{B_i} is the kinetic energy and M_{B_i} the mass of baryon B_i. We note that the G-matrix has been obtained using the discontinuous prescription (i.e. $E_B = T_B + M_B$) for the intermediate states $B_5 B_6$. The single-particle potential U_{B_i} is defined by

$$U_{B_i} = \mathrm{Re} \sum_{B_j \leq F_j} \langle B_i B_j|\, \overline{G}(\omega = E_{B_j} + E_{B_i})\, |B_i B_j\rangle_{\mathcal{A}} \ , \tag{4.15}$$

where the linear momentum of the single-particle state B_j is limited by the size of the Fermi surface F_j for particle species B_j. The matrix element in Eq. (4.15) is properly antisymmetrized when the species B_i and B_j are the same. Detailed expressions for the single-particle potentials and the G-matrices involved can be found in Chapter 2.

The total energy density, ε, is obtained by

$$\varepsilon = \varepsilon_b + \varepsilon_l \ , \tag{4.16}$$

where the baryonic contribution ε_b is constructed from the baryon single-particle potentials (from now on we use $\hbar = c = 1$)

$$\varepsilon_b = \sum_{B_i} 2 \int_0^{k_{F_{B_i}}} \frac{d^3k}{(2\pi)^3} \left(M_{B_i} + \frac{k^2}{2M_{B_i}} + \frac{1}{2} U_{B_i}(k) \right) \;, \tag{4.17}$$

and the leptonic one ε_l, because the electromagnetic interaction plays a negligible role due to charge neutrality, is given by

$$\varepsilon_l = \sum_{L_i} 2 \int_0^{k_{F_{L_i}}} \frac{d^3k}{(2\pi)^3} \sqrt{k^2 + M_{L_i}^2} \tag{4.18}$$

The total energy per baryon E/A, measured with respect to the nucleon mass, is then given by

$$\frac{E}{A} = \frac{\varepsilon}{\rho_b} - M_N \;, \tag{4.19}$$

where ρ_b is the total baryonic density.

The total pressure of the system is given by the sum of the baryonic and leptonic contributions

$$P = P_b + P_l \;, \tag{4.20}$$

where the partial pressure P_i of baryons $(i = b)$ and leptons $(i = l)$ is obtained through the thermodynamic relation

$$P_i = \rho_i \frac{\partial \varepsilon_i}{\partial \rho_i} - \varepsilon_i \;. \tag{4.21}$$

In order to satisfy the set of balance equations (4.12), we need to know the chemical potentials of the particles involved. In Brueckner-Hartree-Fock (BHF) theory, the chemical potential is taken as the single particle energy at the Fermi momentum of the baryon, $k_{F_{B_i}}$, which at the lowest order reads

$$\mu_{B_i} = E_{B_i}(k_{F_{B_i}}) = M_{B_i} + T_{B_i}(k_{F_{B_i}}) + U^N_{B_i}(k_{F_{B_i}}) + U^Y_{B_i}(k_{F_{B_i}}) \ . \tag{4.22}$$

In the last equality, the baryon single-particle potential U_B has been split into a contribution, U^N_B, coming from the nucleonic Fermi seas (p, n) and a contribution, U^Y_B, coming from the hyperonic ones $(\Lambda, \Sigma^-, \Sigma^0, \Sigma^+, \Xi^-, \Xi^0)$. From calculations in pure nucleonic matter, it is well known that the nucleon chemical potential obtained from Eq. (4.22) differs considerably from its thermodynamic definition

$$\mu_{B_i} = \frac{\partial \varepsilon}{\partial \rho_{B_i}} \ . \tag{4.23}$$

Therefore, for the nucleons, we replace the nucleonic contribution to the chemical potential in Eq. (4.22), i.e. $\mu^N_{n,p} = M_{n,p} + T_{n,p}(k_{F_{(n,p)}}) + U^N_{n,p}(k_{F_{(n,p)}})$, by $\mu^N_{n,p} = \partial\varepsilon_{NN}/\partial\rho_{n,p}$, where

$$\varepsilon_{NN} = \sum_{B_i=n,p} 2\int_0^{k_{F_{B_i}}} \frac{d^3k}{(2\pi)^3}\left(M_{B_i} + \frac{k^2}{2M_{B_i}} + \frac{1}{2}U^N_{B_i}(k)\right) \tag{4.24}$$

is the nucleonic contribution to the baryonic energy density including only the interaction between NN pairs. For the hyperons, we keep the prescription of Eq. (4.22). As shown in Ref. [Ba00], these approximations amount to ignore the weak dependence of U^N_N, U^N_Y on the hyperon fractions and of U^Y_N, U^Y_Y on the nucleon ones, and are good enough as long as the proton and hyperon fractions keep moderately small.

4.4.2 Parametrization of the pure nucleonic EoS

The many-body approach developed in this thesis and reviewed above, is the lowest-order Brueckner–Hartree–Fock method extended to the hyperon sector. This means also that we consider only two-body interactions. However, it is well-known from studies of nuclear matter and neutron star matter with only nucleonic degrees of freedom that three-body forces are important in order to reproduce the saturation properties of nuclear matter, see e.g., the work of Akmal *et al.* [Ak98] for the most recent approach. The effect of nucleon three-body forces on the properties of β-stable matter with hyperons has been studied in Refs. [Sc98, Ba00]. It is found that the repulsion induced by the three-body force at high densities enhances substantially the hyperon population which in turn induces a strong softening of the EoS.

In order to include such effects we will alternatively use, for the nucleonic sector, a simple form for the total energy per nucleon developed by Heiselberg and Hjorth-Jensen [He99]. This approach, hereafter referred to as parametrization HH99, parametrizes the variational calculation with three-body forces and relativistic boost corrections of Akmal *et al.* [Ak98]. It consists of a compressional term and a symmetry term

$$\frac{E}{A} = E_{comp}(\rho_N) + S(\rho_N)(1-2x_p)^2 = E_0 u \frac{u-2-\delta}{1+u\delta} + S_0 u^{\gamma}(1-2x_p)^2 \; . \tag{4.25}$$

Here $u = \rho_N/\rho_0$ is the ratio of the nucleonic density to nuclear saturation density and the proton fraction is defined as $x_p = \rho_p/\rho_N$. The compressional term reproduces the saturation density, binding energy and incompressibility modulus $K = 9\partial P/\partial\rho_N$ of nuclear matter at normal saturation density. The best fit of this simple functional is obtained for $E_0 = 15.8$ MeV, $S_0 = 32$ MeV, $\gamma = 0.6$, and $\delta = 0.2$. In order to examine

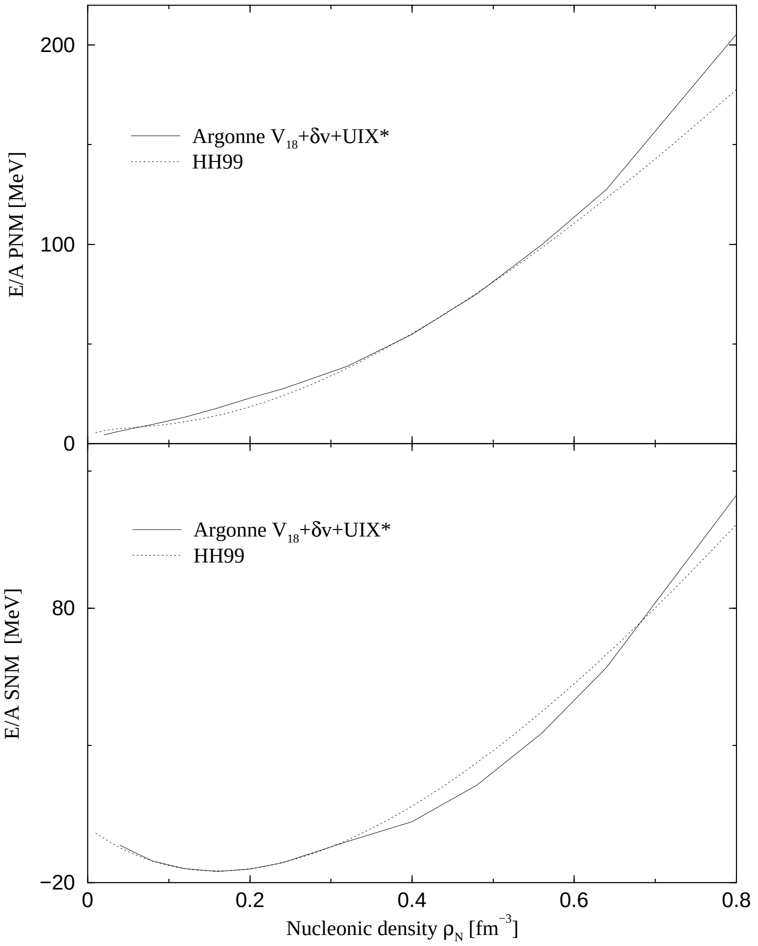

Figure 4.3: Comparison of the total energy per baryon obtained from the parametrization HH99 [He99] and from the results of Akmal *et al.* [Ak98] with boost corrections and three-body forces ($V_{18} + \delta v + UIX^*$) for pure neutron matter (PNM), and for symmetric nuclear matter (SNM) for the values of the parameters defined in the text. Plot taken from Ref. [He99].

the quality of the fit we show for comparison in Fig. 4.3 the total energy per nucleon obtained from parametrization HH99 and the results of Akmal *et al.* for pure neutron matter (PNM) and symmetric nuclear matter (SNM). As can be seen in the figure, the agreement between the parametrization and the microscopic calculation is rather good except at the very high densities where the EoS of Akmal *et al.* becomes superluminal.

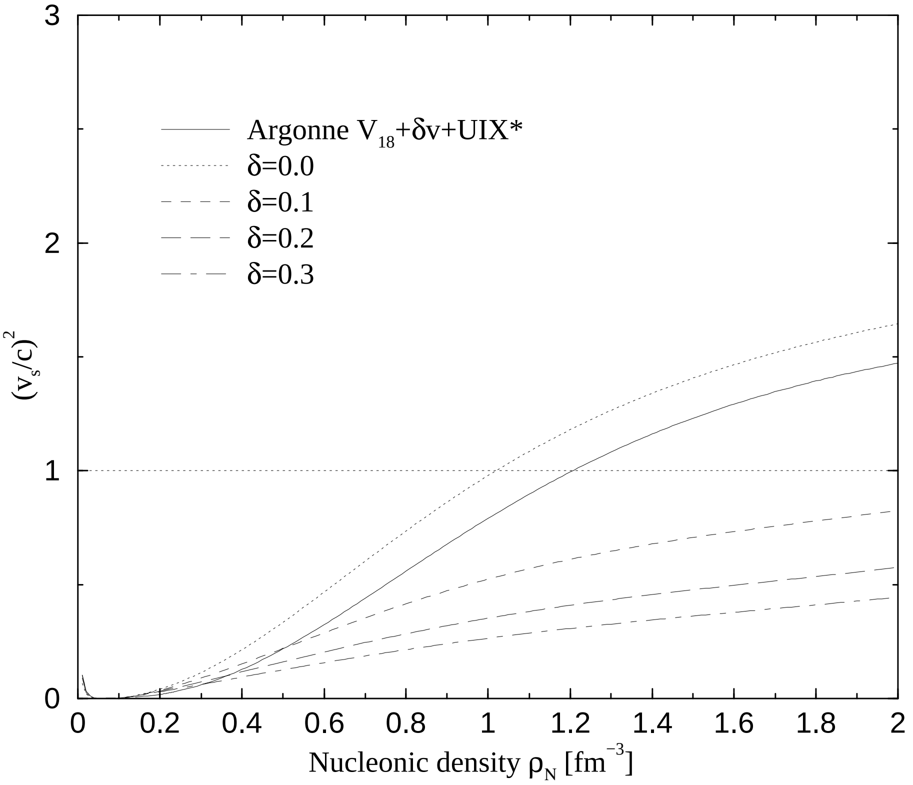

Figure 4.4: Speed of sound $(v_s/c)^2$ in symmetric matter for various values of the parameter δ in comparison with the microscopic result of Akmal *et al.* [Ak98] (solid line). Plot taken from Ref. [He99].

It can be shown from the definition of the speed of sound

$$\left(\frac{v_s}{c}\right)^2 = \frac{dP}{d\varepsilon} = \frac{dP}{d\rho_N}\frac{d\rho_N}{d\varepsilon} = \left(\frac{K}{9(M_N + E/A + P/\rho_N)}\right) , \tag{4.26}$$

and Eq. (4.25) that for

$$\delta \geq \sqrt{\frac{E_0}{M_N}} \simeq 0.13 , \tag{4.27}$$

causality is guaranteed (i.e., $(v_s/c)^2 \leq 1$) for all densities. This can be seen in Fig. 4.4 where we plot the speed of sound for various values of δ and the one corresponding to the microscopic calculation of Akmal *et al.* [Ak98].

4.4.3 The EoS for the neutron star crust

The crust of a neutron star is important for a number of observable properties, although the bulk properties of the star (e.g., mass, radius) depend very weakly on the EoS in this region. For instance, neutrino emission from the crust plays an important role in the thermal evolution of the star. The moments of inertia of the various components of matter in the crust play also a crucial role in models for pulsar glitches.

As we said in section 4.2, matter in the crust of a neutron star consists mainly of a Coulomb lattice of nuclei immersed in a sea of neutrons and a roughly uniform sea of electrons. When the density of matter approaches that of nuclear matter, nuclei merge to form a uniform liquid of neutrons, protons and electrons.

Properties of matter at subnuclear densities ($\rho < \rho_0$) are better known than at supranuclear densities ($\rho > \rho_0$). Many studies on the physics of matter at subnuclear densities have been performed. To describe the crust of the star, in this thesis we have employed the Equation of State of Lorenz, Ravenhall and Pethick [Lo93, Pe95]. We will not enter into the details of the calculation of this Equation of State, because they are out of the scope of this thesis, and the interested reader is referred to the original work of Lorenz *et al.* for detailed information.

4.5 β-stable neutron star matter

The composition of matter at high densities is poorly known. At densities near to the saturation density of nuclear matter ($\rho_0 = 0.16$ fm^{-3}) we expect matter to be mainly composed of neutrons, protons, electrons and muons in β-equilibrium. However, as the density increases, new degrees of freedom, such as hyperons, pion or kaon condensates, or even a possible deconfined phase of quarks and gluons (quark-gluon plasma) at ultrahigh densities, become more and more important.

In this section we show the composition and Equation of State of matter in β-equilibrium considering, first, only nucleonic and leptonic degrees of freedom and secondly, including also hyperons. In our discussion below we employ the parametrization HH99 and the NSC97e model of the recent baryon-baryon interaction of Stoks and Rijken [St99]. Pion or kaon condensates and sub-hadronic degrees of freedom (i.e., quarks and gluons) are out of the scope of this thesis and therefore, nothing about them is said here.

4.5.1 Nucleonic degrees of freedom

Most of the interior of a neutron star can be well represented by nucleonic and leptonic degrees of freedom, namely from the inner part of the crust to the outer part of the core, with densities ranging from 0.5 to $2-3$ times normal nuclear matter saturation density. To begin let us assume that matter is composed only of neutrons, protons and electrons. In this case the equilibrium conditions (4.12) for the weak processes

$$n \rightarrow p + e^- + \bar{\nu}_e, \quad p + e^- \rightarrow n + \nu_e \ , \tag{4.28}$$

reduce to

$$\mu_p = \mu_n - \mu_e \ , \tag{4.29}$$

and charge neutrality requires

$$\rho_p = \rho_e \ . \tag{4.30}$$

The chemical potentials of the neutrons and protons are given by the familiar thermodynamical relations

$$\mu_n = \left(\frac{\partial \epsilon}{\partial \rho_n}\right)_{\rho_p, \rho_e} , \quad \mu_p = \left(\frac{\partial \epsilon}{\partial \rho_p}\right)_{\rho_n, \rho_e} , \tag{4.31}$$

where ϵ is the energy density, $\rho_N = \rho_n + \rho_p$ is the nucleonic density and $x_p = \rho_p / \rho_N$ is the proton fraction.

The electrons can be considered as a free Fermi gas at zero temperature because the role of the electromagnetic interaction is negligible. Therefore, their chemical potential is chosen to be equal to their Fermi energy,

$$\mu_e = E_F = \sqrt{k_{F_e}^2 + M_e^2}, \tag{4.32}$$

which in the ultrarelativistic limit ($E_F \gg M_e$) reduces to

$$\mu_e = k_{F_e} = (3\pi^2 \rho_e)^{1/3} \ . \tag{4.33}$$

Using this last equation and the charge neutrality condition (4.30), Eq. (4.29) can be rewritten as

$$3\pi^2 \rho_N x_p - \left[\mu_n(\rho_N, x_p) - \mu_p(\rho_N, x_p)\right]^3 = 0 \ , \tag{4.34}$$

which defines in an implicit way the proton fraction x_p at equilibrium for each given value of the nucleonic density ρ_N. This equation can be solved numerically, yielding a

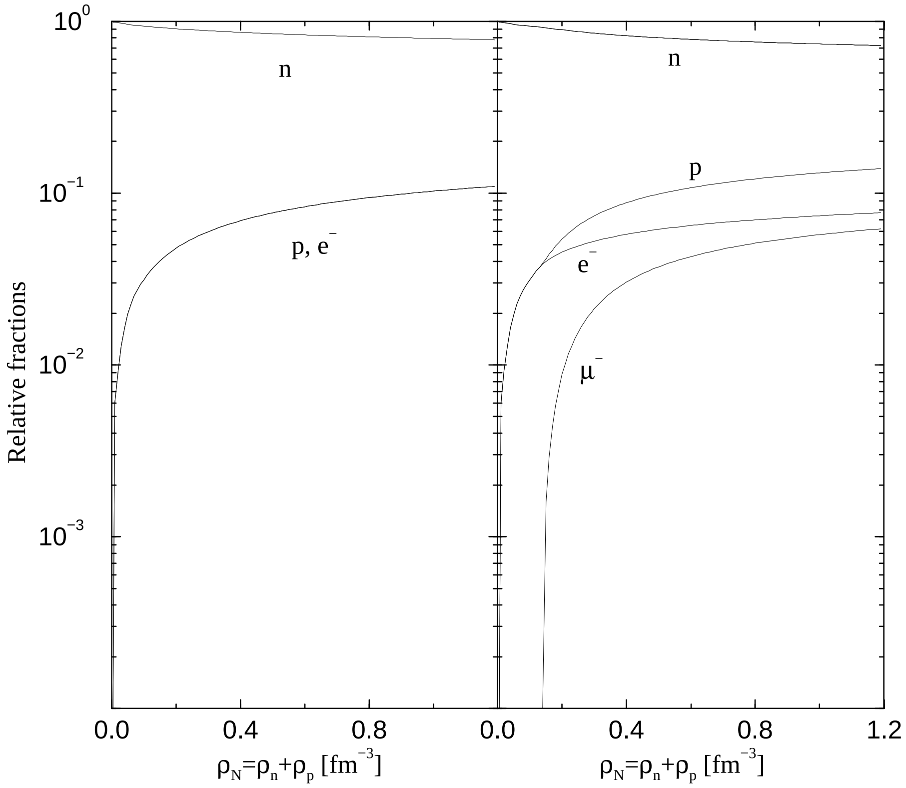

Figure 4.5: Composition of β-stable neutron star matter with neutrons, protons and electrons (left panel), and including muons (right panel), obtained with the parametrization HH99.

composition of β-stable matter like the one shown in the left panel of Fig. 4.5.

The electron chemical potential of β-stable matter at the saturation density of nuclear matter $\rho_0 \sim 0.16$ fm^{-3}, is of the order $\sim$ 100 MeV. Once the rest mass of the muon ($M_\mu = 105.7$ MeV) is exceeded, it becomes energetically favourable for an electron at the top of the e^- Fermi surface to decay into a μ^- via the weak process

$$e^- \rightarrow \mu^- + \bar{\nu}_\mu + \nu_e \ . \tag{4.35}$$

A Fermi sea of degenerate negative muons starts then to develop and, consequently, the charge balance needs to be changed according to

$$\rho_p = \rho_e + \rho_\mu \ , \tag{4.36}$$

and chemical equilibrium, assuming neutrino-free matter, with respect to the process (4.35) requires

$$\mu_e = \mu_\mu \ . \tag{4.37}$$

The muons are also considered a Fermi gas at zero temperature. Hence, the muon density can be written in terms of the muon chemical potential as

$$\rho_\mu = \frac{1}{3\pi^2}\left[\mu_\mu^2 - M_\mu^2\right]^{3/2} \theta(\mu_e - M_\mu) \ , \tag{4.38}$$

where the θ function reminds that muons appear in matter as soon as the chemical potential of the electron equals the mass of the muon. Using (4.38), the charge neutrality condition (4.36) and the equilibrium condition (4.37), equation (4.29) can be written as

$$\begin{gathered} 3\pi^2 \rho_N x_p - (\mu_n(\rho_N, x_p) - \mu_p(\rho_N, x_p))^3 \\ - \left[(\mu_n(\rho_N, x_p) - \mu_p(\rho_N, x_p))^2 - M_\mu^2\right]^{3/2} \theta(\mu_e - M_\mu) = 0 \end{gathered} \tag{4.39}$$

which defines the proton fraction x_p in an implicit way. Note that this equation reduces to Eq. (4.34) for those values of the electron chemical potential smaller than the muon rest mass.

The composition of matter including electrons, muons and nucleonic degrees of freedom obtained by solving Eq. (4.39) is shown in the right panel of Fig. 4.5.

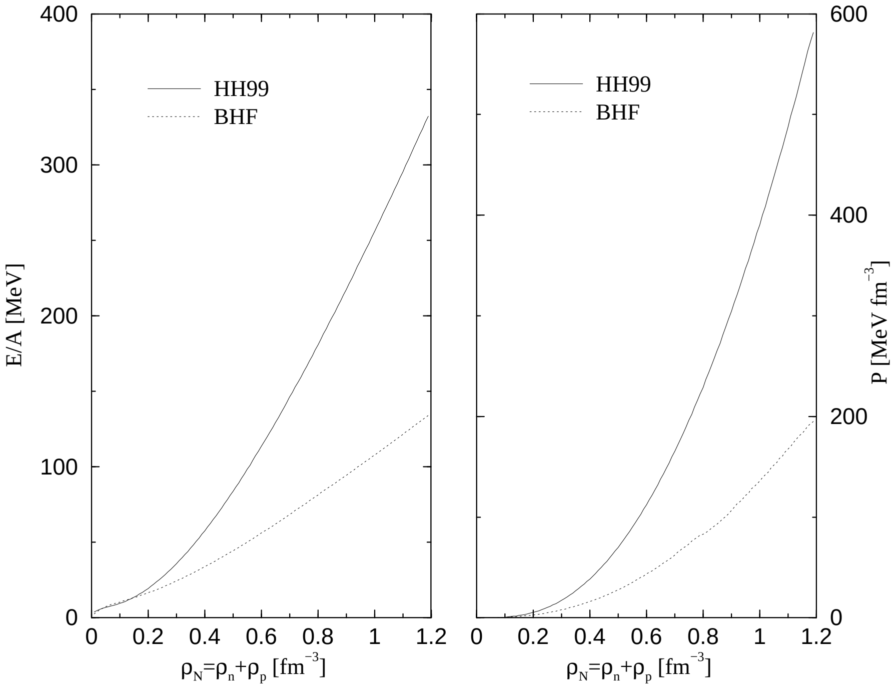

Figure 4.6: Total energy per baryon (left panel) and pressure (right panel) in β-stable matter with nucleonic and leptonic (e^- and μ^-) degrees of freedom as a function of the total nucleonic density. Solid lines show the results obtained with the parametrization HH99. Dotted lines correspond to the results of a Brueckner–Hartree–Fock calculation employing the NSC97e model of Ref. [St99].

In Figure 4.6 we show the total energy per baryon (including both nucleonic and leptonic degrees of freedom) (left panel) and the total pressure (right panel) of matter in β-equilibrium obtained: from the parametrization HH99 (solid lines); and from a Brueckner–Hartree-Fock calculation (dotted lines) performed using as bare interaction the NSC97e model of Ref. [St99]. Differences between solid and dotted lines are mainly due, apart from the different bare interaction employed in the calculation and the method, to the fact that the parametrization HH99 includes the effect of three-body forces. The inclusion of three-body forces, which is necessary to reproduce the saturation properties of nuclear matter, induces a repulsion at high densities making the Equation of State stiffer, as can be seen in the figure.

4.5.2 Hyperonic degrees of freedom

As the density increases, new hadronic degrees of freedom may appear in addition to neutrons and protons. One such degree of freedom is hyperons, baryons with strangeness content. Contrary to terrestrial conditions where hyperons are unstable and decay into nucleons through the weak interaction, the equilibrium conditions in neutron stars can make the inverse process to happen, so that the formation of hyperons becomes energetically favourable. As soon as the chemical potential of the neutron becomes sufficiently large, energetic neutrons can decay via weak strangeness non-conserving interactions into Λ hyperons leading to a Λ Fermi sea with $\mu_\Lambda = \mu_n$. However, one expects Σ^- to appear via

$$e^- + n \rightarrow \Sigma^- + \nu_e \ , \tag{4.40}$$

at lower densities than that of the Λ, even though the Σ^- is more massive, the reason being that the above process removes both an energetic neutron and an energetic electron, whereas the decay to a Λ, being neutral, removes only an energetic neutron. Stated differently, the negatively charged hyperons appear in the ground state of matter when their masses equal $\mu_n + \mu_e$, while the neutral hyperons appear when their masses equal μ_n. Since the electron chemical potential in matter is larger than the mass difference $M_{\Sigma^-} - M_\Lambda = 81.76$ MeV, Σ^- will appear at lower densities than Λ. For matter with hyperons, the chemical equilibrium conditions (4.12) become

$$\begin{aligned}
&\mu_{\Xi^-} = \mu_{\Sigma^-} = \mu_n + \mu_e, \\
&\mu_{\Lambda} = \mu_{\Xi^0} = \mu_{\Sigma^0} = \mu_n, \\
&\mu_{\Sigma^+} = \mu_p = \mu_n - \mu_e \ ,
\end{aligned} \tag{4.41}$$

and charge neutrality imposes

$$\rho_p + \rho_{\Sigma^+} = \rho_e + \rho_\mu + \rho_{\Sigma^-} + \rho_{\Xi^-} \ . \tag{4.42}$$

Hyperonic degrees of freedom have been considered by several authors within the framework of relativistic mean field models [Kn95, Sc96, Pr97] or parametrized effective interactions [Ba97], see also Balberg *et al.* [Ba99] for a recent update. Realistic hyperon-nucleon interactions were employed recently by Schulze *et al.* [Sc98], in a many-body calculation in order to study the onset of hyperon formation in neutron star matter. In a recent paper Baldo *et al.* [Ba00] investigate the properties of neutron stars with hyperons, paying special attention to the role played by three-body nucleon forces. All these works show that hyperons appear at densities of the order $\sim 2\rho_0$.

In Refs. [Sc98, Ba00] the hyperon-hyperon interaction was not included. Nevertheless, it is clear that as soon as the Σ^- hyperon appears, one needs to consider the interaction between hyperon pairs since it will influence the single-particle energy of the hyperons, hence affecting the equilibrium conditions (4.41) for higher densities and the onset of other hyperons (e.g. the Λ). The aim of this section is thus to present results of many-body calculations for β-stable neutron star matter with hyperonic degrees of freedom, employing interactions which also account for strangeness $S < -1$. The main problem we have to face in our case is that the hyperon-nucleon interaction and especially the hyperon-hyperon interaction are less constrained by the experimental data than the nucleon-nucleon one.

In this section we discuss two sets of results for β-stable matter, one where the nucleonic contributions to the self-energy of nucleons are derived from a Brueckner–Hartree–Fock calculation using the NSC97e baryon-baryon potential model of Ref. [St99], and another where the pure nucleonic contribution to the neutron and proton chemical potentials and the energy density are calculated from the parametrization HH99. Hyperonic contributions are all calculated within the Brueckner–Hartree–Fock scheme using the NSC97e baryon-baryon interaction of Ref. [St99]. We emphasize, once more, that, in the present work, hyperon-nucleon (YN) as well as hyperon-hyperon (YY) interactions are taken into account.

The above models for the pure nucleonic part (BHF and HH99 parametrization) combined with the contribution of the strange sector (BHF), hereafter referred to as pure BHF and HH99 + BHF respectively, yield the composition of β-stable matter up to total baryonic density $\rho = 1.2$ fm^{-3}, shown in Fig. 4.7, after solving the set of Eqs. (4.41). In the upper panel, results for the pure BHF calculation (NN, YN and YY sectors) are presented. Results combining the parametrization HH99 for the nucleonic sector with the BHF calculation for the YN and YY interactions are shown in the lower panel. In both panels, solid lines correspond to the case in which all the interactions NN, YN and YY are considered.

As it can be seen by comparing the solid lines in both panels in Fig. 4.7, the composition of β-stable neutron star matter has a strong dependence on the model used to describe the non-strange sector. In both cases, due to its negative charge,

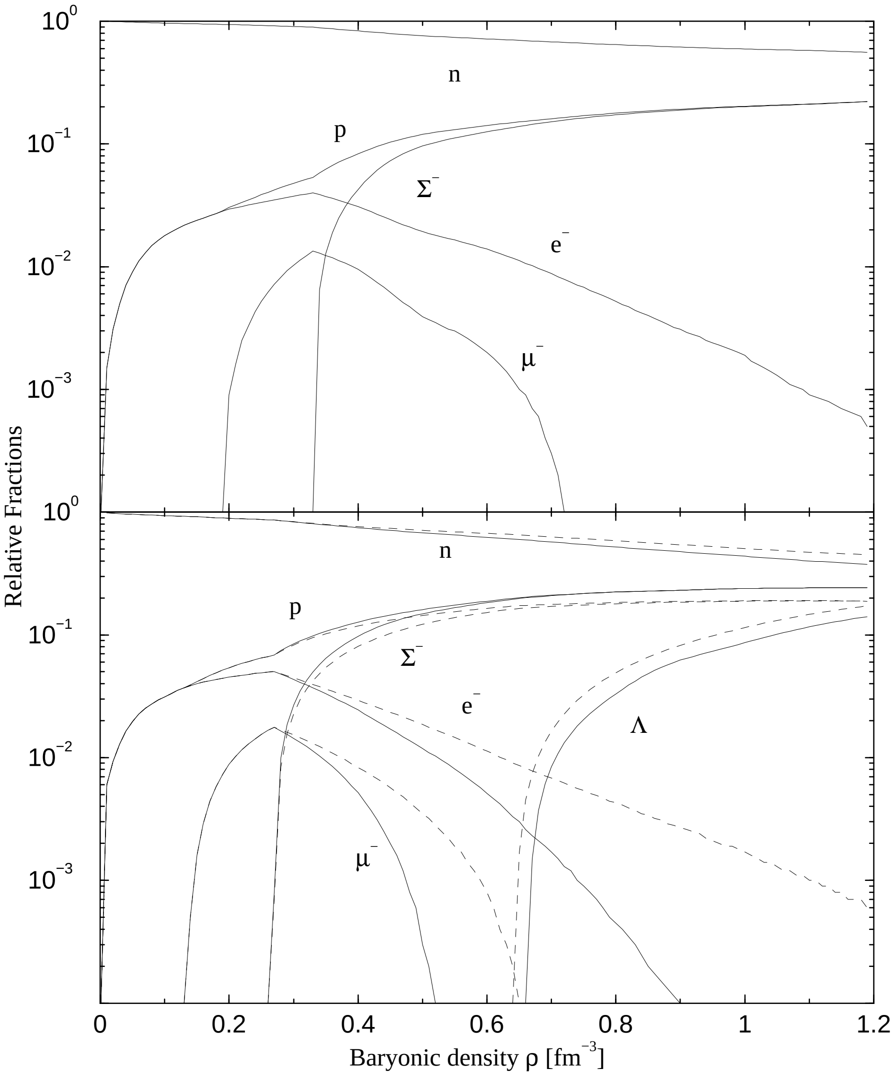

Figure 4.7: Composition of β-stable neutron star matter. In the upper panel are presented the results of a Brueckner–Hartree-Fock calculation using the NSC97e model of Ref. [St99]. In the lower panel the nucleonic part of the self-energy of the nucleons has been replaced by the parametrization HH99. Solid lines in upper and lower panel correspond to the case in which all the interactions (nucleon-nucleon, hyperon-nucleon and hyperon-hyperon) are considered. Dashed lines in the lower panel correspond to the case where the hyperon-hyperon interaction has been switched off.

the Σ^--hyperon is the first one to appear. Since the parametrization HH99 yields a stiffer pure nucleonic matter EoS than the corresponding one obtained from a BHF calculation (see Fig. 4.6), the onset of Σ^-, when the parametrization HH99 is used to describe the nucleonic sector, occurs at a smaller density ($\rho = 0.27$ fm^{-3}) than for the pure BHF calculation ($\rho = 0.34$ fm^{-3}). In both cases, as soon as the Σ^- hyperon appears, leptons tend to disappear, completely in the HH99 + BHF calculation (the electron chemical potential changes sign at $\rho = 1.01$ fm^{-3}, indicating the appearance of positrons), whereas in the pure BHF one only muons disappear. The onset of Λ formation takes place at higher density. Recalling the condition for the appearance of Λ, $\mu_\Lambda = \mu_n = \mu_p + \mu_{e^-}$, and that the parametrization HH99 is stiffer due to the inclusion of three-body forces, this clearly enhances the possibility of creating Λ hyperons at lower density with the HH99 + BHF model than with the pure BHF case. Indeed, the HH99 + BHF calculation produces Λ hyperons from $\rho = 0.67$ fm^{-3} on, whereas the neutron chemical potential from the pure BHF turns out to be too small to equal the Λ chemical potential in the range of densities explored. The absence of Λ hyperons, in the pure BHF results, can also, in addition to a softer EoS, be retraced to a delicate balance between the nucleonic and hyperonic hole state contributions to the self-energy of the baryons considered here (and thereby to features of the baryon-baryon interaction). Stated differently, the contributions from Σ^-, proton and neutron hole states to the Λ chemical potential are not attractive enough to lower the chemical potential of the Λ so that it equals that of the neutron. Furthermore, the increase of the chemical potential of the neutron with density is slowed down with the NSC97e YN interaction model since contributions from Σ^- hole states to the neutron self-energy are attractive. We note that the isospin-dependent component (Lane term) of the Σ^- single-particle potential for the new Nijmegen interactions (NSC97a-f) [St99] is strongly attractive, as opposed to what is found [Vi98, Da99b] for other interactions, including the old Nijmegen one (NSC89) [Ma89]. This in turn implies a strong attraction for $\Sigma^- n$ ($T = 3/2$) pairs, which is 10 times that obtained for the old Nijmegen potential at saturation density. These differences become more noticeable as density increases: while the $\Sigma^- n$ pairs become increasingly more attractive with the new Nijmegen potentials (see e.g. Fig. 2.14 in Chapter 2), they turn out to be strongly repulsive for the old one (see e.g. Figs. 1 and 2 in [Ba00]). This is why in Ref. [Ba00] the onset density for the appearance of Σ^- is larger than that for free hyperons, whereas the reverse situation is found here (compare the Σ^- onset point in Fig. 4.7 with what would be extracted from Fig. 4.8).

Within our many-body approach, no other hyperons appear at densities below $\rho = 1.2$ fm^{-3}. These results differ from present relativistic mean field calculations [Kn95, Sc96, Pr97], where all kinds of hyperons can appear at the densities considered here. Although the variational calculation of Akmal *et al.* [Ak98] may be viewed as the currently most realistic approach to the nucleonic EoS, our results have to be gauged with uncertainties in the hyperon-hyperon and hyperon-nucleon interactions. Especially, if the hyperon-hyperon interactions tend to be more attractive, this may lead to the formation of hyperons such as the Λ, Σ^0, Σ^+, Ξ^- and Ξ^0 at lower densities. The stiffness of the nucleonic contribution, together with the hyperon-nucleon and hyperon-hyperon interactions play crucial roles in the appearance of various hyperons beyond the onset point of Σ^-.

In order to examine the role of the hyperon-hyperon interaction on the composition of β-stable neutron star matter, we have included in the lower panel of Fig. 4.7 dashed lines that show the results of a calculation in which only the NN and YN interactions are taken into account. When the YY interactions are switched off, the scenario described above changes only quantitatively. The onset point of Σ^- does not change, because Σ^- is the first hyperon to appear and therefore the YY interaction plays no role for

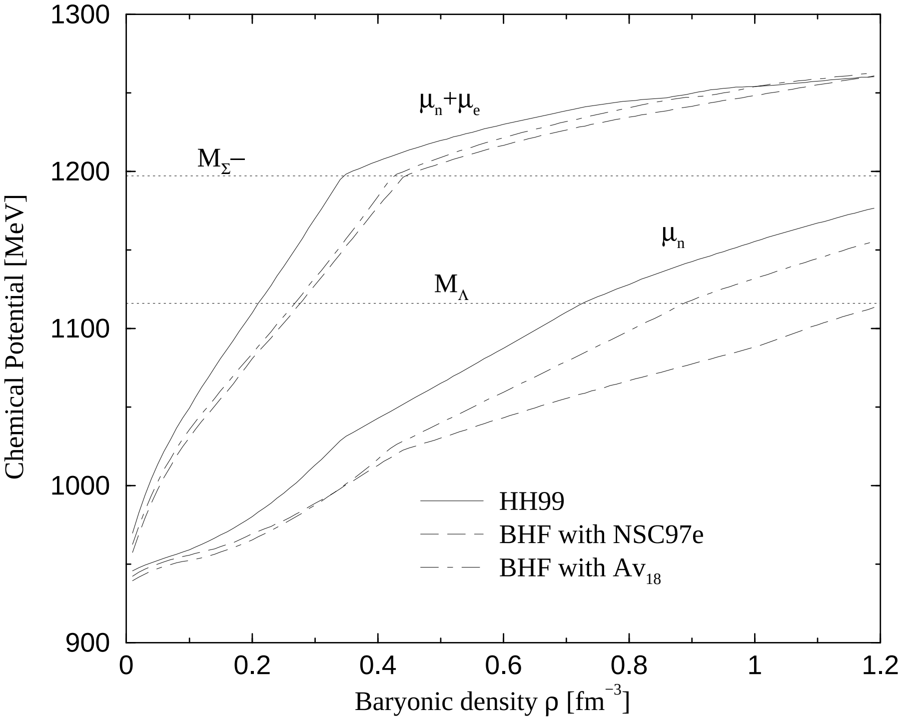

Figure 4.8: Chemical equilibrium condition for the appearance of Σ^- and Λ hyperons for the case of free hyperons and three different nucleon-nucleon interactions. Dotted straight lines denote the rest masses of the hyperons.

densities below this point. We note that the reduction of the Σ^- fraction, compared with the case which includes the YY interaction, is a consequence of neglecting the strongly attractive $\Sigma^-\Sigma^-$ interaction [St99], which allows the energy balance of the reaction $nn \leftrightarrow \Sigma^- p$ to be fulfilled with a smaller Σ^- Fermi sea. In turn, the reduction of the Σ^- fraction yields a moderate increase of the leptonic content in order to keep charge neutrality (in fact only muons disappear now). On the other hand, a smaller amount of Σ^-'s implies less $\Sigma^- n$ pairs. Recalling that the $\Sigma^- n$ interaction is attractive in this model (see e.g. Fig. 2.16 of Chapter 2), this means that the chemical potential of the neutrons becomes now less attractive. As a consequence, the Λ hyperons appear at a smaller density ($\rho = 0.65$ fm^{-3}) and have a larger relative fraction.

As has been mentioned, the composition of β-stable matter depends on the model used to describe the nucleonic sector. In order to study this dependence, Fig. 4.8 shows the chemical potential of the neutron μ_n and the sum $\mu_n + \mu_{e^-}$ for β-stable matter composed of nucleons and free hyperons for three different NN interaction models. The solid lines correspond to the parametrization HH99. The dashed and dot-dashed lines correspond to lowest-order Brueckner–Hartree–Fock calculations using, respectively, the NSC97e and the Argonne V_{18} potentials, the latter extracted from the results of Ref. [Ba00]. Dotted lines denote the Λ and Σ^- masses. In this case, the onset conditions for Λ and Σ^- are, respectively, $\mu_n = M_\Lambda$ and $\mu_n + \mu_{e^-} = M_{\Sigma^-}$. As can be seen from the figure, the onset points of both hyperons are different depending on the NN interaction model employed. With the parametrization HH99 both the Σ^- and Λ hyperons appear at lower densities than in the lowest-order Brueckner–Hartree–Fock models using the Argonne V_{18} or the NSC97e interactions. This is a consequence of the different stiffness of the EoS of each NN interaction model. In fact, the softest EoS corresponds to the NSC97e interaction which is not even able to produce Λ hyperons in the range of densities explored. Note that the hyperon onset points determined from Fig. 4.8 differ slightly from those observed in Fig. 4.7 as a consequence of the effect of the YN and YY interactions. Since the differences are not so large, one concludes that the main features of the composition of β-stable matter are dominated by the pure nucleonic contribution to the EoS.

In Fig. 4.9 we show the chemical potentials in β-stable neutron star matter for different baryons, solution of the set of equations (4.41). Results combining the parametrization HH99 and a BHF calculation for the strangeness sector are shown in the left panel, whereas in the right panel are given the ones corresponding to the pure Brueckner–Hartree–Fock calculation. We note that in both cases neither the Σ^0 nor the Σ^+ do

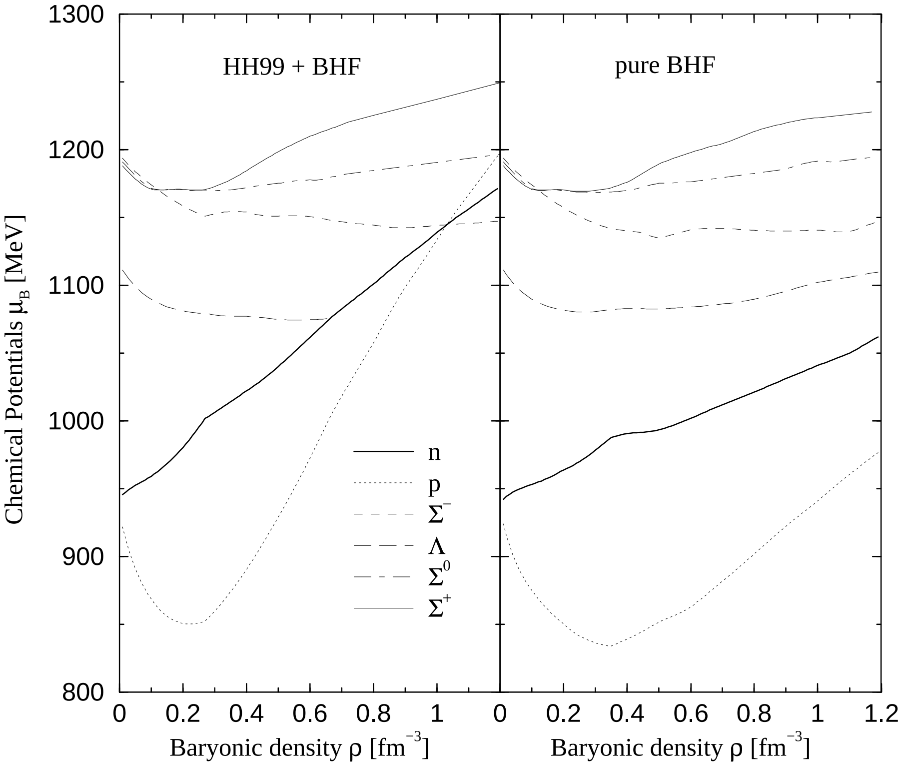

Figure 4.9: Chemical potentials in β-stable neutron star matter as functions of the total baryonic density ρ. Results for the HH99 + BHF are shown in the left panel, whereas in the right panel are given the results for the pure BHF calculation using the NSC97e model.

appear since, as seen from the figure, the respective stability criteria of Eq. (4.41) are not fulfilled. This is, partly, due to the fact that none of the Σ^0-baryon and the Σ^+-baryon self-energies are attractive enough. A similar argument applies to Ξ^0 and Ξ^-. In the latter case the mass of the particle is $\sim$ 1315 MeV and an attraction of around 200 MeV would be needed to fulfil the condition $\mu_{\Xi^0} = \mu_\Lambda = \mu_n$ at the highest density explored in this work. From the figure we see, however, that the Σ^0 hyperon could appear at densities close to 1.3 fm^{-3} in the HH99 + BHF calculation.

Fig. 4.10 shows the energy per baryon (left panel) and pressure (right panel) as a

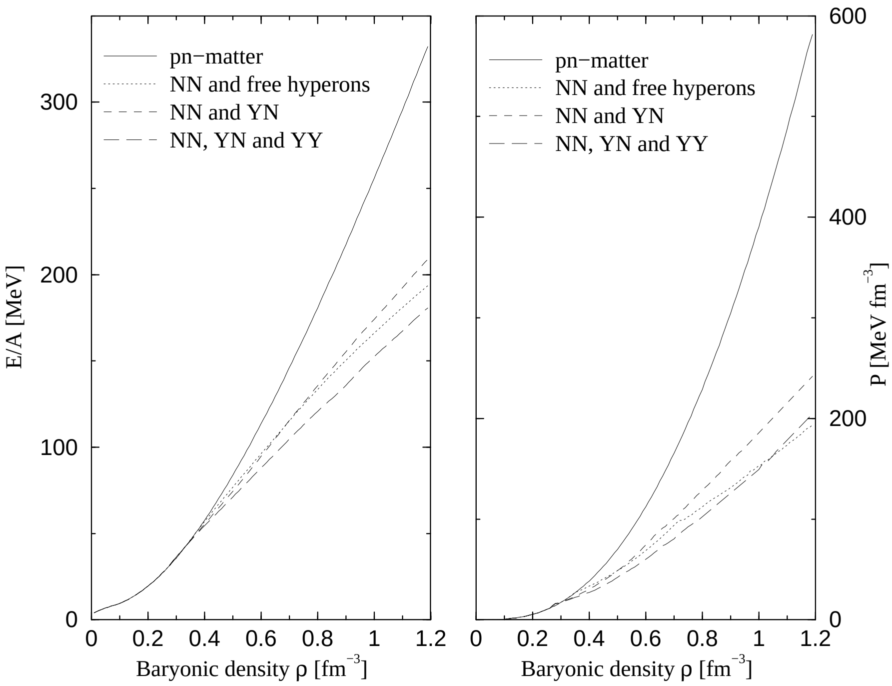

Figure 4.10: Energy per baryon (left panel) and pressure (right panel) in β-stable neutron star matter, obtained combining the HH99 parametrization for the nucleonic sector and a BHF (NSC97e) calculation for the hyperonic one, as function of the total baryonic density ρ, for four scenarios: pure nucleonic matter (solid lines); matter with nucleons and non-interacting hyperons (dotted line); matter with nucleons and hyperons interacting only with nucleons (dashed line); and matter with nucleons and hyperons interacting both with nucleons and hyperons (long-dashed line). The leptonic contribution to the energy per baryon and pressure is included in all cases.

function of the baryonic density obtained from the HH99 + BHF calculation for four different scenarios: pure nucleonic matter (solid line); matter with nucleons and free hyperons (dotted line); matter with nucleons and hyperons interacting only with nucleons (dashed line) and, finally, matter with nucleons and hyperons interacting both with nucleons and hyperons (long-dashed line). Each curve corresponds to a different composition of β-stable neutron star matter, obtained by solving the equilibrium conditions of Eq. (4.41), with the appropriate chemical potentials for each of the four

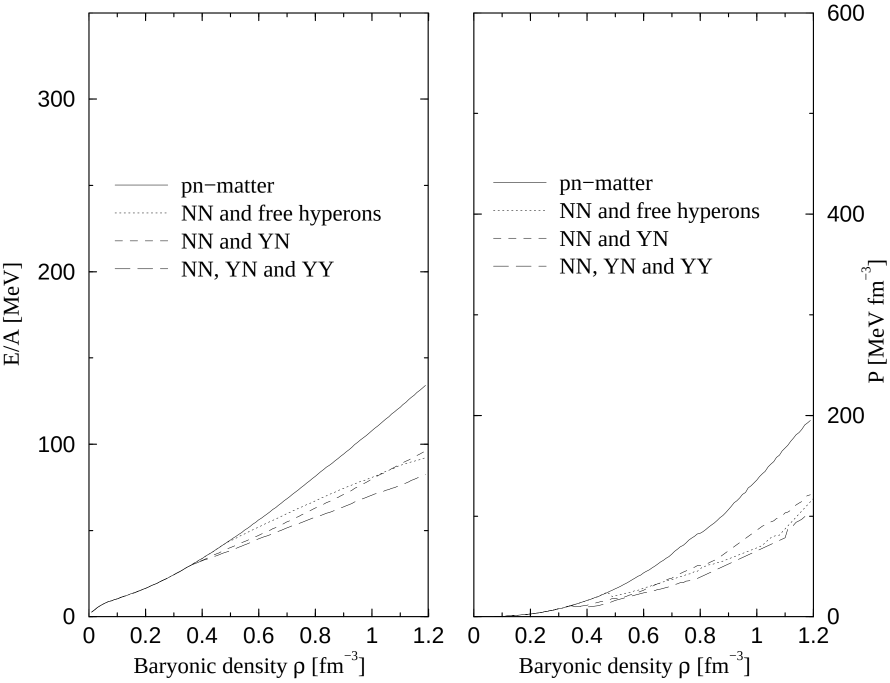

Figure 4.11: As in Fig. 4.10 obtained from a pure Brueckner–Hartree–Fock calculation in all sectors.

cases. The leptonic contribution is also included in all the cases. As can be seen comparing the solid and dotted lines (see both panels) the appearance of hyperons leads to a considerable softening of the EoS (energy and pressure). This softening is essentially due to a decrease of the kinetic energy because the hyperons can be accommodated in lower momentum states and in addition have a large bare mass. The hyperon-nucleon interaction (dashed line) has two effects (see left panel). On the one hand, for densities up to $\rho \sim 0.72$ fm^{-3}, the YN interaction reduces the total energy per baryon, therefore making the EoS even softer. On the other hand, for densities higher than $\rho = 0.72$ fm^{-3}, it becomes repulsive and the EoS becomes slightly stiffer than that for non-interacting hyperons. The contribution from the hyperon-hyperon interaction (long-dashed line) is always attractive, producing a softening of the EoS over the whole range of densities explored.

In a similar way, we show in Fig. 4.11, for the same four scenarios discussed above, the corresponding energy per baryon (left panel) and pressure (right panel) obtained from a pure BHF calculation using the NSC97e interaction model. The pattern observed is exactly the same. The presence of hyperons in matter makes the EoS softer and the role of the YN and YY interactions is the one just described above. The only difference, coming from the treatment of the pure nucleonic part, is that the EoS obtained from the pure BHF calculation is softer than the one obtained with the HH99 + BHF one because it does not include the effect of three body forces.

4.6 Implications on neutron star structure

We end this chapter with a discussion on neutron star properties obtained with the Equations of State described in the previous section. We restrict our results in this section to the parametrization HH99 for the nucleon-nucleon part supplemented with the Brueckner–Hartree–Fock calculation using the NSC97e interaction for the hyperonic sector.

In order to obtain the radius and mass of a neutron star, we have solved the Tolman-Oppenheimer-Volkov (TOV) equations (4.2) and (4.3) with and without rotational corrections. The latter corrections imply an increase of mass to balance the rotational energy. Accounting for rotations leads to corrections to the TOV equation and the total mass that include also deformations from spherical symmetry. Assuming that such contributions from deformations are negligible for a slowly rotating star, one arrives at the modified equations for the pressure and the mass shown in the work of

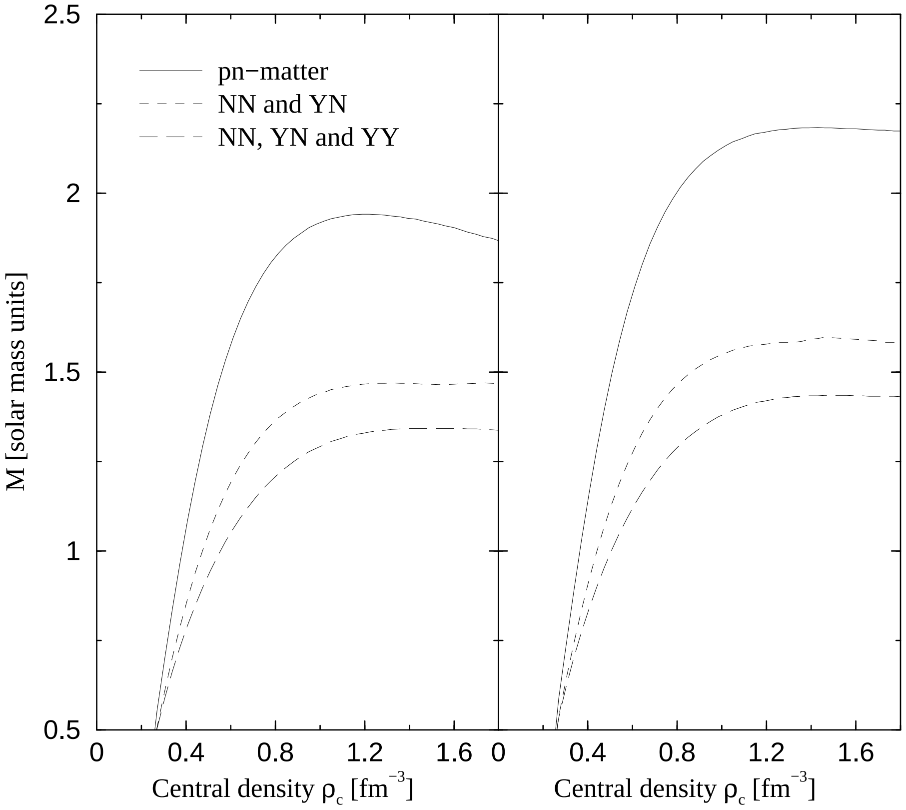

Figure 4.12: Total mass M for various Equations of State with (right panel) and without (left panel) rotational corrections as function of the central density. The solid line corresponds to the case of β-stable matter with nucleonic degrees of freedom only, the short-dashed line includes also the effects of the hyperon-nucleon interaction, while the long-dashed line includes the three types of baryon-baryon interactions.

Hartle [Ha67].

Following the discussion of Figs. 4.8, 4.9 and 4.10, we present results for three different scenarios. The first one only takes into account nucleonic and leptonic degrees of freedom. In the second one, in addition we allow for the presence of hyperons and consider the hyperon-nucleon interaction, but explicitly exclude the hyperon-hyperon one, as done in e.g., Ref. [Ba00]. Finally, the third one includes both the hyperon-nucleon and the hyperon-hyperon interactions.

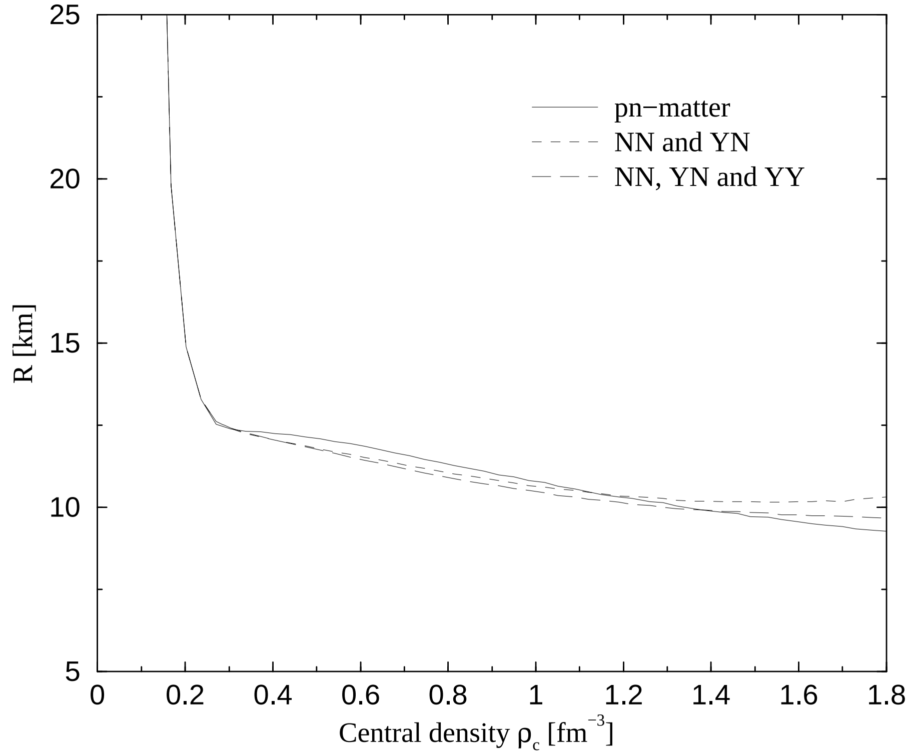

Figure 4.13: Radius as function of the central density. Notations as in Fig. 4.12.

In Fig. 4.12 we show the resulting mass, as function of the central density, for these three scenarios with (right panel) and without (left panel) rotational corrections. The resulting radius of the star for the same scenarios is plotted in Fig. 4.13. The corresponding mass-radius relations with (right panel) and without (left panel) rotational corrections, constructed from Figs. 4.12 and 4.13, are shown in Fig. 4.14.

The EoS for the pure nucleonic scenario is rather stiff compared with the EoS obtained when hyperons are allowed to be present, as we have seen in Fig. 4.10. This produces, as can be seen in Figs. 4.12 and 4.14 (solid lines), the larger maximum mass with a value of $M = 1.89 M_\odot$ without rotational corrections and $M = 2.11 M_\odot$, when rotational corrections are included.

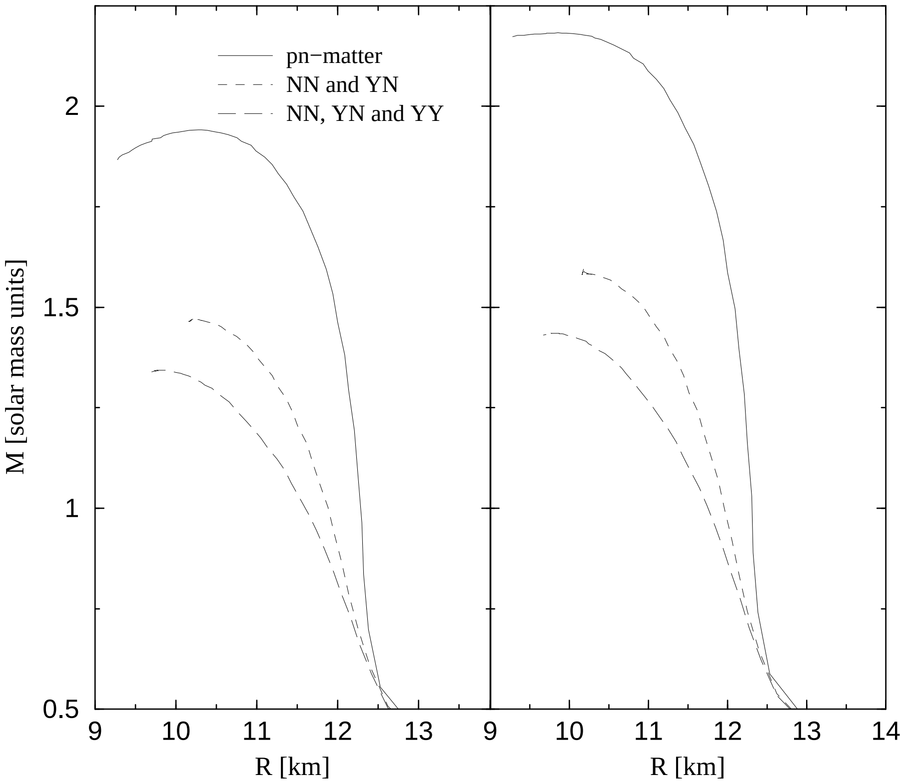

Figure 4.14: Mass-radius relation with (right panel) and without (left panel) rotational corrections. Notations as in Fig. 4.12.

The corresponding results for the second scenario are shown by the short-dashed lines in Figs. 4.12, 4.13 and 4.14. Without rotational corrections we obtain a maximum mass $M = 1.47M_\odot$ whereas the rotational correction increases the mass to $M = 1.60M_\odot$. Thus, the inclusion of the YN interaction with the corresponding formation of Σ^-- and Λ-hyperons leads to a reduction of the mass by $\sim (0.4 - 0.5)M_\odot$. This large reduction is mainly a consequence of the strong softening of the EoS due to the appearance of hyperons.

The last scenario combines the nucleonic part with the computed hyperon contribution including both the hyperon-nucleon and the hyperon-hyperon interactions. These

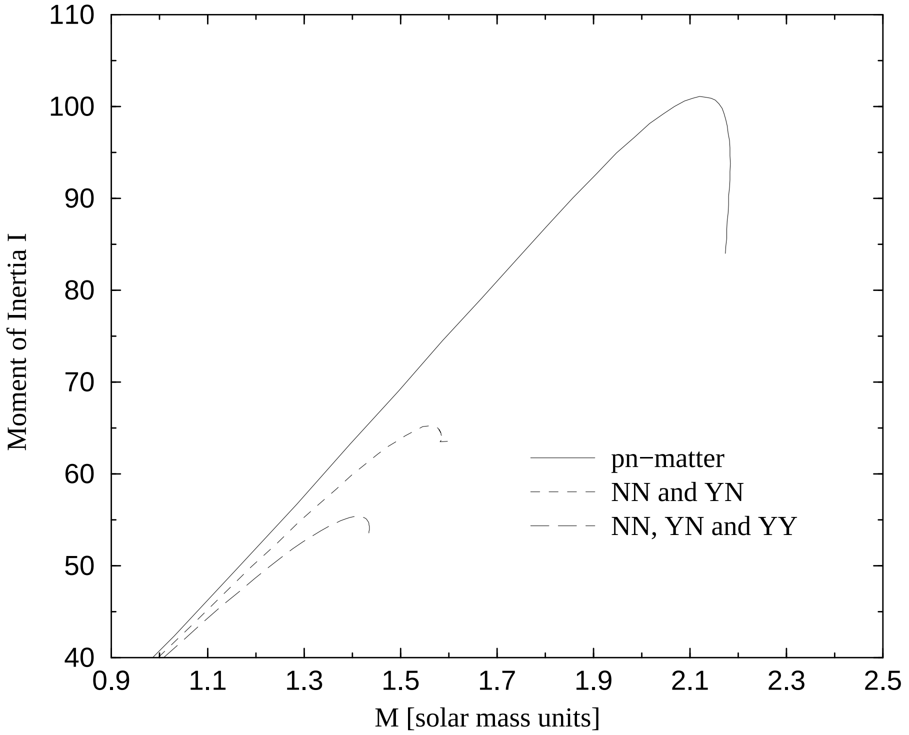

Figure 4.15: Moment of Inertia I in units of $M_{\odot}\mathrm{km}^2$ as function of the mass (including rotational corrections) of the star. Notations as in Fig. 4.12.

results are shown by the long-dashed lines in Figs. 4.12, 4.13 and 4.14. The inclusion of the hyperon-hyperon interaction leads to a further softening of the EoS in Fig. 4.10, and, as can be seen from Fig. 4.12, this leads to an additional reduction of the total mass. Without rotational corrections we obtain a maximum mass $M \sim 1.34 M_{\odot}$, while the rotational correction increases the mass to $M \sim 1.44 M_{\odot}$. The size of the reduction due to the presence of hyperons including the YY interaction goes up to $\Delta M \sim (0.6 - 0.7) M_{\odot}$, and the obtained neutron star masses are comparable to those reported by Balberg *et al.* [Ba99].

For completeness we show in Fig. 4.15 the moment of inertia as function of the stellar mass (calculated with rotational corrections) for the three scenarios considered.

Scenario	Maximum Mass		Radius	I_{max}
	No Rot. Correc.	With Rot. Correc.		
NN	1.89	2.11	10.3	101.1
NN YN	1.47	1.60	10.2	65.2
NN YN YY	1.34	1.44	10.0	55.4

Table 4.1: Maximum mass, radius and maximum moment of inertia for three scenarios considered: only nucleonic degrees of freedom (NN), nucleons and hyperons including only nucleon-nucleon and hyperon-nucleon interactions (NN,YN), and nucleons and hyperons including all the interactions among them (NN, YN, YY). Units of mass, radius and moment of inertia in $M_\odot$, km and $M_\odot \text{km}^2$, respectively.

The moment of inertia increases with the mass of the star almost linearly indicating a small variation in the radius compatible with the results shown in Fig. 4.13. It reaches its maximum value at the maximum value of the mass. Results for the maximum mass, radius and maximum moment of inertia for the three scenarios are summarized in Table 4.1. There are other features as well to be noted from Figs. 4.12 and 4.14. The EoS with hyperons reaches a maximum mass at a central density $\rho_c \sim (1.3 - 1.4)$ fm^{-3}. In Fig. 4.7 we showed that the only hyperons which can appear at these densities are Λ and Σ^-. If other hyperons were to appear at higher densities, this would most likely lead to a further softening of the EoS, and thereby smaller neutron star masses.

The reader should however note that our calculation of hyperon degrees of freedom is based on a non-relativistic Brueckner–Hartree–Fock approach. Although the parametrization HH99 of the nucleonic part, including three-body forces is considered as a benchmark calculation for nucleonic degrees of freedom, relativistic effects in the hyperonic calculation could result in a stiffer EoS and thereby larger mass. Nevertheless, relativistic mean field calculations with parameters which lead to a similar composition of matter as shown in Fig. 4.7, result in masses close to those reported in

Fig. 4.12. In this sense, our results with and without hyperons may provide a lower and upper bound for the maximum mass. This leaves two natural options when compared to the observed neutron star masses. If the heavy neutron star masses determined from high frequency oscillations prove erroneous by more detailed observations and only masses like those of binary pulsars are found, this may indicate that heavier neutron stars simply are not stable, which in turn implies a soft EoS, or that a significant phase transition must occur already at a few times nuclear saturation densities. Our EoS with hyperons would fit into this case, although the mass without rotational corrections is on the lower side. Else, if the large masses from QPO's are confirmed, then the EoS for baryonic matter needs to be stiffer. This would then pose a severe problem to present hadronic models since, when the nucleonic part of the EoS is sufficiently stiff to support large masses, one cannot avoid the appearance of hyperons which, in turn, produce a softening of the EoS.

Although we have only considered the formation of hyperons in neutron stars, transitions to other degrees of freedom such as quark matter, kaon condensation and pion condensation may or may not take place in neutron star matter. We would however like to emphasize that the hyperon formation mechanism is perhaps the most robust one and is likely to occur in the interior of a neutron star, unless the hyperon self-energies are strongly repulsive due to repulsive hyperon-nucleon and hyperon-hyperon interactions, a repulsion which would contradict present data on hypernuclei [Ba90]. The EoS with hyperons yields however neutron star masses without rotational corrections which are even below $1.4M_{\odot}$. This means that our EoS with hyperons needs to be stiffer, a fact which may in turn imply that more complicated many-body terms not included in our calculations, such as three-body forces between nucleons and hyperons and/or relativistic effects, are needed.

Conclusions

"A conclusion is the place where one arrives tired of thinking".

Anonymous

The purpose of this thesis has been to study, within the framework of Brueckner–Hartree–Fock theory, properties of finite (hypernuclei) and infinite (hyperonic matter) nuclear many-body systems with hyperonic degrees of freedom, and to investigate, in the latter case, the implications which the presence of strangeness has in neutron star properties. The starting point of our Brueckner-type calculations has been the Jülich B [Ho89] and the Nijmegen Soft-Core 89 (NSC89) [Ma89] hyperon-nucleon potentials, together with the most recent parametrization of the bare baryon-baryon interaction for the complete octet of baryons constructed by Stoks and Rijken (NSC97a-f) [Ri99, St99]. These three interaction models are meson-exchange potentials. The basic ideas of the meson-exchange model and a revision of the so-called nuclear many-body problem were briefly given in Chapter 1.

In Chapter 2 we have developed the formalism for microscopic Brueckner-type calculations of dense nuclear matter with strangeness, allowing for any concentration of the different baryon species. The main conclusions of this chapter can be summarized as follows

- We have obtained, in isospin unsaturated situations, the M_T dependence of the G-matrix for any two species by relating the Pauli operator to those of the different pairs of physical particles contributing to the particular (T, M_T) channel. We have seen, however, that the M_T dependence is weak enough to allow a simpler strategy consisting of obtaining the effective interactions in isospin saturated situations ($k_{F_n} = k_{F_p}$, $k_{F_{\Sigma^-}} = k_{F_{\Sigma^0}} = k_{F_{\Sigma^+}}$, $k_{F_{\Xi^-}} = k_{F_{\Xi^0}}$). The various single–particle potentials can then be obtained by folding the approximate effective interactions with the Fermi seas of the different species.
- We have studied the dependence of the single–particle potentials on the nucleon and hyperon asymmetries, focusing on situations relevant in studies of β-stable neutron star matter with strangeness content. We have found that the presence of hyperons, especially Σ^-, modifies substantially the single–particle potentials of the nucleons. The neutrons feel an increased attraction due to the $\Sigma^- n$ effective interaction that only happens through the very attractive $T = 3/2$ ΣN channel, while the protons feel a repulsion as the $\Sigma^- p$ pairs also receive contributions from the very repulsive $T = 1/2$ ΣN one.
- By decomposing the Λ and Σ^- single–particle potentials in the contributions from the various species, we have seen the relevance of considering the YY interaction. For the particular situation of total baryonic density $\rho = 0.6$ fm^{-3} containing a 10% fraction of hyperons split into Σ^- and Λ in a proportion 2 : 1 and a fraction

of protons $x_p = 0.25 x_N$, we have found that the hyperonic contribution to the Λ single–particle potential at zero momentum is of the order of 1/3 of the total $U_\Lambda(0)$, and that for the Σ^- is of the order of 1/2 of the total $U_{\Sigma^-}(0)$.

In Chapter 3 we have analyzed a method to obtain the effective hyperon-nucleon interaction in finite nuclei based on an expansion over a G-matrix calculated in nuclear matter at fixed density and starting energy. The purpose of this study has been to set up a reliable frame for hypernuclear structure calculations with the aim of obtaining information about the hyperon-nucleon interaction, complementary to that provided by hyperon-nucleon scattering experiments. The corresponding conclusions of this chapter are the following

- The truncation of the expansion over the nuclear matter G-matrix at second order gives results that are very stable against variations of the density and starting energy used in the G-matrix, as well as to the choice (discontinuous or continuous) adopted in the solution of the Bethe–Goldstone equation.
- Both first and second order terms depend quite strongly on the density and starting energy used in the nuclear matter G-matrix. This is an indication that the density dependent effects considered when treating explicitly the finite size of the nucleus are very important. These effects could be simulated by simpler first-order calculations at an appropriate average density or by a local density approximation. However, if the aim is to fine-tune the bare YN interactions to reproduce the spectroscopic data of hypernuclei, a direct calculation of the effective interaction in the finite hypernucleus, as the one proposed in this thesis, is in order.

- Although the method can be viewed as an alternative way of building up a finite nucleus effective interaction, it provides also the complete energy dependence of the hyperon self–energy. This allows in turn for a study of not only the bound states, as done in this thesis, but also the scattering states. This is especially of interest in the analysis of hypernuclear production reactions which yield a large amount of quasifree hyperons.

- Our results compare quite well with the experimental data, and the small spin-orbit splitting is confirmed microscopically from our calculation.

- We have obtained local Woods-Saxon Λ-nucleus potentials with A-independent depths that reproduce the Λ single-particle energies of several hypernuclei. However, the wave functions obtained from our microscopic non-local self–energy are more extended and can only be simulated when we allow the phenomenological Woods-Saxon potential to have an A-dependent depth and a relatively larger radius. This could have implications in hypernuclear observables sensitive to densities nuclear surface, such as the mesonic weak decay of hypernuclei.

Finally, as an extension of our study of Chapter 2, in Chapter 4 we have performed a microscopic many-body calculation of the structure of β-stable neutron star matter including nucleonic and hyperonic degrees of freedom. We conclude that

- The potential model employed (NSC97e) allows for the presence in the composition of β-stable neutron star matter of only two types of hyperons, the Σ^- and the Λ which appear at $\rho = 0.27$ fm^{-3} and $\rho = 0.67$ fm^{-3}, respectively, up to densities of about seven times nuclear matter saturation density. The interactions for strangeness $S = -2, -3$ and -4 are not attractive enough to allow the formation of other hyperons.

- We have observed that the presence of hyperons produces a softening in the Equation of State. This softening will influence the behaviour of dense matter and the structure of neutron stars.

- Our novel result is that a further softening of the EoS is obtained when including the effect of the YY interaction since it is attractive over the whole density range explored. Whether this additional softening is realistic or not will depend on the details of the YY interaction that is, unfortunately, not well constrained at present. New data in the $S = -2$ sector, from (K^-, K^+) reaction, double–Λ hypernuclei or Ξ^-–atoms, are very much awaited for.

- The softening of the EoS when all the interactions are taken into account translates into a reduction of the maximum mass of the star from $2.11M_\odot$, when only nucleonic degrees of freedom are considered, to $1.44M_\odot$, when hyperons are included.

"Tha, Tha ... That's all folks".

Porky Pig

Appendix A: Pauli operator in the different strangeness channels

In this appendix we show how the Pauli operator $\overline{Q}_{B\widetilde{B}}$, which prevents scattering into occupied $B\widetilde{B}$ intermediate states, acquires a dependence on the third component of isospin due to the different Fermi momenta of the baryons B and $\widetilde{B}$.

Taking the following convention for the isospin states representing the particle basis

$$|n\rangle = |1/2, -1/2\rangle \,;\; |p\rangle = |1/2, +1/2\rangle \tag{A.1}$$

$$|\Lambda\rangle = |0, 0\rangle \tag{A.2}$$

$$\left|\Sigma^-\right\rangle = |1, -1\rangle \,; \quad \left|\Sigma^0\right\rangle = |1, 0\rangle \,; \quad \left|\Sigma^+\right\rangle = -\,|1, +1\rangle \tag{A.3}$$

$$\left|\Xi^-\right\rangle = -\,|1/2, -1/2\rangle \,; \quad \left|\Xi^0\right\rangle = |1/2, +1/2\rangle \tag{A.4}$$

it is easy to obtain the Pauli operator in the coupled-isospin basis, $\overline{Q}_{B\tilde{B}}(K,k;T,M_T)$, for each strangeness sector. Note that in the following expressions we have only retained the dependence on the isospin labels.

A.1. Strangeness 0

$$\overline{Q}_{NN}(T=0,M_T=0)=\frac{1}{2}\left(\overline{Q}_{pn}+\overline{Q}_{np}\right) \tag{A.5}$$

$$\overline{Q}_{NN}(T=1,M_T=-1)=\overline{Q}_{nn} \tag{A.6}$$

$$\overline{Q}_{NN}(T=1,M_T=0)=\frac{1}{2}\left(\overline{Q}_{pn}+\overline{Q}_{np}\right) \tag{A.7}$$

$$\overline{Q}_{NN}(T=1,M_T=+1)=\overline{Q}_{pp} \tag{A.8}$$

A.2. Strangeness -1

$$\overline{Q}_{\Lambda N}\left(T=\frac{1}{2},M_T=-\frac{1}{2}\right)=\overline{Q}_{\Lambda n} \tag{A.9}$$

$$\overline{Q}_{\Lambda N}\left(T=\frac{1}{2},M_T=+\frac{1}{2}\right)=\overline{Q}_{\Lambda p} \tag{A.10}$$

$$\overline{Q}_{\Sigma N}\left(T=\frac{1}{2},M_T=-\frac{1}{2}\right)=\frac{1}{3}\overline{Q}_{\Sigma^0 n}+\frac{2}{3}\overline{Q}_{\Sigma^- p} \tag{A.11}$$

$$\overline{Q}_{\Sigma N}\left(T=\frac{1}{2},M_T=+\frac{1}{2}\right)=\frac{2}{3}\overline{Q}_{\Sigma^+ n}+\frac{1}{3}\overline{Q}_{\Sigma^0 p} \tag{A.12}$$

$$\overline{Q}_{\Sigma N}\left(T=\frac{3}{2},M_T=-\frac{3}{2}\right)=\overline{Q}_{\Sigma^- n} \tag{A.13}$$

$$\overline{Q}_{\Sigma N}\left(T=\frac{3}{2},M_T=-\frac{1}{2}\right)=\frac{2}{3}\overline{Q}_{\Sigma^0 n}+\frac{1}{3}\overline{Q}_{\Sigma^- p} \tag{A.14}$$

$$\overline{Q}_{\Sigma N}\left(T=\frac{3}{2}, M_T=+\frac{1}{2}\right)=\frac{1}{3}\overline{Q}_{\Sigma^+ n}+\frac{2}{3}\overline{Q}_{\Sigma^0 p} \tag{A.15}$$

$$\overline{Q}_{\Sigma N}\left(T=\frac{3}{2}, M_T=+\frac{3}{2}\right)=\overline{Q}_{\Sigma^+ p} \tag{A.16}$$

A.3. Strangeness −2

$$\overline{Q}_{\Lambda\Lambda}(T=0, M_T=0)=\overline{Q}_{\Lambda\Lambda} \tag{A.17}$$

$$\overline{Q}_{\Xi N}(T=0, M_T=0)=\frac{1}{2}\left(\overline{Q}_{\Xi^- p}+\overline{Q}_{\Xi^0 n}\right) \tag{A.18}$$

$$\overline{Q}_{\Sigma\Sigma}(T=0, M_T=0)=\frac{1}{3}\left(\overline{Q}_{\Sigma^+\Sigma^-}+\overline{Q}_{\Sigma^0\Sigma^0}+\overline{Q}_{\Sigma^-\Sigma^+}\right) \tag{A.19}$$

$$\overline{Q}_{\Xi N}(T=1, M_T=-1)=\overline{Q}_{\Xi^- n} \tag{A.20}$$

$$\overline{Q}_{\Xi N}(T=1, M_T=0)=\frac{1}{2}\left(\overline{Q}_{\Xi^- p}+\overline{Q}_{\Xi^0 n}\right) \tag{A.21}$$

$$\overline{Q}_{\Xi N}(T=1, M_T=+1)=\overline{Q}_{\Xi^0 p} \tag{A.22}$$

$$\overline{Q}_{\Lambda\Sigma}(T=1, M_T=-1)=\overline{Q}_{\Lambda\Sigma^-} \tag{A.23}$$

$$\overline{Q}_{\Lambda\Sigma}(T=1, M_T=0)=\overline{Q}_{\Lambda\Sigma^0} \tag{A.24}$$

$$\overline{Q}_{\Lambda\Sigma}(T=1, M_T=+1)=\overline{Q}_{\Lambda\Sigma^+} \tag{A.25}$$

$$\overline{Q}_{\Sigma\Sigma}(T=1, M_T=-1)=\frac{1}{2}\left(\overline{Q}_{\Sigma^0\Sigma^-}+\overline{Q}_{\Sigma^-\Sigma^0}\right) \tag{A.26}$$

$$\overline{Q}_{\Sigma\Sigma}(T=1, M_T=0)=\frac{1}{2}\left(\overline{Q}_{\Sigma^+\Sigma^-}+\overline{Q}_{\Sigma^-\Sigma^+}\right) \tag{A.27}$$

$$\overline{Q}_{\Sigma\Sigma}(T=1, M_T=+1)=\frac{1}{2}\left(\overline{Q}_{\Sigma^0\Sigma^+}+\overline{Q}_{\Sigma^+\Sigma^0}\right) \tag{A.28}$$

$$\overline{Q}_{\Sigma\Sigma}(T=2, M_T=-2)=\overline{Q}_{\Sigma^-\Sigma^-} \tag{A.29}$$

$$\overline{Q}_{\Sigma\Sigma}(T=2, M_T=-1) = \frac{1}{2}\left(\overline{Q}_{\Sigma^0\Sigma^-} + \overline{Q}_{\Sigma^-\Sigma^0}\right) \tag{A.30}$$

$$\overline{Q}_{\Sigma\Sigma}(T=2, M_T=0) = \frac{1}{6}\overline{Q}_{\Sigma^+\Sigma^-} + \frac{2}{3}\overline{Q}_{\Sigma^0\Sigma^0} + \frac{1}{6}\overline{Q}_{\Sigma^-\Sigma^+} \tag{A.31}$$

$$\overline{Q}_{\Sigma\Sigma}(T=2, M_T=+1) = \frac{1}{2}\left(\overline{Q}_{\Sigma^0\Sigma^+} + \overline{Q}_{\Sigma^+\Sigma^0}\right) \tag{A.32}$$

$$\overline{Q}_{\Sigma\Sigma}(T=2, M_T=+2) = \overline{Q}_{\Sigma^+\Sigma^+} \tag{A.33}$$

A.4. Strangeness -3

$$\overline{Q}_{\Lambda\Xi}\left(T=\frac{1}{2}, M_T=-\frac{1}{2}\right) = \overline{Q}_{\Lambda\Xi^-} \tag{A.34}$$

$$\overline{Q}_{\Lambda\Xi}\left(T=\frac{1}{2}, M_T=+\frac{1}{2}\right) = \overline{Q}_{\Lambda\Xi^0} \tag{A.35}$$

$$\overline{Q}_{\Sigma\Xi}\left(T=\frac{1}{2}, M_T=-\frac{1}{2}\right) = \frac{1}{3}\overline{Q}_{\Sigma^0\Xi^-} + \frac{2}{3}\overline{Q}_{\Sigma^-\Xi^0} \tag{A.36}$$

$$\overline{Q}_{\Sigma\Xi}\left(T=\frac{1}{2}, M_T=+\frac{1}{2}\right) = \frac{2}{3}\overline{Q}_{\Sigma^+\Xi^-} + \frac{1}{3}\overline{Q}_{\Sigma^0\Xi^0} \tag{A.37}$$

$$\overline{Q}_{\Sigma\Xi}\left(T=\frac{3}{2}, M_T=-\frac{3}{2}\right) = \overline{Q}_{\Sigma^-\Xi^-} \tag{A.38}$$

$$\overline{Q}_{\Sigma\Xi}\left(T=\frac{3}{2}, M_T=-\frac{1}{2}\right) = \frac{2}{3}\overline{Q}_{\Sigma^0\Xi^-} + \frac{1}{3}\overline{Q}_{\Sigma^-\Xi^0} \tag{A.39}$$

$$\overline{Q}_{\Sigma\Xi}\left(T=\frac{3}{2}, M_T=+\frac{1}{2}\right) = \frac{1}{3}\overline{Q}_{\Sigma^+\Xi^-} + \frac{2}{3}\overline{Q}_{\Sigma^0\Xi^0} \tag{A.40}$$

$$\overline{Q}_{\Sigma\Xi}\left(T=\frac{3}{2}, M_T=+\frac{3}{2}\right) = \overline{Q}_{\Sigma^+\Xi^0} \tag{A.41}$$

A.5. Strangeness -4

$$\overline{Q}_{\Xi\Xi}(T=0, M_T=0) = \frac{1}{2}\left(\overline{Q}_{\Xi^0\Xi^-} + \overline{Q}_{\Xi^-\Xi^0}\right) \tag{A.42}$$

$$\overline{Q}_{\Xi\Xi}(T=1, M_T=-1) = \overline{Q}_{\Xi^-\Xi^-} \tag{A.43}$$

$$\overline{Q}_{\Xi\Xi}(T=1, M_T=0) = \frac{1}{2}\left(\overline{Q}_{\Xi^0\Xi^-} + \overline{Q}_{\Xi^-\Xi^0}\right) \tag{A.44}$$

$$\overline{Q}_{\Xi\Xi}(T=1, M_T=+1) = \overline{Q}_{\Xi^0\Xi^0} \tag{A.45}$$

From the above expressions it is easy to see that in isospin saturated matter matter (i.e., $k_{F_n} = k_{F_p}$, $k_{F_{\Sigma^+}} = k_{F_{\Sigma^0}} = k_{F_{\Sigma^-}}$ and $k_{F_{\Xi^0}} = k_{F_{\Xi^-}}$) the dependence on the third component of isospin disappears.

Appendix B: Angular average of the C.M. and hole momenta

In this appendix we show how to compute an appropriate angular average of the centre–of–mass momentum of the pair B_1B_2 and the hole momentum $\vec{k}_{B_2}$ which enters in the determination of the starting energy in Eq. (2.2). The centre–of–mass momentum $\vec{K}$ and the relative momentum $\vec{k}$ of the pair B_1B_2 are defined in the following way:

$$\vec{K} = \vec{k}_{B_1} + \vec{k}_{B_2} \ , \tag{B.1}$$

$$\vec{k} = \frac{M_{B_2}\vec{k}_{B_1} - M_{B_1}\vec{k}_{B_2}}{M_{B_1} + M_{B_2}} = \beta\vec{k}_{B_1} - \alpha\vec{k}_{B_2} \ . \tag{B.2}$$

From the above expressions it is easy to write $\vec{K}$ and $\vec{k}_{B_2}$ in terms of the external momentum $\vec{k}_{B_1}$ and the relative momentum $\vec{k}$, which is used as integration variable in

Eq. (2.2)

$$\vec{K} = \frac{1}{\alpha}(\vec{k}_{B_1} - \vec{k}) \ , \tag{B.3}$$

$$\vec{k}_{B_2} = \frac{1}{\alpha}(\beta\vec{k}_{B_1} - \vec{k}) \ . \tag{B.4}$$

The angle average of the centre–of–mass momentum is defined as

$$\overline{K^2}(k_{B_1}, k) \ = \ \frac{\displaystyle\int d(\cos\theta) K^2(k_{B_1}, k, \cos\theta)}{\displaystyle\int d(\cos\theta)}, \tag{B.5}$$

where $K^2(k_{B_1}, k, \cos\theta) = \frac{1}{\alpha^2}(k_{B_1}^2 + k^2 - 2k_{B_1}k\cos\theta)$, with θ being the angle between $\vec{k}_{B_1}$ and $\vec{k}$. The integration runs over all the angles for which $|\vec{k}_{B_2}| < k_{F_{B_2}}$. Similarly, for the hole momentum we have

$$\overline{k_{B_2}^2}(k_{B_1}, k) \ = \ \frac{\displaystyle\int d(\cos\theta) k_{B_2}^2(k_{B_1}, k, \cos\theta)}{\displaystyle\int d(\cos\theta)}, \tag{B.6}$$

where $k_{B_2}^2(k_{B_1}, k, \cos\theta) = \frac{1}{\alpha^2}(\beta^2 k_{B_1}^2 + k^2 - 2\beta k_{B_1}k\cos\theta)$.

We can distinguish two cases in performing the angular integrals, $\beta k_{B_1} < \alpha k_{F_{B_2}}$ and $\beta k_{B_1} > \alpha k_{F_{B_2}}$. In the first case, we have two possibilities: $0 < k < \alpha k_{F_{B_2}} - \beta k_{B_1}$, for which all angle values are allowed, giving the result

$$\overline{K^2}(k_{B_1}, k) = \frac{1}{\alpha^2}\left[k_{B_1}^2 + k^2\right] \ , \tag{B.7}$$

$$\overline{k_{B_2}^2}(k_{B_1}, k) = \frac{1}{\alpha^2}\left[\beta^2 k_{B_1}^2 + k^2\right] \ , \tag{B.8}$$

and $\alpha k_{F_{B_2}} - \beta k_{B_1} < k < \alpha k_{F_{B_2}} + \beta k_{B_1}$, which have the following upper limit in the value of $\cos\theta$

$$(\cos\theta)_{\rm max} = \frac{k^2 + (\beta k_{B_1})^2 - (\alpha k_{F_{B_2}})^2}{2\beta k k_{B_1}} \ , \tag{B.9}$$

giving the result

$$\overline{K^2}(k_{B_1},k) = \frac{1}{\alpha^2}\left[k_{B_1}^2 + k^2 - \frac{1}{2\beta}\Big((\beta k_{B_1}+k)^2 - (\alpha k_{F_{B_2}})^2\Big)\right] \ , \tag{B.10}$$

$$\overline{k_{B_2}^2}(k_{B_1},k) = \frac{1}{\alpha^2}\left[\beta^2 k_{B_1}^2 + k^2 - \frac{1}{2}\Big((\beta k_{B_1}+k)^2 - (\alpha k_{F_{B_2}})^2\Big)\right] \ . \tag{B.11}$$

In the second case, there is only one possibility: $\beta k_{B_1} - \alpha k_{F_{B_2}} < k < \alpha k_{F_{B_2}} + \beta k_{B_1}$ and the result is the same as in the previous case for the zone $\alpha k_{F_{B_2}} - \beta k_{B_1} < k < \alpha k_{F_{B_2}} + \beta k_{B_1}$. The result for the values $0 < k < \beta k_{B_1} - \alpha k_{F_{B_2}}$ is zero because $\vec{k}_{B_2}$ is always larger than its Fermi sea.

This kind of average defines an angle–independent centre–of–mass momentum and a hole momentum (and therefore a starting energy) for each pair k_{B_1}, k so the angular integration in Eq. (2.2) can be performed analytically. Nevertheless, we still require to solve the G–matrix equation for each pair of values k_{B_1} and k, making the calculation much time consuming. In order to speed up the procedure we introduce another average, which gives equivalent results and saves a lot of time. For each external momentum k_{B_1}, we will only need to solve the G–matrix equation for two values of the centre–of–mass and hole momenta, which are obtained from

$$\overline{K^2}(k_{B_1}) \ = \ \frac{\displaystyle\int d^3k \, K^2(k_{B_1},k,\cos\theta)}{\displaystyle\int d^3k} , \tag{B.12}$$

$$\overline{k^2_{B_2}}(k_{B_1}) = \frac{\displaystyle\int d^3k\, k^2_{B_2}(k_{B_1}, k, \cos\theta)}{\displaystyle\int d^3k}, \tag{B.13}$$

by limiting the integral over the modulus of $\vec{k}$ to the two possibilities mentioned above. As before, we have the same cases $\beta k_{B_1} < \alpha k_{F_{B_2}}$ and $\beta k_{B_1} > \alpha k_{F_{B_2}}$. Let's consider the first case. Now, when the integral over k in Eqs. (B.12) and (B.13) is limited to $0 < k < \alpha k_{F_{B_2}} - \beta k_{B_1}$ we have

$$\overline{K^2}(k_{B_1}) = \frac{1}{\alpha^2}\Big[k^2_{B_1} + \frac{3}{5}(\alpha k_{F_{B_2}} - \beta k_{B_1})^2\Big] , \tag{B.14}$$

$$\overline{k^2_{B_2}}(k_{B_1}) = \frac{1}{\alpha^2}\Big[\beta^2 k^2_{B_1} + \frac{3}{5}(\alpha k_{F_{B_2}} - \beta k_{B_1})^2\Big] , \tag{B.15}$$

whereas in the zone $\alpha k_{F_{B_2}} - \beta k_{B_1} < k < \alpha k_{F_{B_2}} + \beta k_{B_1}$ the expressions are a little bit more tedious

$$\begin{aligned}
\overline{K^2}(k_{B_1}) &= \Big[- \frac{\beta^2(1+\beta^2)}{\alpha} k_{F_{B_2}} k^4_{B_1} + \beta(1+2\beta^2) k^2_{F_{B_2}} k^3_{B_1} \\
&+ \Big(\frac{\alpha^3}{2} + \frac{\alpha}{12}(4\beta - 26\beta^2 - 6)\Big) k^3_{F_{B_2}} k^2_{B_1} + \alpha^2\beta k^4_{F_{B_2}} k_{B_1} \\
&+ \frac{\beta^3}{15\alpha^2}(5 + 3\beta^2) k^5_{B_1}\Big] \\
&\times \Big[(\alpha k_{F_{B_2}})^2 \beta k_{B_1} + \frac{1}{3}(\beta k_{B_1})^3 - \alpha k_{F_{B_2}}(\beta k_{B_1})^2\Big]^{-1} ,
\end{aligned} \tag{B.16}$$

$$\begin{aligned}
\overline{k^2_{B_2}}(k_{B_1}) &= \Big[- \frac{2\beta^4}{\alpha} k_{F_{B_2}} k^4_{B_1} + 3\beta^3 k^2_{F_{B_2}} k^3_{B_1} \\
&- \frac{7}{3}\alpha\beta^2 k^3_{F_{B_2}} k^2_{B_1} + \alpha^2\beta k^4_{F_{B_2}} k_{B_1} + \frac{8\beta^5}{15\alpha^2} k^5_{B_1}\Big] \\
&\times \Big[(\alpha k_{F_{B_2}})^2 \beta k_{B_1} + \frac{1}{3}(\beta k_{B_1})^3 - \alpha k_{F_{B_2}}(\beta k_{B_1})^2\Big]^{-1} .
\end{aligned} \tag{B.17}$$

When $\vec{k}_{B_1} = 0$ there exists only one zone of integration, $0 < k < \alpha k_{F_{B_2}}$, and the average is very simple

$$\overline{K^2}(k_{B_1}) = \overline{k^2_{B_2}}(k_{B_1}) = \frac{3}{5} k^2_{F_{B_2}} . \tag{B.18}$$

Finally, in the second case, $\beta k_{B_1} > \alpha k_{F_{B_2}}$, there is also only one integration zone, $\beta k_{B_1} - \alpha k_{F_{B_2}} < k < \alpha k_{F_{B_2}} + \beta k_{B_1}$, and the corresponding averages are

$$\overline{K^2}(k_{B_1}) = \frac{3}{5} k^2_{F_{B_2}} + k^2_{B_1} , \tag{B.19}$$

$$\overline{k^2_{B_2}}(k_{B_1}) = \frac{3}{5} k^2_{F_{B_2}} . \tag{B.20}$$

Appendix C: Particle channels in the physical basis

In this appendix we show the particle channel structure of the G-matrix for the different strangeness sectors when the Bethe–Goldstone equation is solved in the physical basis $|(B_1B_2)\vec{K}kLSJMq\rangle$.

C.1. Strangeness 0

In this sector there are three possible total charges, $q = 0, 1$ and 2, being the corresponding particle channels

$$\left(\overline{G}_{nn\to nn} \right) \,, \quad \left(\overline{G}_{np\to np} \right) \,, \quad \left(\overline{G}_{pp\to pp} \right) \,.$$

C.1. Strangeness -1

In this case we have to deal with the channels

$$\begin{pmatrix} \overline{G}_{\Sigma^- n\to\Sigma^- n} \end{pmatrix}, \begin{pmatrix} \overline{G}_{\Lambda n\to\Lambda n} & \overline{G}_{\Lambda n\to\Sigma^0 n} & \overline{G}_{\Lambda n\to\Sigma^- p} \\ \overline{G}_{\Sigma^0 n\to\Lambda n} & \overline{G}_{\Sigma^0 n\to\Sigma^0 n} & \overline{G}_{\Sigma^0 n\to\Sigma^- p} \\ \overline{G}_{\Sigma^- p\to\Lambda n} & \overline{G}_{\Sigma^- p\to\Sigma^0 n} & \overline{G}_{\Sigma^- p\to\Sigma^- p} \end{pmatrix},$$

for total charges $q = -1$ and $q = 0$, respectively, and

$$\begin{pmatrix} \overline{G}_{\Lambda p\to\Lambda p} & \overline{G}_{\Lambda p\to\Sigma^+ n} & \overline{G}_{\Lambda p\to\Sigma^0 p} \\ \overline{G}_{\Sigma^+ n\to\Lambda p} & \overline{G}_{\Sigma^+ n\to\Sigma^+ n} & \overline{G}_{\Sigma^+ n\to\Sigma^0 p} \\ \overline{G}_{\Sigma^0 p\to\Lambda p} & \overline{G}_{\Sigma^0 p\to\Sigma^+ n} & \overline{G}_{\Sigma^0 p\to\Sigma^0 p} \end{pmatrix}, \begin{pmatrix} \overline{G}_{\Sigma^+ p\to\Sigma^+ p} \end{pmatrix},$$

for total charges $q = 1$ and $q = 2$.

C.1. Strangeness -2

In the strangeness -2 sector the channels to consider are

$$\begin{pmatrix} \overline{G}_{\Sigma^-\Sigma^-\to\Sigma^-\Sigma^-} \end{pmatrix}, \begin{pmatrix} \overline{G}_{\Xi^- n\to\Xi^- n} & \overline{G}_{\Xi^- n\to\Sigma^-\Lambda} & \overline{G}_{\Xi^- n\to\Sigma^-\Sigma^0} \\ \overline{G}_{\Sigma^-\Lambda\to\Xi^- n} & \overline{G}_{\Sigma^-\Lambda\to\Sigma^-\Lambda} & \overline{G}_{\Sigma^-\Lambda\to\Sigma^-\Sigma^0} \\ \overline{G}_{\Sigma^-\Sigma^0\to\Xi^- n} & \overline{G}_{\Sigma^-\Sigma^0\to\Sigma^-\Lambda} & \overline{G}_{\Sigma^-\Sigma^0\to\Sigma^-\Sigma^0} \end{pmatrix},$$

for total charges $q = -2$ and $q = -1$, respectively,

$$\begin{pmatrix}
\overline{G}_{\Lambda\Lambda\to\Lambda\Lambda} & \overline{G}_{\Lambda\Lambda\to\Xi^0 n} & \overline{G}_{\Lambda\Lambda\to\Xi^- p} & \overline{G}_{\Lambda\Lambda\to\Sigma^0\Lambda} & \overline{G}_{\Lambda\Lambda\to\Sigma^0\Sigma^0} & \overline{G}_{\Lambda\Lambda\to\Sigma^-\Sigma^+} \\
\overline{G}_{\Xi^0 n\to\Lambda\Lambda} & \overline{G}_{\Xi^0 n\to\Xi^0 n} & \overline{G}_{\Xi^0 n\to\Xi^- p} & \overline{G}_{\Xi^0 n\to\Sigma^0\Lambda} & \overline{G}_{\Xi^0 n\to\Sigma^0\Sigma^0} & \overline{G}_{\Xi^0 n\to\Sigma^-\Sigma^+} \\
\overline{G}_{\Xi^- p\to\Lambda\Lambda} & \overline{G}_{\Xi^- p\to\Xi^0 n} & \overline{G}_{\Xi^- p\to\Xi^- p} & \overline{G}_{\Xi^- p\to\Sigma^0\Lambda} & \overline{G}_{\Xi^- p\to\Sigma^0\Sigma^0} & \overline{G}_{\Xi^- p\to\Sigma^-\Sigma^+} \\
\overline{G}_{\Sigma^0 p\to\Lambda\Lambda} & \overline{G}_{\Sigma^0 p\to\Xi^0 n} & \overline{G}_{\Sigma^0 p\to\Xi^- p} & \overline{G}_{\Sigma^0 p\to\Sigma^0\Lambda} & \overline{G}_{\Sigma^0 p\to\Sigma^0\Sigma^0} & \overline{G}_{\Sigma^0 p\to\Sigma^-\Sigma^+} \\
\overline{G}_{\Sigma^0\Sigma^0\to\Lambda\Lambda} & \overline{G}_{\Sigma^0\Sigma^0\to\Xi^0 n} & \overline{G}_{\Sigma^0\Sigma^0\to\Xi^- p} & \overline{G}_{\Sigma^0\Sigma^0\to\Sigma^0\Lambda} & \overline{G}_{\Sigma^0\Sigma^0\to\Sigma^0\Sigma^0} & \overline{G}_{\Sigma^0\Sigma^0\to\Sigma^-\Sigma^+} \\
\overline{G}_{\Sigma^-\Sigma^+\to\Lambda\Lambda} & \overline{G}_{\Sigma^-\Sigma^+\to\Xi^0 n} & \overline{G}_{\Sigma^-\Sigma^+\to\Xi^- p} & \overline{G}_{\Sigma^-\Sigma^+\to\Sigma^0\Lambda} & \overline{G}_{\Sigma^-\Sigma^+\to\Sigma^0\Sigma^0} & \overline{G}_{\Sigma^-\Sigma^+\to\Sigma^-\Sigma^+}
\end{pmatrix},$$

for total charge $q = 0$ and

$$\begin{pmatrix}
\overline{G}_{\Xi^0 p\to\Xi^0 p} & \overline{G}_{\Xi^0 p\to\Sigma^+\Lambda} & \overline{G}_{\Xi^0 p\to\Sigma^0\Sigma^+} \\
\overline{G}_{\Sigma^+\Lambda\to\Xi^0 p} & \overline{G}_{\Sigma^+\Lambda\to\Sigma^+\Lambda} & \overline{G}_{\Sigma^+\Lambda\to\Sigma^0\Sigma^+} \\
\overline{G}_{\Sigma^0\Sigma^+\to\Xi^0 p} & \overline{G}_{\Sigma^0\Sigma^+\to\Sigma^+\Lambda} & \overline{G}_{\Sigma^0\Sigma^+\to\Sigma^0\Sigma^+}
\end{pmatrix}, \quad \begin{pmatrix} \overline{G}_{\Sigma^+\Sigma^+\to\Sigma^+\Sigma^+} \end{pmatrix},$$

for total charges $q = 1$ and $q = 2$.

C.1. Strangeness −3

In this case we have

$$\begin{pmatrix} \overline{G}_{\Xi^-\Sigma^-\to\Xi^-\Sigma^-} \end{pmatrix}, \quad \begin{pmatrix}
\overline{G}_{\Xi^-\Lambda\to\Xi^-\Lambda} & \overline{G}_{\Xi^-\Lambda\to\Xi^0\Sigma^-} & \overline{G}_{\Xi^-\Lambda\to\Xi^-\Sigma^0} \\
\overline{G}_{\Xi^0\Sigma^-\to\Xi^-\Lambda} & \overline{G}_{\Xi^0\Sigma^-\to\Xi^0\Sigma^-} & \overline{G}_{\Xi^0\Sigma^-\to\Xi^-\Sigma^0} \\
\overline{G}_{\Xi^-\Sigma^0\to\Xi^-\Lambda} & \overline{G}_{\Xi^-\Sigma^0\to\Xi^0\Sigma^-} & \overline{G}_{\Xi^-\Sigma^0\to\Xi^-\Sigma^0}
\end{pmatrix},$$

for total charges $q = -2$ and $q = -1$, respectively, and

$$\begin{pmatrix} \overline{G}_{\Xi^0\Lambda\to\Xi^0\Lambda} & \overline{G}_{\Xi^0\Lambda\to\Xi^0\Sigma^0} & \overline{G}_{\Xi^0\Lambda\to\Xi^-\Sigma^+} \\ \overline{G}_{\Xi^0\Sigma^0\to\Xi^0\Lambda} & \overline{G}_{\Xi^0\Sigma^0\to\Xi^0\Sigma^0} & \overline{G}_{\Xi^0\Sigma^0\to\Xi^-\Sigma^+} \\ \overline{G}_{\Xi^-\Sigma^+\to\Xi^0\Lambda} & \overline{G}_{\Xi^-\Sigma^+\to\Xi^0\Sigma^0} & \overline{G}_{\Xi^-\Sigma^+\to\Xi^-\Sigma^+} \end{pmatrix} , \quad \begin{pmatrix} \overline{G}_{\Xi^0\Sigma^+\to\Xi^0\Sigma^+} \end{pmatrix} ,$$

for total charges $q = 0$ and $q = 1$.

C.1. Strangeness -4

Finally, in in the strangeness -4 sector there are also three possible total charges, $q = -2, -1$ and 0, being the respective particle channels

$$\begin{pmatrix} \overline{G}_{\Xi^-\Xi^-\to\Xi^-\Xi^-} \end{pmatrix} , \quad \begin{pmatrix} \overline{G}_{\Xi^-\Xi^0\to\Xi^-\Xi^0} \end{pmatrix} , \quad \begin{pmatrix} \overline{G}_{\Xi^0\Xi^0\to\Xi^0\Xi^0} \end{pmatrix} .$$

Appendix D: Single-particle potential in the BHF approach

Let us consider two baryons B_1 and B_2 belonging to the same isomultiplet. In the BHF approach, the single-particle potential felt by B_1 due to the Fermi sea of baryons B_2 reads

$$U_{B_1}^{(B_2)} = \mathrm{Re} \sum_{B_2} \langle B_1 B_2 | \overline{G}(\omega = E_{B_1} + E_{B_2}) | B_1 B_2 \rangle_{\mathcal{A}} \ , \tag{D.1}$$

which in the decoupled basis basis $|(B_1B_2)\vec{k}_1 s_1 \sigma_1 t_1 \tau_1, \vec{k}_2 s_2 \sigma_2 t_2 \tau_2\rangle$ can be written as

$$\begin{aligned} U_{B_1}^{(B_2)}(k_1) = \mathrm{Re} \sum_{\vec{k}_2 \sigma_2 \tau_2} \theta(k_{F_{B_2}} - |\vec{k}_2|) \\ \times \Big[\langle (B_1B_2)\vec{k}_1 s_1 \sigma_1 t_1 \tau_1, \vec{k}_2 s_2 \sigma_2 t_2 \sigma_2 | \overline{G} | (B_1B_2)\vec{k}_1 s_1 \sigma_1 t_1 \tau_1, \vec{k}_2 s_2 \sigma_2 t_2 \tau_2 \rangle \\ - \langle (B_1B_2)\vec{k}_1 s_1 \sigma_1 t_1 \tau_2, \vec{k}_2 s_2 \sigma_2 s_2 \tau_2 | \overline{G} | (B_1B_2)\vec{k}_2 s_2 \sigma_2 t_2 \sigma_2, \vec{k}_1 s_1 \sigma_1 t_1 \tau_1 \rangle \Big] \end{aligned} \ . \tag{D.2}$$

Now introducing the average centre-of-mass $\overline{K}$ and relative momenta $\vec{k}$, coupling the spin and isospin via

$$\begin{aligned} |\sigma_1\sigma_2\rangle &= \sum_{SM_S}(s_1s_2\sigma_1\sigma_2|SM_S)|SM_S\rangle \\ |\tau_1\tau_2\rangle &= \sum_{TM_T}(t_1t_2\tau_1\tau_2|TM_T)|TM_T\rangle \end{aligned} \quad , \tag{D.3}$$

and expanding the states $|\vec{k}\rangle$ in terms of the states $|kLM_L\rangle$

$$|\vec{k}\rangle = \sum_{LM_L} Y^*_{LM_L}(\hat{k})|kLM_L\rangle \ , \tag{D.4}$$

one has

$$\begin{aligned} |(B_1B_2)\overline{K}ks_1\sigma_1t_1\tau_1, s_2\sigma_2t_2\tau_2\rangle = &\sum_{\substack{LM_LSM_S \\ JMTM_T}} (s_1s_2\sigma_1\sigma_2|SM_S)(t_1t_2\tau_1\tau_2|TM_T) \\ &\times(LSM_LM_S|JM)Y^*_{LM_L}(\hat{k})|(B_1B_2)\overline{K}kLSJMTM_T\rangle \end{aligned} \quad , \tag{D.5}$$

where we have also coupled L and S.

Similarly, for the exchange term we have

$$\begin{aligned} -|(B_1B_2)\overline{K}ks_2\sigma_2t_2\tau_2, s_1\sigma_1t_1\tau_1\rangle = &\sum_{\substack{LM_LSM_S \\ JMTM_T}} (-1)^{L+S+T-s_1-s_2-t_1-t_2}(s_1s_2\sigma_1\sigma_2|SM_S) \\ &\times(t_1t_2\tau_1\tau_2|TM_T)(LSM_LM_S|JM)Y^*_{LM_L}(\hat{k})|(B_1B_2)\overline{K}kLSJMTM_T\rangle \end{aligned} \quad , \tag{D.6}$$

where we have employed the identities

$$(j_2j_1m_2m_1|jm) = (-1)^{j-j_1-j_2}(j_1j_2m_1m_2|jm) \ , \tag{D.7}$$

and

$$Y_{LM_L}(-\hat{k}) = (-1)^L Y_{LM_L}(\hat{k}) \ . \tag{D.8}$$

Hence, taking into account Eqs. (D.5) and (D.6) and that $\overline{G}$ is diagonal in J, M, T, M_T and S, we can write

$$\begin{aligned} U_{B_1}^{(B_2)}(k_1) = \sum_{\vec{k}_2\sigma_2\tau_2} \theta(k_{F_{B_2}} - |\vec{k}_2|) & \sum_{\substack{LM_L L'M'_L SM_S M'_S \\ JMTM_T}} [1-(-1)^{L+S+T-s_1-s_2-t_1-t_2}] \\ \times Y^*_{LM_L}(\hat{k}) Y_{L'M'_L}(\hat{k}) & (s_1s_2\sigma_1\sigma_2|SM_S)(s_1s_2\sigma_1\sigma_2|SM'_S)(t_1t_2\tau_1\tau_2|TM_T)^2 \\ & \times (LSM_LM_S|JM)(L'SM'_LM_S|JM)(s_1s_2\sigma_1\sigma_2|SM'_S) \\ & \times \mathrm{Re}\langle (B_1B_2)\overline{K}kL'SJMTM_T|\overline{G}|(B_1B_2)\overline{K}kLSJMTM_T\rangle \end{aligned} \quad . \tag{D.9}$$

We define now the average over the spin third component σ_1

$$U_{B_1}^{(B_2)}(k_1) \equiv \frac{1}{2s_1+1}\sum_{\sigma_1} U_{B_1}^{(B_2)}(k_1) \ . \tag{D.10}$$

Using the orthogonal property

$$\sum_{m_1m_2} (j_1j_2m_1m_2|jm)(j_1j_2m_1m_2|j'm') = \delta_{jj'}\delta_{mm'} \ , \tag{D.11}$$

and the symmetry property of the Clebsch-Gordan coefficients,

$$(j_1j_2m_1m_2|jm) = (-1)^{j_1-j+m_2}\sqrt{\frac{2j+1}{2j_1+1}}(jj_2m-m_2|j_1m_1) \ , \tag{D.12}$$

we can write

$$\begin{aligned}
U_{B_1}^{(B_2)}(k_1) = \frac{1}{2s_1+1} \sum_{\vec{k}_2 \tau_2} \theta(k_{F_{B_2}} - |\vec{k}_2|) \sum_{\substack{LM_L L'M'_L SM_S \\ JMTM_T}} & [1-(-1)^{L+S+T-s_1-s_2-t_1-t_2}] \\
& \times Y^*_{LM_L}(\hat{k}) Y_{L'M'_L}(\hat{k}) (t_1 t_2 \tau_1 \tau_2 | T M_T)^2 \\
& \times (-1)^{L+L'} \tfrac{2J+1}{\sqrt{(2L+1)(2L'+1)}} (JSM-M_S|LM_L)(JSM-M_S|L'M'_L) \\
& \times \mathrm{Re}\langle (B_1B_2)\overline{K}kL'SJMTM_T|\overline{G}|(B_1B_2)\overline{K}kLSJMTM_T\rangle
\end{aligned} . \tag{D.13}$$

Employing Eq. (D.11) to perform the sums over M and M_S and employing the identity

$$\sum_{M_L} Y^*_{LM_L}(\hat{q}_1) Y_{LM_L}(\hat{q}_2) = \frac{2L+1}{4\pi} P_L(\hat{q}_1 \cdot \hat{q}_2) \ , \tag{D.14}$$

one obtains

$$\begin{aligned}
U_{B_1}^{(B_2)}(k_1) = \frac{1}{4\pi(2s_1+1)} \sum_{\vec{k}_2 \tau_2} \theta(k_{F_{B_2}} - |\vec{k}_2|) \sum_{LSJTM_T} & [1-(-1)^{L+S+T-s_1-s_2-t_1-t_2}] \\
& \times (2J+1) (t_1 t_2 \tau_1 \tau_2 | T M_T)^2 \\
& \times \mathrm{Re}\langle (B_1B_2)\overline{K}kL'SJMTM_T|\overline{G}|(B_1B_2)\overline{K}kLSJMTM_T\rangle
\end{aligned} . \tag{D.15}$$

Finally, transforming the sum over $\vec{k}_2$ into an integral over k

$$\sum_{\vec{k}_2} \to \int d^3\vec{k}_2 = \int \mid J \mid d^3\vec{k} = 2\pi(1+\xi_{B_1})^3 \int_0^{k_{max}} dk k^2 \int d(\cos\theta) \ , \tag{D.16}$$

being $\mid J \mid = (1+\xi_{B_1})^3$ the jacobian of the change,

$$\vec{k}_2 = \frac{\beta}{\alpha}\vec{k}_1 - \frac{1}{\alpha}\vec{k} = \xi_{B_1}\vec{k}_1 - (1+\xi_{B_1})\vec{k} \ . \tag{D.17}$$

Finally, one arrives at

$$
\begin{aligned}
U_{B_1}^{(B_2)}(k_1) = \frac{(1+\xi_{B_1})^3}{2s_1+1} & \sum_{J,L,S,T,M_T} (2J+1)[1-(-1)^{L+S+T-s_1-s_2-t_1-t_2}] \\
& \times (t_1 t_2 \tau_1 \tau_2 | T M_T)^2 \int_0^{k_{max}} k^2 dk f(k, k_{B_1}) \\
\times \mathrm{Re}\langle (B_1 B_2) \overline{K} k L S J M T M_T | \overline{G} | & (B_1 B_2) \overline{K} k L S J M T M_T \rangle \ ,
\end{aligned}
\tag{D.18}
$$

where the angular integral have been performed with the aid of the weight function $f(k, k_{B_1})$ defined in appendix E.

Appendix E: Angular integration

Once the angular dependence of the G-matrix has been eliminated by the introduction of the average centre-of-mass and hole momenta defined in appendix B, the integral over $\cos\theta$ which appears in the construction of the single-particle potential is replaced by the following weight function

$$f(k,k_{B_1}) \equiv \frac{1}{2}\int_{-1}^{1} d(\cos\theta)\ , \tag{E.1}$$

where the integration is restricted to certain range of angles by the fact that the hole momentum $\vec{k}_{B_2} = \xi_{B_1}\vec{k}_{B_1} - (1+\xi_{B_1})\vec{k}$ should be inside its Fermi surface, as can be seen in Fig. E.1. According to the figure we can consider the following cases:

Case A: $|\xi_{B_1}\vec{k_{B_1}}| < k_{F_{B_2}}$

- A.1: $(1+\xi_{B_1})k < k_{F_{B_2}} - \xi_{B_1}k_{B_1}$; the hole momentum lies always inside its Fermi surface, all the angles are allowed and therefore $f(k,k_{B_1}) = 1$.

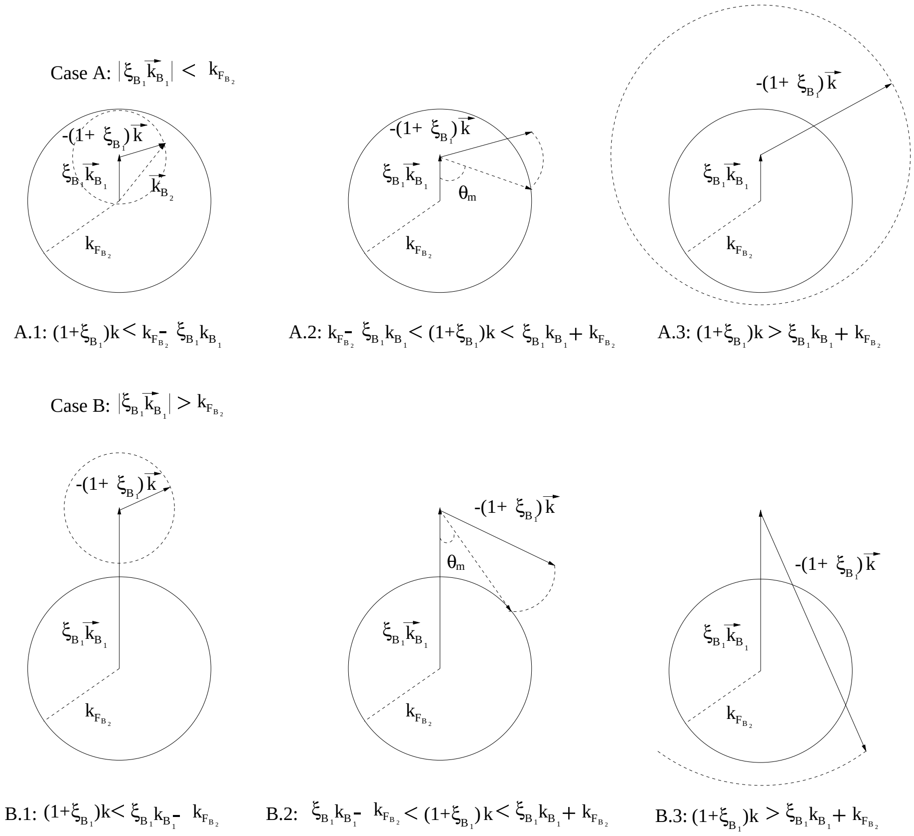

A.1: $(1+\xi_{B_1})k < k_{F_{B_2}} - \xi_{B_1}k_{B_1}$ A.2: $k_{F_{B_2}} - \xi_{B_1}k_{B_1} < (1+\xi_{B_1})k < \xi_{B_1}k_{B_1} + k_{F_{B_2}}$ A.3: $(1+\xi_{B_1})k > \xi_{B_1}k_{B_1} + k_{F_{B_2}}$

B.1: $(1+\xi_{B_1})k < \xi_{B_1}k_{B_1} - k_{F_{B_2}}$ B.2: $\xi_{B_1}k_{B_1} - k_{F_{B_2}} < (1+\xi_{B_1})k < \xi_{B_1}k_{B_1} + k_{F_{B_2}}$ B.3: $(1+\xi_{B_1})k > \xi_{B_1}k_{B_1} + k_{F_{B_2}}$

Figure E.1: Illustration of the different cases discussed in the text.

- A.2: $k_{F_{B_2}} - \xi_{B_1}k_{B_1} < (1+\xi_{B_1})k < \xi_{B_1}k_{B_1} + k_{F_{B_2}}$; there is a maximum angle from which the hole momentum lies outside its Fermi surface. According to the figure the cosine of this angle reads

$$\cos\theta_m = \frac{(\xi_{B_1}k_{B_1})^2 + (1+\xi_{B_1})^2k^2 - k_{F_{B_2}}^2}{2\xi_{B_1}k_{b_1}(1+\xi_{B_1})k} \ , \tag{E.2}$$

and therefore

$$f(k,k_{B_1}) \equiv \frac{1}{2}\int_{\cos\theta_m}^{1} d(\cos\theta) = \frac{1}{2}(1-\cos\theta_m) = \frac{k_{F_{B_2}}^2 - [\xi_{B_1}k_{B_1} - (1+\xi_{B_1})k]^2}{4\xi_{B_1}k_{b_1}(1+\xi_{B_1})k} \ . \tag{E.3}$$

- A.3: $(1+\xi_{B_1})k > \xi_{B_1}k_{B_1} + k_{F_{B_2}}$; the hole momentum is always outside its Fermi surface and therefore there are no contributions from this kind of configuration, being in this case $f(k, k_{B_1}) = 0$.

Case B: $|\xi_{B_1}\vec{k_{B_1}}| > k_{F_{B_2}}$

- B.1: $(1+\xi_{B_1})k < \xi_{B_1}k_{B_1} - k_{F_{B_2}}$, the hole momentum lies always outside the Fermi surface and as in the case A.3, therefore, $f(k, k_{B_1}) = 0$.
- B.2: $\xi_{B_1}k_{B_1} - k_{F_{B_2}} < (1+\xi_{B_1})k < \xi_{B_1}k_{B_1} + k_{F_{B_2}}$, as in the case A.2 there is a maximum angle from which the hole momenta lies outside its Fermi surface. This angle has the same value as in A.2. Hence also in this case $f(k, k_{B_1})$ is given by Eq. (E.3).
- B.3: $(1+\xi_{B_1})k > \xi_{B_1}k_{B_1} + k_{F_{B_2}}$, as in the cases A.3 and B.1, the hole momentum is always outside its Fermi surface, being therefore $f(k, k_{B_1}) = 0$.

All these cases can be put together, yielding finally,

$$f(k, k_{B_1}) = \begin{cases} 1 & \text{for } k \leq \frac{k_{F_{B_2}} - \xi_{B_1}k_{B_1}}{1+\xi_{B_1}}, \\ 0 & \text{for } |\xi_{B_1}k_{B_1} - (1+\xi_{B_1})k| > k_{F_{B_2}}, \\ \dfrac{k_{F_{B_2}}^2 - [\xi_{B_1}k_{B_1} - (1+\xi_{B_1})k]^2}{4\xi_{B_1}(1+\xi_{B_1})k_{B_1}k} & \text{otherwise.} \end{cases} \tag{E.4}$$

Resum

1. Introducció

La presència de barions extranys, hiperons (Λ, Σ, Ξ) en sistemes nuclears finits i infinits ha rebut molta atenció durant les darreres dècades tant des del punt de vista teòric com experimental [Ga77, Po78, Ba85, Do89, Os90, Co90, Ba90, Gi95, Ak97, Os98]. L'estranyesa afegeix una nova dimensió a l'imatge evolutiva de la física nuclear i ens dóna una oportunitat per estudiar les interaccións barió-barió fonamentals des d'una nova perspectiva.

Els hipernuclis són sistemes lligats de neutrons, protons i un o més hiperons. Van ser observats per primer cop l'any 1951 amb el descobriment d'un hiperfragment per Danysz i Pniewsli [Da53]. Les primeres observacions d'hipernuclis en rajos còsmics van ser seguides de produccions en emulsions de feixos de pions i protons i cambres de bombolles de ^{4}He. La desintegració feble de la partícula Λ en un π^- i un protó fou utilitzada per identificar hipernuclis Λ i per determinar energies de lligam, espins i vides mitjes fins $A = 15$ [Ju73, Da91]. Les propietats mitjes dels sistemes pesats foren estimades amb posterioritat i dos hipernuclis doble Λ van ser obtinguts a partir de la captura de Ξ^- [Da63, Pr66]. Investigacions més sistemàtiques dels hipernuclis van començar amb la possibilitat de generar feixos separats de K^-, el què va permetre l'utilització d'experiments de comptatge [Pa73].

Tot i que els avenços de la física d'hipernuclis han estat molt lents degut al limitat nombre d'esdeveniments, els experiments de comptatge de la reacció en vol (K^-, π^-) realitzats al CERN [Br75, Be79] i Brookhaven (BNL) [Ch79] han revelat una gran quantitat de les característiques dels hiperons, tals com què la partícula Λ manté essencialment la seva identitat dins del nucli, el petit acoblament espín-òrbita, les estretes amplades (avui dia descartades) dels hipenuclis Σ, injectant un renovat interès en el camp. Des d'aleshores, els recursos experimentals han estat millorats i experiments usant les reaccions (π^+, K^+) i $(K^-_{\rm parat}, \pi^0)$ estan essent realitzats als acceleradors AGS i KEK de Brookhaven amb intensitats dels feixos més altes i resolucions en energia millorades.

La producció electromagnèrica d'hipernuclis al laboratori TJNL, mitjantçant la reacció $(e, e'K^+)$, és una nova eina d'alta precisió per l'estudi de l'espectroscopia hipernuclear [Hu94]. A més, l'estudi de les desintegracions de nivells hipernuclears utilitzant detectors de germani amb àngles sòlids grans, pot ajudar a definr l'espectre d'hipernuclis lleugers. També és possible que feixos de kaons i ions pesats més intensos, acoblats amb noves tecnologies de detecció, proporcionin els mitjans per detectar hipernuclis amb diversos hiperons [Gr88].

Relacionat amb aquest darrer aspecte, menys coses són conegudes sobre els hipernuclis Ξ o hipernuclis amb diversos hiperons [Do83]. Uns pocs esdeveniments [Wi59, Ba63, Bh63, Be68, Mo79] han estat interpretats com a hipernuclis multiestranys, però els experiments de comptatge no han estat capaços d'observar la creació d'aquests sistemes. Des del punt de vista de la teoria convencional de molts cossos, un estudi de la interacció hiperó-hiperó (YY) és molt important, i es pot fer amb hipernuclis amb diversos hiperons. Naturalment, un estudi directe de la dispersió hiperó-hiperó seria molt interessant, però donat que aquestes partícules tenen vides mitjes molt curtes, això no és possible. Hi ha esdeveniments que han estat interpretats bé com a hipernuclis Ξ, bé com a hipernuclis doble Λ. D'aquests esdeveniments, si s'interpreten correctament, es pot extreure informació sobre la profunditat del potencial $\Lambda\Lambda$ [Do91], però les interpretacions encara són obertes a debat. Clarament s'ha d'obtenir més informació experimental sobre aquest aspecte.

Des del punt de vista teòric, un dels objectius de la investigació hipernuclear és relacionar els observables hipernuclears amb la interacció nua hiperó-nucleó (YN) i hiperó-hiperó (YY). Les dificultats experimentals associades a la curta vida mitja dels hiperons i la baixa intensitat dels feixos han limitat el nombre d'esdeveniments de dispersió ΛN i ΣN a menys de mil [En66, Al68, Se68, Ka71, Ei71], que no són suficients per tal de restringir totalment la interacció YN. Avui dia, hi ha dos models d'intercanvi mesònic per descriure la interacció YN: un del grup de Nijmegen [Na77, Ma89], on els corresponents vèrtexs es determinen per mitjà de la simetria SU(3), i el del grup de Jülich [Ho89], que assumeix una simetria SU(6) més forta i on, per tant, totes les constants d'acoblament dels vèrtexs estranys poden relacionar-se amb les de la interacció nucleó-nucleó (NN). Recentment, el grup de Nijmegen ha construït una extensió del les seves interaccions NN i YN a tot l'octet complet de barions, incloent la interacció YY

[Ri99, St99]. Tot i que els models de Nijmegen i Jülich són capaços de descriure el conjunt de dades experimentals, les seves estructures d'espín i isospín són molt diferents. Per tant, més dades sobre observables d'espín són molt desitjables.

Sense aquestes dades, informació alternativa pot obtenir-se de l'estudi dels hipernuclis. Una possibilitat es centra en l'estudi d'hipernuclis lleugers, tals com ${}^{3}_{\Lambda}$H, ${}^{3}_{\Lambda}$He i ${}^{4}_{\Lambda}$He, que poden ser tractats "exactament" resolent les equacions a 3 cossos de Fadeev [Mi93, Mi95] o a 4 cossos de Yakubovsky [Gi88].

Una altra possibilitat és l'estudi d'hipernuclis amb masses més grans. Tradicionalment, els hipernuclis han estat descrits amb un model de capes utilitzant potencials Λ-nucli de tipus Woods-Saxon que reprodueixen força bé els estats hipernuclears mesurats per hipernuclis mitjans i pesants [Bo76, Do80, Mo88]. La inclusió d'efectes de no localitat i de densitat en càlculs no relativistes de tipus Hartree–Fock amb forces YN de tipus Skyrme [Mi88, Ya88, Fe89, La97, Vi01] ha millorat les energies monoparticulars de lligam. Les propietats dels hipernuclis han estat estudiades també dins de marcs relativistes, tals com la fenomenologia de Dirac on el potencial hiperó-nucli s'ha obtingut a partir d'un potencial nucleó-nucli [Br81, Ch91], o en la teoria relativista de camp mig [Ma89b, Ma94, Lo95, Gl93, In96, Su94, Ma96, Ts97].

També són possibles els càlculs microscòpics d'estructura hipernuclear. Aquests poden ser realitzats amb una interacció YN efectiva o matriu G obtinguda a partir de la interacció nua mitjantçant l'equació de Bethe–Goldstone. En càlculs previs es van utilitzar parametritzacions gaussianes de la matriu G calculades a matèria nuclear a una densitat promig [Ya85, Ya90, Ya92, Ya94]. Una matriu G obtinguda directament al nucli finit es va fer servir per estudiar el nivells monoparticulars de diversos hipernuclis [Ha93]. La matriu G de matèria nuclear es va utilitzar també en un càlcul de l'estructura del ${}^{17}_{\Lambda}$O [Ha93b]. En aquesta tesi derivarem microscòpicament, d'una manera similar a la dels autors de la Ref. [Hj96], les propietats monoparticulars de la partícula Λ a les ones s i p per diversos hipernuclis, des de ${}^{5}_{\Lambda}$He fins a ${}^{208}_{\Lambda}$Pb, construint una matriu G pel nucli finit a partir d'una matriu G de matèria nuclear. Aquest mètode fou utilitzat per l'estudi de les propietats del nucleó i la Δ al nucli [Bo92, Hj94].

A més dels hipernuclis, els físics nuclears s'han interessat també en la matèria hiperònica (matèria nuclear amb graus de llibertat nucleònics i hiperònics), especialment en connexió amb la física dels estels de neutrons. Aquests objectes són un excel.lent observatori per comprovar el nostre coneixement de la teoria de les interaccions fortes a densitats extremes. L'interior dels estels de neutrons és força dens per tal de permetre l'aparició de noves partícules amb contingut d'estranyesa a més dels nucleons i leptons convencionals per mitjà de l'equilibri feble. Hi ha una forta evidència que els hiperons són els primers hadrons en aparèixer a la matèria densa i ho fan a una densitat típicament el doble de la densitat normal de la matèria nuclear [Gl85], com ha estat recentment confirmat amb potencials efectius no relativistes [Ba97], el model d'acoblament quark-mesó [Pa99], models relativistes de camp mig [Kn95, Sc96], Hartree–Fock relativista [Hu98] i dins de la teoria de Brueckner–Hartree–Fock [Ba00, Vi00b].

Les propietats dels estels de neutrons estan molt relacionades amb l'Equació d'Estat de la matèria a altes densitats. Aquestes propietats són afectades per la presència d'estranyesa [Gl97, Pr97]. Una forta deleptonització de la matèria dels estels de neutrons passa quan els hiperons apareixen, per què és energèticament més convenient mantenir la neutralitat de càrrega amb hiperons. A més, sembla clar que el principal efecte del hiperons sobre la matèria densa es que suavitza la seva Equació d'Estat, el què es tradueix en una massa màxima de l'estel més petita. Altres propietats com són les evolucións tèrmica i estructural de l'estel són molt sensibles a la composició, i per tant al contingut en estranyesa de l'interior de l'estel.

Tot i que la matèria hiperònica és un sistema ideal, la determinació teòrica de la seva Equació d'Estat representa un pas essencial pel coneixement de les propietats físiques dels estels de neutrons. A més, la comparació de les prediccions teòriques amb les observacions poden proporcionar informació sobre les interaccions entre els seus constituents. Per tant, es requereix un coneixement detallat de l'Equació d'Estat per un ample rang de densitats [Sh83]. Això representa una gran tasca des del punt de vista teòric. Tradicionalment, s'ha seguit dues aproximacions per tal de descriure la interacció barió-barió en el medi nuclear i per tant, per construir l'Equació d'Estat: les anomenades aproximació fenomenològica i aproximació microscòpica.

A l'aproximació fenomenològica el punt de partida és una interacció efectiva dependent de la densitat que conté un cert nombre de paràmetres ajustats per tal de reproduir dades experimentals com per exemple propietats dels nuclis o les propietats de saturació de la matèria nuclear. Hi ha moltes interaccions efectives, tals com la força de Migdal [Mi67] o la força de Gogny [Go75]. Però la més popular de totes és la interacció de Skyrme [Sk56, Va72]. Aquesta interacció ha guanyat molta importancia per què reprodueix les energies de lligam i els radis nuclears de tots el nuclis de la taula periòdica amb un conjunt raonable de paràmetres [Va72]; és pot connectar [Ne72] amb la matriu G que és més fonamental i la seva forma matemàtica és bastant simple. Balberg i Gal [Ba97, Ba99] han derivat recentment una Equació d'Estat efectiva i analítica utilitzant potencials barió-barió dependents de la densitat basats en forces de tipus Skyrme incloent graus de llibertat hiperònics. Les característiques d'aquesta Equació d'Estat es basen en les propietats dels nuclis pel que respecta a la interacció nucleó-nucleó i principalment en les dades experimentals d'hipernuclis pel que fa a les interaccions hiperó-nucleó i hiperó-hiperó. A més, aquesta Equació d'Estat reprodueix les propietats típiques de la matèria a altes densitats que es troben amb models microscòpics.

Una aproximació fenomenològica alternativa involucra la formulació d'una teoria efectiva relativista de camp mig [Se86, Se97]. Aquesta aproximació trata els graus de llibertat bariònics i mesònics de forma explícita, és completament relativista i, en general és més sencilla per què només fa servir densitats i camps locals. L'Equació d'Estat per la matèria densa amb hiperons fou descrita dins del model relativista de camp mig per Glendenning [Gl82, Gl85, Gl87]. El model de camp mig, però, no és capaç de reproduir la forta atracció de la interacció hiperó-hiperó observada en els hipernuclis doble Λ. Tot i això, Schaffner i els seus col.laboradors [Sc93, Sc94] han solucionat aquest problema incorporant camps mesònics estranys adicionals al lagrangià estàndar del model. El conjunt de paràmetres d'aquest model s'ha fixat amb les propietats del nuclis i de la matèria nuclear perl sector nucleònic, mentre que les constants d'acoblament dels hiperons s'han determinat amb relacions de simetria SU(6) i amb observables hipernuclears.

Per altra banda, en una aproximació microscòpica el punt de partida és una interacció barió-barió a dos cossos que descriu els observables de dispersió, tals com els potencials de Bonn-Jülich [Ma87, Ho89] o Nijmegen [Na78, Ma89, St94, Ri99, St99]. Aquestes interaccions realistes es construeixen dins del marc de la teoria d'intercanvi mesònic. Per tal d'obternir l'Equació d'Estat hom ha de resoldre el complicat problema dels molts cossos. La dificultat més gran d'aquest problema és el tractament del "core" fortament repulsiu, que domina el comportament de la interacció a curt abast. S'han considerat diversos mètodes per resoldre aquest problema, essent els més utilitzats el métode variacional i la teoria de Brueckner–Bethe–Goldstone.

El mètode variacional suggerit per Jastrow [Ja55], fa ús d'una funció de prova per tractar les correlacions de dos nucleons. L'Equació d'Estat per matèria nuclear asimètrica ha estat considerada per diferents autors dins d'aquesta aproximació [Wi88, Ak97b, Bo98], i de fet el càlcul d'Akmal i els seus col.laboradors [Ak98], utilitzant la interacció nucleó-nucleó Argonne V_{18} [Wi95] amb correccions relativistes i una interacció a tres cossos, pot ser considerat com el càlcul actual més realista pel sector nucleònic. Els hiperons no han estat considerats encara dins d'aquesta aproximació.

Una aproximació alternativa al mètode variacional per tractar el problema dels molts cossos ve donada per la teroria de Brueckner–Bethe–Goldstone (BBG). Brueckner i els seus col.laboradors [Br54] van desenvolupar un mètode per tal de sumar fins ordre infinit els anomenats diagrames escala partícula-partícula que tenen en compte les correlacions de curt abast. Un pas endavant vers l'aplicació d'aquest mètode als sistemes nuclears va ser donat per Bethe [Be56] mitjantçant el desenvolupament de l'expansió de línia de forat. El desenvolupament formal d'aquesta aproximació el va fer Goldstone [Go57] qui utilitzant mètodes pertorbatius va establir l'anomenada expansió de grups enllaçats. La teoria BBG s'ha aplicat molt a l'estudi de la matèria nuclear, i recentment a la matèria hiperònica. Schulze i els seus col.laboradors [Sc98] han realitzat un càlcul de molts cossos de tipus Brueckner per estudiar el punt d'aparició dels hiperons a la matèria dels estels de neutrons. Recentment aquests autors han ampliat el seu estudi als estels de neutrons amb hiperons [Ba00], posant especial atenció al paper jugat per les forces a tres cossos entre els nucleons. Tot i això, aquests estudis no inclouen la interacció hiperó-huperó, que és essencial des del moment en que apareix el primer hiperó en la matèria, la Σ^-. En aquest sentit, un dels objectius d'aquesta tesi és el d'incloure la interacció hiperó-hiperó en un càlcul microscòpic de molts cossos de tipus Brueckner i estudiar les propietats de la matèria β-estable dels estels de neutrons amb graus de llibertat hiperònics.

Per tal de fer les coses més sencilles per al lector donem aquí una idea de com està organitzada aquesta tesi:

Al Capítol 2, mostrem els resultats d'un càlcul microscòpic de tipus Brueckner per matèria densa que inclou tots els tipus d'interaccions barió-barió i permet tractar qualsevol asimetria en les fraccions dels diferents barions ($n, p, \Lambda, \Sigma^-, \Sigma^0, \Sigma^+, \Xi^-$ i Ξ^0). En aquest capítol presentem resultats pels potencials monoparticulars i les energies de lligam per barió, centrant-nos en densitats bariòniques i fraccions d'hiperons que poden ser rellevants en l'estudi de la matèria β-estable dels estels de neutrons.

Pel que fa a les propietats dels hiperons en el nucli finit, al Capítol 3, determinem l'energia monoparticular i la funció d'ona de l'hiperó Λ en diferents nuclis obtingudes a partir de la seva autoenergia. Aquesta autoenergia s'ha construït dins del marc d'una aproximació pertorbativa al problema dels molts cossos utilitzant interaccions hiperó-nucleó realistes tals com les dels grups de Jülich i Nijmegen. Investigem els efectes de no localitat i la dependència en densitat de l'autoenergia dels estats lligats. Mostrem, que tot i que les energies monoparticulars dels hiperons es poden reproduir força bé amb potencials de tipus Woods-Saxon, les funcions d'ona obtingudes amb l'autoenergia no local són més esteses.

Al Capítol 4 presentem resultats per un càlcul Brueckner–Hartree–Fock de la matèria

β-estable dels estels de neutrons amb graus de llibertat nucleònics i hiperònics, utilitzant la parametrització més recent de la interacció barió-barió del grup de Nijmegen. Es troba que els únics barions estranys presents fins a una densitat de 1.2 fm^{-3} són la Σ^- i la Λ. Calculem les corresponents Equacions d'Estat i determinem propietats dels estels de neutrons com la massa, el radi i el moment d'inèrcia.

Les conclusions principals d'aquesta tesi estan resumides al final del manuscrit.

2. Matèria hiperònica

Les propietats i la composició de la matèria densa a densitats supranuclears determina el comportament estàtic i dinàmic dels estels de neutrons [Gl92, La91, Co94, Kn95, Pr97]. L'estudi de la matèria densa a densitats i temperatures extremes ha rebut un interès renovat degut a la possibilitat d'assolir aquestes condicions en les col.lisions relativistes d'ions pesats a GSI, Brookhaven (BNL) i al CERN.

Es creu que a densitats extremadament altes pot tenir lloc una transició de matèria hadrònica a matèria de quarks. El punt de transició i les seves característiques depenen crucialment de l'Equació d'Estat de la matèria en totes dues fases. És ben conegut que la presència d'estranyesa, en forma d'hiperons (Λ, Σ, Ξ) o mesons (K^-) fa més suau l'Equació d'Estat i enderrerirà la transició. Moltes investigacions s'han fet dins del marc d'aproximació de camp mig [El95, Sc96] o utilitzant interaccions efectives de Skyrme [Ba97]. Les teories microscòpiques intenten obtenir les propietats dels hadrons en matèria densa a partir de la interacció nua a l'espai lliure. En aquest sentit, la teoria de Brueckner va permetre entendre les propietats de la matèria nuclear no estranya a partir d'interaccions realistes.

Un primer intent d'incorporar l'estranyesa en forma d'hiperons dins de la teoria de Brueckner pot trobar-se a les referències [Sc95, Sc98]. En aquest treballs no es va tenir en compte el paper de la interacció hiperó-hiperó, de manera que els resultats pels potencials monoparticulars i de l'energia per barió amb una quantitat finita d'hiperons s'han de considerar com simplement orientatius.

Els recents potencials barió-barió (NSC97a-f) pel octet complet de barions desenvolupats pel grup de Nijmegen [St99], han permès la incorporació de la interacció hiperó-hiperó als càlculs microscòpics de matèria densa amb una fracció no nula d'hiperons [St99b]. Per tal de tenir en compte alhora totes les possibles interaccions barió-barió s'ha de solucionar l'equació de Bethe–Goldstone en canals acoblats pels diferents sectors d'estranyesa: nucleó-nucleó NN ($S = 0$), hiperó-nucleó YN ($S = -1, -2$) i hiperó-hiperó YY ($S = -2, -3$ i -4). El treball presentat a [St99b] es va concentrar principalment en sistemes saturats d'isospín, és a dir, sistemes amb la mateixa fracció de partícules dins del mateix isomultiplet. En aquest sentit, les complicacions associades als diferents mars de Fermi es van evitar de forma que la matriu G de cada sector d'estranyesa fos independent de la tercera component d'isospín.

No obstant això l'estudi microscòpic de la matèria β-estable dels estels de neutrons amb hiperons requereix el tractament de matèria altament asimètrica tant en el sector no estrany com en l'estrany.

En aquest capítol estenem l'estudi de [St99] per tal de permetre qualsevol fracció de les diferents espècies [Vi00] i explorarem l'efecte de la interacció hiperó-hiperó en els potencials monoparticulars dels hiperons, centrant-nos en situacions rellevants per l'estudi dels estels de neutrons.

La matriu G que descriu la transició $B_1B_2 \rightarrow B_3B_4$ s'obté a partir de la interacció nua barió-barió resolent l'anomenada equació de Bethe–Goldstone

$$\begin{aligned} \langle B_3B_4|G|B_1B_2\rangle &= \langle B_3B_4|V|B_1B_2\rangle \\ &+ \sum_{B_5B_6} \langle B_3B_4|V|B_5B_6\rangle \frac{Q_{B_5B_6}}{\omega - E_{B_5} - E_{B_6} + i\eta} \langle B_5B_6|G|B_1B_2\rangle \ . \end{aligned} \tag{R.1}$$

En comparació amb el cas purament nucleònic, aquest problema és més complicat degut a la seva estructura de canals acoblats: mentre pels sectors d'estranyesa 0 i -4 només hi ha un canal, NN → NN i $\Xi\Xi \rightarrow \Xi\Xi$, respectivament; en el d'estranyesa -1 (-3) n'hi ha tres: ΛN → ΛN, ΣN → ΣN i ΛN → ΣN ($\Xi\Lambda \rightarrow \Xi\Lambda$, $\Xi\Sigma \rightarrow \Xi\Sigma$ i $\Xi\Lambda \rightarrow \Xi\Sigma$); i en el d'estranyesa -2, nou: $\Lambda\Lambda \rightarrow \Lambda\Lambda$, $\Lambda\Lambda \rightarrow \Xi$N, $\Lambda\Lambda \rightarrow \Sigma\Sigma$, ΞN → ΞN, ΞN → $\Sigma\Sigma$, $\Sigma\Sigma \rightarrow \Sigma\Sigma$, ΞN → $\Lambda\Sigma$, $\Lambda\Sigma \rightarrow \Lambda\Sigma$ i $\Lambda\Sigma \rightarrow \Sigma\Sigma$.

El potencial monoparticular U_{B_i} que sent un barió B_i inmers en el mars de Fermi de barions $B_1, B_2, \cdots$ ve donat a l'aproximació de Brueckner–Hartree–Fock per

$$U_{B_i} = \mathrm{Re} \sum_{B_j} \sum_{k_j \leq k_{F_j}} \langle B_iB_j|\, G(\omega = E_{B_i} + E_{B_j})\, |B_iB_j\rangle_{\mathcal{A}} \ , \tag{R.2}$$

on

$$E_{B_i} = T_{B_i} + U_{B_i} + M_{B_i} \ , \tag{R.3}$$

essent T_{B_i} l'energia cinètica del barió B_i.

L'enegia total per barió ve donada per

$$\frac{E}{A} = \frac{\epsilon}{\rho} = \frac{2}{\rho} \sum_{B_i} \int_0^{k_{F_i}} \frac{d^3k}{(2\pi)^3} \left(M_{B_i} + \frac{\hbar^2 k^2}{2M_{B_i}} + \frac{1}{2} U_{B_i}(k) \right) \tag{R.4}$$

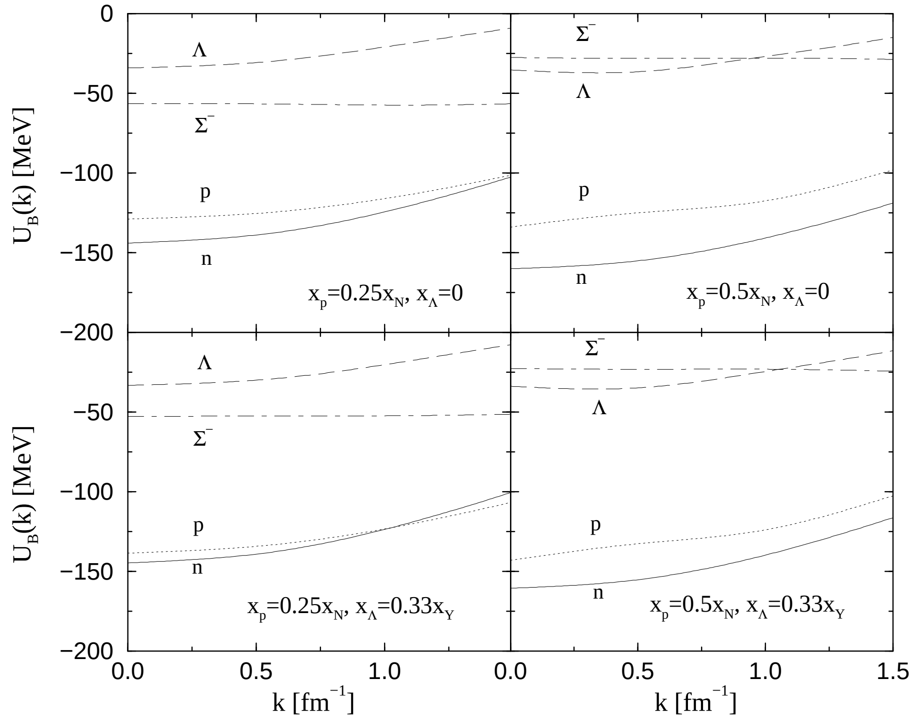

Figura R.1: Potencial monoparticular dels neutrons, protons, Λ i Σ^- a $\rho = 0.6$ fm^{-3} i una fracció d'hiperons $x_Y = 0.1$. El panells de la dreta corresponen a matèria nuclear simètrica, $x_n = x_p = 0.5x_N$, mentre que els de l'esquerra mostren resultats per matèria asimètrica amb $x_n = 3x_p = 0.75x_N$. Als panells superiors la fracció d'hiperons composta és exclusivament per Σ^- ($x_{\Sigma^-} = x_Y$), mentre que als inferiors l'estranyesa es reparteix entre Σ^-'s ($x_{\Sigma^-} = 2x_Y/3$) i Λ's ($x_\Lambda = x_Y/3$).

i els potencials químics dels diferents barions, agafats iguals a les seves corresponents energies de Fermi, per

$$\mu_B = E_B(k_{F_B}) = M_B + T_B(k_{F_B}) + U_B^N(k_{F_B}) + U_B^Y(k_{F_B}) \ , \tag{R.5}$$

on el superíndex en els potencials es refereix a la interacció del barió B amb els nucleons (N) o amb els hiperons (Y).

A la figura R.1 mostrem el potencial monoparticular dels neutrons, protons, Λ i

Σ^- a $\rho = 0.6$ fm^{-3} i una fracció d'hiperons $x_Y = 0.1$ composta exclusivament a Σ^-, $x_{\Sigma^-} = x_Y$, (panells superiors), o repartida entre Σ^-'s i Λ's en una proporció $2 : 1$ (panells inferiors). Els panells de la dreta corresponen a matèria nuclear simètrica, $x_n = x_p = 0.5x_N$, mentre que els de l'esquerra mostren resultats per matèria asimètrica amb $x_n = 3x_p = 0.75x_N$. La presència de la Σ^- trenca la simetria entre protons i neutrons. Els neutrons es fan més atractius. Això es degut al diferent comportament de la interacció $\Sigma^- n$, que només rep contribucions del canal ΣN d'isospín $T = 3/2$ que és molt atractiu, mentre la interacció $\Sigma^- p$ també rep contribucions del canal ΣN d'isospín $T = 1/2$ que és molt repulsiva. Quan anem a una situació asimètrica s'observa que la Σ^- es fa més atractiva degut al major nombre de parelles $\Sigma^- n$. La Λ perd atracció en moure'ns de la situació simètrica a l'asimètrica perque el mar de Fermi dels neutrons és més gran i la seva contribució al potencial monoparticular de la Λ explora regions de moment relatiu més alt que són menys atractives. Donat que els mars de Fermi dels hiperons són petits, les diferencies observades quan substituïm algunes Σ^- per Λ són petites.

Per tal de veure la influència de la interacció hiperó-hiperó, a les figures R.2 i R.3 mostrem les contribucions dels diferents barions als potencials monoparticulars de la Λ i la Σ^- respectivament, per una densitat $\rho = 0.6$ fm^{-3} i una fracció d'hiperons $x_Y = 0.1$ repartida entre Σ^-'s i Λ's en una proporció $2 : 1$. En el cas de la Λ, podem veure que la contribució de la pròpia Λ és atractiva i gairebé menyspreable; per altra banda la contribució de la Σ^- és comparable a les dels protons i neutrons. Això és un exemple clar de la importància que la interacció hiperó-hiperó té sobre les propietats de la Λ. Aquesta adquireix més atracció i apareix a la matèria densa a densitats més baixes que quan aquesta interacció no es considera.

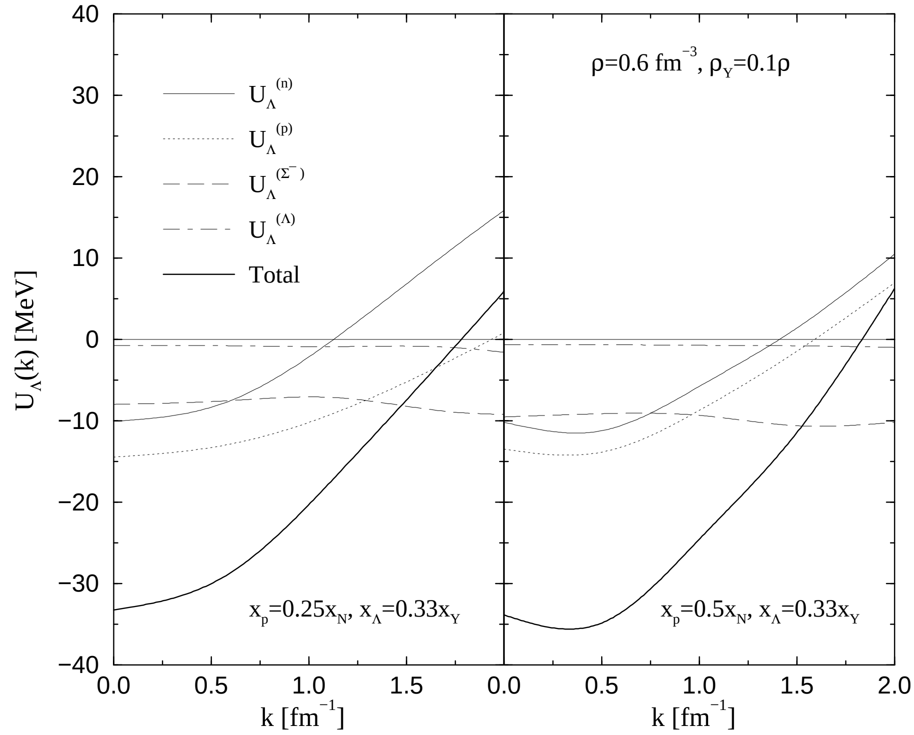

Figura R.2: Contribucions al potencial monoparticular de l'hiperó Λ a $\rho = 0.6$ fm^{-3}, fracció d'hiperons $x_Y = 0.1$ amb $x_{\Sigma^-} = 2x_Y/3$ i $x_\Lambda = x_Y/3$, per matèria simètrica (panell dret) i asimètrica (panell esquerra).

Les diferents contribucions al potencial monoparticular de la Σ^- es mostren a la figura R.3. La Λ contribueix molt poc donat que el seu mar de Fermi és molt petit. La contribució dels parells $\Sigma^-\Sigma^-$ és molt important i esdevé crucial degut al fet que les contribucions de neutrons i protons gairebé cancelen una a l'altra.

Finalment a la figura R.4 es pot veure l'energia per barió en funció de la densitat bariònica. Els panells de la dreta i l'esquerra mostren resultats per matèria nuclear simètrica i asimètrica ($x_n = 3x_p = 0.75x_N$), respectivament. Als panells superiors, es donen resultats per $x_{\Sigma^-} = 0$ i diversos valors de la densitat de Λ, ρ_Λ. Als panells inferiors es considera $x_\Lambda = 0$ i es varia la concentració de Σ^-. L'energia per barió és el

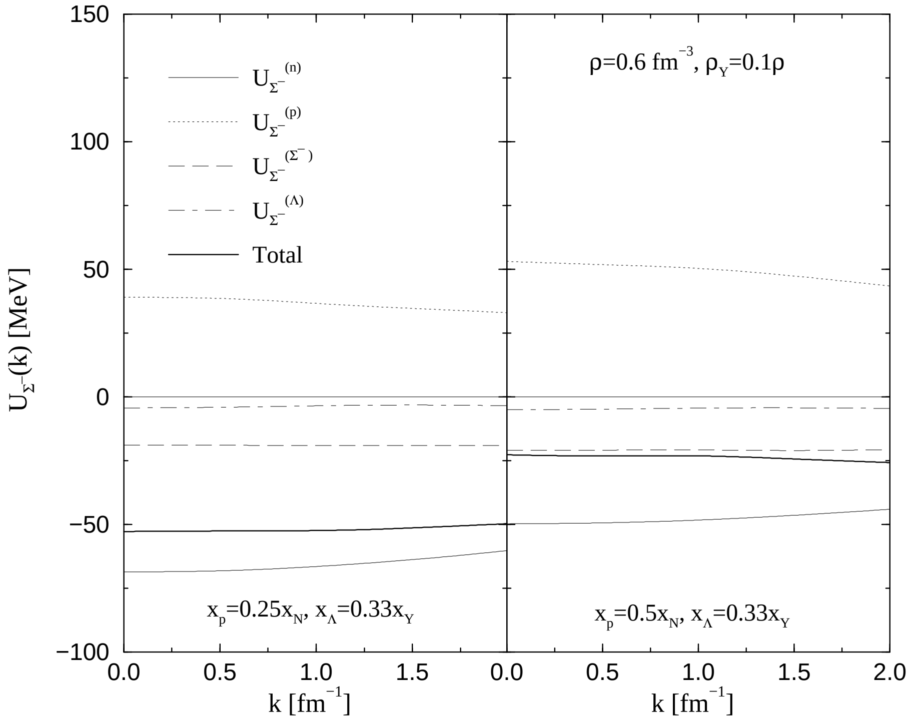

Figura R.3: Contribucions al potencial monoparticular de l'hiperò Σ^-. Les condicions són les mateixes que les de la figura R.2.

resultat d'un balanç entre l'energia cinètica promig de cada mar de Fermi dels barions i de la contribució de les interaccions mútues, donada per un promig sobre el potencial monoparticular de cada espècie. Per tal d'identificar els efectes de la interacció hiperó-hiperó sobre l'energia per barió, hem inclòs també una corba que correspon a un càlcul on el percentatge d'hiperons és d'un 10% (Λ o Σ^-) on la interacció hiperó-hiperó no s'ha tingut en compte. En tots dos casos, quan es desconnecta la interacció hiperó-hiperó es perd energia de lligam. El punt de saturació de l'energia per barió es veu poc afectat quan s'incrementa la fracció d'hiperons. Quan una petita quantitat de nucleons se substitueix per hiperons, automàticament es produeix una disminució de la contribució d'energia cinètica degut que els hiperons poden acomodar-se en estats

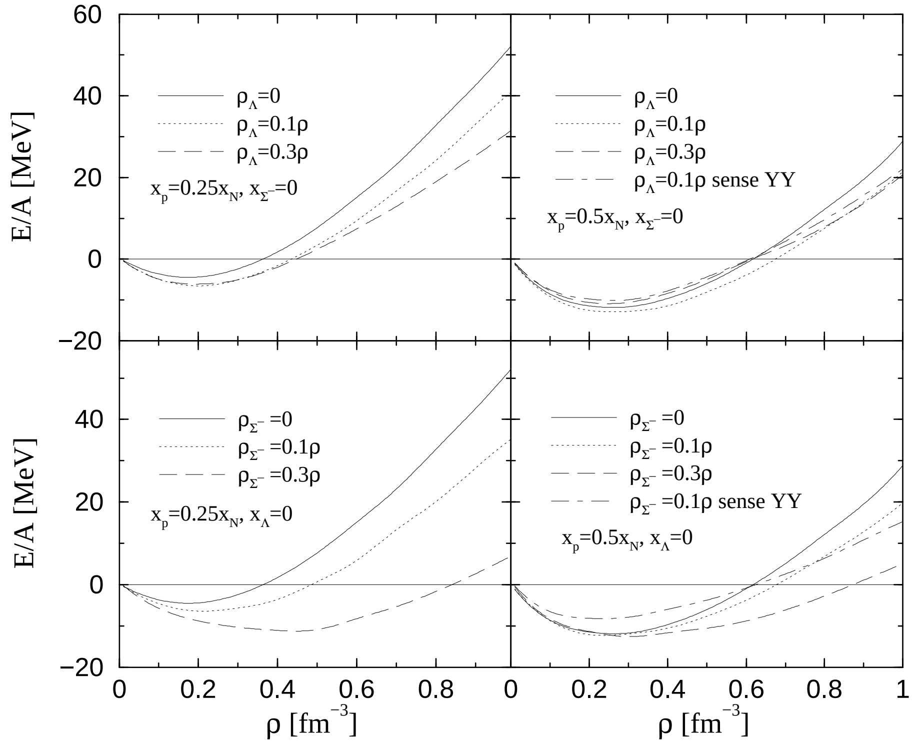

Figura R.4: Energia per barió en funció de la densitat bariònica.

de moment més baix i a més són més massius. Tot i que les interaccions ΛN i $\Lambda\Lambda$ són clarament menys atractives que la NN, la reducció en l'energia cinètica és suficient per compensar la pèrdua de lligam quan un 10% de nucleons són substituits per Λ's. No obstant això, per una fracció $x_\Lambda = 30\%$ la pèrdua d'energia cinètica no és suficient per compensar aquesta pèrdua d'atracció. Si mirem als panells inferiors on tots els hiperons són Σ^-, s'observa més lligam que respecte al cas on només hi ha Λ. Això és degut, bàsicament, a la major pèrdua d'energia cinètica perquè la massa de la Σ^- és més gran. En general, la substitució de nucleons per hiperons produeix un guany en energia de lligam i una suavització de l'Equació d'Estat, que tindrà conseqüències molt importants en l'estructura dels estels de neutrons.

3. Propietats dels hiperons als nuclis finits

Els hipernuclis són sistemes lligats de neutrons, protons i un o més barions estranys, tals com els hiperons Λ, Σ o Ξ. Entendre el comportament dels hipernuclis (com es produeixen, la seva espectroscopia i els seus mecanismes de desintegració) ha estat intensament investigat durant les darreres dècades, veure per exemple les referències [Ga77, Po78, Ba85, Do89, Os90, Co90, Ba90, Gi95, Ak97, Os98].

Un dels principals objectius d'aquests estudis ha estat explorar com la presència de l'estranyesa pot alterar i ampliar el coneixement adquirit de la física nuclear convencional. D'aquests esforços han emergit diverses característiques de les propietats monoparticulars de l'hiperó Λ en el nucli. És ben acceptat que la profunditat del potencial Λ-nucli es ~ -30 MeV, que és uns 20 MeV menys atractiu que el corresponent nucleó-nucli. S'ha trobat que el desdoblament espín-òrbita dels nivells monoparticulars de l'hiperó Λ és típicament més d'un ordre de magnitud més petit que el corresponent pels nucleons. A més, l'hiperó Λ, al contrari que el nucleó, manté el seu caràcter monoparticular fins i tot per estats molt per sota de la superfície de Fermi [Pi91, Ha96], cosa que indica una interacció més feble amb els altres nucleons. Els estudis sobre la desintegració mesònica del hipernuclis Λ lleugers [Mo91, St93, Ku95] han mostrat que les dades [Sz91] són favorables a un potencial Λ-nucli que mostra una repulsió a curtes distàncies. Això sembla ser també una característica del potencial Σ-nucli per hipernuclis Σ lleugers [Ha90].

Des del punt de vista teòric, s'han fet diverses aproximacions per tal de derivar les propietats dels hiperons en nuclis finits. Tradicionalment la gent ha utilitzat potencials de tipus Woods-Saxon [Bo76, Do80, Mo88] que reprodueixen força bé les energies mesurades per la Λ en hipernuclis mitjans i pesats. Les no localitats i els efectes depenents de la densitat han estat inclosos en càlculs Hartree–Fock no relativistes amb forces de Skyrme hiperó-nucleó [Ya88, Mi88, Fe89, La97] per tal de millorar l'ajust de les energies monoparticulars. Els hipernuclis també han estat estudiats dins del marcs relativistes, com la fenomenologia de Dirac [Br81, Ch91] o la teoria relativista de camp mig [Ma89b, Ma94, Lo95, Gl93, In96, Su94, Ma96, Ya85]. També s'han realitzat càlculs microscòpics de l'estructura d'hipernuclis [Ha93, Ha93b].

El nostre treball segueix aquesta darrera aproximació amb l'objectiu de comprovar les interaccións hiperó-nucleó actuals (Jülich B [Ho89], NSC89 [Ma89] i NSC97a-f [Ri99, St99]). A tal efecte, hem evaluat l'energia i les funcions d'ona dels estats monoparticulars $1s_{1/2}$, $1p_{3/2}$ i $1p_{1/2}$ de l'hiperó Λ en diversos hipernuclis des de l'${}^{5}_{\Lambda}$He fins el ${}^{209}_{\Lambda}$Pb. La comparació amb l'experiment pot ajudar a restringir la interacció hiperó-nucleó. El punt de partida d'aquest treball és una matriu G avaluada a matèria nuclear per una densitat i una energia inicial fixes. Aquesta matriu G s'utilitza per construir una matriu G al nucli finit que després s'utilitzarà per tal d'avaluar l'autoenergia de l'hiperó al nucli. Finalment, la part real d'aquesta autoenergia es fa servir com a potencial no local en una equació de Schrödinger per tal d'obtenir les energies i les funcions d'ona dels diferents orbitals.

Una possible manera de construir la matriu G_{NF} al nucli finit és resoldre la seva corresponent equació de Bethe–Golstone,

$$G_{NF} = V + V \left(\frac{Q}{E}\right)_{NF} G_{NF} \ . \tag{R.6}$$

No obstant això, podem treure profit del fet que ja hem obtingut una matriu G a matèria nuclear, i intentar trobar la matriu G_{NF} del nucli finit relacionant-la amb la de matèria nuclear. Recordant que la corresponent matriu G de matèria nuclear ve donada per

$$G = V + V \left(\frac{Q}{E}\right)_{MN} G \; , \tag{R.7}$$

podem eliminar la interacció nua V a les equacions anteriors per obtenir G_{NF} mitjantçant la següent equació integral

$$\begin{aligned} G_{NF} &= G + G \left[\left(\tfrac{Q}{E}\right)_{NF} - \left(\tfrac{Q}{E}\right)_{MN}\right] G_{NF} \\ &= G + G \left[\left(\tfrac{Q}{E}\right)_{NF} - \left(\tfrac{Q}{E}\right)_{MN}\right] G + \\ &+ G \left[\left(\tfrac{Q}{E}\right)_{NF} - \left(\tfrac{Q}{E}\right)_{MN}\right] G \left[\left(\tfrac{Q}{E}\right)_{NF} - \left(\tfrac{Q}{E}\right)_{MN}\right] G + \dots \; , \end{aligned} \tag{R.8}$$

que involucra la matriu G de matèria nuclear i la diferència entre els propagadors de nucli finit i matèria nuclear. Aquesta última té en compte els estats intermitjos rellevants. L'expansió (R.8) pot tallar-se a segon ordre perquè la diferència entre els propagadors és de fet bastant petita. Per tant es té

$$G_{NF} \simeq G + G \left[\left(\frac{Q}{E}\right)_{NF} - \left(\frac{Q}{E}\right)_{MN}\right] G \; . \tag{R.9}$$

En l'aproximació de Brueckner–Hartree–Fock l'autoenergia en nucli finit dels hiperons Λ o Σ pot escriure's esquemàticament de la forma

$$\begin{aligned} \Sigma^{BHF} &= \sum_N \langle YN|G_{NF}|YN\rangle \simeq \sum_N \langle YN|G|YN\rangle \\ &+ \sum_{Y'N} \langle YN|G|Y'N\rangle \left[\left(\frac{Q}{E}\right)_{NF} - \left(\frac{Q}{E}\right)_{MN}\right] \langle Y'N|G|YN\rangle \; , \end{aligned} \tag{R.10}$$

que es pot descomposar, com es pot veure a l'equació i a la figura R.5, en la suma d'una

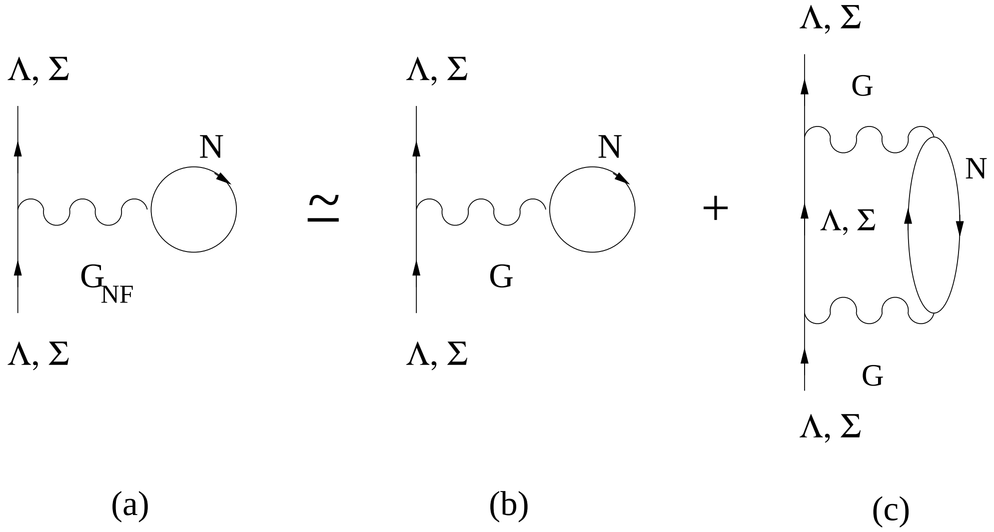

Figura R.5: Aproximació Brueckner–Hartree–Fock de l'autoenergia de l'hiperó al nucli finit (diagrama (a)), descomposada en la suma d'una contribució de primer ordre (diagrama (b)), i una correcció $2p1f$ (diagram (c)).

contribució de primer ordre representada pel diagrama b, i la correcció dues partícules i un forat ($2p1f$) representada pel diagrama c. Aquesta autoenergia és no local i depèn de l'energia de l'estat inicial.

Primerament, hem de comprovar l'estabilitat dels nostres resultats en front de variacions de la densitat nuclear i l'energia inicial utilitzades en el càlcul de la matriu G de matèria nuclear. A tal efecte a les Taules R.1 i R.2 es mostra respectivament l'energia de lligam de la Λ en ${}^{17}_{\Lambda}$O per diferents valors de la densitat i de l'energia inicial obtinguda amb les interaccions Jülich B i NSC89. Com es pot veure, els termes de primer i segon ordre depenen fortament d'aquests paràmetres, la qual cosa és una indicació que els efectes de densitat són importants quan es té en compte el tamany finit del nucli. Tot i això, el càlcul total fins a segon ordre dóna resultats molt estables.

Un cop el nostre mètode ha estat comprovat, és el moment d'estudiar la sistemàtica

$\omega = -50$ MeV	Jülich B		NSC89	
k_F (fm^{-1})	1^{er}	$1^{er} + 2p1f$	1^{er}	$1^{er} + 2p1f$
1.00	-13.71	-11.74	-9.33	-7.30
1.25	-12.56	-11.83	-7.66	-7.34
1.36	-11.73	-11.84	-5.59	-7.36

Taula R.1: Dependència de l'energia monoparticular de l'hiperó Λ en ${}^{17}_{\Lambda}$O en el moment de Fermi de la matriu G de matèria nuclear. En la nostra notació $\omega = \langle B_N \rangle + B_\Lambda(k=0)$, on $\langle B_N \rangle = -50$ MeV. Les unitats venen donades en MeV.

$k_F = 1.36$ fm^{-1}	Jülich B		NSC89	
ω (MeV)	1^{er}	$1^{er} + 2p1f$	1^{er}	$1^{er} + 2p1f$
-100	-9.25	-11.85	-3.83	-7.43
-80	-10.15	-11.83	-4.76	-7.39
-50	-11.73	-11.84	-5.59	-7.36

Taula R.2: Dependència de l'energia monoparticular de l'hiperó Λ en ${}^{17}_{\Lambda}$O en l'energia inicial de la matriu G de matèria nuclear.

de les energies de lligam de la Λ a través de la taula periòdica. A la Taula R.3 presentem resultats obtinguts amb les interaccions Jülich B i NSC89. La comparació amb les dades experimentals és bastant bona, especialment per l'orbital $1s_{1/2}$. Cal notar que, d'acord amb la informació empírica, el desdoblament espín-òrbita és molt petit. En el cas de la interacció de Jülich notem que l'orbital $1p_{1/2}$ és més lligat que l'orbital $1p_{3/2}$, la qual cosa és una característica de l'estructura d'espín de la interacció de Jülich.

Finalment, a la figura R.6, mostrem la funció d'ona de l'orbital $1s_{1/2}$ de la Λ en ${}^{13}_{\Lambda}$C, ${}^{17}_{\Lambda}$O i ${}^{41}_{\Lambda}$Ca, obtinguda a partir de la nostra autoenergia no local (línies contínues) o a partir d'un potencial local de tipus Woods-Saxon (línies discontínues) de profunditat -30.2 MeV i un radi ajustat a reproduir la mateixa energia de lligam. Tot i això, com es pot veure, la nostra funció d'ona és més estesa i això pot tenir conseqüències impor-

Nucli	Orbital	Jülich B		NSC89		Exp.
		1^{er}	$1^{er}+2p1f$	1^{er}	$1^{er}+2p1f$	
${}^{5}_{\Lambda}$He						(${}^{5}_{\Lambda}$He)
	$1s_{1/2}$	-1.43	-2.28	-0.04	-0.58	-3.12
${}^{13}_{\Lambda}$C						(${}^{13}_{\Lambda}$C)
	$1s_{1/2}$	-7.93	-9.48	-3.42	-5.69	-11.69
${}^{17}_{\Lambda}$O						(${}^{16}_{\Lambda}$O)
	$1s_{1/2}$	-10.15	-11.83	-4.76	-7.39	-12.5
	$1p_{3/2}$		-0.87			-2.5 ($1p$)
	$1p_{1/2}$	-0.08	-1.06			
${}^{41}_{\Lambda}$Ca						(${}^{40}_{\Lambda}$Ca)
	$1s_{1/2}$	-16.85	-19.60	-10.24	-15.04	$-20.$
	$1p_{3/2}$	-6.70	-9.64	-3.07	-6.92	$-12.$ ($1p$)
	$1p_{1/2}$	-6.92	-9.92	-2.33	-6.29	
${}^{91}_{\Lambda}$Zr						(${}^{89}_{\Lambda}$Zr)
	$1s_{1/2}$	-22.24	-25.80	-16.35	-22.77	$-23.$
	$1p_{3/2}$	-14.74	-18.19	-10.13	-17.08	$-16.$ ($1p$)
	$1p_{1/2}$	-14.86	-18.30	-9.73	-16.68	
${}^{209}_{\Lambda}$Pb						(${}^{208}_{\Lambda}$Pb)
	$1s_{1/2}$	-26.28	-31.36	-23.58	-29.52	$-27.$
	$1p_{3/2}$	-21.22	-27.13	-21.42	-26.01	$-22.$ ($1p$)
	$1p_{1/2}$	-21.30	-27.18	-21.18	-25.72	

Taula R.3: Energies de lligam de la Λ (en MeV) en els orbitals $1s_{1/2}$, $1p_{3/2}$ i $1p_{1/2}$ per diferents nuclis. Les dades experimentals han estat agafades de [Ba90, Pi91, Ha96]. Es mostren resultats per les interaccions Jülich B i NSC89.

tants en la desintegració mesònica dels hipernuclis. Només si permetem al potencial Woods-Saxon tenir una profunditat inferior (-23.11, -23.56 i -27.84 MeV respectivament) i un radi més gran podrem no solament reproduir l'energia de lligam sino també maximitzar el solapament de les funcions d'ona resultants (línies discontínues amb punts) amb la nostra. De fet s'ha observat que les probabilitats de desintegració d'hipernuclis lleugers, tals com ${}^{4}_{\Lambda}$H, ${}^{4}_{\Lambda}$He i ${}^{5}_{\Lambda}$He, poden reproduir-se millor si la funció

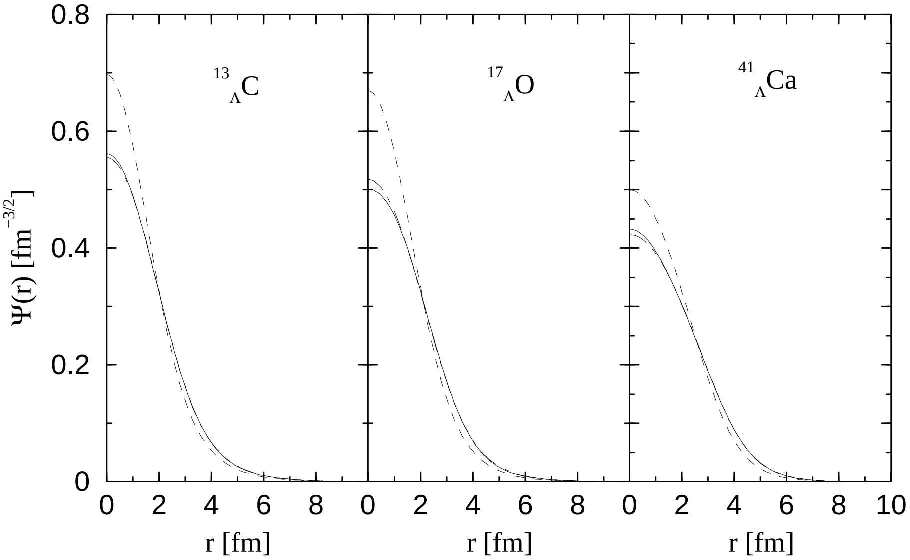

Figura R.6: Funció d'ona $1s_{1/2}$ de la Λ en $^{13}_{\Lambda}$C, $^{17}_{\Lambda}$O i $^{41}_{\Lambda}$Ca, obtinguda a partir de l'autoenergia de la Λ (línies contínues) comparada amb les obtingudes a partir d'un potencial Woods-Saxon de profunditat fixa (línies discontínues) o a partir d'un Woods-Saxon amb el radi i la profunditat ajustats per reproduir l'energia i maximitzat el solapament amb la funció d'ona obtinguda amb l'autoenergia (línies discontínues amb punts). La interacció de Jülich s'ha fet servir en tots els casos.

d'ona de la Λ és empesa cap a la superfície del nucli. Això afavoriria la desintegració mesònica d'hipernuclis perquè la Λ exploraria regions amb densitats nuclears més petites i els efectes del bloqueig de Pauli serien menys pronunciats. Les implicacions dels nostres resultats en la desintegració mesònica d'hipernuclis Λ és fora dels objectius d'aquesta tesi però seran explorats en un futur.

4. Matèria dels estels de neutrons

Els estels de neutrons ofereixen una interessant conexió entre els processos nuclears i els observables astrofísics. Les condicions de la matèria a l'interior d'aquests objectes són molt diferents de les que hom pot trobar a la Terra, per tant és necessari un bon coneixement de l'Equació d'Estat a tan altes densitats per tal de compendre les propietats dels estels de neutrons. A densitats properes a la densitat normal de saturació ($\rho_0 \sim 0.16$ fm^{-3}) la matèria es composa fonamentalment de neutrons, protons i electrons en equilibri β, perquè els neutrins tenen, en promig, un camí lliure més gran que el radi de l'estel de neutrons. Les condicions d'equilibri venen donades en aquest cas per

$$\mu_n = \mu_p + \mu_e \qquad \rho_p = \rho_e \ . \tag{R.11}$$

Un cop el potencial químic de l'electró supera la massa en repòs del muó ($M_\mu =$ 105.7 MeV), és energèticament més favorable per un electró a la superfície de Fermi decaure en un muó via el procès feble $e^- \rightarrow \mu^- + \bar{\nu}_\mu + \nu_e$. Llavors es comença a desenvolupar un mar de Fermi de muons i en conseqüència, el balanç de càrrega es modifica d'acord amb $\rho_p = \rho_e + \rho_\mu$ i, a més, es requereix $\mu_e = \mu_\mu$.

Quan la densitat augmenta, poden aparèixer nous graus de llibertat tals com condensats de pions o de kaons, matèria de quarks o hiperons. La presència d'aquests darrers en la matèria dels estels de neutrons i la seves implicacions en les propietats dels estels de neutrons és el tema del present capítol.

Contràriament al que passa a la Terra, on els hiperons són inestables i decauen en nucleons mitjantçant la interacció feble, les condicions d'equilibri a l'interior dels estels de neutrons poden fer que passi el procès invers, de forma que la formació d'hiperons resulti energèticament favorable. Tan aviat com el potencial químic del neutró es fa suficientment gran, neutrons energètics poden decaure en hiperons Λ via processos febles que no conserven l'estranyesa, donant lloc a un mar de Fermi d'hiperons Λ amb

$\mu_\Lambda = \mu_n$. No obstant, hom espera que l'hiperó Σ^- aparegui mitjançant el procès

$$e^- + n \rightarrow \Sigma^- + \nu_e \ , \tag{R.12}$$

a densitats més petites que la d'aparició de la Λ, tot i que la Σ^- és més massiva. Els hiperons carregats negativament apareixen a l'estat fonamental de la matèria quan les seves masses es fan iguals a $\mu_n + \mu_e$, mentre que el hiperons neutres, com ara la Λ, ho fan quan la seva massa iguala μ_n. Com que el potencial químic de l'electró és més gran que la diferència de massa entre la Σ^- i la Λ ($M_{\Sigma^-} - M_\Lambda = 81.76$ MeV), l'hiperó Σ^- apareixerà a densitats menors que la de la Λ. Per matèria amb graus de llibertat nucleònics i hiperònics les condicions d'equilibri s'escriuen

$$\begin{aligned} &\mu_{\Xi^-} = \mu_{\Sigma^-} = \mu_n + \mu_e, \\ &\mu_\Lambda = \mu_{\Xi^0} = \mu_{\Sigma^0} = \mu_n, \\ &\mu_{\Sigma^+} = \mu_p = \mu_n - \mu_e \ , \end{aligned} \tag{R.13}$$

i la neutralitat de càrrega imposa

$$\rho_p + \rho_{\Sigma^+} = \rho_e + \rho_\mu + \rho_{\Sigma^-} + \rho_{\Xi^-} \ . \tag{R.14}$$

Els graus de llibertat hiperònics han estat considerats per diversos autors, principalment en el marc de la teoria relativista de camp mig [Kn95, Sc96, Pr97] o utilitzant interaccions efectives parametritzades [Ba97]. Recentment Schulze i col.laboradors [Sc98, Ba00] han realitzat càlculs de molt cossos amb interaccions hiperó-nucleó (YN) realistes per tal d'estudiar el punt d'aparició dels hiperons en la matèria dels estels de neutrons i el paper de les forces a tres cossos. Tot i això, aquests autors no han considerat el paper jugat per la interacció hiperó-hiperó que, nogensmenys, és fonamental des del moment en què apareix el primer hiperó en la matèria, perquè modifica les energies monoparticulars de totes les espècies, i en conseqüència, els potencials químics i les condicions d'equilibri.

En aquest capítol, presentem resultats per a un càlcul microscòpic de tipus Brueckner–Hartree–Fock per matèria β-estable amb graus de llibertat nucleònics i hiperònics, incloent-hi no únicament les interaccions nucleó-nucleó i hiperó-nucleó, sino també les interaccions hiperó-hiperó. Dedicarem una atenció especial al paper jugat per aquestes últimes interaccions.

El nostre estudi s'inicia amb la parametrització més recent de la interacció nua barió-barió per l'octet complet de barions, construïda per Stoks i Rijken [St99]. Aquest potencial descriu tots els sectors d'estranyesa des de $S = 0$ fins a $S = -4$ i està basat en extensions SU(3) de les interaccions nucleó-nucleó (NN) i hiperó-nucleó del grup de Nijmegen. Introduïm els efectes del medi per mitjà de l'anomenada matriu G i resolem les equacions per les energies monoparticulars dels diversos barions de manera autoconsistent.

Per tal de reproduir les propietats de saturació de la matèria nuclear, hem substituit la part purament nucleònica de l'Equació d'Estat per la parametrització que Heiselberg i Hjorth-Jensen [He99] van fer del càlcul variacional de Akmal i col.laboradors [Ak98]

$$\frac{E}{A} = E_{comp}(\rho_N) + S(\rho_N)(1-2x_p)^2 = E_0 u \frac{u-2-\delta}{1+u\delta} + S_0 u^{\gamma}(1-2x_p)^2 \ . \qquad \text{(R.15)}$$

La figura R.7 mostra la composició de la matèria dels estels de neutrons en equilibri β fins a una densitat $\rho = 1.2$ fm^{-3}. Les línies contínues corresponen a un càlcul en

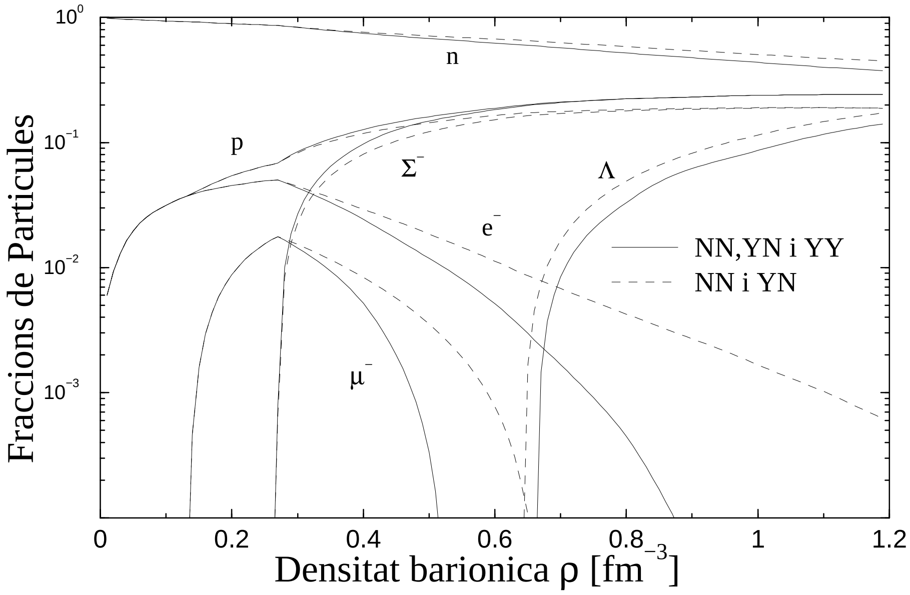

Figura R.7: Composició de la matèria β. Les línies contínues corresponen al cas en què totes les interaccions (nucleó-nucleó, hiperó-nucleó i hiperó-hiperó) es consideren. Les línies discontínues al panell inferior corresponen al cas on la interacció hiperó-hiperó no ha estat tinguda en compte.

què es consideren totes les interaccions, nucleó-nucleó, hiperó-nucleó i hiperó-hiperó. Les línies discontínues mostren el resultat quan la interacció hiperó-hiperó no es té en compte. Els hiperons Σ^- apareixen en els dos casos a la mateixa densitat perquè aquest és el primer hiperó en aparèixer i, per tant, la interacció hiperó-hiperó no juga cap paper per densitats més baixes que la marcada per aquest punt. Hi ha una reducció de la seva fracció quan la interacció hiperó-hiperó no és considerada degut a la absència del canal $\Sigma^-\Sigma^-$ que és fortament atractiu. A més, es pot observar un moderat increment de la fracció de leptons a fi de mantenir la neutralitat de càrrega. D'altra banda, menys hiperons Σ^- impliquen menys parells $\Sigma^- n$, que són molt atractius en aquest model. Això significa que el potencial químic del neutró es fa menys atractiu i en conseqüència, l'hiperó Λ apareix a una densitat més petita, i presenta una fracció

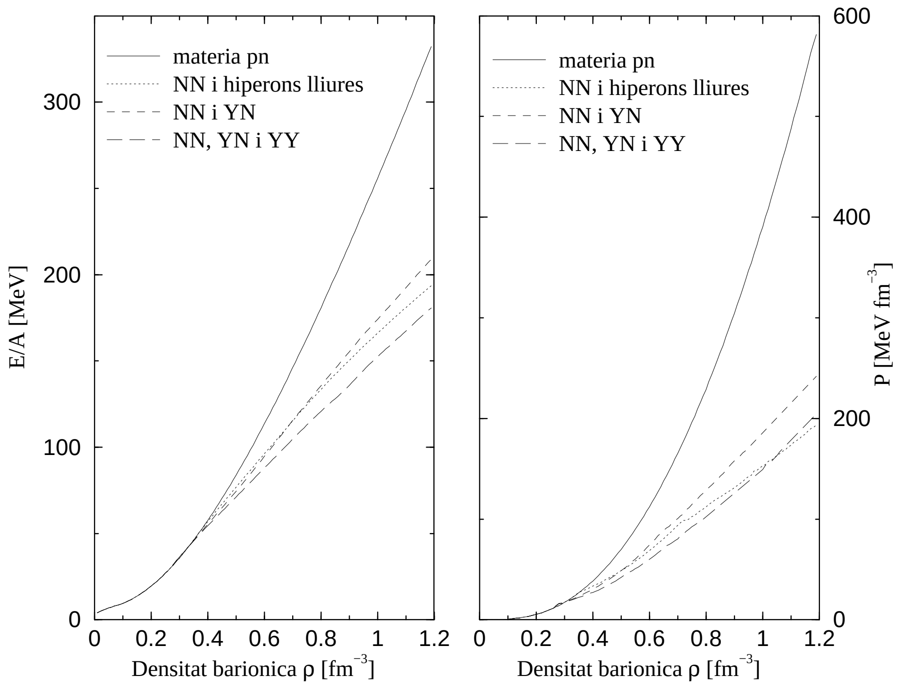

Figura R.8: Energia per barió (panell esquerra) i pressió (panell dret) per matèria β-estable com a funció de la densitat bariònica ρ per quatre escenaris diferents: matèria purament nucleònica; matèria amb nucleons i hiperons lliures; matèria amb nucleons i hiperons que només interaccionen amb nucleons; i matèria amb nucleons i hiperons interaccionant amb nucleons i hiperons. La contribució dels leptons ha estat inclosa en cada cas.

relativa més gran. La figura R.8 mostra l'energia per barió i la pressió per quatre escenaris diferents: matèria purament nucleònica; matèria amb nucleons i hiperons lliures; matèria amb nucleons i hiperons que només interaccionen amb nucleons; i matèria amb nucleons i hiperons interaccionant amb nucleons i hiperons. L'aparició dels hiperons condueix a una considerable suavització de l'Equació d'Estat, què és degut essencialment a una reducció de l'energia cinètica. La interacció hiperó-nucleó té dos efectes. Fins a densitats de l'ordre de ~ 0.72 fm^{-3}, és atractiva i fa l'Equació d'Estat encara més suau. Però per densitats més grans es fa repulsiva i l'Equació

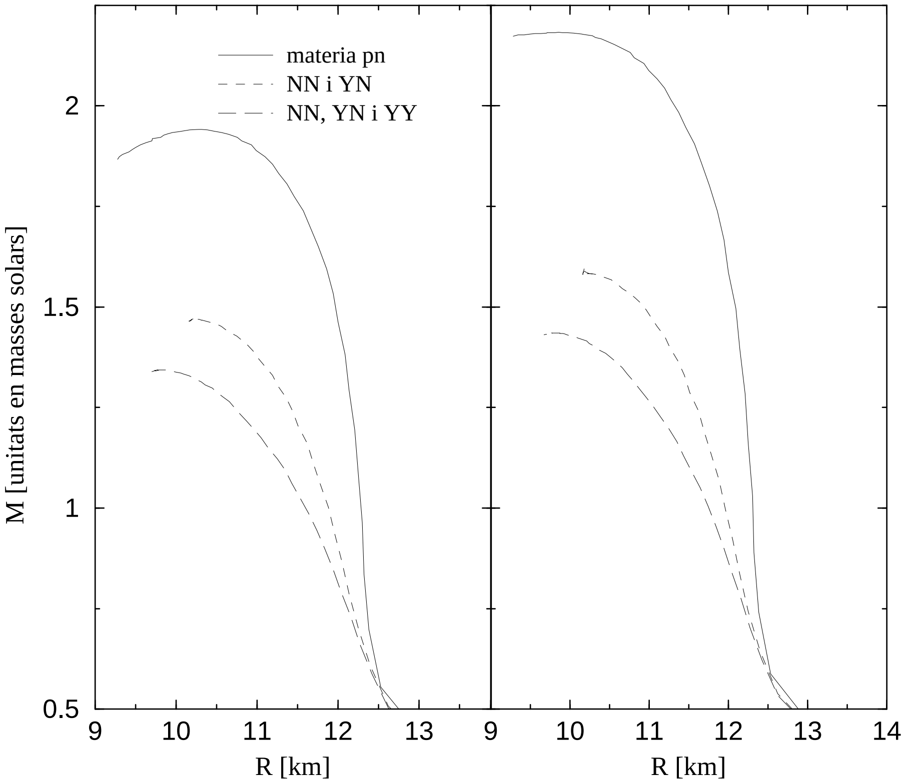

Figura R.9: Relació massa-radi amb (panell dret) i sense (panell esquerra) correccions rotacionals. Notació com a la figura R.8.

d'Estat esdevé més rígida. La interacció hiperó-hiperó és sempre atractiva en tot el rang de densitats explorat i produeix una suavització adicional de l'Equació d'Estat.

Les equacions de Tolman–Oppenheimer–Volkoff [To39, Op39] determinen l'estructura dels estels relativistes

$$\frac{dp(r)}{dr} = -\frac{G}{c^2}\frac{(p(r)+\epsilon(r)c^2)(M(r)c^2+4\pi r^3 p(r))}{r(rc^2-2GM(r))} \tag{R.16}$$

$$\frac{dM(r)}{dr} = 4\pi r^2 \epsilon(r). \tag{R.17}$$

Hem resolt aquestes equacions amb i sense correccions degudes a la rotació dels estels per tres dels quatre escenaris considerats abans. A la figura R.9 mostrem la relació massa-radi obtinguda pels escenaris considerats. L'Equació d'Estat per la matèria β-estable amb només graus de llibertat nucleònics, és la més rígida, i dóna una massa màxima de $1.89 M_{\odot}$ sense correccions rotacionals i $2.11 M_{\odot}$, quan aquestes correccions s'inclouen, on $M_{\odot}$ és la massa del sol. El segon escenari correspon al cas en què permetem la presència dels hiperons, considerem explícitament la interacció hiperó-nucleó, però excloïm la hiperó-hiperó. En aquest cas, sense correccions rotacionals, obtenim una massa màxima de $1.47 M_{\odot}$, mentre que, quan les correccions rotacionals es tenen en compte aquest valor s'incrementa fins $1.60 M_{\odot}$. Aquesta gran reducció, respecte al cas en què només hi ha nucleons al medi, és una conseqüència de la forta suavització de l'Equació d'Estat degut a l'aparició dels hiperons. El darrer escenari inclou també la interacció hiperó-hiperó. Aquesta interacció fa l'Equació d'Estat encara més suau, la qual cosa porta a una reducció adicional de la massa màxima de l'estel. En aquest cas, obtenim una massa màxima de $1.34 M_{\odot}$ quan les correccions rotacionals no són tingudes en compte, i $1.44 M_{\odot}$ quan s'inclouen aquestes correccions. La presència d'altres hiperons a més altes densitats, donaria lloc a una major suavització de l'Equació d'Estat i, en conseqüència, una massa màxima de l'estel encara menor. Com a resum dels nostres resultats a la Taula R.4, mostrem les masses màximes, els radis i els moments d'inèrcia màxims obtinguts pels diferents escenaris.

Tot i que només hem considerat la formació d'hiperons als estels de neutrons, transicions a d'altres graus de llibertat com ara matèria de quarks, o condensats de pions o kaons poden o no tenir lloc als estels de neutrons. No obstant això, voldríem emfatitzar que el mecanisme de formació d'hiperons és, potser, el què té una probabilitat més alta d'ocòrrer a l'interior dels estels de neutrons, a menys que les autoenergies del hiperons

Escenari	Massa Màxima		Radi	I_{max}
	No Correc. Rot.	Amb Correc. Rot.		
NN	1.89	2.11	10.3	101.1
NN YN	1.47	1.60	10.2	65.2
NN YN YY	1.34	1.44	10.0	55.4

Taula R.4: Massa màxima, radi i moment d'inèrcia màxim pels tres escenaris considerats. Les unitats de la massa, el radi i el moment d'inèrcia són respectivament $M_\odot$, km i $M_\odot \text{km}^2$.

resultin fortament repulsives degut a possibles interaccions repulsives hiperó-nucleó i hiperó-hiperó, una repulsió que estaria en contradicció amb les dades actuals sobre hipernuclies [Ba90]. L'Equació d'Estat amb hiperons dóna, tanmateix, una massa màxima al voltant de $1.4M_\odot$, en el límit inferior de les observacions. Això significa que la nostra Equació d'Estat amb hiperons necessita ser més rígida, un fet que a la seva vegada implica la necessitat de termes a molts cossos més complicats que no han estat inclosos en el nostre càlcul, tals com forces a tres cossos entre nucleons i hiperons i/o efectes relativistes.

5. Conclusions

L'objectiu d'aquesta tesi ha estat l'estudi, dins de la teoria de Brueckner–Hartree–Fock, de les propietats de sistemes nuclears finits (hipernuclis) i infinits (matèria hiperònica) amb graus de llibertat hiperònics, i investigar, en el darrer cas, les implicacions que la presència d'estranyesa té en les propietats dels estels de neutrons. El punt de partida pels nostres càlculs tipus Brueckner, ha estat les interaccions hiperó-nucleó Jülich B [Ho89] i Nijmegen Soft-Core 89 [Ma89], i la més recent parametrització de la interacció nua barió-barió per l'octet complet de barions construïda per Stoks i Rijken [St99]. Aquestes tres interaccions es basen en models d'intercanvi mesònic.

Al Capítol 2 vam desenvolupar un formalisme per càlculs microscòpics de tipus Brueckner per matèria nuclear densa amb estranyesa, permetent qualsevol concentració de les diferents espècies de barions. Les principals conclusions d'aquest capítol poden resumir-se com segueix

- Hem obtingut, en situacions no saturades d'isospín, la dependència de la matriu G de dues espècies qualsevol en la tercera component de l'isospín M_T relacionant l'operador de Pauli amb els diferents parells de partícules que contribueixen al canal particular d'isospín T i tercera component M_T. Hem vist, tanmateix, que aquesta dependència és bastant petita a fi de permetre una estratègia de càlcul més simple que consisteix en obtenir les interaccions efectives als sistemes saturats d'isospín ($k_{F_n} = k_{F_p}$, $k_{F_{\Sigma^-}} = k_{F_{\Sigma^0}} = k_{F_{\Sigma^+}}$, $k_{F_{\Xi^-}} = k_{F_{\Xi^0}}$) i integrant després sobre els respectius mars de Fermi de cada espècie per obtenir els potentials monoparticulars.
- Hem estudiat la dependència dels potencials monoparticulars en les asimetries nucleòniques i hiperòniques, centrant-nos en situacions rellevants en estudis de la matèria β-estable amb contingut d'estranyesa. Hem trobat que la presència dels hiperons, especialment la Σ^-, modifica substancialment els potencials monoparticulars dels nucleons. Els neutrons senten un augment en la seva atracció degut a la interacció efectiva $\Sigma^- n$ que únicament passa per mitjà del canal ΣN d'isospín $T = 3/2$ que és molt atractiu, mentre que els protons senten una repulsió perquè els parells $\Sigma^- p$ també reben contribucions del canal ΣN d'isospín $T = 1/2$, que és molt repulsiu.

- Descomposant els potentials monoparticulars de la Λ i la Σ^- en les contribucions degudes a les diferents espècies, hem vist la importància de considerar la interacció hiperó-hiperó (YY). Hem trobat, per la situació particular de densitat bariònica total $\rho = 0.6$ fm^{-3} amb un 10% d'estranyesa repartida entre Σ^- i Λ en una proporció $2:1$ i una fracció de protons $x_p = 0.25x_N$, que la contribució dels hiperons al potencial monoparticular de la Λ a moment zero és de l'ordre d'un terç del total $U_\Lambda(0)$, i per la Σ^- és d'un mig del total $U_{\Sigma^-}(0)$.

Al Capítol 3 hem analizat un mètode per obtenir la interacció efectiva hiperó-nucleó al nucli finit basat en una expansió sobre la matriu G calculada a matèria nuclear a una densitat i una energia inicial fixades. L'objectiu d'aquest estudi ha estat establir un marc de confiança per càlculs d'estructura hipernuclear amb l'idea d'obtenir informació sobre la interacció hiperó-nucleó, complementària a la proporcionada pels experiments de dispersió hiperó-nucleó. Les conclusions corresponents a aquest capítol són les següents

- Truncant l'expansió sobre la matriu G de matèria nuclear al segon ordre, obtenim resultats que són molt estables enfront de variacions de la densitat i l'energia inicial utilitzades en el càlcul de la matriu G, i en l'espectre (discontinu o continu) escollit per resoldre l'equació de Bethe–Goldstone.

- Tots dos ordres, primer i segon, depenen bastant d'aquells paràmetres (densitat i energia inicial). Això és una indicació que els efects de dependència en densitat considerats en tractar explícitament el tamany finit del nucli són molt importants. Aquests efectes poden simular-se amb càlculs més simples a primer ordre a una densitat promig apropiada o amb una aproximació de densitat local. De tota manera, si el que un vol es afinar la interacció nua YN per tal de reproduir les dades espectroscòpiques, un càlcul directe de la interacció efectiva al hipernucli finit, com el que es proposa en aquesta tesi, és més adequat.

- Tot i que el mètode pot ser considerat com una manera alternativa de construir una interacció efectiva pel nucli finit, proporciona també la dependència completa en energia de l'autoenergia de l'hiperó.
- Els nostres resultats es comparen prou bé amb els resultats experimentals, i confirmem miscrocòpicament la petita separació de l'espín-òrbita.
- Hem obtingut un potencial Λ-nucli local de tipus Woods-Saxon amb una profunditat independent del nombre màssic A que reprodueix les energies monoparticulars de l'hiperó Λ en diversos hipernuclis. No obstant, les funcions d'ona obtingudes amb la nostra autoenergia no local són més esteses i poden ser simulades únicament quan permetem que potencial Woods-Saxon tingui un profunditat i un radi depenents d'A. Això pot tenir importants implicacions en els observables hipernuclears sensibles a les densitats nuclears de la superfície, com per exemple la desintegració mesònica dels hipernuclis Λ.

Finalment, com a extensió del nostre estudi del Capítol 2, al Capítol 4 hem realitzat un estudi microscòpic de l'estructura de la matèria β-estable amb graus de llibertat nucleònics i hiperònics.

- El model de potencial utilitzat (NSC987e) només permet la presència de dos tipus d'hiperons fins a densitats de l'ordre de set vegades la densitat de saturació de la matèria nuclear. Aquests hiperons són la Σ^- i la Λ. Les interaccions per estranyeses $S = -1, -2, -3$ i -4 no són suficientment atractives a fi de permetre la formació d'altres hiperons.

- Hem observat que la presència dels hiperons produeix una suavització de l'Equació d'Estat. Aquesta suavització influirà en el comportament de la matèria densa i en l'estructura dels estels de neutrons.

- El nostre resultat més innovador és que obtenim una suavització adicional de l'Equació d'Estat quan s'inclou l'efecte de la interacció hiperó-hiperó, perquè és atractiva sobre tot el rang de densitats explorat. Si aquesta suavització adicional és realista o no dependrà dels detalls de la interacció hiperó-hiperó que no està, desafortunadament, ben determinada actualment. Noves dades en el sector d'estranyesa $S = -2$, ja sigui obtingudes d'hipernuclis doble Λ o de àtoms Ξ^-, són molt desitjables.

- Aquesta suavització adicional de l'Equació d'Estat quan es tenen en compte totes les interaccions es tradueix en una reducció de la massa màxima de l'estel de neutrons de $2.11 M_\odot$, quan es consideren només graus de llibertat nucleònics, a $1.44 M_\odot$, quan s'inclou l'efecte dels hiperons.

Bibliography

[Al68] G. Alexander *et al.*, Phys. Rev. **173**, 1452 (1968).

[Ak97] Y. Akaishi and T. Yamazaki, Prog. Part. Nucl. Phys. **39**, 565 (1997).

[Ak97b] A. Akmal, V. R. Pandharipande, Phys. Rev. C **56**, 2261 (1997).

[Ak98] A. Akmal, V. R. Pandharipande, and D. G. Ravenhall, Phys. Rev. C **58**, 1804 (1998).

[Ba34] W. Baade and F. Zwicky, Phys. Rev. **45**, 138 (1934).

[Ba63] W. H. Barkas, M. A. Dyer and H. H. Heckman, Phys. Rev. Lett. **11**, 429 (1963).

[Ba78] C. J. Batty et al, Phys. Lett. **74B**, 27 (1978).

[Ba85] H. Bandō, K. Ikeda, T. Motoba, Y. Yamada and T. Yamamoto, Prog. Theor. Phys. Suppl. **81**, (1985).

[Ba90] H. Bandō, T. Motoba, and J. Žofka, Int. J. Mod. Phys. A **5**, 4021 (1990).

[Ba92] P. D. Barns, Nucl. Phys. A **547c**, 3 (1992).

[Ba94] C. J. Batty, E. Friedman and A. Gal, Phys. Lett. **335**, 273 (1994); Prog. Theor. Phys. Suppl. **117**, 227 (1994).

[Ba97] S. Balberg and A. Gal, Nucl. Phys. A **625**, 435 (1997).

[Ba97b] C. J. Batty, E. Friedman and A. Gal, Phys. Rep. **287**, 385 (1997).

[Ba98] M. Baldo, G.F. Burgio, and H.-J. Schulze, Phys. Rev. C **58**, 3688 (1998).

[Ba99] S. Balberg, I. Lichtenstadt, and G. B. Cook, Ap. J. Suppl. **121**, 515 (1999).

[Ba99b] S. Barziv *et al.*, (unpublished).

[Ba00] M. Baldo, G.F. Burgio, and H.-J. Schulze, Phys. Rev. C, **61**, 055801 (2000)

[Be56] H. A. Bethe, Phys. Rev. **103**, 1353 (1956).

[Be63] H. A. Bethe, B. H. Brandow and A. G. Petschek, Phys. Rev. **129**, 225 (1963).

[Be68] A. Bechdolff, G. Baumann, J. P. Gerber and P. Cüer, Phys. Lett. B **26**, 174 (1968).

[Be79] R. Bertini *et al.*, Phys. Lett. B **83**, 306 (1979); Nucl. Phys. A **360**, 315 (1981); Nucl. Phys. A **368**, 365 (1981).

[Bh63] B. Bhownik, Nuovo Cimento **29**, 1 (1963).

[Bl66] R. Blakenbecler and R. Sugar, Phys. Rev. **142**, 1051 (1966).

[Bo76] A. Bouyssy, J. Hüfner, Phys. Lett. **64B**, 276 (1976); A. Bouyssy, Phys. Lett. **84B**, 41 (1979).

[Bo91] I. Bombaci and U. Lombardo, Phys. Rev. C **44**, 1892 (1991).

[Bo92] M. Borromeo, D. Bonatsos, H. Müther and A. Polls, Nucl. Phys. A **539**, 189 (1992).

[Bo98] G. H. Bordbar and M. Modarres, Phys. Rev. C **57**, 714 (1998).

[Br54] K. A. Brueckner, Phys. Rev. **96**, 508 (1954); K. A. Brueckner and C. A. Levinson, Phys. Rev. **97**, 1344 (1955); K. A. Brueckner, Phys. Rev. **97**, 1353 (1955); K. A. Brueckner, C. A. Levinson and H. M. Mahmoud, Phys. Rev. **95**, 217 (1957).

[Br58] K. A. Brueckner and J. L. Gammel, Phys. Rev. **109**, 1023 (1958).

[Br60] K. A. Brueckner and D. T. Goldman, Phys. Rev. **117**, 207 (1960).

[Br75] W. Brückner *et al.*, Phys. Lett. B **55**, 107 (1975); Phys. Lett. B **62**, 481 (1976).

[Br76] G. E. Brown and A. D. Jackson, *The Nucleon-Nucleon interaction*, North-Holland, Amsterdam (1976).

[Br78] W. Brückner et al., Phys. Lett. B **79**, 157 (1978).

[Br79] G. E. Brown, in *Mesons in Nuclei* (M. Rho and D. H. Wilkinson, eds.), Vol. I, p. 330, North-Holland, Amsterdam (1979).

[Br81] R. Brockmann and W. Weise, Nucl. Phys. A **355**, 365 (1981).

[Ca69] J. Catala, F. Senent, A. F. Tejerina and E. Villar, *Proceedings on the Int. Conference on Hypernuclear Physics.*, vol 2, edited by A. R. Bodmer and L. G. Hyman pag. 758 (Argonne, 1969).

[Ch79] R. E. Chrien *et al.*, Phys. Lett. B **89**, 31 (1979); B. Povh, Nucl. Phys. A **335**, 233 (1980); M. May *et al.*, Phys. Rev. Lett. **47**, 1106 (1981).

[Ch91] M. Chiapparini, A.O. Gattone and B.K. Jennings, Nucl. Phys. A **529**, 589 (1991).

[Co90] J. Cohen, Prog. Part. Nucl. Phys. **25**, 139 (1990).

[Co94] G. B. Cook, S. L. Shapiro and S. A. Teukolsky, Astrophys. J. **424**, 823 (1994).

[Da53] M. Danysz and J. Pniewski, Phil. Mag. **44**, 348 (1953).

[Da63] M. Danysz *et al.*, Phys. Rev. Lett. **11**, 29 (1963).

[Da78] B. D. Day, Rev. Mod. Phys. **50**, 495 (1978).

[Da91] D. H. Davis, *Proc. of the LAMPF Workshop on* (π, K) *Physics*, AIP Conf. Proc. **224**, ed. by B. F. Gibson, W. R. Gibbs and M. B. Johnson, p. 38 (AIP, New York, 1991).

[Da99] J. Dabrowski, Phys. Rev. C **60**, 025205 (1999).

[Da99b] J. Dabrowski, Phys. Rev. C **61**, 025802 (1999).

[Do80] C. B. Dover, L. Ludeking and G.E. Walker, Phys. Rev. C **22**, 2073 (1980).

[Do83] C. B. Dover and A. Gal, Ann. Phys. (N.Y.) **146**, 309 (1983).

[Do89] C. B. Dover, D.J. Millener and A. Gal, Phys. Rep. **184**, 1 (1989).

[Do91] C. B. Dover *et al.*, Phys. Rev. C **44**, 1905 (1991).

[Ei71] J. Eisele *et al.*, Phys. Lett. B **37**, 204 (1971).

[En94] L. Engvik, M. Hjorth-Jensen, E. Osnes, G. Bao and E. Østgaard, Phys. Rev. Lett. **73**, 2650 (1994).

[El95] P. J. Ellis, R. Knorren and M. Prakash, Phys. Lett. B **349**, 11 (1995).

[El96] Ø. Elgarøy, L. Engvik, M. Hjorth-Jensen and E. Osnes, Phys. Rev. Lett. **77**, 1421 (1996).

[En66] R. Engelmann *et al.*, Phys. Lett. **21**, 587 (1966).

[En96] L. Engvik, M. Hjorth-Jensen, E. Osnes, G. Bao and E. Østgaard, Astrophys. J. **469**, 794 (1996).

[En99] L. Engvik, Ph. D. Thesis, University of Oslo, January 1999, unpublished.

[Fe89] F. Fernández, T. López-Arias and C. Prieto, Z. Phys. A **334**, 349 (1989).

[Fu98] T. Fukuda *et al.*, Phys. Rev. C **58**, 1306 (1998).

[Ga77] A. Gal, Adv. Nucl. Sci. **8**, 1 (1977).

[Gi88] B. F. Gibson and D. R. Lehman, Phys. Rev. C **37**, 679 (1988).

[Gi95] B.F. Gibson and E.V. Hungerford, Phys. Reports **257**, 349 (1995).

[Gl82] N. K. Glendenning, Phys. Lett B **114**, 392 (1982).

[Gl85] N. K. Glendenning, Astrophys. J. **293**, 470 (1985).

[Gl87] N. K. Glendenning, Z. Phys. A **326**, 57 (1987).

[Gl92] N. K. Glendenning, Phys. Rev. D **46**, 1274 (1992).

[Gl93] N.K. Glendenning, D. Von-Eiff, M. Haft, H. Lenske and M.K. Weigel, Phys. Rev. C **48**, 889 (1993).

[Gl97] N. K. Glendenning, *COMPACT STARS, Nuclear Physics, Particle Physics, and General Relativity*, (Springer-Verlag, New York, 1997).

[Go57] J. Goldstone, Proc. Roy. Soc. A **293**, 267 (1957).

[Go68] T. Gold, Nature **218**, 731 (1968).

[Go75] D. Gogny, Nucl. Phys. A **237**, 399 (1975); *Proceeding of the International Conference on Nuclear Self-consistent Fields*, Trieste, 1975. G. Ripka and M. Porneuf, Eds. North Holland, Amsterdam, 1975.

[Gr88] C. Greiner *et al.*, Phys. Rev. D **38**, 2797 (1988).

[Ha67] J. B. Hartle, Ap. J. **150**, 1005 (1967).

[Ha70] M. I. Haftel and F. Tabakin, Nucl. Phys. A **158**, 1 (1970).

[Ha89] R.S. Hayano et al, Nuovo Cimento 102A (1989) 437; Phys. Lett. B **231**, 355 (1989).

[Ha90] T. Harada, S. Shinmura Y. Akaishi and H. Tanaka, Nucl. Phys. A **507**, 715 (1990).

[Ha93] D. Halderson, Phys. Rev. C **48**, 581 (1993).

[Ha93b] J. Hao, T.T.S. Kuo, A. Reuber, K. Holinde, J. Speth and D.J. Millener, Phys. Rev. Lett. **71**, 1498 (1993).

[Ha96] T. Hasegawa et al, Phys. Rev. C **53**, 1210 (1996).

[He68] A. Hewish, S. J. Bell, J. D. H. Pilkington, P. F. Scott and R. A. Collins, Nature **217**, 709 (1968).

[He93] H. Heiselberg, C. J. Pethick and E. F. Staubo, Phys. Rev. Lett. **70**, 1355 (1993).

[He94] H. Heiselberg, C. J. Pethick and E. F. Staubo, Nucl. Phys. A **566**, 577c (1994).

[He99] H. Heiselberg and M. Hjorth-Jensen, Phys. Rep. **328**, 237 (2000); Ap. J., **525**, L41 (1999).

[Hj94] M. Hjorth-Jensen, H. Müther and A. Polls, Phys. Rev. C **50**, 551 (1994).

[Hj96] M. Hjorth-Jensen, A. Polls, A. Ramos and H. Müther, Nucl. Phys. A **605**, 458 (1996).

[Ho75] K. Holinde and R. Machleidt, Nucl. Phys. A **247**, 495 (1975).

[Ho89] B. Holzenkamp, K. Holinde, and J. Speth, Nucl. Phys. A **500**, 485 (1989).

[Hu94] E. V. Hungerford, Prog. Theor. Phys. Supll. **117**, 135 (1994).

[Hu98] H. Huber, F. Weber, M. K. Weigel and C. Schaab, Int. J. Mod. Phys. E **7**, 301 (1998).

[In96] F. Ineichen, D. Von-Eiff and M. K. Weigel, J. Phys. **G22**, 1421 (1996).

[Ja55] R. Jastrow, Phys. Rev. **98**, 1479 (1955).

[Je74] J. P. Jeukenne, A. Lejeune and C. Mahaux, Phys. Rev. C **10**, 1391 (1974).

[Je76] J. P. Jeukenne, A. Lejeune and C. Mahaux, Phys. Rep. **25**, 83 (1976).

[Ju73] M. Juric *et al.*, Nucl. Phys. B **52**, 1 (1973).

[Ka71] J. A. Kadyk *et al.*, Nucl. Phys. B **27**, 13 (1971).

[Ka86] D. B. Kaplan and A. E. Nelson, Phys. Lett. B **291**, 57 (1986).

[Ka96] V. Kalogera, G. Baym, Astrophys. J **470**, L61 (1996).

[Ka97] P. Kaaret, E. C. Ford, and K. Chen, Ap. J. **480**, L27 (1997).

[Ke95] M. H. van Kerwijk, J. van Paradijs and E. J. Zuiderwijk, Astron. Astrophys. **303**, 497 (1995).

[Kh00] P. Khaustov *et al.*, Phys. Rev. C **61** 054603 (2000).

[Kn95] R. Knorren, M. Prakash, and P. J. Ellis, Phys. Rev. C **52**, 3470 (1995).

[Ko99] U. van Kolck, Prog. Part. Nucl. Phys. **43**, 337 (1999).

[Ku79] C.L. Kung, T.T.S. Kuo and K.F. Ratcliff, Phys. Rev. C **19**, 1063 (1979).

[Ku95] I. Kumagai-Fuse, S. Okabe and Y. Akaishi, Phys. Lett. B **345**, 386 (1995).

[La91] J. Lattimer, C. Pethick, M. Prakash and P. Haensen, Phys. Lett. **66**, 2701 (1991).

[La97] D.E. Lanskoy and Y. Yamamoto, Phys. Rev. C **55**, 2330 (1997).

[Lo93] C. P. Lorenz, D. G. Ravenhall and C. J. Pethick, Phys. Rev. Lett. **70**, 379 (1993).

[Lo95] R.J. Lombard, S. Marcos and J. Mareš, Phys. Rev. C **51**, 1784 (1995).

[Ma80] C. Mahaux, *Brueckner theory of Fermi systems*, in the Proceedings of the Third Topical School, Granada (Spain) p. 50. Edited by R. Guardiola and J. Ros (Springer Verlag, 1980).

[Ma87] R. Machleidt, K. Holinde and Ch. Elster, Phys. Rep. **149**, 1 (1987).

[Ma89] P. M. M. Maessen, T. A. Rijken, and J. J. de Swart, Phys. Rev. C **40**, 2226 (1989).

[Ma89b] J. Mareš and J. Žofka, Z. Phys. A **33**, 209 (1989).

[Ma94] J. Mareš and B. K. Jennings, Phys. Rev. C **49**, 2472 (1994).

[Ma95] J. Mareš, E. Friedman, A. Gal and B. K. Jennings, Nucl. Phys. A **594**, 311 (1995).

[Ma96] Z. Ma, J. Speth, S. Krewald, B. Chen and A. Reuber, Nucl. Phys. A **608**, 305 (1996).

[Mi67] A. B. Migdal, *Theory of Fermi Systems and Applications to Atomic Nuclei*, Wiley Interscience, New York, 1967.

[Mi73] C. W. Misnes, K. S. Thorne and J. A. Wheeler, *Gravitation* (W. H. Freeman, San Francisco, 1973).

[Mi88] D. J. Millener, C. B. Dover and A. Gal, Phys. Rev. C **38**, 2700 (1988).

[Mi93] K. Migayawa and W. Glöckle, Phys. Rec. C **48**, 2576 (1993).

[Mi95] K. Migayawa, H. Kamada, W. Glöckle and V. Stoks , Phys. Rec. C **51**, 2905 (1995).

[Mi98] M. C. Miller, F. K. Lamb, and P. Psaltis, Ap. J. **508**, 791 (1998).

[Mo53] P. M. Morse and H. Feshbach, *Methods of Theoretical Physics*, (McGraw-Hill, New York, 1953).

[Mo79] A. S. Mondal, A. K. Basak, M. M. Kasim and A. Husain, Nuovo Cimento A **54**, 333 (1979).

[Mo88] T. Motoba, H. Bandō, R. Wünsch and J. Žofka, Phys. Rev. C **38**, 1322 (1988).

[Mo91] T. Motoba, H. Bandō, T. Fukuda and J. Žofka, Nucl. Phys. A **534**, 597 (1991).

[Na69] N. Nakanishi, Prog. Theor. Phys. (Kyoto), Suppl. **43**, 1 (1969).

[Na73] M. M. Nagels, Th. A. Rijken and J. J. de Swart, Phys. Rev. Lett. **31**, 569 (1973).

[Na77] M. M. Nagels, Th. A. Rijken and J. J. de Swart, Phys. Rev. D **15**, 2547 (1977).

[Na78] M. M. Nagels, Th. A. Rijken and J. J. de Swart, Phys. Rev. D **17**, 768 (1978).

[Na98] T. Nagae et al, Phys. Rev. Lett. **80**, 1605 (1998).

[Ne72] J. W. Negele and D. Vautherin, Phys. Rev. C **5**, 1472 (1972).

[Op39] J. R. Oppenheimer and G. M. Volkoff, Phys. Rev. **55**, 374 (1939).

[Or99] J.A. Orosz and E. Kuulkers, Mon. Not. R. Astron. Soc., in press and astro-ph/9901177.

[Os90] E. Oset, P. Fernández de Córdoba, L.L. Salcedo and R. Brockmann, Phys. Reports **188**, 79 (1990).

[Os98] E. Oset and A. Ramos, Prog. Part. Nucl. Phys. **41**, 191 (1998).

[Pa73] *Proceedings Summer Study Meeting on Nuclear and Hypernuclear Physics with Kaon beams*, BNL report **18335**, edited by H. Palevsky (1973).

[Pa99] S. Pal, M. Hanauske, I. Zakout, H. Stöker and W. Greiner, Phys. Rev. C **60**, 015802 (1999).

[Pa99b] J. van Paradijs, astro-ph/9802177 and in: *The Many Faces of Neutron Stars*, Eds. R. Buccheri, J. van Paradijs and M.A. Alpar, (Kluwer, Dordrecht, 1999) in press

[Pe95] C. J. Pethick, D. G. Ravenhall and C. P. Lorenz, Nucl. Phys. A **584**, 675 (1995).

[Pi91] P.H. Pile et al, Phys. Rev. Lett. **66**, 2585 (1991).

[Po78] B. Povh, Ann. Rev. Nucl. Part. Sci. **28**, 1 (1978).

[Pr66] D. J. Prowse, Phys. Rev. Lett. **17**, 782 (1966); M. Danysz et al., Nucl. Phys. **49**, 121 (1963) reanalized in R.H. Dalitz, Proc. Roy. Soc. London A **426**, 1 (1989); S. Aoki et al., Prog. Theor. Phys. **85**, 1287 (1991); G. B. Franklin, Nucl. Phys. A **585**, 83c (1995).

[Pr97] M. Prakash, I. Bombaci, M. Prakash, P. J. Ellis, J.M. Lattimer, and R. Knorren, Phys. Rep. **280**, 1 (1997).

[Ra63] R. Rajaraman, Phys. Rev. **131**, 1244 (1963); H. A. Bethe, Phys. Rev. **138**, B804 (1965); R. Rajaraman and H. A. Bethe, Rev. Mod. Phys. **39**, 745 (1967).

[Ri99] Th. A. Rijken, V. G. J. Stoks, and Y. Yamamoto, Phys. Rev. C **59**, 21 (1999).

[Sa98] R. Sawafta, Nucl. Phys. A **639**, 103c (1998); S. Bart *et al.*, Phys. Lett. **83**, 5238 (1999).

[Sc93] J. Schaffner, C. B. Dover, A. Gal, D. J. Millener, C. Greiner and H. Stöker, Phys. Rev. Lett. **71**, 1328 (1993).

[Sc94] J. Schaffner, C. B. Dover, A. Gal, D. J. Millener, C. Greiner and H. Stöker, Ann. Phys. (N.Y.) **235**, 35 (1994).

[Sc95] H.-J. Schulze, A. Lejeune, J. Cugnon, M. Baldo and U. Lombardo, Phys. Lett. B **355**, 21 (1995).

[Sc96] J. Schaffner and I. Mishustin, Phys. Rev. C **53**, 1416 (1996).

[Sc98] H.-J. Schulze, M. Baldo, U. Lombardo, J. Cugnon, and A. Lejeune, Phys. Rev. C **57**, 704 (1998).

[Se68] B. Sechi-Zorn *et al.*, Phys. Rev. **175**, 1735 (1968).

[Se86] B. D. Serot and J. D. Walecka, Adv. Nucl. Phys. **16**,1 (1986).

[Se97] B. D. Serot and J. D. Walecka, Int. J. Mod. Phys. E **6**, 515 (1997).

[Sh83] S. L. Shapiro and S. A. Teukolsky, *Black Holes, White Dwarfs and Neutron Stars*, (John Wiley & Sons, New York, 1983).

[Sk56] T. H. R. Skyrme, Phylos. Mag. **1**, 1043 (1956); Nucl. Phys. A **9**, 615 (1959).

[So98] H. Q. Song, M. Baldo, G. Giansiracusa and U. Lombardo, Phys. Rev. Lett. **81**, 1585 (1998).

[St93] U. Straub, J. Nieves, A. Faessler and E. Oset, Nucl. Phys. A **556**, 531 (1993).

[St94] V. G. Stoks, R. A. M. Klomp, C. P. F. Terheggen and J. J. de Swart, Phys. Rev. C **49**, 2950 (1994).

[St99] V. G. J. Stoks and Th. A. Rijken, Phys. Rev. C **59**, 3009 (1999).

[St99b] V. G. J. Stoks and T.-S. H. Lee, Phys. Rev. C **60**, 024006 (1999).

[Su94] Y. Sugahara and H. Toki, Prog. Theor. Phys. **92**, 803 (1994).

[Sz91] J. J. Szymanski et al., Phys. Rev. C **43**, 849 (1991).

[Th70] R. H. Thompson, Phys. Rev. D **1**, 110 (1970).

[Th99] S. E. Thorsett and D. Chakrabarty, Ap. J. **512**, 288 (1999).

[To39] R. C. Tolman, Phys. Rev. **55**, 364 (1939).

[Ts97] K. Tsushima, K. Saito and A. W. Thomas, Phys. Lett. B **411**, 9 (1997); K. Tsushima, K. Saito, J. Haidenbauer and A. W. Thomas, Nucl. Phys. A **630**, 691 (1998).

[Va72] D. Vautherin and D. M. Brink, Phys. Rev. C **5**, 626 (1972).

[Vi98] I. Vidaña, A. Polls, A. Ramos, and M. Hjorth-Jensen, Nucl. Phys. A **644**, 201 (1998).

[Vi00] I. Vidaña, A. Polls, A. Ramos, M. Hjorth-Jensen, and V. G. J. Stoks, Phys. Rev. C **61**, 025802 (2000) .

[Vi00b] I. Vidaña, A. Polls, A. Ramos, L. Engvik and M. Hjorth-Jensen, Phys. Rev. C **62**, 035801 (2000) .

[Vi01] I. Vidaña, A. Polls, A. Ramos and H.-J. Schulze, submited to Phys. Rev. C.

[We67] S. Weinberg, Phys. Rev. Lett. **18**, 188 (1967).

[We72] S. Weinberg, *Gravitation and Cosmology* (John Wiley & Sons, New York, 1972).

[We91] F. Weber, N. K. Glendenning and M. K. Weigel, Astrophys. J. **373**, 579 (1991); in *Rotating Neutron Stars and the Equation of State of Dense Matter*, p. 309. Eds. W.Y. Pauchy Hwang, Shik-Chang Lee, Chin-Er Lee and D.J. Ernst, (Elsevier, Amsterdam, 1991).

[Wi59] D. H. Wilkinson, S. J. St. Lorant, D. K. Robinson and S. Lokanathan, Phys. Rev. Lett. **3**, 397 (1959).

[Wi88] R. B. Wiringa, V. Fiks and A. Fabrocini, Phys. Rev. C **38**, 1010 (1988).

[Wi95] R. B. Wiringa, V. G. J. Stoks, and R. Schiavilla, Phys. Rev. C **51**, 38 (1995).

[Wo72] C.W. Wong and D.M. Clement, Nucl. Phys. A **183**, 210 (1972).

[Wo73] R. Woloshyn and A. D. Jackson, Nucl. Phys. B **64**, 269 (1973).

[Ya85] Y. Yamamoto and H. Bandō, Prog. Theor. Phys. Suppl. **81**, 9 (1985).

[Ya88] Y. Yamamoto, H. Bandō and J. Žofka, Prog. Theor. Phys. **80**, 757 (1988).

[Ya90] Y. Yamamoto and H. Bandō, Prog. Theor. Phys. **83**, 254 (1990).

[Ya92] Y. Yamamoto, A. Reuber, H. Himeno, S. Nagata and T. Motoba, Czec. Jour. Phys. **42**, 1249 (1992).

[Ya94] Y. Yamamoto, T. Motoba, H. Himeno, K. Ikeda and S. Nagata, Prog. Theor. Phys. Suppl. **117**, 361 (1994).

[Zh98] W. Zhang, T. E. Strohmayer, and J. H. Swank, Ap. J. **482**, L167 (1997); W. Zhang, A. P. Smale, T. E. Strohmayer, and J. H. Swank, Ap. J. **500**, L171 (1998).